University of Nottingham

School of Mathematical Sciences

Plant calcium dynamics: signalling the way to sustainable food production

Hayley Mills

PhD Mathematics

May 2021

Acknowledgements

There are many people I would like to thank for making this thesis possible. Thank you to my supervisors Dr Rüdiger Thul and Prof Stephen Coombes for all of your help and guidance. To my supervisor Dr Darren Wells for training me in experimental work from scratch and for always sharing your infectious enthusiasm. To Prof Marc Knight and team for hosting me at Durham University and helping to develop our experimental procedure. To Prof Simon Gilroy and Dr Thomas Defalco for supplying the seeds used in the experiments. To Dr Nick Redman for supporting with microscopy and creating the FlowCell. To Emma for so generously sharing your time and experience in my first years and becoming a great friend along the way. To the entire MASS community for the support, the laughs, and giving me a research group that feels like home. To my Mum and Dad for making me believe that I can do anything, and for teaching me the foundation of my mathematical knowledge, that $x = 2$. To Mum and Dad Mills for your love and unwavering support. Finally, to Steve, for sharing in every single high and low of this work as if it were your own.

Abstract

In this work we explore the calcium signalling pathway mediating symbiotic associations between legumes and Nitrogen-fixing bacteria. This symbiotic process has been identified as a possible 'biological' alternative to using environmentally damaging synthetic fertilisers in crop production. Therefore, motivated by the challenge of ensuring worldwide food security whilst utilising increasingly degraded soils, we look to advance the knowledge of the signalling pathway that facilitates nodulation in order to progress towards the transfer of this favourable trait from legumes to cereal crops.

A mathematical model representing the flux and diffusion of calcium in the plant cell nucleus was derived for up to 3-dimensions in both spherical and prolate spheroidal coordinates. Our final model is the first 3-dimensional representation of nuclear plant calcium signalling. It is also the first to reproduce the exact spiking dynamics reported in the literature, without the need for any additional inputs such as refractory periods or buffers. In a novel and exciting finding, we show that nuclear calcium oscillations can be generated autonomously provided that the channels which facilitate them form clusters. The resulting calcium signatures are presented for clustered and distributed channels and we examine the microdomains over which these patterns occur. It is also found that the formation of these microdomains is necessary for calcium concentrations to exceed the binding threshold of downstream sensory protein CCaMK. This provides new insight into the possible mechanism of generation of the nuclear calcium signature, suggesting a potential multi-functional role for cluster formation.

The mathematical method through which this was achieved involved solving the heat equation semi-analytically in order to obtain a series of Green's functions. This provides us with a useful 3-dimensional framework which allows us to perform simulations significantly faster than could be achieved through traditional finite-element methods.

An experimental methodology, using plant lines expressing GCAMP suspended in a FlowCell device, was developed in order to successfully image calcium signalling over longer times, with easier stimulus application. This was used to compare the calcium response in *Arabidopsis thaliana*, hereby Arabidopsis, with *Nicotiana benthamiana* highlighting the difference in calcium signalling between species with and without nodulation abilities. Original data on the geometry of the nucleus was collected for parameterisation of our model. Analysis of this data revealed statistically significant differences in nuclear morphology between cortical and root hair cells and also revealed a correlation between the nuclear morphology of cells in the elongation zone and their distance from the root apex.

Abbreviations

AM - Arbuscular mycorrhiza(l)

CaM - Calmodulin

CCaMK - Calcium/calmodulin-dependent protein kinase

CICR - Calcium-induced calcium release

CNGC - Cyclic nucleotide-gated channel

CSP - Common symbiotic pathway

FDF - Fire-diffuse-fire

FRET - Fluorescence resonance energy transfer

INM - Inner nuclear membrane

MS - Murashige and Skoog media

NE - Nuclear envelope

NPC - Nuclear pore complex

NupYC - Nucleoplasmin-tagged yellow cameleon

ODE - Ordinary differential equation

ONM - Outer nuclear membrane

PDE - Partial differential equation

PM - Plasma membrane

PNS - Perinuclear space

PSWF - Prolate spheroidal wave-function

SERCA - Sarco/endoplasmic reticulum calcium ATPase

VM - Vacuolar membrane

YC - Yellow cameleon

Y/G/R/CFP - Yellow/Green/Red/Cyan fluorescent protein

CONTENTS

1

INTRODUCTION

1.1 THESIS OVERVIEW

This work begins with a discussion of the motivation of the project with respect to its wider context within sustainability. We explore the challenge of ensuring worldwide food security whilst utilising the increasingly degraded soils available for crop production, with a view to developing more sustainable ‘biological’ solutions. This is in contrast to the current practice of supplementing our soils with environmentally damaging synthetic fertilisers, the manufacture of which produces emissions that contribute towards climate change, contaminated water supplies and dead zones in our oceans. We highlight long-standing proposals, first appearing in the literature in the 1917 paper "Is symbiosis possible between legume bacteria and non-legume plants?" [19], to transfer to agriculturally important cereal crops the ability of leguminous plants to fulfil their nutritional requirements through mutually-beneficially relationships with ‘Nitrogen-fixing’ bacteria. In order to achieve this, the calcium signalling pathway which mediates these interactions at a cellular level must be unravelled, and it is this component that is the focus of this thesis.

The details of the calcium signalling pathway known to date will be covered in a review of the literature in Chapter 2. This, predominately biological, review will begin with a background description of calcium signalling including how these signals are generated through coordinated storage and release between cellular compartments. We will then narrow our focus to the nuclear compartment, where symbiosis signalling is generally accepted to occur, and the current understanding in relation to our application. In regards to mathematical modelling, the field remains comparatively unexplored. However, limited modelling attempts have been made and will also be covered in this chapter.

The mathematical background will be explored in Chapter 3, where the theory and derivation of Green's functions in one and two dimensions will be shown for varying boundary conditions. This will introduce the method of solving the heat equation semi-analytically in order to obtain a Green's function. This methodology is key to our approach as it allows for increased efficiency of numerical simulations. This occurs through modelling the diffusion of calcium concentration through the plant cell nucleus by taking a source concentration and applying a ready-made diffusion profile at each time-step. We will also look here at the special functions required when using this method as these will provide the basis of those necessary for the full 3D model.

Chapter 4 then builds upon this theory to produce the full 3D representation of the two nuclear compartments, the nucleoplasm and its surrounding perinuclear space, involved in signal-generation. This is applied to both spherical and spheroidal coordinate systems, with the full details of the calculations left to Appendices A and B, respectively. To complete the model, we describe how this system of Green's functions is coupled through the fluxes between them. This requires the channels and pumps, found on the adjoining membrane, to be modelled by equations describing the mechanism of calcium release and sequestration and to be applied to our model as non-constant boundary conditions. We show the dynamics of the pump and channel system in the absence of diffusion, demonstrating the importance of including the spatial component in our modelling.

The details behind how our Green's functions work computationally are given in Chapter 5. Here we look at how our functions are checked numerically in order to ensure correct levels of convergence for a chosen truncation of the infinite sum, whilst providing graphs of our successful checks and some test simulations in each dimension. It is also shown how the method is limited by numerical difficulties in computing some of the more complicated special functions, with examples of those encountered during experimentation and supported by the literature.

Methodology and results of experimental work can be found in Chapter 6 where we describe the biological experiments undertaken to support our modelling work through parameterisation and comparison of results. Firstly, we look at how the real geometric data was generated to be input into the model followed by an in-depth analysis of those findings as we quantify the nuclear morphology within and between cell types. Secondly, details of the experimental process developed for measuring the calcium response are provided along with results of these experiments in two plant species, comparing the calcium signature in *N.benthamiana*, which is able to undergo nodulation, to Arabidopsis which does not. This section also includes a table of parameter values collected from the literature which were used as input into the mathematical models.

The simulation results generated from the numerical evaluation of the mathematical model can be seen in Chapter 7. The key objective of this chapter was to explore varying influx distributions, in particular by creating 'clusters' of channels. The resulting calcium signatures are presented for clustered and distributed channels and we examine the microdomains over which these patterns occur. This provides a new insight into the possible mechanism of generation of the nuclear calcium signature.

Each non-introductory chapter will conclude with a summary of outcomes from that body of work, whilst a more thorough discussion of the key findings of this thesis can be found in Chapter 8. Here we also include suggestions for future work which could be completed in order to bring us ever closer to unravelling nuclear calcium signalling in plants and hence transforming this knowledge into a viable tool for sustainable food production.

1.2 BACKGROUND MOTIVATION

1.2.1 *The food security problem*

World agricultural demand for soil nitrogen compounds is currently increasing at a rate of 1.4% year on year [5], a problem accentuated by increasingly infertile soils which are incapable of supporting plant growth due to their undesirable physical, chemical or biological characteristics. To tackle this problem, and meet food requirements, vast amounts of synthetically pro-

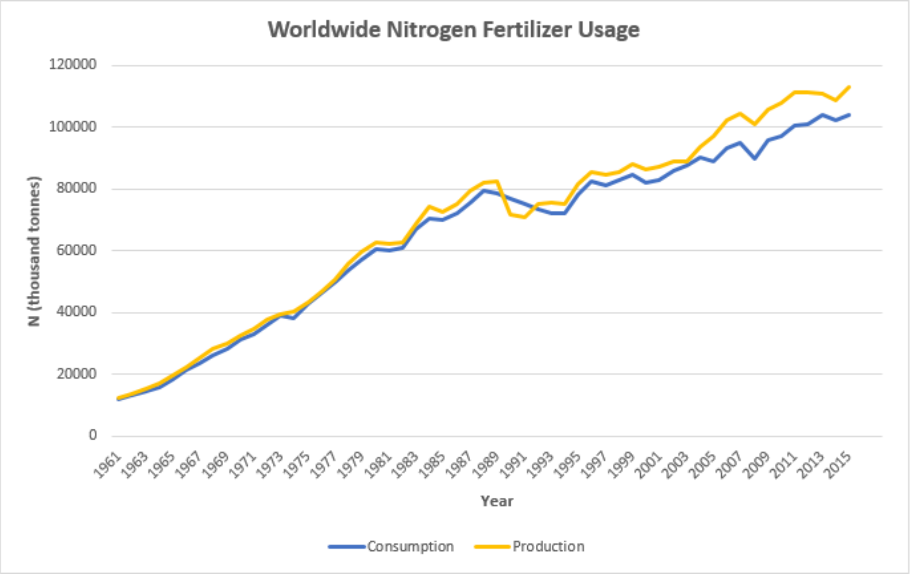

Figure 1.: The upwards trend in nitrogen production required to meet the demands of an expanding population. Data from the IFA [52].

duced chemical fertilizers are applied to crops. As seen in Figure. 1, fertilizer production increased more than 10 fold between 1961-2015, a trend that is only bound to continue in an effort to feed the projected 2 billion population increase by 2050 [52].

The International Fertilizer Association (IFA) estimates that nitrogen fertilizer application accounts for the sustenance of around 40% of the world's population, however they have also acknowledged that the resultant environmental costs are no longer considered sustainable. This is due to fertilizer over-usage being "proven to cause a number of environmental and ecological problems" [59], with nitrous oxide damage from fertilizer production costing Europe £60−80 billion per year. In addition to the release of harmful greenhouse gases into the atmosphere, production of nitrogen fertilizers is costly and energy-expensive. Other problems include soil acidification and degradation, water eutrophication and even crop yield reductions [59]. Furthermore, runoff of fertilizers from crop fields into rivers means that 5% of the European population are exposed to drinking water contaminated with unsafe levels of nitrate. A well-known example of the effects of fertilizer run-off is the Gulf of Mexico dead zone as seen in Figure. 2. The low oxygen area, which reached a record 8,776 square miles in 2017 [3], is caused by an increased nitrate load producing huge algal blooms which eventually decompose, using up oxygen. Once levels become hypoxic (red areas in Figure. 2) these zones are unsuitable habitats to support marine life.

1.2.2 *Plant-microbe symbiosis*

Alternative solutions are therefore being sought, most famously the replacement of chemical fertilisers with naturally occurring biological systems. Despite the huge amounts of nitrogenous fertilisers applied to our crops, nitrogen actually makes up 78% of the surrounding atmosphere. This is not however, in a form that can be used as a nutrient source by most plants.

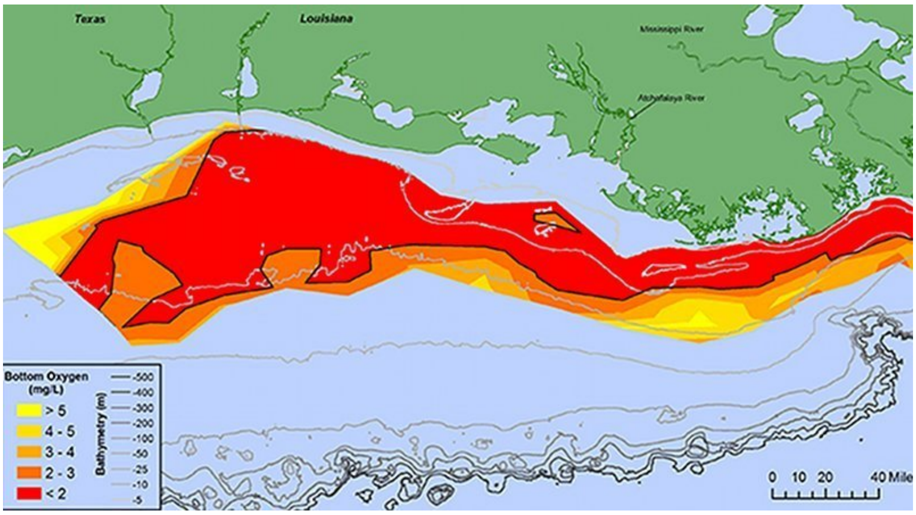

Figure 2.: The Gulf of Mexico dead zone. Red areas indicate a dissolved oxygen concentration of less than 2mg/L - the level at which marine life becomes unsustainable. Figure from the National Atmospheric and Oceanic Administration website [3].

The exception is the *Leguminosae* family, which includes beans and peas, who are able to 'fix' nitrogen symbiotically through a mutually beneficial relationship with *Rhizobial* bacteria. This natural biological process has long been postulated as a possible and highly desirable replacement for nitroge-

Figure 3.: Root nodules formed on the root of the runner bean *Phaseoluscoccineus*. Figure from 'Beyond the Human Eye' blog by Phil Gates [1].

nous fertilisers. In these associations *Rhizobia* are housed in nodules on root hairs of the plant, depicted in Figure. 3, which form on receipt of chemical signals from the bacteria. Here the bacteria gain sugars from the legume, and in return they convert the inert atmospheric di-nitrogen (N_2) into forms such as ammonia (NH_3), which is required for growth and development of vital plant tissues and structures. The *Nitrogenase* enzyme, possessed by *Rhizobia*, is necessary for this nitrogen reduction although it is deactivated by oxygen. Organogenesis is therefore a vital part of this process as the root nodules shield this crucial enzyme from harmful oxygen exposure.

The intermediary signalling molecule, governing these plant-rhizobial interactions, is calcium (Ca^{2+}). There is therefore a need to unravel the calcium signalling pathway if we are to transfer this special ability to cereal crops, by, for example, establishing symbiotic association through synthetically generated root nodules on wheat. In the following literature review we will detail our current understanding of this pathway, in terms of the signal from the bacteria, the resultant spatio-temporal calcium profile and how this calcium pattern (or signature) is sensed and decoded to lead to downstream gene transcription. A model will then be formulated, focusing on discovering the specific details of the mechanism behind calcium signal generation in symbiosis.

2

LITERATURE REVIEW

In this section we will review the relevant literature, beginning with a more general overview of plant calcium signalling before narrowing our focus to nuclear plant calcium signalling and finally our specific application in symbiosis. After covering the up-to-date knowledge of our topic, we will go on to review the current progress made in the mathematical modelling of nuclear plant calcium signal generation and, in particular, identify the gaps in the literature and the necessary next steps.

2.1 CALCIUM SIGNALLING IN PLANTS

In plants cells, many developmental and environmental factors are coordinated through a calcium (Ca^{2+}) signalling pathway. It has been shown that dehydration, salt and oxidative stress induce stimulus-specific spatiotemporal patterns of calcium in the cytosol [93] and it is also well documented in the literature that cytosolic calcium gradients drive growth of root hairs [65, 20, 75, 8, 13] and pollen tubes [22, 49, 90, 9, 37]. Experimental techniques use fluorescent markers bound to calcium which show varying light intensities upon binding to a calcium buffer. These can be viewed and measured using confocal microscopy and used as a proxy to reflect variations in calcium concentration. As demonstrated in Figure. 4, both pollen tube elongation (4a) and root hair growth (4b) correspond to a maximal calcium concentration at the structures apex, with the absence of a gradient synonymous with no growth or growth cessation.

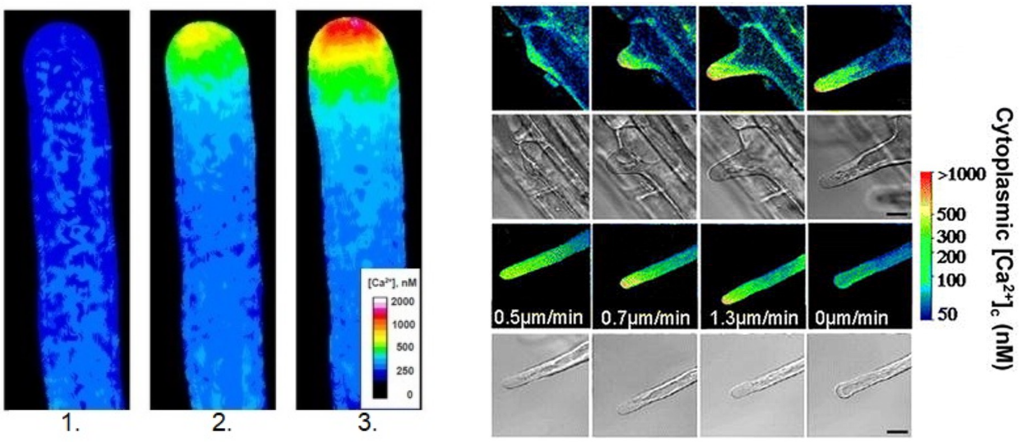

(a) Pollen tubes.

(b) Root hairs.

Figure 4.: (a) Spatial distribution of [Ca^{2+}] in a growing pollen tube shown at three time points: (1) minimal cytoplasmic Ca^{2+} throughout the cell, corresponding to no growth, (2) initial establishment of the tip [Ca^{2+}] gradient even while growth remains minimal, (3) significant [Ca^{2+}] gradient during growth, with the maximum concentration at the tip. Figure from Winship (2017) [90]. (b) The top row shows the cytoplasmic free calcium concentration gradient established in initial root hair branching. The third row is a time course showing the tip-focused calcium gradient in an elongating root hair, and its disappearance when growth ceases. Figure from Grierson (2014) [45].

Figure 5.: The calcium signalling pathway.

2.1.1 *The calcium signalling pathway*

A general calcium signalling pathway is described by Berridge (2000) to be made up of four functional units: the perception of an external biotic or abiotic stimulus; the generation of a specific calcium concentration profile; the decoding of this signature by sensory proteins; and the resultant cellular response [12]. In plants the signal often pertains to environmental conditions such as osmotic stress, wind or the presence of pathogens. After this stage the pathway is similar to that in animal cells, although we note that plants possess a distinct toolkit with their own individual set of channels, messengers and mechanisms [57]. The recognition of a stimulus leads to elevations in calcium concentration of a unique amplitude, duration, frequency and spatial distribution - together called the calcium signature - which encode for the particular scenario detected. Importantly we note that specificity of the calcium signature requires both spatial and temporal components, and hence it is local changes in calcium concentration that facilitate the specific response to a stimulus [83].

Along with the calcium signature, a further layer of specificity is obtained through the presence, concentration, spatial localization and binding affinities of sensory proteins. These molecules generally belong to one of two major classes: sensor relays such as Calmodulin (CaM); and sensor responders such as calcium dependent protein kinase (CDPK). Both types contain the “EF hand" motif - a high-affinity Ca^{2+}-binding domain [31] - which allows them to form a complex with calcium. Mechanistically, complex formation causes a conformational change in the structure of the sensory protein, allowing binding with a promoter for gene transcription (CaM) or a change in enzyme activity for protein phosphorylation (CDPK). Binding of calcium by sensory proteins depends on their individual thresholds, or association constants, which, once surpassed, triggers a signalling cascade of chemical reactions ultimately translating the signal into a molecular or biochemical response [54].

2.1.2 *Compartmentalized signalling*

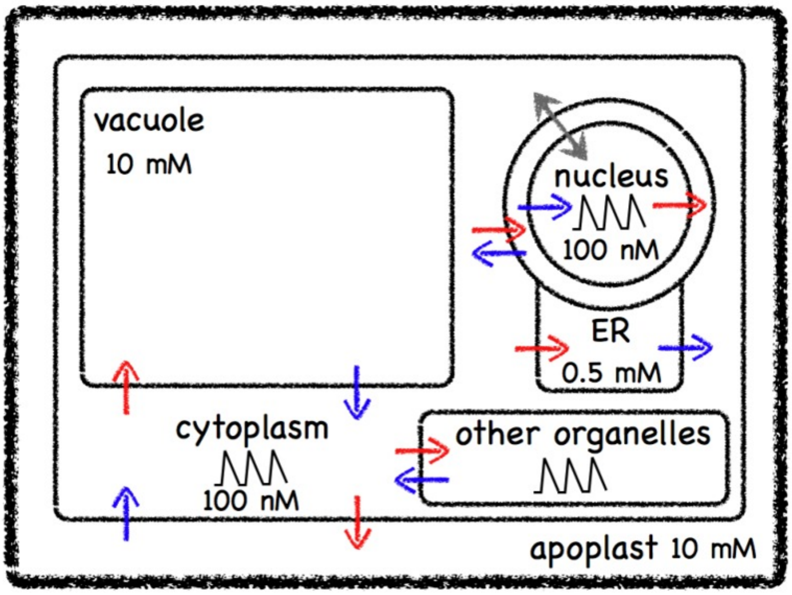

Figure 6.: Cellular compartments in a plant cell, with typical calcium concentrations given in each domain. Calcium moves between compartment's against the concentration gradient by pumps (red arrows) and diffuses along the concentration gradient through channels (blue arrows). Figure from Vaz Martins (2013) [60].

The sequestration of calcium, against the concentration gradient, into organelles such as the vacuole and the endoplasmic reticulum (ER) allows these compartments to act as calcium stores. In these domains the calcium concentrations are orders of magnitude higher than the rest of the cell. This is demonstrated in Figure. 6 which shows concentrations in the calcium stores to typically reside in the millimolar (mM) range as compared to around only 100 nanomolar (nM) in the cytoplasm and nucleoplasm. Compartmentalisation provides a means of generating a calcium signature by the opening or closing of the calcium channels on compartment boundaries, shaping the specific concentration pattern through controlling the delicate balance in influx and efflux between domains.

Influx into the cytoplasm is controlled by voltage-dependent and ligand-dependent ion channels on both the plasma (PM) and vaculoar membranes (VM). Voltage gated channels on the PM are split into depolarization- and hyperpolarisation-activated Ca^{2+}-permeable channels (DACC/HACCs) which modulate transient and sustained influx respectively. Two important ligand-gated examples are the glutamate receptors (GLRs), which have been linked to electrical potential generation in the root, and the cyclic nucleotide-gated channels (CNGCs) which are modulators of calcium-induced calcium release (CICR). Importantly, CNGCs have also been found on the nuclear membrane and are strongly linked to signal generation in symbiosis [27]. Re-balancing of cellular homeostasis by extrusion is equally as important in

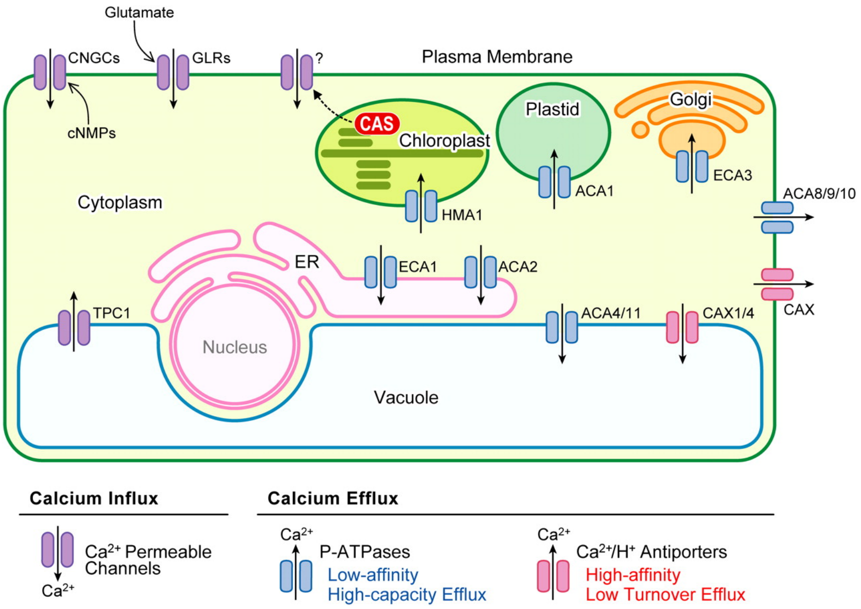

Figure 7.: "Overview of Ca^{2+} Transport Systems in an Arabidopsis Cell. Shown are the Ca^{2+} influx-efflux pathways that have been identified at the molecular level. CNGC, cyclic nucleotide channel; GLR, glutamate receptor; TPC1, two pore channel 1; CAS, Ca^{2+}-sensing receptor; ACA, autoinhibited calcium ATPase; ECA, ER type calcium ATPase; HMA1, heavy metal ATPase1; CAX, cation exchanger". Figure from Kudla (2010) [57].

defining the Ca^{2+} signature and is regulated by a biphasic efflux through anti-porters and ATPases. The Ca^{2+}-proton anti-porter is a high-affinity, low turnover channel which sequesters Ca^{2+} from the cytosol back into the vacuole store to re-establish resting cytosolic concentration. The low resting state is then maintained over longer timescales by the low affinity, high capacity, P-type Ca^{2+}-ATPase. The expression of each type of channel and pump provides the cell with the ability to generate a calcium signature for a required physiological output and hence reflects the particular needs of the specific cell or tissue type. A review of identified channels on plant cell and organelle membranes is given by Kudla (2010) and a summary of which is shown in Figure. 7 [57]. Following publication, channels on the nuclear membrane have since been identified and will be described in the following section.

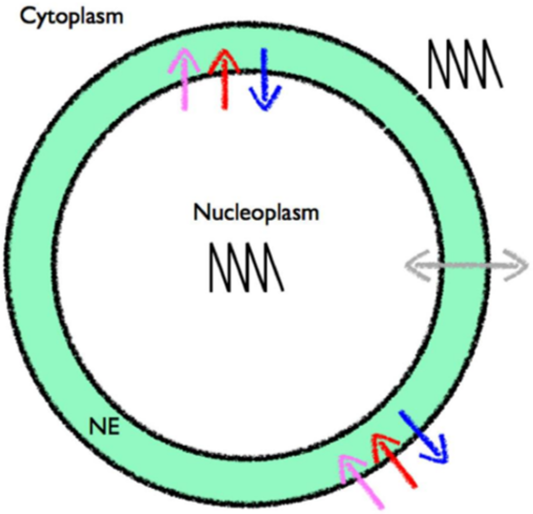

Figure 8.: Two compartments of the nucleus consisting of the nucleoplasm and the nuclear envelope. Red arrows - calcium pumps; blue arrows - calcium channels; purple arrows - potassium channels; grey arrows - nuclear pores. Figure from Vaz Martins (2013) [60].

2.2 THE NUCLEUS AND CALCIUM SIGNALLING

The basic structure of the nuclear domain can be seen in Figure. 8. The central compartment is the nucleoplasm, which contains the DNA as well as all the proteins involved in transcription and regulation of gene expression. This is surrounded by the nuclear envelope (NE) which is comprised of the inner (INM) and outer nuclear membranes (ONM) enclosing the region called the peri-nuclear space (PNS). The nuclear envelope contains numerous nuclear pore complexes (NPC's) which provide a direct route for transport of small molecules between the nucleoplasm and the cytoplasm - bypassing the PNS. Initially it was debated whether calcium signatures detected in the nucleoplasm had originated in the cytoplasm and extended to the nucleus as a result of free diffusion through the NPC's, however both experimental and modelling results have confirmed that this is not the case [83, 21], and it is now widely accepted that the nucleus is able to generate its calcium signature autonomously [26, 51, 54]. The ability to make this assertion was greatly aided by the development of fluorescent calcium reporters such as the 'nucleoplasmin-tagged yellow cameleon' (NupYC) which fluoresce only due to $[Ca^{2+}]$ changes in the nucleus and hence allow us to make quantitative measurements of the nuclear signal without interference from cytoplasmic $[Ca^{2+}]$ fluctuations [78]. Characterization of calcium pumps and channels on both the nuclear membranes further supports these findings [27, 32] as does the existence of calcium transients in isolated nuclei [91, 15] and the discovery of the localisation of numerous calcium sensory proteins, such as CaM, to the nucleus along with the identification of a variety of transcription factors which it can directly or indirectly regulate [54].

The mechanism of calcium signature generation in the nucleus is somewhat unclear, although it is thought that the PNS acts as the nucleus' own calcium store and it is the coordinated uptake/release of calcium to/from this domain which creates the spatio-temporal calcium profile we observe in the nucleoplasm. This appears sensible as the NE is continuous with another cellular calcium store - the ER. Active transport of calcium across the INM returns Ca^{2+} ions to the PNS against the electrochemical gradient through a sarco/endoplasmic reticulum calcium ATPase (SERCA) type pump called MCA8 (red arrows in Figure. 8). Inversely, flux out of the PNS into the nucleoplasm/cytoplasm occurs through the CNGC15 Ca^{2+} channel (blue arrows in Figure. 8) [27] - the recent (2016) discovery of which in *Medicago truncatula*, as a plant nuclear-localized calcium channel, has been described as "a major breakthrough" for the field [86]. To restore the electrical potential across the membrane, potassium (K^+) flux is thought to take place simultaneously to calcium transport, in the opposite direction [44]. This occurs by the movement of K^+ into the PNS through the potassium-permeable cation channel DMI1 (purple arrows in Figure. 8).

Physiological processes for which a nuclear calcium signal have been observed include: abiotic factors such as cold shock and osmotic stress; hormone signalling; and biotic interactions with pathogens or endosymbionts [25]. Drought and salt stress have both been found to possess a biphasic response, in which distinct cytosolic and nuclear signalling pathways work simultaneously. In the salt stress pathway, saline soils cause an increase of reactive oxygen species (ROS) which trigger independent Ca^{2+} oscillations in the cytosol and nucleus. Cytosolic calcium, Ca^{2+}_{cyt}, binds the sensory proteins Salt Overly Sensitive (SOS)2/3 which activate the Na^+/H^+ antiporter for extrusion of toxic sodium ions, whilst in the nucleus Ca^{2+}_{nuc} promotes transcription of the genes At3g for detoxification and SOS1 for homeostasis [46]. In the drought nuclear transduction pathway, upon recognition of soil drying, up-regulation of abscisic acid (ABA) levels propagates a signal from root to shoot to induce closure of the stoma for water conservation. In the short term, an increase in Ca^{2+}_{cyt} above a threshold causes an increase in turgor pressure of the specialised guard cells and hence stomatal closure, whilst longer term Ca^{2+} oscillations in the nucleus activate gene expression to prevent reopening [89]. The described salt- and drought-stress responses are two known pathways in which nuclear Ca^{2+} signalling possesses a distinct biological role. The most comprehensively studied case, perhaps due to the potential major agricultural benefits, is symbiosis. However there is still a way to go, with the next steps involving unravelling this signalling pathway at single cell level.

2.3 SIGNALLING IN SYMBIOSIS

2.3.1 *Nuclear calcium signals in rhizobial symbiosis*

An important example of a signalling pathway with autonomous nuclear generation of the calcium signature is symbiosis - the formation of a mutually beneficial relationship between a host plant and a root colonizing microbe. As early as 1996 it was observed that, upon stimulus application, calcium spiking in root hairs was localized predominantly to the nucleus [39]. Nuclear $[Ca^{2+}]$ oscillations in response to rhizobial chemical signals (nod factors) in the legume *Medicago sativa* were measured by Ehrhardt (1996) to have an amplitude of around 500 nm and a periodicity of about 60 seconds, as shown in Figure. 9B. We note from these results that further away from the nuclear region calcium activity remains low with no clear patterning, supporting the theory of nuclear initiation. Sun (2007) reproduced similar results [83], with application of 1 nm of nod factor to *M.truncatula* resulting in a periodic Ca^{2+} trace in the root hair nucleus with very little activity in the cytoplasm. Spike frequency corroborated the results of Ehrhardt, at 0.7 min^{-1}, but concentrations were not specified.

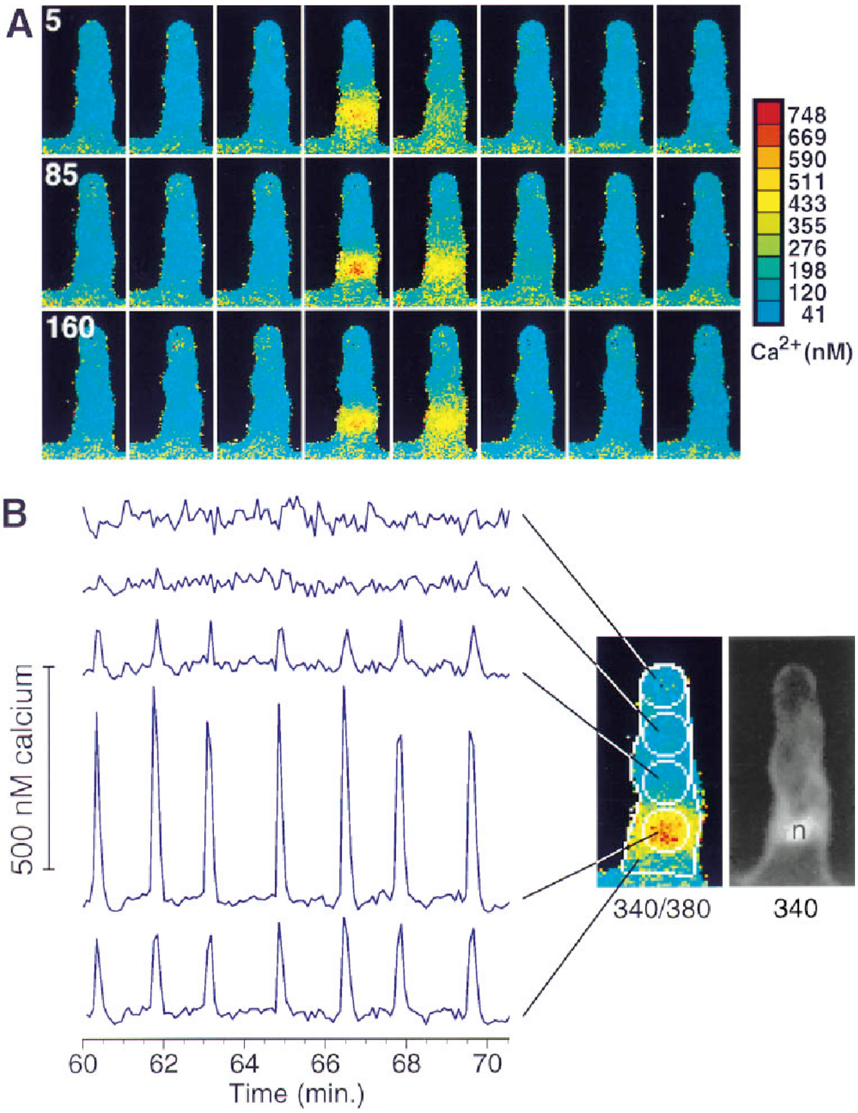

Figure 9.: A. Time series of images - showing changes in Ca^{2+} concentration 50 minutes post Nod factor application. B. Calcium concentration trace given for 4 distinct locations in the root hair cell, with the bottom-most trace giving an average concentration profile corresponding to the region drawn over the entire hair body. The bright-field image shows the location of the nucleus (n) and we see the greatest response to be localized in the nuclear domain. Figure from Ehrhardt (1996) [39].

2.3.2 *The common symbiotic pathway*

Although bacterial (Rhizobial) symbiosis is only present in legumes, symbiosis with phosphorus acquiring arbuscular mycorrhizal (AM) fungi is a widespread and ancestral characteristic with up to 90% of seed plants thought to contain fungal structures (arbuscules) within the cortical cells of their roots. Although the morphological results are different, with *Rhizobia* perception initiating the development of root hair nodules while *Mychorriza* promote rearrangement of plant cell components to allow intracellular invasion, Rhizobial and AM symbioses are both established through a cascade of signalling events which have numerous similarities, such that the general framework, seen in Figure. 10, has been named the common symbiotic pathway (CSP). The conservation of many parts of this pathway is extremely important as it suggests that many land plants already possess much of the signalling machinery required for bacterial symbiosis.

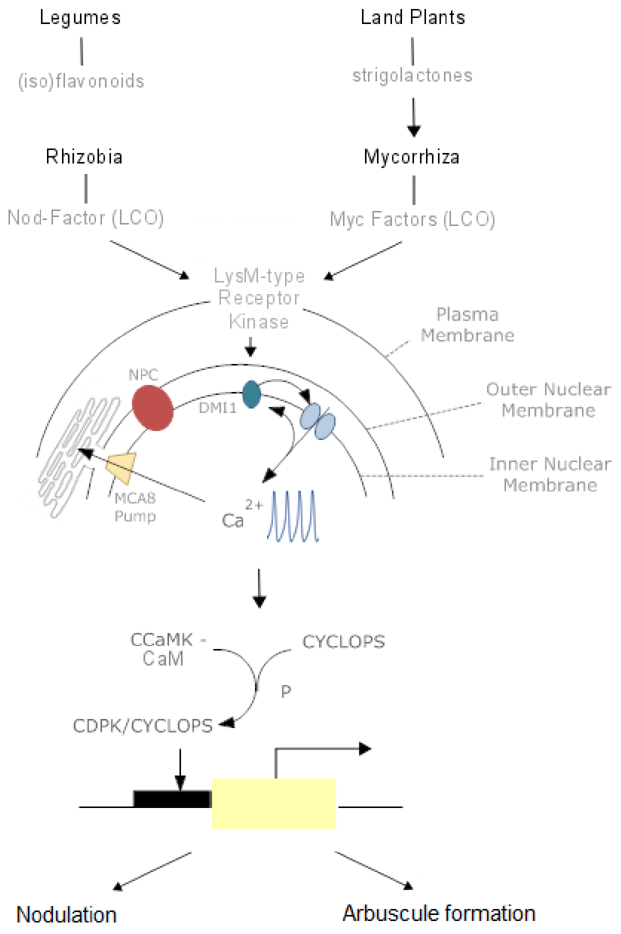

Figure 10.: The common symbiotic pathway, showing the mechanism of Ca^{2+} signal generation and resulting gene transcription to prepare the host cell for infection.

The CSP begins with perception of the microorganism. This involves the exchange of signalling molecules between the plant and microbe, where chemical secretions from the plant induce a responsive secretion of lipochitooligosacharides (LCOs) from the microbes. Nod-LCOs (*Rhizobia*) and Myc-LCOs (*mycorrhiza*) are perceived by the lysM-type receptor kinases on the root cell membrane. A subsequent set of cellular reactions triggers the release of Ca^{2+} from the PNS through the coordinated activity of the CNGC15 Ca^{2+} channel and the DMI1 K^{+} channel, allowing calcium influx into the nucleoplasm whilst maintaining membrane polarity. Meanwhile signature generation is completed by the MCA8 Ca^{2+} transporter, which pumps Ca^{2+} back into the NE to restore resting nuclear concentration [87, 28].

The resultant spiking of calcium in the nucleus is said to characterize symbiosis [95] and form a core component of the CSP [10]. There are some inconsistencies in the description of these spikes in each type of symbioses, which may be due to experimental conditions with possible variations in plant type; concentration of stimulant applied; and the volume over which the Ca^{2+} concentrations are measured. Charpentier (2013) describes calcium oscillations in the root hair cell in response to Nod-factor to have an asymmetric shape defined by a rapid Ca^{2+} release followed by a slower reuptake. After a lag of between 6 and 20 minutes there is an initial high frequency burst of 3-6 spikes followed by regular sustained nuclear oscillations with an approximate 100 s periodicity [26]. This gives a spike frequency of 0.6 min^{-1} as compared to the 0.7 min^{-1} discussed above to be found by Sun (2007) [83] and 1 min^{-1} by Ehrhardt (1996) [39] and later confirmed again by Sun (2015) [82] when comparing rhizobial spiking patterns with those of AM origin.

Calcium spiking in response to Myc-factors is initially irregular and low frequency, however, upon contact with the fungus, oscillations strongly resemble those in the rhizobial pathway in their shape and frequency [26]. As

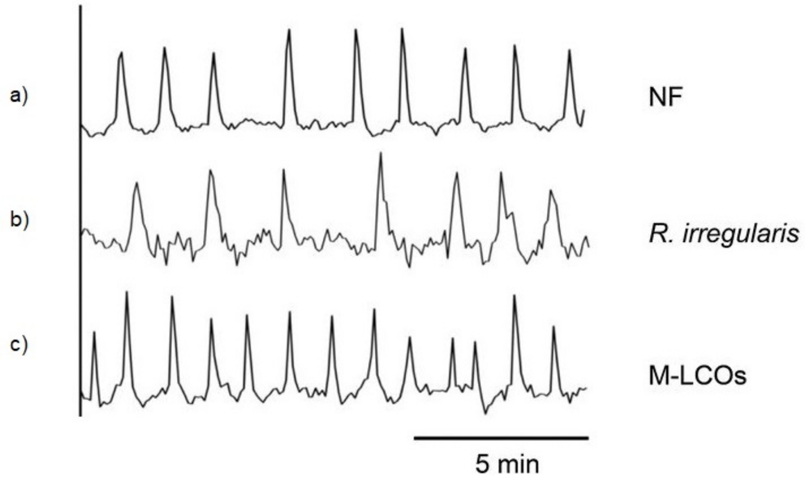

Figure 11.: Calcium oscillations in the nuclear region of the root hair in response to a) Nod factors which signals for rhizobial symbiosis, b) *R.irregularis* a fungal species which forms AM symbiosis, c) M-LCO - the specific chemical signal of AM symbiosis. Figure from Sun (2015) [82].

shown in Figure. 11, measurements suggest that the Ca^{2+} signature may be specific to the microorganism, and hence despite their common mechanism of generation, may be the point of disparity in specification of symbioses type. Figures. 11a) and 11c) show the cellular Ca^{2+} response to the purified chemical signals of rhizobial and mycorrhizal symbioses, respectively, and we see that the latter consists of comparatively higher frequency spiking. In addition there is a further Ca^{2+} signature in Figure. 11b), the response to a type of fungi, which appears to be of lower frequency and contain more noise, possibly due to the lower purity of the stimulus. A more advanced analysis was undertaken by Kosuta (2008) who found oscillation patterns (shown in Figure. 12) similar to those of Sun. In agreement with Charpentier (2013) the analysis seen in Figure. 12c) shows that Nod factor response consisits of a sharp increase in [Ca^{2+}], with a much slower reuptake, whilst AM transients are much shorter. Some uncertainty remains however, and it is currently unknown if the distinction between AM and rhizobial symbiosis is encoded within the Ca^{2+} oscillations, parallel signaling with plant hormones [26], or if the differences are simply due to cell differentiation.

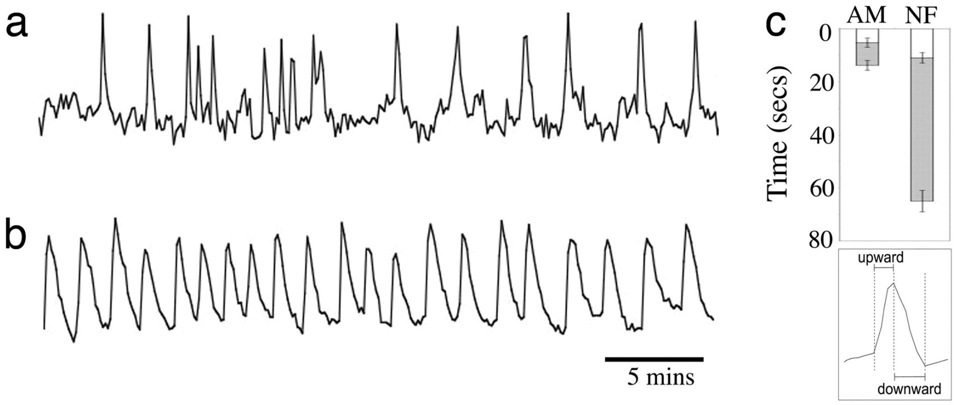

Figure 12.: a) AM oscillations, b) nod-factor induced oscillations, c) analysis of individual transients where the upward phase of the spike (in white) is compared with the downward phase (in gray). Figure from Kosuta (2008) [56].

In both cases Ca^{2+} elevations are decoded by the sensory protein's calcium/ calmodulin-dependent protein kinase (CCaMK) in association with CaM, to result in the downstream expression of genes required to prepare the host cell for symbiosis. This occurs via the CCaMK catalysed phosphorylation of CYCLOPS and the subsequent activation of the nodulation-specific and AM-specific GRAS transcription factors NSP1 and RAM1, which promote the synthesis of proteins required for cell re-modelling [10]. The existence of the CSP provides a means for the translocation of root-nodule symbiosis to non-legumes, for example by artificially inducing the Rhizobial Ca^{2+} signature, utilizing the pre-existing 'symbiotic toolkit' [34] present in all AM-plants. The translocation of this key root trait to cereal crops requires the elucidation of the signalling network to uncover the missing links in the pathway, an endeavor which can be greatly aided through an interdisciplinary cross-talk between mathematical modelling and biological experimentation [66].

2.4 CURRENT MODELLING APPROACHES

2.4.1 *Ordinary differential equation models*

A ordinary differential equation (ODE) model of a closed nuclear system was proposed by Briére (2006) to test the autonomous generation of the calcium signature in isolated nuclei [15]. Although this model does not apply the parameters for our particular application, and at time of publishing the characterisation of both pumps and channels was unknown, the model is extremely similar to that in Rhizobia-Legume symbiosis in both its compartmental set-up and flux dynamics as well as focusing on treating the nucleus as a closed system with its own distinct Ca^{2+} signature. The simple model consists of equations for the concentration of calcium, $[\mathrm{Ca}^{2+}]$, in each of the two nuclear compartments as a balance of the flux, J, between them, as well as a conservation equation to ensure that the total calcium concentration, Q, remains constant. The model is formulated as:

$$\begin{aligned} \frac{\mathrm{d}[Ca^{2+}]_{\mathrm{nuc}}}{\mathrm{d}t} &= \beta(J_{\mathrm{in}} - J_{\mathrm{out}}), \\ \frac{\mathrm{d}[Ca^{2+}]_{\mathrm{store}}}{\mathrm{d}t} &= -\alpha\rho(J_{\mathrm{in}} - J_{\mathrm{out}}), \\ \frac{[Ca^{2+}]_{\mathrm{nuc}}}{\beta} + \frac{[Ca^{2+}]_{\mathrm{store}}}{\alpha\rho} &= Q, \end{aligned} \tag{1}$$

where β represents the ratio of free versus total calcium in the nucleoplasm, α represents the ratio of free versus total calcium in the store and ρ is a weighting of the volume ratio between the two compartments. The flux into the nucleoplasm from the stores, J_{in}, was modelled as the sum of a constant leaking effect and a transient channel opening effect, with both proportional to the concentration difference between compartments. The re-uptake from the nuceloplasm to the stores, J_{out}, was modelled as a simple Hill function, as often used to model Ca^{2+} pumps in animal cells. Due to the conservation of calcium the model can be reduced to one ODE for the calcium concentration in the nucleus and steady state analysis can be easily performed to find the equilibrium level and its effectors. Results showed that the model was able to reproduce calcium transients, where a single rapid influx was followed by a slower re-uptake, however the model does not allow for sustained oscillations and further influxes require repeated stimuli.

Oscillations were reproduced however, in a three component electro- physiological model, shown in Figure. 13a, by Granqvist (2012). The model in this case does not include concentrations in the store but focuses on the potentials generated across the INM through the coordinated movement of both calcium and potassium. As well as voltage-gated ion channels for Ca^{2+} flux (now known to be CNGC15) and the active transporter MCA8 for the replenishment of the Ca^{2+} store, we have DMI1 K^+ pumps for hyper-polarisation of the nuclear envelope [44]. It was found that these components alone were enough to evoke a stable limit cycle solution, recreating some of the temporal calcium patterns observed experimentally in the nucleus. Additionally, inclusion of Ca^{2+}-binding proteins as buffers allowed the elucidation of key additional features including the initial period of rapid spiking; spike shape; variation in periodicity; and initiation and termination of the oscillations. The model with N buffers consists of $N+2$ coupled ordinary differential equations:

$$\frac{\mathrm{d}v}{\mathrm{d}t} = \frac{1}{C_\mathrm{m}}(I_\mathrm{c} + I_\mathrm{k}), \tag{2}$$

$$\frac{\mathrm{d}c}{\mathrm{d}t} = E_\mathrm{ps}(\alpha I_\mathrm{c} - \mu c) + \sum_{i=1}^{\mathrm{N}} R_\mathrm{i}, \tag{3}$$

$$\frac{\mathrm{d}p_\mathrm{i}}{\mathrm{d}t} = -R_\mathrm{i}, \tag{4}$$

the first describing voltage changes across the INM; the second changes in nucleoplasmic Ca^{2+} concentration; and one for the concentration of each buffer present to bind Ca^{2+}. The system is dependent on the Ca^{2+} and K^+ currents through their respective channels, with the Ca^{2+} current a function, f, of the voltage such that $I_\mathrm{c} = f(v)$ and the K^+ current a function,

g, of both the voltage and calcium concentration, $I_k = g(c, v)$. Parameters include C_m the capacitance of the nuclear envelope, E_{ps} a scaling factor relating total Ca^{2+} changes to changes in free Ca^{2+}, α a factor for conversion

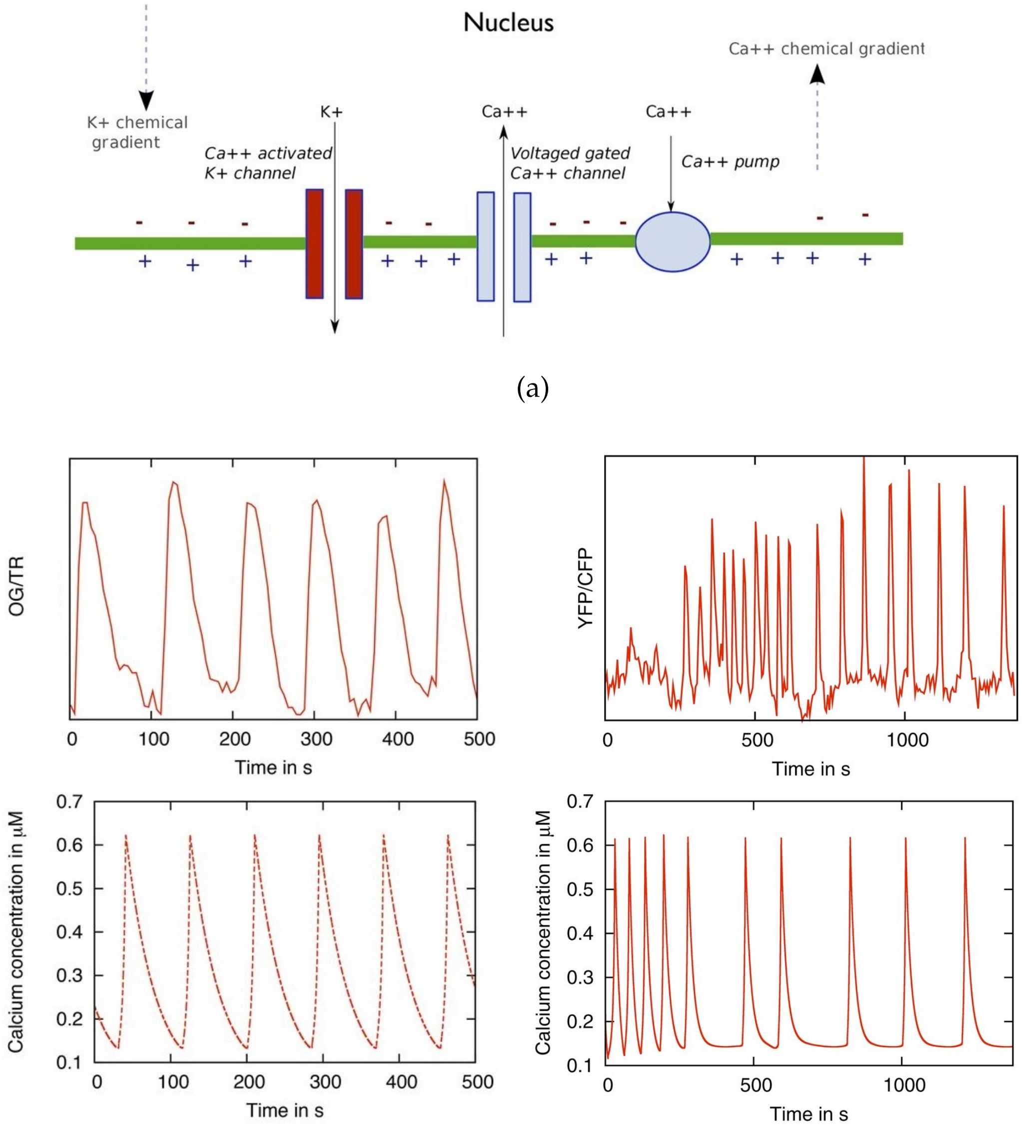

(a)

(b)

(c)

Figure 13.: a) Model schematic showing the 3 components and the polarization of the nuclear lamina to be negatively charged on the nucleoplasmic side relative to the perinuclear space. b) The simple 2 ODE model, $(R_i = 0, \forall i)$, allows self-sustained oscillations. c) The addition of a buffer explains signal variation. The upper time-series show experimental data whilst the lower figures give simulation results. Figure from Granqvist (2012) [44].

of Ca^{2+} current to Ca^{2+} flux, μ the rate of transport into the nuclear envelope and R_i dependent upon buffer association and dissociation constants. Simulation results taken from Granqvist (2012) can be seen in Figure. 13. In the absence of buffering ($R_i = 0, \forall i$) the resulting [Ca^{2+}] time series shows oscillations of a fixed period (13b) which would continue indefinitely. The addition of 2 buffers ($R_1, R_2 \neq 0$), on the other hand, perturbs the temporal calcium profile to produce oscillations with irregular frequencies and an initial rapid spiking period (13c), replicating those experimentally observed features which were previously described in Section 2.3.2.

Charpentier (2013) extended this model to elucidate the mechanism of complex formation between DMI1 and the Ca^{2+} channel. It was found that there exists a positive feedback loop necessary for spiking, in which DMI1 conductivity is modulated by Ca^{2+}, possibly through physical binding, whilst flux through Ca^{2+} channels is increased by increased K^+ current through DMI1 [28].

2.4.2 *Partial differential equation models*

With previous models only considering the dynamics on, but not away from, the nuclear membrane, in a single dimension, and with calcium concentrations only dependant upon time but not space, Vaz Martins (2016) developed at 2-dimensional fire-diffuse-fire (FDF) model to couple signals between the inner and outer surfaces of the INM. The partial differential equation (PDE) model for the diffusion of Ca^{2+} across each surface with a uniform uptake rate, k_s is given as:

$$\frac{\partial c(\mathbf{r},t)}{\partial t} = D\nabla^2 c(\mathbf{r},t) - k_s c(\mathbf{r},t) + \sum_{i=1}^{N} f_i(t)\delta(\mathbf{r}-\mathbf{r}_i) + \sum_{k=1}^{n_p} \Omega_k(t)\delta(\mathbf{r}-\mathbf{r}_k), \quad (5)$$

with point sources representing N calcium channels at positions $\mathbf{r}_i$ and n_p nuclear pores at $\mathbf{r}_k$, the latter being the only term coupling the two surfaces. Simulation results demonstrated that autonomous spatio-temporal patterns of Ca^{2+} could still exist in the presence of nuclear pores, and were able to explain the differences in inter-compartment coupling seen experimentally by varying pore permeability's and channel refractory periods. The model however only includes the spherical surface of each side of the NE and hence does not allow for diffusion away from the membrane and cannot explain the patterning seen in the nuclear body. Further, the model does not allow for realistic Calcium-Induced Calcium Release (CICR) between channels unless they are immediately adjacent to one another, as shown in Figure. 14a [61].

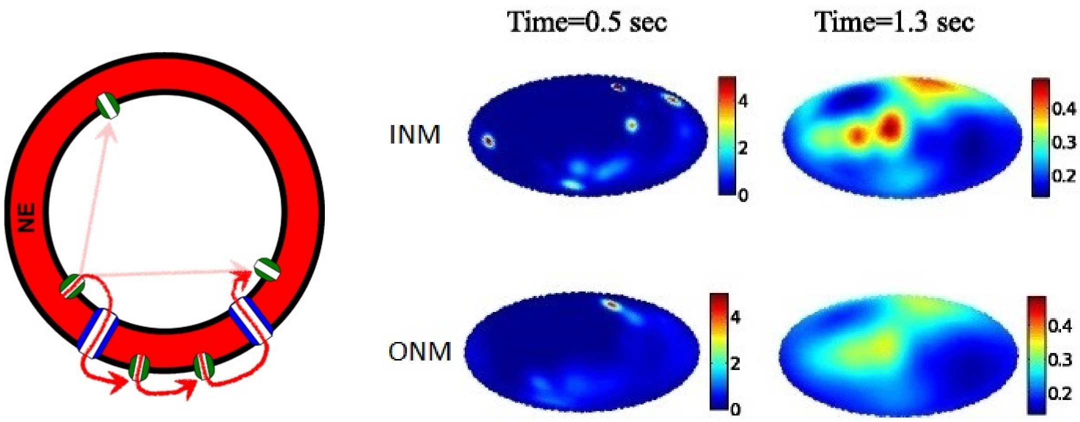

(a) (b)

Figure 14.: a) Schematic of the model of Vaz Martins (2016), nuclear pores are in blue and Ca^{2+} channels in green. Red arrows show a feasible route of CICR, with pink arrows showing the diffusion pathway's which are not possible due to the model's geometrical limitations. b) Ca^{2+} concentration profiles on two surfaces, coupled by nuclear pores, shown for two times where global calcium concentrations are the same, yet local concentration profiles are very different due to differences in spike phase. T=0.5 s: we see that micro-domains formation on one side of the NE does not automatically infer one on the other when Ca^{2+} flow does not trigger channel firing. T=1.3 s: $D_{cyt} > D_{nuc}$ results in micro-domain variations. Figure from Vaz Martins (2016) [61].

Many available models generating calcium oscillations use ODE's and do not consider spatial concentration variations [44]. The minority that include a spatial element do not retain 3-dimensional geometries, use inaccurate nuclear morphology's and do not explicitly include Ca^{2+} pumps [61]. It is likely however, that this could have a profound affect on patterning [79]. As shown in Figure. 15, Queisser (2011) demonstrated that nuclear morphology in human hippocampal neurons could have a direct effect on the activity of Ca^{2+}-dependent transcription factors [70]. We will therefore go beyond current work to introduce a 3–dimensional PDE model, whilst allowing for more realistic calcium release currents, in an attempt to discover patterns of calcium elevation in the nucleus. Distribution of ion channels on the nuclear membrane will also be considered. These are known to vary among species and may therefore represent a specificity which distinguishes between plant types able to undergo fungal and bacterial symbiosis.

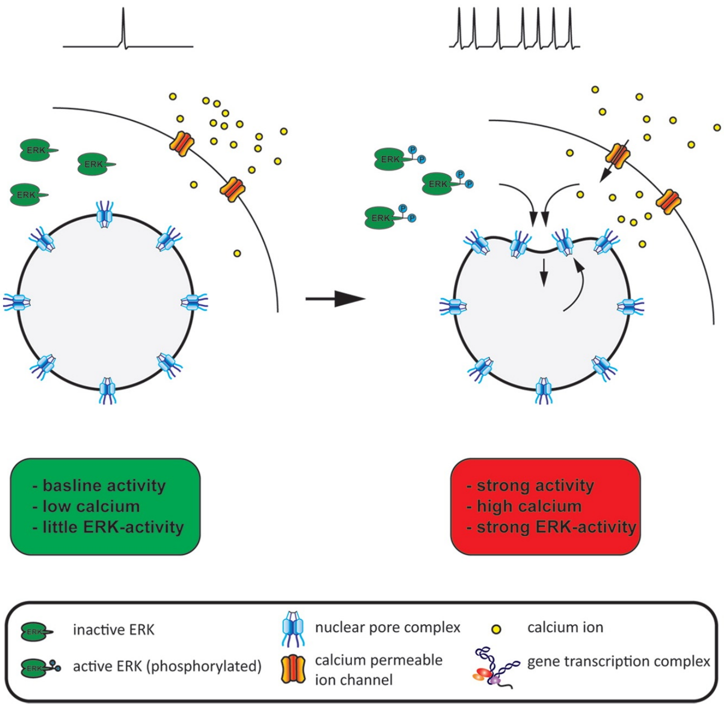

Figure 15.: The direct consequences of nuclear geometry changes include changes in associated transcriptional levels. Figure from Queisser (2011) [70].

2.5 LITERATURE SUMMARY

- The calcium signalling pathway is made up of stimuli perception, calcium signature generation, decoding by sensors and cellular response.
- The calcium signalling toolbox, comprising of channels, messengers and transporters, contains the components of the calcium signalling pathway.
- The calcium signature is a unique combination of changes in local calcium concentration in space and time, and is defined by its stimulus-specific amplitude, duration, frequency and spatial distribution.
- The localisation of sensory proteins adds a furthur layer to the pathways spatial specificity.
- A calcium signature is generated through concentration fluxes between cellular compartments, either against the concentration gradient into stores through pumps or along the gradient through channels.
- In compartmental terms the nucleus comprises of the nucleoplasm and the PNS, separated by the INM and connected through CNGC channels and MCA8 calcium pumps.
- It is widely accepted that in symbiosis, among other functions, the nucleus is able generate its own calcium signatures autonomously.
- The majority of non-leguminous plants can form symbiotic relationships with AM fungi, using a common symbiotic pathway whose central features overlap with bacterial symbiosis, suggesting that the transfer of traits is possible.
- Nuclear calcium spiking in response to Nod factors (as released by Rhizoba) has been found to have a frequency of between 0.6-1 min^{-1}.

- A single calcium spike profile was reproduced by Briére (2006), through a simple ODE Model of fluxes between the nucleoplasm and the calcium store.

- An ODE model by Granqvist (2012), which was later extended by Charpentier (2013), was able to reproduce sustained calcium oscillations, including initial fast spiking, through the addition of calcium buffers.

- A fire-diffuse-fire PDE model on a 2D spherical surface was proposed by Vaz Martins (2016) who demonstrated that autonomous calcium signal generation could still take place in the presence of nuclear pores.

3

MATHEMATICAL BACKGROUND

In this section we will look at the background theory and derivation of the Green's function for the heat equation in one-dimensional Cartesian and two-dimensional polar and elliptic coordinates for various boundary conditions. A Green's function is the impulse response of a linear differential operator, and is chosen here for it's capacity to apply a ready-made diffusion profile during numerical simulation, and, due to the decreased computational power required, increase the speed of computation. All of the work in this section can be found in various forms and notations in textbooks such as Arfken, Weber and Harris' *Mathematical Methods for Physicists* [7] and Carslaw and Jaeger's *Conduction of Heat in Solids* [24]. It is useful however, to introduce the methodology of finding our Green's functions in order to help build up to the more complicated derivations in Section 4. We shall also see later that many of the special functions introduced in this section remain important when defining our full model.

3.1 DIFFUSION IN 1-DIMENSION

3.1.1 *Deriving the Green's function for Neumann boundary conditions*

We begin by looking at the diffusion of a concentration, $c(x,t)$, in time, t, along a line, $x \in [0, L]$, with homogeneous boundary conditions. We wish to solve the 1D diffusion equation:

$$\frac{\partial c}{\partial t} = D\frac{\partial^2 c}{\partial x^2}, \tag{6}$$

with diffusion coefficient D. Using a separation of variables technique we let:

$$c(x,t) = X(x)T(t), \tag{7}$$

to find the two ODE's:

$$\begin{aligned} &1. \qquad X''(x) + k^2 X(x) = 0, \\ &2. \qquad T'(t) + Dk^2 T(t) = 0, \end{aligned} \tag{8}$$

with solutions:

$$\begin{aligned} &1. \qquad X(x) = A\sin(kx) + B\cos(kx), \\ &2. \qquad T(t) = T_0 \mathrm{e}^{-Dk^2 t}. \end{aligned} \tag{9}$$

For Neumann boundary conditions:

$$\left.\frac{\partial c}{\partial x}\right|_{x=0,L} = 0, \tag{10}$$

we find:

$$k(A\cos(kx) - B\sin(kx))|_{x=0,L} = 0. \tag{11}$$

As $k \neq 0$ by construction, we have:

$$\begin{aligned} x = 0: &\qquad A = 0, \\ x = L: &\qquad B\sin(kL) = 0. \end{aligned} \tag{12}$$

As $B = 0$ would give the trivial solution we have the eigenvalue problem:

$$\sin(k_{\mathrm{n}} L) = 0, \tag{13}$$

and hence the eigenvalues: $k_{\mathrm{n}} = \frac{n\pi}{L}$ for $n = 0, 1, 2, \ldots$, and Eq. 1. of (9) becomes:

$$X(x) = \sum_{n=0}^{\infty} B_{\mathrm{n}} \cos\left(\frac{n\pi}{L} x\right). \tag{14}$$

By orthogonality we know that:

$$\langle X_{\mathrm{n}}, X_{\mathrm{m}} \rangle = \int_0^{\mathrm{L}} \cos\left(\frac{n\pi}{L} x\right) \cos\left(\frac{m\pi}{L} x\right) \mathrm{d}x = \begin{cases} 0, & n \neq m, \\ \frac{L}{2}, & n = m, \end{cases} \tag{15}$$

and hence, using our initial condition, $c(x, 0) = C_0$, we can find our constant B_{n} for $n \in \mathbb{Z}_{>0}$:

$$B_{\mathrm{n}} = \frac{\langle C_0, X_{\mathrm{n}} \rangle}{\langle X_{\mathrm{n}}, X_{\mathrm{m}} \rangle} = \frac{2}{L} \int_0^{\mathrm{L}} C_0(x') \cos\left(\frac{n\pi}{L} x'\right) \mathrm{d}x', \tag{16}$$

and for the zero eigenvalue at $n = 0$ we have $B_0 = \frac{\int_0^{\mathrm{L}} C_0(x) \mathrm{d}x}{L}$.
Combining solutions, and absorbing our constant T_0 into $C_0(x)$, we find:

$$c(x, t) = \frac{1}{L} \int_0^{\mathrm{L}} C_0(x') \left(2 \sum_{n=1}^{\infty} \cos\left(\frac{n\pi}{L} x'\right) \cos\left(\frac{n\pi}{L} x\right) \mathrm{e}^{-D(\frac{n\pi}{L})^2 dt} + 1 \right) \mathrm{d}x', \tag{17}$$

where we have used the time-translation invariance of the propagator:

$$K(x, x', t, t') = K(x, x', dt), \qquad dt = t - t'. \tag{18}$$

Our solution is of the form:

$$c(x, t) = \int_0^{\mathrm{L}} G(x, x', dt) C_0(x') \mathrm{d}x', \tag{19}$$

and hence we have the Green's function:

$$G(x, x', dt) = \frac{2}{L} \sum_{n=1}^{\infty} \cos\left(\frac{n\pi}{L} x'\right) \cos\left(\frac{n\pi}{L} x\right) \mathrm{e}^{-D(\frac{n\pi}{L})^2 dt} + \frac{1}{L}. \tag{20}$$

3.1.2 *Deriving the Green's function for Dirichlet boundary conditions*

For Dirichlet boundary conditions:

$$\begin{aligned} c(0, t) &= 0, \\ c(L, t) &= 0, \end{aligned} \tag{21}$$

and we have:

$$\begin{aligned} x = 0: &\qquad B = 0, \\ x = L: &\qquad A\sin(kL) = 0. \end{aligned} \tag{22}$$

As $A = 0$ would give the trivial solution we have the eigenvalue problem from Eq. 13 and hence the eigenvalues $k_\mathrm{n} = \frac{n\pi}{L}$ for $n = 0, 1, 2, ...$, and Eq. 1. of (9) now becomes:

$$X(x) = A_\mathrm{n} \sin\left(\frac{n\pi}{L}x\right). \tag{23}$$

We find A_n, $n = 1, 2, ...$ by orthogonality using:

$$\langle X_\mathrm{n}, X_\mathrm{m} \rangle = \int_0^\mathrm{L} \sin\left(\frac{n\pi}{L}x\right) \sin\left(\frac{m\pi}{L}x\right) \mathrm{d}x = \begin{cases} 0, & n \neq m \\ \frac{L}{2}, & n = m \end{cases} \tag{24}$$

to give:

$$A_\mathrm{n} = \frac{2}{L}\int_0^\mathrm{L} C_0(x') \sin\left(\frac{n\pi}{L}x'\right) \mathrm{d}x'. \tag{25}$$

In this case for $n = 0$ we have $x_\mathrm{n} = 0$ and hence require no A_0. Finally we combine solutions to find:

$$c(x,t) = \frac{2}{L}\sum_{n=1}^{\infty}\int_0^\mathrm{L} C_0(x') \sin\left(\frac{n\pi}{L}x'\right) \sin\left(\frac{n\pi}{L}x\right) \mathrm{e}^{-D(\frac{n\pi}{L})^2 dt} \mathrm{d}x', \tag{26}$$

with Green's function:

$$G(x, x', dt) = \frac{2}{L}\sum_{n=1}^{\infty} \sin\left(\frac{n\pi}{L}x'\right) \sin\left(\frac{n\pi}{L}x\right) \mathrm{e}^{-D(\frac{n\pi}{L})^2 dt}. \tag{27}$$

3.1.3 *Deriving the Green's function for a domain which does not contain the origin*

Here we change our domain to $x \in [L, L+h]$ where h is the width of the line. Solutions from the separation of variables are as previously derived in Eq. (9). When considering flux between domains we use Neumann boundary conditions to prescribes a zero flux everywhere on the adjoining points such that we can later prescribe fluxes at specific times as required. We therefore apply the conditions:

$$\left.\frac{\partial c(x)}{\partial x}\right|_{x=L,L+h} = 0. \tag{28}$$

We perform the change of variables, $y = x - L$, and for Eq. 1. of (9) write:

$$X(y) = A\sin(ky) + B\cos(ky), \tag{29}$$

such that the boundary conditions become:

$$\left.\frac{\partial c}{\partial y}\right|_{y=0,h} = 0, \tag{30}$$

and we find:

$$\begin{aligned} y = 0: &\qquad A = 0, \\ y = h: &\qquad B\sin(kh) = 0, \end{aligned} \tag{31}$$

and therefore again retrieve the eigenvalue problem of Eq. 13, with $k = \frac{n\pi}{h}$, for $n = 0, 1, 2, ...$ Eq. 1. of (9) becomes:

$$X = \sum_{n=0}^{\infty} B_{\mathrm{n}} X_{\mathrm{n}}, \tag{32}$$

where, returning back to our original variables:

$$X_{\mathrm{n}} = \cos\left(\frac{n\pi}{h}(x - L)\right). \tag{33}$$

Again we use orthogonality to find:

$$\begin{aligned} B_{\mathrm{n}} &= \frac{2}{h}\int_{L}^{\mathrm{L+h}} C_0(x - L)\cos(\frac{n\pi}{h}(x - L))\mathrm{d}x, \qquad n > 0, \\ B_0 &= \frac{1}{h}\int_{L}^{\mathrm{L+h}} C_0(x - L)\mathrm{d}x, \end{aligned} \tag{34}$$

Combining solutions gives:

$$\begin{aligned} c(x,t) = \frac{1}{h}\int_{L}^{\mathrm{L+h}} & C_0(x - L) \\ & \times \left(2\sum_{n=1}^{\infty}\cos\left(\frac{n\pi}{h}(x - L)\right)\cos\left(\frac{n\pi}{h}(x' - L)\right)\mathrm{e}^{-D(\frac{n\pi}{h})^2 dt} + 1\right)\mathrm{d}x', \end{aligned} \tag{35}$$

with Green's function:

$$G(x, x', dt) = \frac{2}{h}\sum_{n=1}^{\infty}\cos\left(\frac{n\pi}{h}(x - L)\right)\cos\left(\frac{n\pi}{h}(x' - L)\right)\mathrm{e}^{-D(\frac{n\pi}{h})^2 dt} + \frac{1}{h}. \tag{36}$$

3.2 DIFFUSION IN 2-DIMENSIONS: POLAR COORDINATE SYSTEM

3.2.1 *Deriving the Green's function for Neumann boundary conditions*

We take the heat equation in 2-dimensional polar coordinates:

$$\frac{\partial c}{\partial t} = D\left[\frac{\partial^2 c}{\partial r^2} + \frac{1}{r}\frac{\partial c}{\partial r} + \frac{1}{r^2}\frac{\partial^2 c}{\partial \theta^2}\right], \tag{37}$$

and solve for a disc with radius a such that, $r \in (0, a)$, $\theta \in (0, 2\pi]$. Using the separation anzatz:

$$c(r, \theta, t) = R(r)\Theta(\theta)T(t), \tag{38}$$

we reduce the PDE to the set of ODE'S:

$$\begin{aligned} &1. \qquad \Theta''(\theta) + \mu^2\Theta(\theta) = 0, \\ &2. \qquad T'(t) + Dk^2 T(t) = 0, \\ &3. \qquad r^2 R''(r) + rR'(r) + (k^2r^2 - \mu^2)R(r) = 0. \end{aligned} \tag{39}$$

We use the change of variables $s = kr$ to transform Equation.3 of (39) to the Bessel equation:

$$s^2 R''(s) + sR'(s) + (s^2 - \mu^2)R(s) = 0, \tag{40}$$

and hence we find the solutions:

$$\begin{aligned} &1. \qquad \Theta(\theta) = A\sin(\mu\theta) + B\cos(\mu\theta), \\ &2. \qquad T(t) = T_0 \mathrm{e}^{-Dk^2 t}, \\ &3. \qquad R(s) = CJ_\mu(s) + DY_\mu(s), \end{aligned} \tag{41}$$

where $J_\mu(s)$ and $Y_\mu(s)$ are the Bessel functions of order μ of the first and second kind respectively, for which plots with $\mu = 0, 1, .., 4$ are shown in Figure. 16a and Figure. 16b. The corresponding boundary conditions are written:

$$\begin{aligned} &\text{Radial :} \qquad \left.\frac{\partial c}{\partial r}\right|_{r=a} = 0, \qquad \lim_{r\to 0}(c) \neq \infty, \\ &\text{Angular :} \qquad c(r, \tilde{\theta}) = c(r, \tilde{\theta} + 2\pi), \qquad \left.\frac{\partial c}{\partial \theta}\right|_{\tilde{\theta}} = \left.\frac{\partial c}{\partial \theta}\right|_{\tilde{\theta}+2\pi}. \end{aligned} \tag{42}$$

It is clear the angular boundary conditions are satisfied for $\mu = m \in \mathbb{Z}_+$. Applying the second radial boundary condition, we find $D = 0$, as the $Y_{\mathrm{m}}(s)$ are unbounded at the origin $\forall m$ and hence, returning to the original variables, Equation.3. of (41) becomes $R(r) = CJ_{\mathrm{m}}(kr)$. We can then apply the Neumann boundary condition and, recalling that $k \neq 0$ by construction and $C \neq 0$ as this would give the trivial solution, we obtain the eigenvalue problem:

$$J'_{\mathrm{m}}(\lambda_{\mathrm{mn}}) = 0, \tag{43}$$

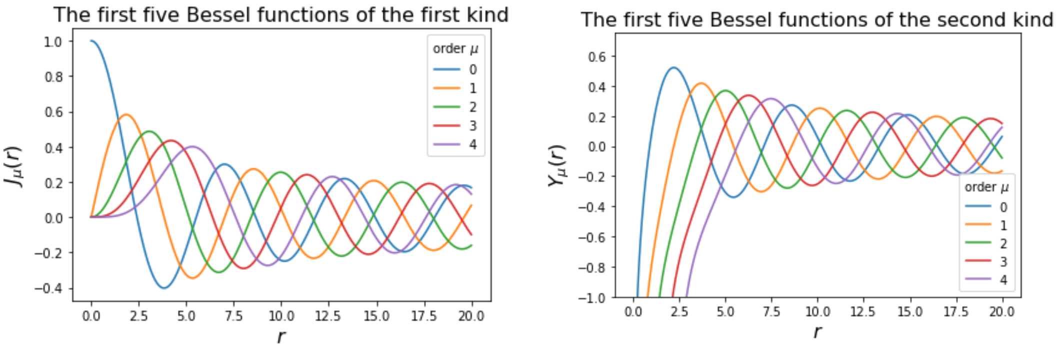

(a) (b)

Figure 16.: Examples of the Bessel functions of a) the first kind and b) the second kind.

where we have set $\lambda_{\mathrm{mn}} = ka$ to be the n^{th} zero of the m^{th} order Bessel function derivative.

Our combined solutions are:

$$c(r, \theta, t) = \sum_{m=0}^{\infty} \sum_{n=1}^{\infty} J_{\mathrm{m}}(\frac{\lambda_{\mathrm{mn}}}{a} r)(A_{\mathrm{mn}} \sin(m\theta) + B_{\mathrm{mn}} \cos(m\theta))\mathrm{e}^{-D(\frac{\lambda_{\mathrm{mn}}}{a})^2 t}, \tag{44}$$

where we have absorbed C and T_0 into A_{mn} and B_{mn}. We take this solution at $t = 0$:

$$c(r, \theta, 0) =$$

$$C_0(r, \theta) = \begin{cases} \sum_{n=1}^{\infty} J_0(\frac{\lambda_{0n}}{a} r) B_{0n}, & m = 0, \\ \sum_{m=1}^{\infty} \sum_{n=1}^{\infty} J_{\mathrm{m}}(\frac{\lambda_{\mathrm{mn}}}{a} r)(A_{\mathrm{mn}} \sin(m\theta) + B_{\mathrm{mn}} \cos(m\theta)), & m > 0, \end{cases} \tag{45}$$

and use the orthogonality of the Bessel functions:

$$\langle R_\mathrm{n}, R_\mathrm{m}\rangle = \int_0^\mathrm{a} J_\mathrm{n}(kr)J_\mathrm{m}(kr)r\mathrm{d}r = \begin{cases} 0, & n \neq m, \\ N_\mathrm{nm}, & n = m, \end{cases} \tag{46}$$

where

$$N_\mathrm{nm} = \frac{a^2}{2}\left[1 - \frac{m^2}{k^2a^2}\right](J_\mathrm{m}(ka))^2 + \frac{a^2}{2}\left(J'_\mathrm{m}(ka)\right)^2, \tag{47}$$

whose second term is equal to zero for the Neumman case, along with the orthogonality of $\Theta(\theta)$:

$$\langle \Theta_\mathrm{n}, \Theta_\mathrm{m}\rangle =$$

$$\int_0^{2\pi} (\sin(m\theta) + \cos(m\theta))(\sin(n\theta) + \cos(n\theta))\mathrm{d}\theta = \begin{cases} 0, & n \neq m, \\ 2\pi, & n = m, \end{cases} \tag{48}$$

to find our constants. We take the inner product of Eq. 45 for the case $m = 0$, and $J_\mathrm{m}(kr)$ to find:

$$B_{0n} = \frac{\langle C_0, R_\mathrm{m}\rangle}{\langle R_\mathrm{n}, R_\mathrm{m}\rangle} = \frac{\int_0^{2\pi}\int_0^\mathrm{a} C_0(r',\theta')J_\mathrm{m}(kr')r'\mathrm{d}r'\mathrm{d}\theta'}{2\pi N_\mathrm{mn}}. \tag{49}$$

To find A_mn we take the inner product of Eq. 45 for $m > 0$ and $J_\mathrm{m}(kr)\sin(m\theta)$:

$$A_\mathrm{mn} = \frac{\langle C_0, R_\mathrm{m}\sin(m\theta)\rangle}{\langle R_\mathrm{n}\Theta_\mathrm{n}, R_\mathrm{m}\sin(m\theta)\rangle} = \frac{\int_0^{2\pi}\int_0^\mathrm{a} C_0(r',\theta')J_\mathrm{m}(kr')\sin(m\theta)r'\mathrm{d}r'\mathrm{d}\theta'}{\pi N_\mathrm{mn}}, \tag{50}$$

and similarly for B_mn we take the inner product of Eq. 45 for $m > 0$ and $J_\mathrm{m}(kr)\cos(m\theta)$ to obtain:

$$B_\mathrm{mn} = \frac{\langle C_0, R_\mathrm{m}\cos(m\theta)\rangle}{\langle R_\mathrm{n}\Theta_\mathrm{n}, R_\mathrm{m}\cos(m\theta)\rangle} = \frac{\int_0^{2\pi}\int_0^\mathrm{a} C_0(r',\theta')J_\mathrm{m}(kr')\cos(m\theta)r'\mathrm{d}r'\mathrm{d}\theta'}{\pi N_\mathrm{mn}}. \tag{51}$$

Using the identity:

$$\cos(m\theta)\cos(m\theta') + \sin(m\theta)\sin(m\theta') = \cos(m(\theta - \theta')), \tag{52}$$

our final solution is therefore:

$$c(r,\theta,t) = \\ \sum_{m=1}^{\infty}\sum_{n=1}^{\infty} \frac{\int_0^{\mathrm{a}}\int_0^{2\pi} C_0(r',\theta')J_{\mathrm{m}}(\frac{\lambda_{\mathrm{mn}}}{a}r)J_{\mathrm{m}}(\frac{\lambda_{\mathrm{mn}}}{a}r')(\cos(m(\theta-\theta')))r'\mathrm{d}r'\mathrm{d}\theta'\mathrm{e}^{-D\left(\frac{\lambda_{\mathrm{mn}}}{a}\right)^2 dt}}{\pi N_{\mathrm{mn}}} \\ + \sum_{n=1}^{\infty} \frac{\int_0^{\mathrm{a}}\int_0^{2\pi} C_0(r',\theta')J_0(\frac{\lambda_{0n}}{a}r)J_0(\frac{\lambda_{0n}}{a}r')r'\mathrm{d}r'\mathrm{d}\theta'\mathrm{e}^{-D\left(\frac{\lambda_{0n}}{a}\right)^2 dt}}{2\pi N_{0n}}, \tag{53}$$

with Green's function:

$$G(r,r',\theta,\theta',dt) = \\ \sum_{m=0}^{\infty}\sum_{n=1}^{\infty} \frac{J_{\mathrm{m}}(\frac{\lambda_{\mathrm{mn}}}{a}r)J_{\mathrm{m}}(\frac{\lambda_{\mathrm{mn}}}{a}r')\left[2\cos(m(\theta-\theta'))+1\right]\mathrm{e}^{-D\left(\frac{\lambda_{\mathrm{mn}}}{a}\right)^2 dt}}{2\pi N_{\mathrm{mn}}}. \tag{54}$$

3.2.2 *Deriving the Green's function for Dirichlet boundary conditions*

In the 2-dimensional Dirichlet case the Green's function remains of the same form as in that of the Neumann case given in Eq. (54). For the Dirichlet condition on the outer radial boundary:

$$c(a,\theta,t) = 0, \tag{55}$$

we retrieve the eigenvalue problem:

$$J_{\mathrm{m}}(ka) = 0, \tag{56}$$

which are the Bessel function zeros, that is the points in which our function plotted in Figure. 16a a) crosses the horizontal axis, with the eigenvalues $\Psi_{\mathrm{mn}} = ka$. This also means that the orthogonality constant N_{mn} is, in this case, given by the second term of Equation (47) as the first term becomes zero.

3.2.3 *Deriving the Green's function for an annulus*

For an annular region our radial domain becomes $r \in [a, b]$, that is we model the area between two concentric circles of radii a and b, $a < b$. Separation of variables produces solutions as previously given in Eq. (41). The second radial boundary condition, given in Eq. 42, is automatically satisfied as our domain does not contain $r = 0$, and hence in this case we cannot set $D = 0$. We are therefore required to apply the no flux boundary condition to both radial boundaries:

$$\left.\frac{\partial c}{\partial r}\right|_{r=a} = \left.\frac{\partial c}{\partial r}\right|_{r=b} = 0, \tag{57}$$

whilst the angular boundary conditions remain as previously. With foresight, we set the coefficients of the radial solution (3) from Eq. (41) to be:

$$\begin{aligned} C &= Y_{\mathrm{m}}'(ka), \\ D &= -J_{\mathrm{m}}'(ka), \end{aligned} \tag{58}$$

and hence the equation becomes:

$$R(r) \equiv Z_{\mathrm{m}}(kr) = Y_{\mathrm{m}}'(ka)J_{\mathrm{m}}(kr) - J_{\mathrm{m}}'(ka)Y_{\mathrm{m}}(kr). \tag{59}$$

The boundary condition at $r = a$ is therefore satisfied by construction as:

$$R'(a) = kY_{\mathrm{m}}'(ka)J_{\mathrm{m}}'(ka) - kJ_{\mathrm{m}}'(ka)Y_{\mathrm{m}}'(ka) = 0. \tag{60}$$

Applying the no flux condition at $r = b$ gives us our second boundary condition, satisfied by the eigenvalue problem:

$$Y_{\mathrm{m}}'(ka)J_{\mathrm{m}}'(kb) - J_{\mathrm{m}}'(ka)Y_{\mathrm{m}}'(kb) = 0, \tag{61}$$

with eigenvalues $k = k_{\mathrm{mn}}$.

Combining solutions we have:

$$c(r, \theta, t) = T_0(A\sin(m\theta) + B\cos(m\theta))Z_{\mathrm{m}}(kr)\mathrm{e}^{-Dk^2t}, \tag{62}$$

whilst our orthogonality relationships are given by Eq. (48) and:

$$\langle R_{\mathrm{n}}, R_{\mathrm{m}}\rangle = \int_a^{\mathrm{b}} Z_{\mathrm{n}}(kr)Z_{\mathrm{m}}(kr)r\mathrm{d}r = \begin{cases} 0, & n \neq m, \\ N_{\mathrm{mn}}, & n = m. \end{cases} \tag{63}$$

The normalisation constant is now given by:

$$N_{\mathrm{nm}} = \frac{b^2}{2}\left[1 - \frac{m^2}{k^2b^2}\right](Z_{\mathrm{m}}(kb))^2 + \frac{b^2}{2}\left(Z'_{\mathrm{m}}(kb)\right)^2 - \frac{a^2}{2}\left[1 - \frac{m^2}{k^2a^2}\right](Z_{\mathrm{m}}(ka))^2 - \frac{a^2}{2}\left(Z'_{\mathrm{m}}(ka)\right)^2, \tag{64}$$

and here, because of our no flux condition on each boundary, the second and fourth term are equal to zero. We take our solution at $t = 0$:

$$c(r,\theta,0) =$$

$$C_0(r,\theta) = \begin{cases} \sum_{n=1}^{\infty} Z_0(k_{0n}r)B_{0n}, & m = 0, \\ \sum_{m=1}^{\infty}\sum_{n=1}^{\infty} Z_{\mathrm{m}}(k_{\mathrm{mn}}r)\left[A_{\mathrm{mn}}\sin(m\theta) + B_{\mathrm{mn}}\cos(m\theta)\right], & m > 0, \end{cases} \tag{65}$$

and find our constants by firstly taking the inner product of $C_0(r,\theta)$ for $m = 0$ with $Z_0(kr)$ to find:

$$B_{0n} = \frac{\langle C_0, R_{\mathrm{m}}\rangle}{\langle R_{\mathrm{n}}, R_{\mathrm{m}}\rangle} = \frac{\int_0^{2\pi}\int_a^{\mathrm{b}} C_0(r',\theta')Z_0(kr')r'\mathrm{d}r'\mathrm{d}\theta'}{N_{\mathrm{mn}}}. \tag{66}$$

Next, to find A_{mn}, we take the inner product of $C_0(r,\theta)$ for $m > 0$ with $Z_{\mathrm{m}}(kr)\sin(m\theta)$ so that:

$$A_{\mathrm{mn}} = \frac{\langle C_0, R_{\mathrm{m}}\sin(m\theta)\rangle}{\langle R_{\mathrm{n}}\Theta_{\mathrm{n}}, R_{\mathrm{m}}\sin(m\theta)\rangle} = \frac{\int_0^{2\pi}\int_a^{\mathrm{b}} C_0(r',\theta')Z_{\mathrm{m}}(kr')\sin(m\theta)r'\mathrm{d}r'\mathrm{d}\theta'}{2\pi N_{\mathrm{mn}}}, \tag{67}$$

and similarly for B_{mn} we take the inner product with $Z_{\mathrm{m}}(kr)\cos(m\theta)$ and obtain:

$$B_{\mathrm{mn}} = \frac{\langle C_0, R_{\mathrm{m}}\cos(m\theta)\rangle}{\langle R_{\mathrm{n}}\Theta_{\mathrm{n}}, R_{\mathrm{m}}\cos(m\theta)\rangle} = \frac{\int_0^{2\pi}\int_a^{\mathrm{b}} C_0(r',\theta')Z_{\mathrm{m}}(kr')\cos(m\theta)r'\mathrm{d}r'\mathrm{d}\theta'}{2\pi N_{\mathrm{mn}}}. \tag{68}$$

Our final solution is therefore:

$$c(r,\theta,t) = \sum_{m=1}^{\infty}\sum_{n=1}^{\infty} \frac{\int_a^{\mathrm{b}}\int_0^{2\pi} C_0(r',\theta') Z_{\mathrm{m}}(k_{\mathrm{mn}}r) Z_{\mathrm{m}}(k_{\mathrm{mn}}r')(\cos(m(\theta-\theta')))r'\mathrm{d}r'\mathrm{d}\theta'\mathrm{e}^{-Dk_{\mathrm{mn}}^2 dt}}{\pi N_{\mathrm{mn}}} + \sum_{n=1}^{\infty} \frac{\int_a^{\mathrm{b}}\int_0^{2\pi} C_0(r',\theta') Z_0(k_{0n}r) Z_0(k_{0n}r') r'\mathrm{d}r'\mathrm{d}\theta'\mathrm{e}^{-Dk_{0n}^2 dt}}{2\pi N_{0n}}, \tag{69}$$

with Green's function:

$$G(r,r',\theta,\theta',dt) = \sum_{m=0}^{\infty}\sum_{n=1}^{\infty} \frac{Z_{\mathrm{m}}(k_{\mathrm{mn}}r) Z_{\mathrm{m}}(k_{\mathrm{mn}}r')\left[2\cos(m(\theta-\theta'))+1\right]\mathrm{e}^{-Dk_{\mathrm{mn}}^2 dt}}{2\pi N_{\mathrm{mn}}}. \tag{70}$$

3.3 DIFFUSION IN 2-DIMENSIONS: ELLIPTIC COORDINATE SYSTEM

3.3.1 *Deriving the Green's function for Neumann boundary conditions*

The elliptic coordinate system can be defined in algebraic form as:

$$\begin{aligned} x &= c\xi\nu, \\ y &= c\sqrt{(\xi^2-1)(1-\nu^2)}, \end{aligned} \tag{71}$$

where, for an ellipse with semi-minor axis of length a and semi-major axis of length b, ($b > a$):

$$\xi \in (1,\xi_0], \qquad \nu \in (-1,1), \tag{72}$$

with,

$$\xi_0 = \frac{b}{c}, \qquad c = \sqrt{b^2-a^2}. \tag{73}$$

We wish to solve:

$$\frac{\partial v}{\partial t} = D\nabla^2 v, \tag{74}$$

where in elliptic coordinates:

$$\nabla^2 = \frac{\tilde{\nabla}}{c^2(\xi^2-\nu^2)}, \tag{75}$$

for,

$$\tilde{\nabla} = \sqrt{(\xi^2 - 1)}\frac{\partial}{\partial \xi}\left(\sqrt{(\xi^2 - 1)}\frac{\partial}{\partial \xi}\right) + \sqrt{(1 - \nu^2)}\frac{\partial}{\partial \nu}\left(\sqrt{(1 - \nu^2)}\frac{\partial}{\partial \nu}\right). \quad (76)$$

Setting:

$$v(\xi, \nu, t) = u(\xi, \nu)T(t), \quad (77)$$

we find:

$$\frac{\mathrm{d}T(t)}{\mathrm{d}t}\frac{1}{DT(t)} = \frac{1}{c^2(\xi^2 - \nu^2)u(\xi, \nu)}\tilde{\nabla}u(\xi, \nu) = -k^2, \quad (78)$$

and therefore separate the time dependent part to give our first ODE:

$$1. \qquad T' + k^2DT = 0, \quad (79)$$

leaving:

$$\tilde{\nabla}u(\xi, \nu) = -k^2c^2(\xi^2 - \nu^2)u(\xi, \nu). \quad (80)$$

We let $k^2c^2 = 4\gamma^2$, and write:

$$u(\xi, \nu) = p(\xi)q(\nu), \quad (81)$$

to find:

$$\begin{aligned}&\frac{\sqrt{(\xi^2 - 1)}}{p(\xi)}\frac{\partial}{\partial \xi}\left(\sqrt{(\xi^2} - 1)\frac{\partial p(\xi)}{\partial \xi} + \frac{\sqrt{(1 - \nu^2)}}{q(\nu)}\frac{\partial}{\partial \nu}\left(\sqrt{(1 - \nu^2)}\frac{\partial q(\nu)}{\partial \nu}\right)\right.\\ &\quad = -4\gamma^2(\xi^2 - \nu^2).\end{aligned} \quad (82)$$

Separating the variables and, with foresight towards later using the trigonometric double angle formula, subtracting $2\gamma^2$ from both sides gives:

$$\begin{aligned}&\frac{\sqrt{(\xi^2 - 1)}}{p(\xi)}\frac{\partial}{\partial \xi}\left(\sqrt{(\xi^2 - 1)}\frac{\partial p(\xi)}{\partial \xi}\right) + 4\gamma^2\xi^2 - 2\gamma^2\\ &\qquad = -\frac{\sqrt{(1 - \nu^2)}}{q(\nu)}\frac{\partial}{\partial \nu}\left(\sqrt{(1 - \nu^2)}\frac{\partial q(\nu)}{\partial \nu}\right) + 4\gamma^2\nu^2 - 2\gamma^2\\ &\qquad = \lambda,\end{aligned} \quad (83)$$

and hence we have our ODE's in the ξ and ν variables:

$$2. \qquad (\xi^2 - 1)\frac{\mathrm{d}^2p}{\mathrm{d}\xi^2} + \xi\frac{\mathrm{d}p}{\mathrm{d}\xi} + (2\gamma^2(2\xi^2 - 1) - \lambda)p = 0, \quad (84)$$

$$3. \qquad (1-\nu^2)\frac{\mathrm{d}^2 q}{\mathrm{d}\nu^2} - \nu\frac{\mathrm{d}q}{\mathrm{d}\nu} - (2\gamma^2(2\nu^2-1)-\lambda)q = 0. \tag{85}$$

[As an aside, these can be transformed into the standard form modified (radial) and ordinary (angular) Mathieu functions using:

$$\xi = \cosh r, \qquad r \in (0, \tilde{\xi}_0] \qquad\qquad \nu = \cos\theta, \qquad \theta \in (0, 2\pi], \tag{86}$$

where,

$$\tilde{\xi}_0 = \tanh^{-1}\left(\frac{a}{b}\right). \tag{87}$$

Using the chain rule to find:

$$\begin{aligned} \frac{\mathrm{d}}{\mathrm{d}r} &= \sinh r\frac{\mathrm{d}}{\mathrm{d}\xi}, \\ \frac{\mathrm{d}^2}{\mathrm{d}r^2} &= \sinh^2 r\frac{\mathrm{d}}{\mathrm{d}\xi^2} + \cosh r\frac{\mathrm{d}}{\mathrm{d}\xi}, \\ \frac{\mathrm{d}}{\mathrm{d}\theta} &= -\sin\theta\frac{\mathrm{d}}{\mathrm{d}\nu}, \\ \frac{\mathrm{d}^2}{\mathrm{d}\theta^2} &= \sin^2\theta\frac{\mathrm{d}^2}{\mathrm{d}\nu^2} - \cos\theta\frac{\mathrm{d}}{\mathrm{d}\nu}, \end{aligned} \tag{88}$$

and noting,

$$\sinh r = \sqrt{(\xi^2-1)}, \qquad\qquad \sin\theta = \sqrt{(1-\nu^2)}, \tag{89}$$

we write Eq. 84 as:

$$\sinh^2 r\frac{\mathrm{d}^2 p}{\mathrm{d}\nu^2} + \cosh r\frac{\mathrm{d}p}{\mathrm{d}\xi} + (2\gamma^2(2\cosh^2 r - 1)-\lambda)p = 0, \tag{90}$$

and hence, using the double angle formula and Eqs. 88, we retrieve:

$$\frac{\mathrm{d}^2 p}{\mathrm{d}r^2} + (2\gamma^2\cosh 2r - \lambda)p = 0, \tag{91}$$

which is the Modified Mathieu equation in standard form.

Similarly, we write Eq. 85 as:

$$\sin^2\theta\frac{\mathrm{d}^2 q}{\mathrm{d}\nu^2} - \cos\theta\frac{\mathrm{d}q}{\mathrm{d}\nu} - (2\gamma^2(2\cos^2\theta - 1)-\lambda)q = 0, \tag{92}$$

to find:

$$\frac{\mathrm{d}^2 q}{\mathrm{d}\theta^2} - (2\gamma^2\cos 2\theta - \lambda)q = 0, \tag{93}$$

which is the Ordinary Mathieu equation in standard form.

Our solutions corresponding to Eqs. 79, 84 and 85 are given by:

$$\begin{aligned}
&1. \qquad T = T_0 \mathrm{e}^{-k^2 D t}, \qquad k^2 = \frac{4\gamma^2}{c^2} \\
&2. \qquad p_{\mathrm{m}}(\xi) = \begin{cases} Jo_{\mathrm{m}}(\xi, \gamma^{\mathrm{o}}) \\ Je_{\mathrm{m}}(\xi, \gamma^{\mathrm{e}}) \\ No_{\mathrm{m}}(\xi, \gamma^{\mathrm{o}}) \\ Ne_{\mathrm{m}}(\xi, \gamma^{\mathrm{e}}) \end{cases} \\
&3. \qquad q_{\mathrm{m}}(\nu) = \begin{cases} se_{\mathrm{m}}(\nu, \gamma^{\mathrm{o}}) & m = 1, 2, 3, \ldots \\ ce_{\mathrm{m}}(\nu, \gamma^{\mathrm{e}}) & m = 0, 1, 2, \ldots \end{cases}
\end{aligned} \tag{94}$$

respectively, where Jo_{m} and Je_{m} are the odd and even radial Mathieu functions of the first kind, No_{m} and Ne_{m} are the odd and even radial Mathieu functions of the second kind, and se_{m} and ce_{m} are the odd and even angular Mathieu functions. All of these functions are plotted in Figure. 17 for small values of m. As the odd and even functions are solutions to different equations, they require different values of the parameter γ and hence we denote γ^{o} and γ^{e} as parameterising the odd and even functions respectively. The values of these will be found separately using the boundary conditions in the radial variable.

Boundary conditions

We require continuity and differentiability of solutions across the line segment at $\xi = 1$, and therefore we are required to write our solutions as even:

$$ve_{\mathrm{m}}(\xi, \nu, t) = A_1 (Je_{\mathrm{m}}(\xi, \gamma^{\mathrm{e}}) + B_1 Ne_{\mathrm{m}}(\xi, \gamma^{\mathrm{e}})) ce_{\mathrm{m}}(\nu, \gamma^{\mathrm{e}}) \mathrm{e}^{-k^2 D t}, \qquad m \geq 0, \tag{95}$$

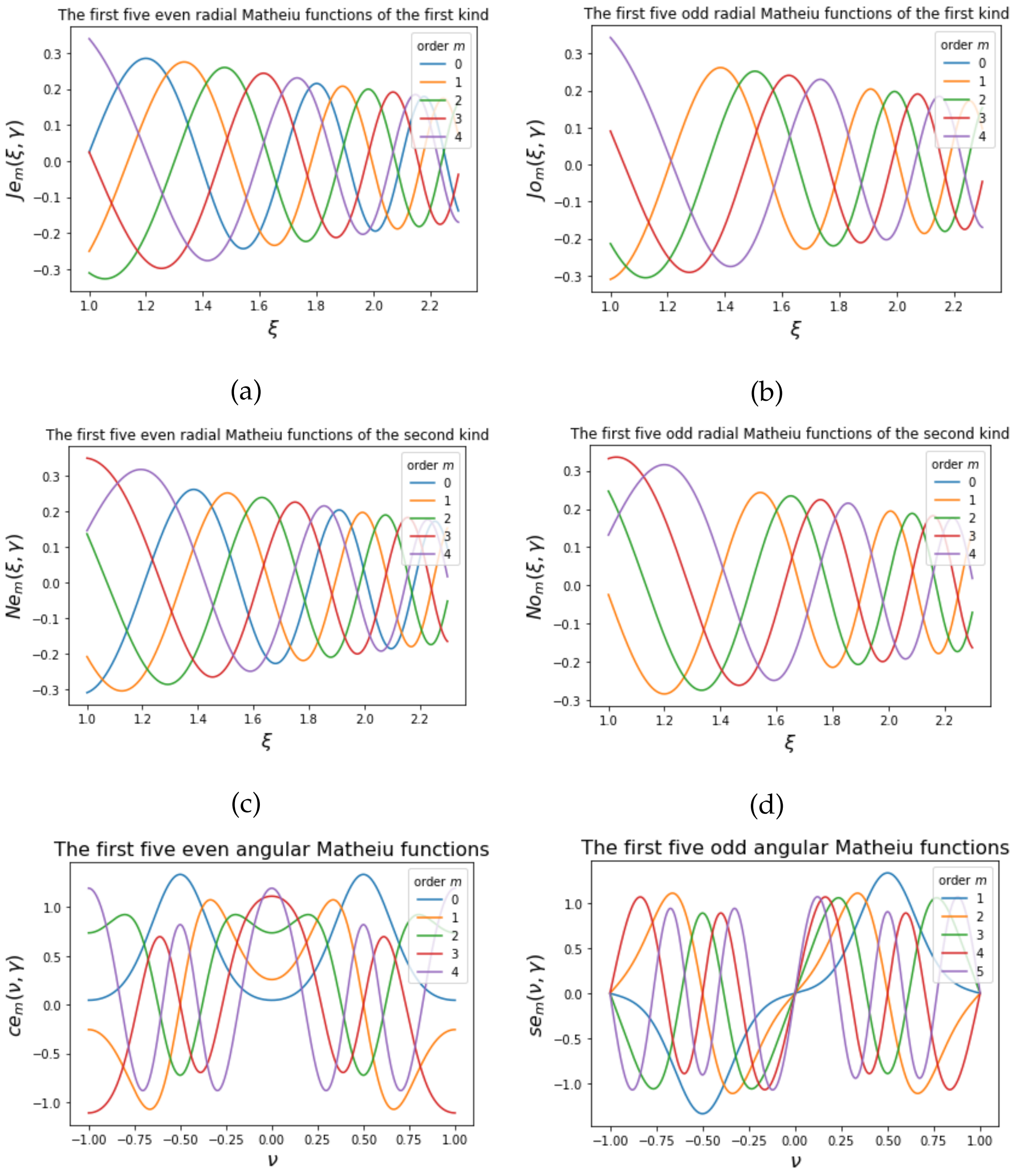

(a) (b) (c) (d) (e) (f)

Figure 17.: Examples of the Mathieu functions of integer order. a)/b) and c)/d) show the even/odd radial Mathieu functions of the first kind and second kind respectively whilst e)/f) show the even/odd angular functions.

and odd:

$$vo_{\mathrm{m}}(\xi,\nu,t) = A_2(Jo_{\mathrm{m}}(\xi,\gamma^{\mathrm{o}}) + B_2No_{\mathrm{m}}(\xi,\gamma^{\mathrm{o}}))se_{\mathrm{m}}(\nu,\gamma^{\mathrm{o}})\mathrm{e}^{-k^2Dt}, \qquad m \geq 1, \tag{96}$$

[7]. Due to the singularity at $\xi = 1$ we set $B_1 = B_2 = 0$ and solutions reduce to:

$$ve_{\mathrm{m}}(\xi, \nu, t) = A_1 Je_{\mathrm{m}}(\xi, \gamma^{\mathrm{e}}) ce_{\mathrm{m}}(\nu, \gamma^{\mathrm{e}}) \mathrm{e}^{-k^2 Dt}, \qquad m \geq 0, \tag{97}$$

and,

$$vo_{\mathrm{m}}(\xi, \nu, t) = A_2 Jo_{\mathrm{m}}(\xi, \gamma^{\mathrm{o}}) se_{\mathrm{m}}(\nu, \gamma^{\mathrm{o}}) \mathrm{e}^{-k^2 Dt}, \qquad m \geq 1. \tag{98}$$

As we initially require the outer boundary to be impermeable, we require a no flux condition across ξ_0:

$$ve'_{\mathrm{m}}(\xi_0, \nu, t) = vo'_{\mathrm{m}}(\xi_0, \nu, t) = 0. \tag{99}$$

This gives us two separate eigenvalue problems:

$$\left. \frac{\mathrm{d}Je_{\mathrm{m}}(\xi, \gamma^{\mathrm{e}}_{\mathrm{mp}})}{\mathrm{d}\xi} \right|_{\xi = \xi_0} = 0, \tag{100}$$

and:

$$\left. \frac{\mathrm{d}Jo_{\mathrm{m}}(\xi, \gamma^{\mathrm{o}}_{\mathrm{mp}})}{\mathrm{d}\xi} \right|_{\xi = \xi_0} = 0, \tag{101}$$

for which the zeros are $\gamma^{\mathrm{e}}_{\mathrm{mp}}$ and $\gamma^{\mathrm{o}}_{\mathrm{mp}}$ respectively. Finally, solutions must be of period 2π in ν. Both our odd and even solutions have period 2π for order, m odd. Our solutions with m even have period π, however, as this is an interval of 2π, these are also allowed and we have $m \geq 0$ for our even solutions, ce_{m}, and $m \geq 1$ for our odd solutions se_{m}.

Normalisation

Our angular Mathieu functions are normalised using the orthogonality relations:

$$\int_0^{2\pi} se_{\mathrm{m}} se_{\mathrm{n}} \mathrm{d}\theta = \int_0^{2\pi} ce_{\mathrm{m}} ce_{\mathrm{n}} \mathrm{d}\theta = \begin{cases} 0 & m \neq n, \\ \pi & m = n \geq 1, \end{cases} \tag{102}$$

and:

$$\int_0^{2\pi} [ce_0]^2 \mathrm{d}\theta = 2\pi. \tag{103}$$

Following on from the analogous sine and cosine functions, we note orthogonality between the odd and even angular functions:

$$\int_0^{2\pi} se_{\mathrm{m}} ce_{\mathrm{n}} \mathrm{d}\theta = 0 \quad \forall \;\; m, n. \tag{104}$$

Considering now all of our boundary conditions, we write our full solution as:

$$V_{\mathrm{m}}(\xi, \nu, t) = \sum_{m=-\infty}^{\infty} \sum_{p=1}^{\infty} A_{\mathrm{mp}} Me_{\mathrm{m}}(\xi, \gamma_{\mathrm{mp}}) me_{\mathrm{m}}(\nu, \gamma_{\mathrm{mp}}) \mathrm{e}^{-k_{\mathrm{mp}}^2 Dt}, \tag{105}$$

where:

$$Me_{\mathrm{m}}(\xi, \gamma_{\mathrm{m}}) = \begin{cases} Jo_{-m}(\xi, \gamma_{-m}^{\mathrm{o}}), & m < 0, \\ Je_{\mathrm{m}}(\xi, \gamma_{\mathrm{m}}^{\mathrm{e}}), & m \geq 0, \end{cases} \tag{106}$$

and,

$$me_{\mathrm{m}}(\xi, \gamma_{\mathrm{m}}) = \begin{cases} se_{-m}(\nu, \gamma_{-m}^{\mathrm{o}}), & m < 0, \\ ce_{\mathrm{m}}(\nu, \gamma_{\mathrm{m}}^{\mathrm{e}}), & m \geq 0. \end{cases} \tag{107}$$

Assuming orthogonality of *Me*:

$$\int_1^{\xi_0} Me_{\mathrm{m}} Me_{\mathrm{n}} (\xi^2 - 1)^{-\frac{1}{2}} \mathrm{d}\xi = \begin{cases} 0 & m \neq n, \\ N_{\mathrm{mn}} & m = n, \end{cases} \tag{108}$$

and recalling orthogonality of *ce* and *se*:

$$\int_{-1}^{1} me_{\mathrm{m}} me_{\mathrm{n}} (1 - \nu^2)^{-\frac{1}{2}} \mathrm{d}\nu = \begin{cases} 0 & m \neq n, \\ \pi & m = n, \end{cases} \tag{109}$$

we multiply our initial condition:

$$V_{\mathrm{m}}(\xi, \nu, 0) = p_0(\xi) q_0(\nu) = \sum_{m=-\infty}^{\infty} \sum_{p=1}^{\infty} A_{\mathrm{mp}} Me_{\mathrm{m}}(\xi, \gamma_{\mathrm{mp}}) me_{\mathrm{m}}(\nu, \gamma_{\mathrm{mp}}) \tag{110}$$

by $Me_{\mathrm{n}}(\xi, \gamma_{\mathrm{np}}) me_{\mathrm{n}}(\nu, \gamma_{\mathrm{np}})$ and integrate over our domain to find our coefficient:

$$A_{\mathrm{mp}} = \frac{1}{N_{\mathrm{mn}}\pi} \int_{-1}^{1} \int_1^{\xi_0} p_0(\xi) q_0(\nu) Me_{\mathrm{m}}(\xi', \gamma_{\mathrm{mp}}) me_{\mathrm{m}}(\nu', \gamma_{\mathrm{mp}}) (\xi^2 - 1)^{-\frac{1}{2}} \mathrm{d}\xi (1 - \nu^2)^{-\frac{1}{2}} \mathrm{d}\nu. \tag{111}$$

Our full solution is therefore:

$$V_{\mathrm{m}}(\xi,\nu,t) = \sum_{m=-\infty}^{\infty}\sum_{p=1}^{\infty}\int_{-1}^{1}\int_{1}^{\xi_0}\frac{F\mathrm{d}\xi\mathrm{d}\nu}{\sqrt{(\xi^2-1)(1-\nu^2)}N_{\mathrm{mp}}\pi}\times \mathrm{e}^{-k_{\mathrm{mp}}^2 Dt}, \tag{112}$$

$$F = p_0(\xi)q_0(\nu)Me_{\mathrm{m}}(\xi,\gamma_{\mathrm{mp}})Me_{\mathrm{m}}(\xi',\gamma_{\mathrm{mp}})me_{\mathrm{m}}(\nu,\gamma_{\mathrm{mp}})me_{\mathrm{m}}(\nu',\gamma_{\mathrm{mp}}),$$

with Green's function:

$$G(\xi,\xi',\nu,\nu',t) = \sum_{m=-\infty}^{\infty}\sum_{p=1}^{\infty}\frac{1}{N_{\mathrm{mn}}\pi}Me_{\mathrm{m}}(\xi,\gamma_{\mathrm{mp}})Me_{\mathrm{m}}(\xi',\gamma_{\mathrm{mp}})me_{\mathrm{m}}(\nu,\gamma_{\mathrm{mp}})me_{\mathrm{m}}(\nu',\gamma_{\mathrm{mp}}) \times \mathrm{e}^{-k_{\mathrm{mp}}^2 Dt}. \tag{113}$$

3.3.2 *Deriving the Green's function for Dirichlet boundary conditions*

In the 2-dimensional Dirichlet case the Green's function remains of the same form as in that of the Neumann case given in Equation. (113). For the Dirichlet condition on the outer radial boundary:

$$ve_{\mathrm{m}}(\xi,\nu,t)|_{\xi=\xi_0} = vo_{\mathrm{m}}(\xi,\nu,t)|_{\xi=\xi_0} = 0, \tag{114}$$

we find the pair of eigenvalue problems:

$$Je_{\mathrm{m}}(\xi_0,\gamma_{\mathrm{mp}}^{\mathrm{e}}) = 0, \tag{115}$$

and:

$$Jo_{\mathrm{m}}(\xi_0,\gamma_{\mathrm{mp}}^{\mathrm{o}}) = 0, \tag{116}$$

which are the zeros of the even and odd Matheiu functions with the eigenvalues $\gamma_{\mathrm{mp}}^{\mathrm{e}}$ and $\gamma_{\mathrm{mp}}^{\mathrm{o}}$ respectively.

3.3.3 *Deriving the Green's function for an elliptic annulus*

Here we look at the elliptic coordinate system again, with the 'radial' component now between two membranes, $\xi \in (\xi_0, \xi_1)$, where the outer membrane has:

$$\xi_1 = \frac{b_1}{c_1} \tag{117}$$

for $b_1 = b + h$, $a_1 = a + h$ and $c_1 = \sqrt{b_1^2 - a_1^2}$. The separation of variables and solutions are the same as given in the previous section up to 105. The point that differs here is the boundary conditions, as we now require no flux across our inner boundary as well as the outer boundary. Our no flux condition therefore becomes:

$$ve'_{\mathrm{m}}(\xi_0, \nu, t) = ve'_{\mathrm{m}}(\xi_1, \nu, t) = vo'_{\mathrm{m}}(\xi_0, \nu, t) = vo'_{\mathrm{m}}(\xi_1, \nu, t) = 0. \tag{118}$$

For our even solutions the Neumann boundary condition gives:

$$Je'_{\mathrm{m}}(\xi_0, \gamma^{\mathrm{e}}) + B_1 Ne'_{\mathrm{m}}(\xi_0, \gamma^{\mathrm{e}}) = Je'_{\mathrm{m}}(\xi_1, \gamma^{\mathrm{e}}) + B_1 Ne'_{\mathrm{m}}(\xi_1, \gamma^{\mathrm{e}}) = 0, \tag{119}$$

which can be written as:

$$\begin{bmatrix} Je'_{\mathrm{m}}(\xi_0, \gamma^{\mathrm{e}}) & Ne'_{\mathrm{m}}(\xi_0, \gamma^{\mathrm{e}}) \\ Je'_{\mathrm{m}}(\xi_1, \gamma^{\mathrm{e}}) & Ne'_{\mathrm{m}}(\xi_1, \gamma^{\mathrm{e}}) \end{bmatrix} \begin{bmatrix} 1 \\ B_1 \end{bmatrix} = \begin{bmatrix} 0 \\ 0 \end{bmatrix}, \tag{120}$$

and hence we find our eigenvalue problem:

$$Je'_{\mathrm{m}}(\xi_0, \gamma^{\mathrm{e}}_{\mathrm{mp}}) Ne'_{\mathrm{m}}(\xi_1, \gamma^{\mathrm{e}}_{\mathrm{mp}}) - Je'_{\mathrm{m}}(\xi_1, \gamma^{\mathrm{e}}_{\mathrm{mp}}) Ne'_{\mathrm{m}}(\xi_0, \gamma^{\mathrm{e}}_{\mathrm{mp}}) = 0, \tag{121}$$

to be solved numerically for $\gamma^{\mathrm{e}}_{\mathrm{mp}}$; the p^{th} zero for the m^{th} order even solution.

From this condition we can write:

$$Je'_{\mathrm{m}}(\xi_0, \gamma^{\mathrm{e}}_{\mathrm{mp}}) = \frac{Je'_{\mathrm{m}}(\xi_1, \gamma^{\mathrm{e}}_{\mathrm{mp}})}{Ne'_{\mathrm{m}}(\xi_1, \gamma^{\mathrm{e}}_{\mathrm{mp}})} Ne'_{\mathrm{m}}(\xi_0, \gamma^{\mathrm{e}}_{\mathrm{mp}}), \tag{122}$$

and therefore, when compared to Eq. 119, we find our coefficient:

$$B_1 = -\frac{Je'_{\mathrm{m}}(\xi_1, \gamma^{\mathrm{e}}_{\mathrm{mp}})}{Ne'_{\mathrm{m}}(\xi_1, \gamma^{\mathrm{e}}_{\mathrm{mp}})}. \tag{123}$$

Similarly for our odd solutions we have the eigenvalue problem:

$$Jo'_{\mathrm{m}}(\xi_0,\gamma^{\mathrm{o}}_{\mathrm{mp}})No'_{\mathrm{m}}(\xi_1,\gamma^{\mathrm{o}}_{\mathrm{mp}}) - Jo'_{\mathrm{m}}(\xi_1,\gamma^{\mathrm{o}}_{\mathrm{mp}})No'_{\mathrm{m}}(\xi_0,\gamma^{\mathrm{o}}_{\mathrm{mp}}) = 0, \tag{124}$$

for $\gamma^{\mathrm{o}}_{\mathrm{mp}}$; the p^{th} zero for the m^{th} order odd solution, and our coefficient:

$$B_2 = -\frac{Jo'_{\mathrm{m}}(\xi_1,\gamma^{\mathrm{o}}_{\mathrm{mp}})}{No'_{\mathrm{m}}(xi_1,\gamma^{\mathrm{o}}_{\mathrm{mp}})}. \tag{125}$$

Our full solution can also be written in the form of Eq. 105, as:

$$V_{\mathrm{m}}(\xi,\nu,t) = \sum_{m=-\infty}^{\infty}\sum_{p=1}^{\infty} A_{\mathrm{mp}}Ze_{\mathrm{m}}(\xi,\gamma_{\mathrm{mp}})me_{\mathrm{m}}(\nu,\gamma_{\mathrm{mp}})\mathrm{e}^{-k^2_{\mathrm{mp}}Dt}, \tag{126}$$

where:

$$Ze_{\mathrm{m}}(\xi,\gamma_{\mathrm{m}}) = Me^{(1)}_{\mathrm{m}}(\xi,\gamma_{\mathrm{m}}) + B_{\mathrm{m}}Me^{(2)}_{\mathrm{m}}(\xi,\gamma_{\mathrm{m}}), \tag{127}$$

for $Me^{(1)}_{\mathrm{m}} = Me_{\mathrm{m}}$ as given in Eq. 106, me_{m} as given in Eq. 107 and:

$$B_{\mathrm{m}}Me^{(2)}_{\mathrm{m}}(\xi,\gamma_{\mathrm{m}}) = \begin{cases} B_2No_{-m}(\xi,\gamma^{\mathrm{o}}_{-m}), & m < 0, \\ B_1Ne_{\mathrm{m}}(\xi,\gamma^{\mathrm{e}}_{\mathrm{m}}), & m \geq 0. \end{cases} \tag{128}$$

Assuming orthogonality of Ze:

$$\int_{\xi_0}^{\xi_1} Ze_{\mathrm{m}}Ze_{\mathrm{n}}(\xi^2-1)^{-\frac{1}{2}}\mathrm{d}\xi = \begin{cases} 0 & m \neq n, \\ N_{\mathrm{mn}} & m = n, \end{cases} \tag{129}$$

and, recalling the orthogonality relationship for me_{m} given in Eq. 109, we multiply our initial condition:

$$V_{\mathrm{m}}(\xi,\nu,0) = p_0(\xi)q_0(\nu) = \sum_{m=-\infty}^{\infty}\sum_{p=1}^{\infty} A_{\mathrm{mp}}Ze_{\mathrm{m}}(\xi,\gamma_{\mathrm{mp}})me_{\mathrm{m}}(\nu,\gamma_{\mathrm{mp}}), \tag{130}$$

by $Ze_{\mathrm{n}}(\xi,\gamma_{\mathrm{np}})me_{\mathrm{n}}(\nu,\gamma_{\mathrm{np}})$ and integrate over our domain to find our second coefficient:

$$A_{\mathrm{mp}} = \frac{1}{N_{\mathrm{mn}}\pi}\int_{-1}^{1}\int_{\xi_0}^{\xi_1} p_0(\xi)q_0(\nu)Ze_{\mathrm{m}}(\xi',\gamma_{\mathrm{mp}})me_{\mathrm{m}}(\nu',\gamma_{\mathrm{mp}})(\xi^2-1)^{-\frac{1}{2}}\mathrm{d}\xi(1-\nu^2)^{-\frac{1}{2}}\mathrm{d}\nu. \tag{131}$$

Our full solution is therefore:

$$V_{\mathrm{m}}(\xi,\nu,t) = \sum_{m=-\infty}^{\infty}\sum_{p=1}^{\infty}\int_{-1}^{1}\int_{\xi_0}^{\xi_1}\frac{F\mathrm{d}\xi\mathrm{d}\nu}{\sqrt{\xi^2-1}\sqrt{1-\nu^2}N_{\mathrm{mp}}\pi}\mathrm{e}^{-k_{\mathrm{mp}}^2 Dt} \tag{132}$$

$$F = p_0(\xi)q_0(\nu)Ze_{\mathrm{m}}(\xi,\gamma_{\mathrm{mp}})Ze_{\mathrm{m}}(\xi',\gamma_{\mathrm{mp}})me_{\mathrm{m}}(\nu,\gamma_{\mathrm{mp}})me_{\mathrm{m}}(\nu',\gamma_{\mathrm{mp}})$$

with Green's function:

$$G(\xi,\xi',\nu,\nu',t) = \sum_{m=-\infty}^{\infty}\sum_{p=1}^{\infty}\frac{1}{N_{\mathrm{mn}}\pi}Ze_{\mathrm{m}}(\xi,\gamma_{\mathrm{mp}})Ze_{\mathrm{m}}(\xi',\gamma_{\mathrm{mp}})me_{\mathrm{m}}(\nu,\gamma_{\mathrm{mp}})me_{\mathrm{m}}(\nu',\gamma_{\mathrm{mp}})\mathrm{e}^{-k_{\mathrm{mp}}^2 Dt}. \tag{133}$$

3.4 MATHEMATICAL BACKGROUND SUMMARY

The mathematical method of semi-analytically solving a PDE using the separation of variables technique, in order to derive a Green's function, was demonstrated for:

- Two 1D domains with Neumann and Dirichlet boundary conditions,
- 2D polar coordinates on a disk and an annulus for both Neumann and Dirichlet boundary conditions, making use of the Bessel functions,
- 2D elliptic coordinates on an elliptic disk and annulus for both Neumann and Dirichlet boundary conditions, using the radial and angular Mathieu functions.

This has provided the background mathematical material required to model the diffusion of calcium through various compartments, which will be extended to the full 3D model before including the pump and channel dynamics in the next chapter.

4

MODEL DEVELOPMENT

Here, we develop a novel 3-dimensional model for the generation of calcium signals in the plant cell nucleus. We begin by deriving the Green's functions, following our methods in Section 3, to describe the diffusion of calcium in both the nucleolus and the surrounding peri-nuclear space. This is achieved for both spherical and spheroidal polar coordinates. Finally we add coupling terms to our equations, representing the pumps and channels which transport calcium across the adjoining membrane in order to obtain a representative model of the mechanism of nuclear calcium signal generation.

4.1 DIFFUSION OF CALCIUM IN SPHERICAL COMPARTMENTS

We initially approximate the nuclear geometry to be spherical. We shall see in Section 6 that this is acceptable in certain tissue types, however others, such as root hair cells, ideally require a less generalised morphology such as a spheroid or ellipsoid. Here, the nucleoplasm is modelled as a closed ball of radius a which is to be determined from experimental measurements. To model the PNS we require a spherical shell comprised of the volume contained between two concentric 2-spheres, the INM and ONM, with radii a and b where $b = a + h$ for $h > 0$. For ease of calculation we write $b = \lambda a$ for $\lambda > 1$. A schematic can be seen in Figure. 18a, where the solid black lines depicts the INM enclosing the nucleoplasm, and the dashed lines represent the ONM which is a 2D-surface in 3D $\mathbb{E}$-space. This may be visualised more easily as the 3D generalisation of an annulus confined by the two membranes, that is the rotation of the structure shown in Figure. 18b through π. To describe the diffusion of calcium through this system we require the Green's function in each of the domains which we initially treat as closed from one another and their environment. These will later be coupled through flux across the compartment boundaries using the equations describing the dynamics of the pumps and channels given at the end of this section.

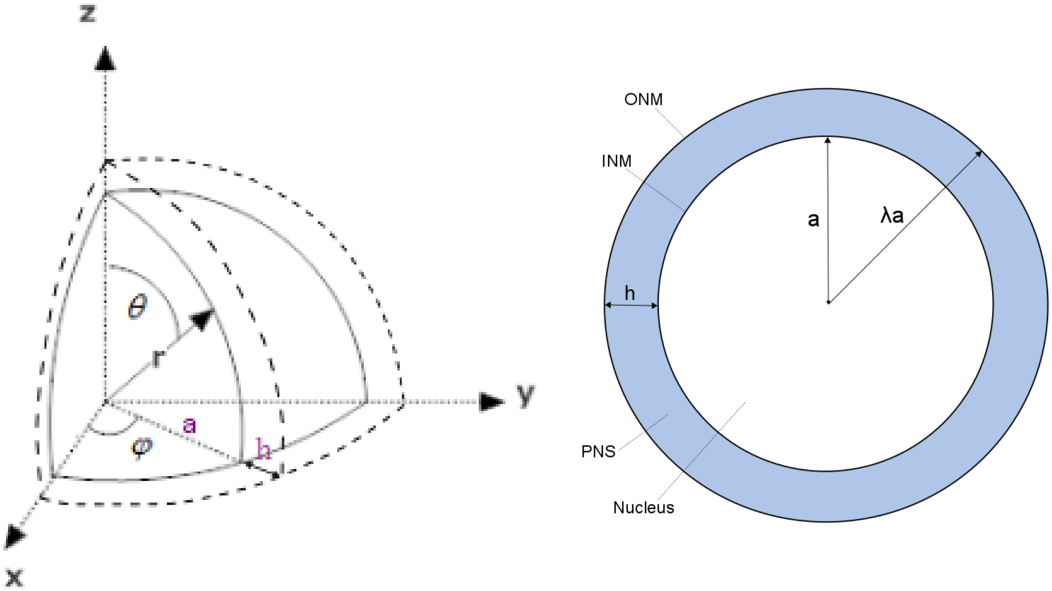

(a) (b)

Figure 18.: The domain to be modelled shown as a) the spherical shell b) the 2D representation of the nucleus.

4.1.1 *Derivation of the Green's function for a ball*

We begin by considering the diffusion of calcium within a spherical nucleus of radius a. Taking a typical spatio-temporal diffusion equation:

$$\frac{\partial u(\mathbf{r},t)}{\partial t} = D_{\text{nuc}} \nabla^2 u(\mathbf{r},t), \tag{134}$$

where $u(\mathbf{r},t)$ is the calcium concentration at time t and position $\mathbf{r} = (r,\theta,\phi)$, in the domain:

$$0 \leq r \leq a, \qquad 0 \leq \theta \leq \pi, \qquad 0 \leq \phi < 2\pi, \tag{135}$$

and D_{nuc} is the diffusion coefficient in the nucleoplasm. We write the gradient, ∇^2, in spherical polar coordinates and expand Eq. (134) to find:

$$\frac{\partial u}{\partial t} = D_{\text{nuc}} \left[\frac{\partial^2 u}{\partial r^2} + \frac{2}{r}\frac{\partial u}{\partial r} + \frac{1}{r^2}\frac{\partial^2 u}{\partial \theta^2} + \frac{\cot\theta}{r^2}\frac{\partial u}{\partial \theta} + \frac{1}{r^2 \sin^2\theta}\frac{\partial^2 u}{\partial \phi^2} \right]. \tag{136}$$

We normalise the equations such that we have a unit radius, by writing a new radial variable as:

$$\hat{r} = \frac{r}{a}, \tag{137}$$

with our new radial domain given by:

$$0 \leq \hat{r} \leq 1. \tag{138}$$

Our diffusion equation becomes:

$$\frac{\partial u}{\partial t} = \widehat{D}_{\text{nuc}} \left[\frac{\partial^2 u}{\partial \hat{r}^2} + \frac{2}{\hat{r}}\frac{\partial u}{\partial \hat{r}} + \frac{1}{\hat{r}^2}\frac{\partial^2 u}{\partial \theta^2} + \frac{\cot\theta}{\hat{r}^2}\frac{\partial u}{\partial \theta} + \frac{1}{\hat{r}^2 \sin^2\theta}\frac{\partial^2 u}{\partial \phi^2} \right], \tag{139}$$

where our normalisation has resulted in the scaling of our diffusion coefficient:

$$\widehat{D}_{\text{nuc}} = \frac{D_{\text{nuc}}}{a^2}. \tag{140}$$

Initially neglecting the azimuthal angle, ϕ, by arguments of symmetry [79], and dropping the 'hats' for convenience, we reduce our equation to,

$$\frac{\partial u}{\partial t} = D_{\text{nuc}} \left[\frac{\partial^2 u}{\partial r^2} + \frac{2}{r}\frac{\partial u}{\partial r} + \frac{1}{r^2}\frac{\partial^2 u}{\partial \theta^2} + \frac{\cot\theta}{r^2}\frac{\partial u}{\partial \theta} \right], \tag{141}$$

and solve semi-analytically using the separation of variables technique. Writing:

$$u(r,\theta,t) = p(r)q(\theta)T(t), \tag{142}$$

and setting $p(r) = \dfrac{z(r)}{(kr)^{\frac{1}{2}}}$ and $x = \cos\theta$, we reduce the PDE to a system of ODEs:

$$\begin{aligned}
&1. \qquad T' + k^2 D_{\text{nuc}} T = 0,\\
&2. \qquad r^2 z'' + rz' + (k^2 r^2 - (l + \frac{1}{2})^2) z = 0,\\
&3. \qquad (1 - x^2) q'' - 2xq' + \mu^2 q = 0,
\end{aligned} \tag{143}$$

where $-k^2$ and $-\mu^2 = -l(l+1)$, $l \in \mathbb{Z}_{\geq 0}$, are the separation constants. Eq. 2 and Eq. 3 of (143) are the Bessel equation and the Legendre differential equation respectively. These are each solved subject to the initial/boundary conditions:

$$\begin{aligned}
&1. \qquad T(0) = T_0, \quad T(t) = t,\\
&2. \qquad |\lim_{r \to 0} z(r)| < \infty, \quad z'(kr)|_{r=a} = 0,\\
&3. \qquad |\lim_{x \to \pm 1} q(x)| < \infty,
\end{aligned} \tag{144}$$

to give:

$$\begin{aligned}
&1. \qquad T(t) = T_0 \mathrm{e}^{-k^2 D_{\text{nuc}} t},\\
&2. \qquad z(kr) = C j_{\text{l}}(kr),\\
&3. \qquad q(x) = A P_{\text{l}}(x).
\end{aligned} \tag{145}$$

where $j_{\text{l}}(\frac{\alpha_{\text{lp}}}{a} r)$ is the spherical Bessel function of the first kind of order l, plotted in Figure. 19a, and $P_{\text{l}}(x)$ is the Legendre polynomial of the first kind of degree l, plotted in Figure. 20. We can write the spherical Bessel functions in terms of the standard Bessel functions, $J_{\text{n}}(x)$, previously used in Chapter 3 for the 2D case, by the relation:

$$j_{\text{l}}(\frac{\alpha_{\text{lp}}}{a} r) = \sqrt{\frac{\pi}{2r}} J_{\text{l}+\frac{1}{2}}(\frac{\alpha_{\text{lp}}}{a} r). \tag{146}$$

Solutions are then re-combined, as in Eq. (142), and we find:

$$u(r,\theta,t) = \sum_{l=0}^{\infty} \sum_{p=1}^{\infty} T_0 A_{\text{l}} C_{\text{lp}} j_{\text{l}}(\frac{\alpha_{\text{lp}}}{a} r) P_{\text{l}}(x) \mathrm{e}^{-\left(\frac{\alpha_{\text{lp}}}{a}\right)^2 D_{\text{nuc}} t}. \tag{147}$$

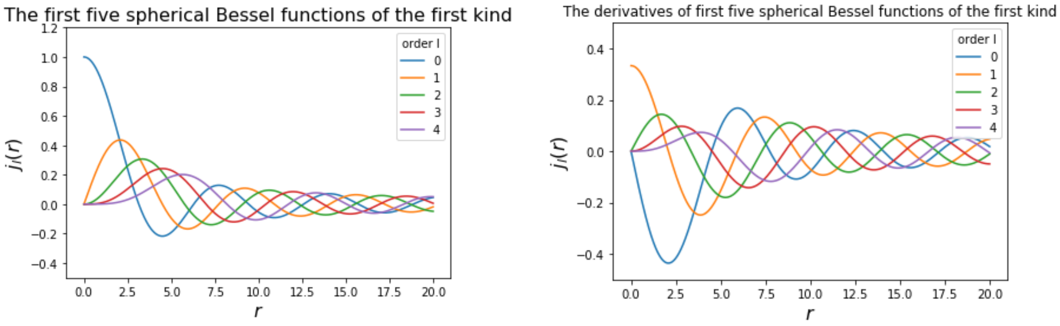

(a) (b)

Figure 19.: Examples of a) the Spherical Bessel functions of the first kind and b) their derivatives.

The term α_{lp} arises from the no flux radial boundary condition which gives the eigenvalue problem:

$$j_l'(\alpha_{lp}) = 0, \tag{148}$$

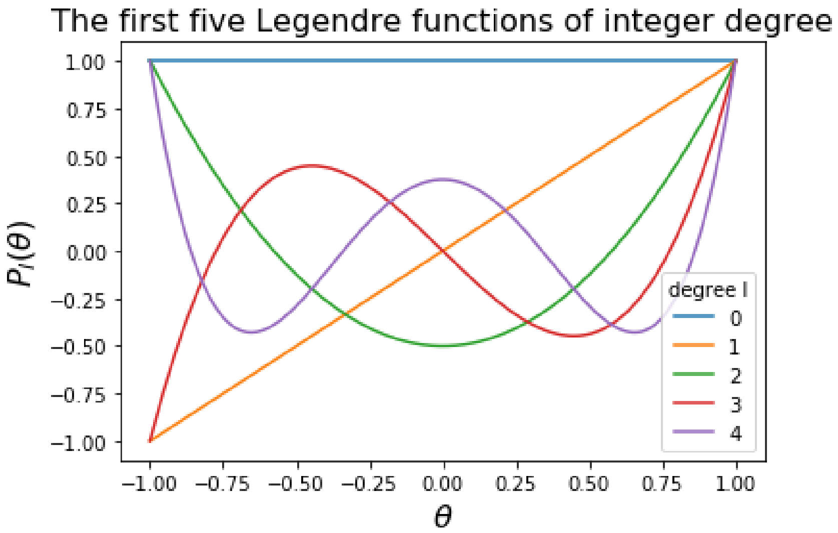

Figure 20.: The Legendre functions of integer degree.

and hence α_{lp} is the p^{th} zero of the derivative of the l^{th} order spherical Bessel function, as illustrated for $l = 0, 1, ...4$ by the points crossing the horizontal axis in Figure. 19b. The weighting coefficients A_l and C_{lp} are found using the orthogonality relations of the Legendre polynomials and spherical Bessel functions respectively to give:

$$A_{\mathrm{l}}C_{\mathrm{lp}} = \frac{2l+1}{2}\int_0^{\pi} q_0(\theta')P_{\mathrm{l}}(\cos\theta')\sin\theta'\mathrm{d}\theta' \frac{2\int_0^{\mathrm{a}} z_0(r')J_{\mathrm{l}+\frac{1}{2}}(\frac{\alpha_{\mathrm{lp}}}{a}r')r'^2\mathrm{d}r'}{a^2\sqrt{r'}\left[J^2_{\mathrm{l}+\frac{1}{2}}(\alpha_{\mathrm{lp}}) - J_{\mathrm{l}-\frac{1}{2}}(\alpha_{\mathrm{lp}})J_{\mathrm{l}+\frac{3}{2}}(\alpha_{\mathrm{lp}})\right]}, \tag{149}$$

for an initial source at $q_0(\theta')$ amd $z_0(r')$.

Finally we revisit the ϕ dependence and explicitly include this by considering a point on the sphere, $P(r,\theta,\phi)$, in relation to the point source $P'(r',\theta',\phi')$. Here the ϕ dependence depends only on the cosines of the angles of these two points, and hence for each source the coordinate system can be rotated, forcing one of the angles to be zero. The angle ψ between the points is then given by the spherical law of cosines:

$$h(\psi) = \cos(\psi) = \cos(\theta)\cos(\theta') + \sin(\theta)\sin(\theta')\cos(\phi - \phi'), \tag{150}$$

which, for initial condition $h_0(\psi')$, has normalization constant:

$$A_0 = \frac{1}{2\pi}\int_0^{2\pi} h_0(\psi')\mathrm{d}\psi'. \tag{151}$$

Our complete solution is therefore:

$$u(r,\theta,\psi,t) = \frac{T_0}{2\pi}\int_0^{2\pi} h_0(\psi')\mathrm{d}\psi' \sum_{l=0}^{\infty}(2l+1)\int_0^{\pi} q_0(\theta')P_{\mathrm{l}}(\cos\psi)\sin\theta'\mathrm{d}\theta' \sum_{p=1}^{\infty} \frac{\int_0^{\mathrm{a}} z_0(r')J_{\mathrm{l}+\frac{1}{2}}(\frac{\alpha_{\mathrm{lp}}}{a}r')J_{\mathrm{l}+\frac{1}{2}}(\frac{\alpha_{\mathrm{lp}}}{a}r)r'^2\mathrm{d}r'}{a^2\sqrt{r}\sqrt{r'}\left[J^2_{\mathrm{l}+\frac{1}{2}}(\alpha_{\mathrm{lp}}) - J_{\mathrm{l}-\frac{1}{2}}(\alpha_{\mathrm{lp}})J_{\mathrm{l}+\frac{3}{2}}(\alpha_{\mathrm{lp}})\right]} \mathrm{e}^{-\left(\frac{\alpha_{\mathrm{lp}}}{a}\right)^2 D_{\mathrm{nuc}}t}, \tag{152}$$

which is in the form:

$$u(r,\theta,\psi,t) = \int_{\Omega} u(r',\theta',\psi',0)G(r,\theta,\psi,t,r',\theta',\psi',t')\mathrm{d}V, \tag{153}$$

where:

$$u(r',\theta',\psi',0) = z_0(r')q_0(\theta')h_0(\psi')T_0, \tag{154}$$

with Green's function:

$$G(r,\theta,\psi,t,r',\theta',\psi') =$$

$$\sum_{l=0}^{\infty}\frac{(2l+1)}{2\pi}P_{\mathrm{l}}(\cos\psi)\sum_{p=1}^{\infty}\frac{J_{\mathrm{l}+\frac{1}{2}}(\frac{\alpha_{\mathrm{lp}}}{a}r')J_{\mathrm{l}+\frac{1}{2}}(\frac{\alpha_{\mathrm{lp}}}{a}r)}{a^{2}\sqrt{r}\sqrt{r'}\left[J^{2}_{\mathrm{l}+\frac{1}{2}}(\alpha_{\mathrm{lp}})-J_{\mathrm{l}-\frac{1}{2}}(\alpha_{\mathrm{lp}})J_{\mathrm{l}+\frac{3}{2}}(\alpha_{\mathrm{lp}})\right]} \tag{155}$$

$$\times\, \mathrm{e}^{-\left(\frac{\alpha_{\mathrm{lp}}}{a}\right)^{2}D_{\mathrm{nuc}}t}.$$

4.1.2 *Derivation of the Green's function for a spherical shell*

In the PNS we also write our diffusion equation as:

$$\frac{\partial u(\mathbf{r},t)}{\partial t} = D_{\mathrm{pns}}\nabla^{2}u(\mathbf{r},t), \tag{156}$$

however, we now have a radial domain of $r \in (a, \lambda a]$, and a diffusion coefficient, D_{pns}, which, as we shall see in Section 6.3, is different to that in the nucleoplasm. The Green's function is derived as in the previous case, with the separated system of ODEs given in Eq. (143). Whilst the 1st and 3rd boundary conditions, given in Eq. (144), remain the same, we now set a no flux condition on both of the radial boundaries:

$$z'(kr)|_{r=a} = 0, \quad z'(kr)|_{r=\lambda a} = 0. \tag{157}$$

This gives our radial solution to be a linear combination of the spherical Bessel functions of the first and second kind:

$$z(kr) = Cj_{\mathrm{l}}(kr) + Dy_{\mathrm{l}}(kr). \tag{158}$$

The plot in Figure. 21a highlights how the spherical Bessel functions of the second kind diverge at the origin. As our domain for the PNS does not include $r = 0$, we do not consider this region where $y_{\mathrm{l}}(kr)$ becomes unbounded and hence are unable to set $D = 0$ as previously. Applying the Neumann boundary conditions, ensuring $C, D \neq 0$, we obtain the eigenvalue problem:

$$j'_{\mathrm{l}}(\alpha_{\mathrm{lp}})y'_{\mathrm{l}}(\lambda\alpha_{\mathrm{lp}}) - y'_{\mathrm{l}}(\alpha_{\mathrm{lp}})j'_{\mathrm{l}}(\lambda\alpha_{\mathrm{lp}}) = 0, \tag{159}$$

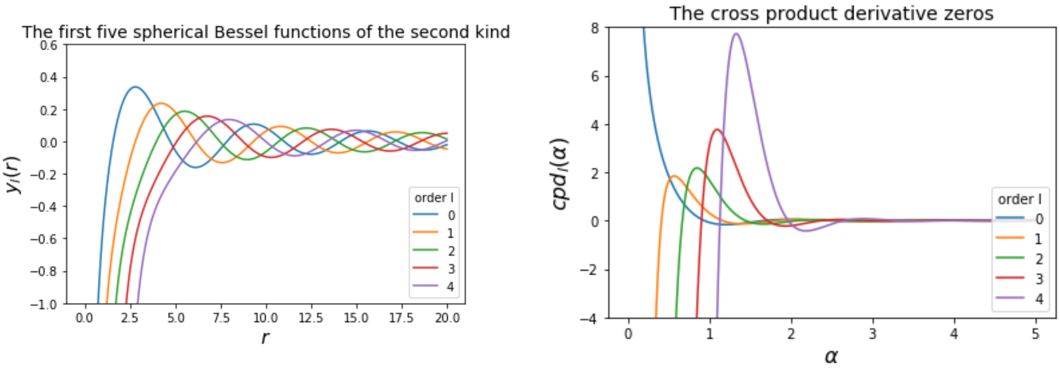

(a)

(b)

Figure 21.: Examples of a) the Spherical Bessel functions of the second kind and b) the cross product derivatives.

where we have set $k = \dfrac{\alpha_{\mathrm{lp}}}{a}$, for α_{lp} - the p^{th} solution to the l^{th} order problem. This boundary condition is plotted in Figure. 21b, with the eigenvalues, α, given by the points that cross product derivative, $cpd_{\mathrm{l}}(\alpha)$ crosses the horizontal axis.

We also see from our boundary conditions that we can combine C and D from Eq. (158), into a single constant, $\bar{C}$, by writing:

$$z(kr) = \bar{C}\bar{z}(kr), \tag{160}$$

where:

$$\bar{z}(kr) = j_{\mathrm{l}}(kr) - \frac{j_{\mathrm{l}}'(\alpha_{\mathrm{lp}})}{y_{\mathrm{l}}'(\alpha_{\mathrm{lp}})} y_{\mathrm{l}}(kr), \tag{161}$$

and by orthogonality of our solutions we find this constant to be:

$$\bar{C}_{\mathrm{lp}} = \frac{2\int_a^{\lambda a} \bar{z}_0(r')\bar{z}_{\mathrm{l}}(\frac{\alpha_{\mathrm{lp}}}{a}r')r'^2 dr'}{\left((\lambda a)^3 - \lambda a l\dfrac{(l+1)}{\alpha_{\mathrm{lp}}^2}\right)\left[\bar{z}_{\mathrm{l}}(\lambda\alpha_{\mathrm{lp}})\right]^2 - \left(a^3 - al\dfrac{(l+1)}{\alpha_{\mathrm{lp}}^2}\right)\left[\bar{z}_{\mathrm{l}}(\alpha_{\mathrm{lp}})\right]^2}. \tag{162}$$

Combining this result with the temporal and angular solutions found in the previous section, Eqs. 1. and 3. of Eq. (145), we have the overall solution:

$$
\begin{aligned}
u(r,\theta,t) = {} & \frac{T_0}{2\pi}\int_0^{2\pi} h_0(\psi')\mathrm{d}\psi' \sum_{l=0}^{\infty}(2l+1)\int_0^{\pi} q_0(\theta')P_{\mathrm{l}}(\cos\psi)\sin\theta'\mathrm{d}\theta' \\
& \times \sum_{p=1}^{\infty} \frac{\int_a^{\lambda a} \bar{z}_0(r')\bar{z}_{\mathrm{l}}(\frac{\alpha_{\mathrm{lp}}}{a}r')\bar{z}_{\mathrm{l}}(\frac{\alpha_{\mathrm{lp}}}{a}r)r'^2dr'}{\left((\lambda a)^3-\lambda a l\frac{(l+1)}{\alpha_{\mathrm{lp}}^2}\right)\left[\bar{z}_{\mathrm{l}}(\lambda\alpha_{\mathrm{lp}})\right]^2-\left(a^3-al\frac{(l+1)}{\alpha_{\mathrm{lp}}^2}\right)\left[\bar{z}_{\mathrm{l}}(\alpha_{\mathrm{lp}})\right]^2} \\
& \times \mathrm{e}^{-\left(\frac{\alpha_{\mathrm{lp}}}{a}\right)^2 D_{\mathrm{pns}}t}.
\end{aligned}
\tag{163}
$$

The solution is in the form of Eq. (153) where:

$$
u(r',\theta',\psi',0) = \bar{z}_0(r')q_0(\theta')h_0(\psi')T_0, \tag{164}
$$

with Green's function:

$$
\begin{aligned}
& G(r,\theta,\phi,t,r',\theta',\phi') = \\
& \sum_{l=0}^{\infty}\frac{(2l+1)}{2\pi}P_{\mathrm{l}}(\cos\psi)\sum_{p=1}^{\infty}\frac{\bar{z}_{\mathrm{l}}(\frac{\alpha_{\mathrm{lp}}}{a}r')\bar{z}_{\mathrm{l}}(\frac{\alpha_{\mathrm{lp}}}{a}r)}{N_{\mathrm{lp}}}\mathrm{e}^{-\left(\frac{\alpha_{\mathrm{lp}}}{a}\right)^2 D_{\mathrm{pns}}t},
\end{aligned}
$$

$$
N_{\mathrm{lp}} = \left((\lambda a)^3-\lambda a l\frac{(l+1)}{\alpha_{\mathrm{lp}}^2}\right)\left[\bar{z}_{\mathrm{l}}(\lambda\alpha_{\mathrm{lp}})\right]^2-\left(a^3-al\frac{(l+1)}{\alpha_{\mathrm{lp}}^2}\right)\left[\bar{z}_{\mathrm{l}}(\alpha_{\mathrm{lp}})\right]^2. \tag{165}
$$

Full details of all calculations from this section can be found in Appendix A.

4.2 DIFFUSION OF CALCIUM IN SPHEROIDAL COMPARTMENTS

Here the Green's function for the spheroidal case is obtained. It will be demonstrated in Section 6, that the spheroid is a more realistic approximation for the nuclei of root hair cells. Furthermore, the importance of using the more generalised spheroidal geometry for a more realistic application is noted in several papers including [6] and [18]. In this work, the nucleoplasm is modelled as prolate spheroid, which is obtained by rotating the elliptic coordinates about the major axis such that, at $z = 0$, the surface on the two principle axis gives a circle of radius a. The spheroidal coordinate system is written in terms of the Cartesian coordinates, (x, y, z), as:

$$\begin{aligned} x &= c\sqrt{(\xi^2 - 1)(1 - \nu^2)}\cos\phi, \\ y &= c\sqrt{(\xi^2 - 1)(1 - \nu^2)}\sin\phi, \\ z &= c\xi\nu, \end{aligned} \tag{166}$$

where c is the focal point of the ellipse, given by:

$$c = \sqrt{b^2 - a^2}, \tag{167}$$

for the prolate spheroid in which $b > a$ as illustrated in Figure. 22. The PNS is the volume contained within the two surfaces of the INM and ONM which, in this case, are 2D prolate spheroidal surfaces at ξ_0 and ξ_1, where:

$$\xi_0 = \frac{b_0}{c_0}. \tag{168}$$

and

$$\xi_1 = \frac{b_0 + h}{c_0 + h} = \frac{b_1}{c_1}. \tag{169}$$

We have set the width of the PNS as h with foresight to ensure that $\xi_0 \neq \xi_1$ and hence that the eigenvalue problem in Eq. 188 is nontrivial. This means that, due to the nature of the coordinate system, the INM is 'less spherical' than the ONM.

4.2.1 *Derivation of the Green's function for a prolate spheroid*

We wish to solve the diffusion Eq. :

$$\frac{\partial u(\mathbf{r}, t)}{\partial t} = D_{\text{nuc}}\nabla^2 u(\mathbf{r}, t), \tag{170}$$

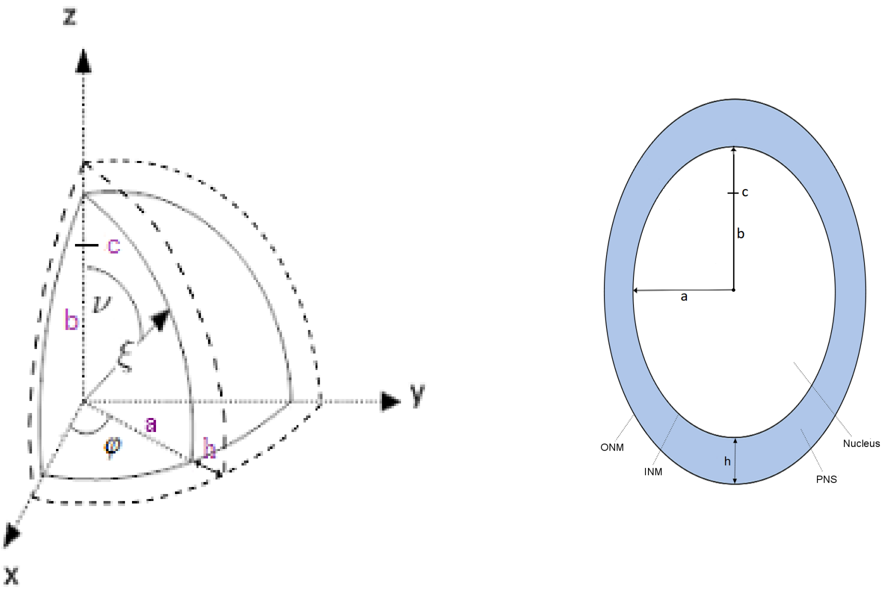

(a)

(b)

Figure 22.: Representation of the domain to be modelled as a) the spheroidal shell and b) an extension of the 2D ellipse.

with the calcium concentration, $u(\mathbf{r}, t)$, denoted at time t and position $\mathbf{r} = (\xi, \nu, \phi)$, in the domain:

$$1 \leq \xi \leq \xi_0, \qquad -1 \leq \nu \leq 1, \qquad 0 \leq \phi < 2\pi, \tag{171}$$

with $\xi_0 = \frac{b}{c}$, for focal point $c = \sqrt{b^2 - a^2}$. In prolate spheroidal coordinates our Laplacian is

$$\nabla^2 = \frac{1}{c^2(\xi^2 - \nu^2)} \left[\frac{\partial}{\partial \xi} \left((\xi^2 - 1) \frac{\partial}{\partial \xi} \right) + \frac{\partial}{\partial \nu} \left((1 - \nu^2) \frac{\partial}{\partial \nu} \right) + \frac{(\xi^2 - \nu^2)}{(\xi^2 - 1)(1 - \nu^2)} \frac{\partial^2}{\partial \phi^2} \right]. \tag{172}$$

We write:

$$v(\xi, \nu, \phi, t) = p(\xi) q(\nu) s(\phi) T(t), \tag{173}$$

and using separation of variables, we recover 4 ODEs:

$$\begin{aligned}
&1. \qquad T'(t) + k^2 D T(t) = 0,\\
&2. \qquad s''(\phi) + \mu^2 s(\phi) = 0,\\
&3. \qquad \frac{\partial}{\partial \xi}\left((\xi^2-1)\frac{\partial p(\xi)}{\partial \xi}\right) - \left(\lambda - \gamma^2\xi^2 + \frac{\mu^2}{(\xi^2-1)}\right)p(\xi) = 0,\\
&4. \qquad \frac{\partial}{\partial \nu}\left((1-\nu^2)\frac{\partial q(\nu)}{\partial \nu}\right) + \left(\lambda - \gamma^2\nu^2 - \frac{\mu^2}{(1-\nu^2)}\right)q(\nu) = 0,
\end{aligned} \tag{174}$$

where k, μ and λ are separation constants, and $\gamma^2 = k^2c^2$. The corresponding solutions to the set of ODEs are:

$$\begin{aligned}
&1. \qquad T(t) = T_0 \mathrm{e}^{-k^2 D t},\\
&2. \qquad s(\phi) = \begin{cases} \sin(\mu\phi) \\ \cos(\mu\phi), \end{cases}\\
&3. \qquad p(\xi) = R^{(1)}_{\mu l}(\gamma,\xi) + B R^{(2)}_{\mu l}(\gamma,\xi),\\
&4. \qquad q(\nu) = S_{\mu l}(\gamma,\nu),
\end{aligned} \tag{175}$$

where $R^{(i)}_{\mu l}(\gamma,\xi)$ is the prolate radial wave function of the i^{th} kind, plotted in Figure. 23, and $S_{\mu l}(\gamma,\nu)$ is the prolate angular wave function, plotted in Figure. 24, with both functions having order μ and degree l, along with a shared eigenvalue $\lambda^1_\mu(\gamma)$. We have two sets of possible solutions in the ϕ direction, which we keep separate for ease of normalisation, however, we can linearly combine these two sets of solutions later for computation.

Boundary conditions

$$\begin{aligned}
&1. \qquad T(0) = T_0,\\
&2. \qquad s(0) = s(2\pi)\\
&3. \qquad \lim_{\xi\to 1} p(\xi) < \infty, \qquad p'(\zeta_0,\gamma) = 0,\\
&4. \qquad \lim_{\nu\to\pm 1} q(\nu) < \infty,
\end{aligned} \tag{176}$$

For our time component we have the initial condition given in Eq. 1. of 176 which is already reflected in our solution in Eq. 1. of 175. For $s(\phi)$

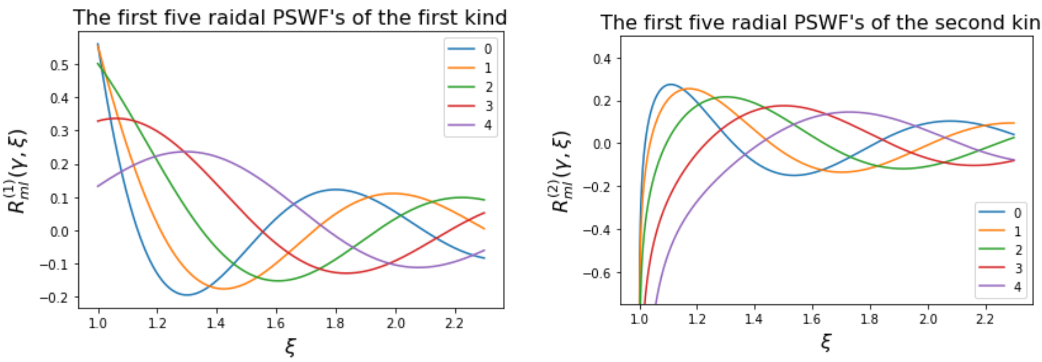

(a) (b)

Figure 23.: Examples of the radial prolate spheroidal wave-functions (PSWF's) with $m = 0$ of the a) first and b) second kind.

we require the periodicity condition given in Eq. 2. of 176 which holds for $\mu \in \mathbb{Z}$ and so we have $\mu = m = 0, 1, 2, ...$ In our 'radial' coordinate we have the inhomogeneous conditions stated in Eq. 3. of 176. We require that the solution is bounded at the line segment $\xi = 1$ and hence, as $R^{(2)}(\xi, \gamma)$ divergences at the origin, we set $B = 0$ and henceforth refer to $R^{(1)}(\xi, \gamma)$ as $R(\xi, \gamma)$. At the opposite end of the domain we demand there is no flux across the outer boundary, that is, at $\xi = \xi_0$:

$$\left.\frac{\mathrm{d}R_{\mathrm{ml}}(\xi, \gamma_{\mathrm{mlp}})}{\mathrm{d}\xi}\right|_{\xi=\xi_0} = 0, \tag{177}$$

which we solve for γ_{mlp} - the p^{th} zero of the derivative of the radial spheroidal wave function of order m and degree l. Finally the angular spheroidal wave functions are bounded on $(-1, 1)$ as specified in Eq. 176 (4). These solutions exist only for the eigenvalues $\lambda_{\mathrm{ml}}(\gamma_{\mathrm{mlp}}^2)$ of the separation parameter λ where $l = m, m+1, m+2...$ and hence we restrict our degree to these values.

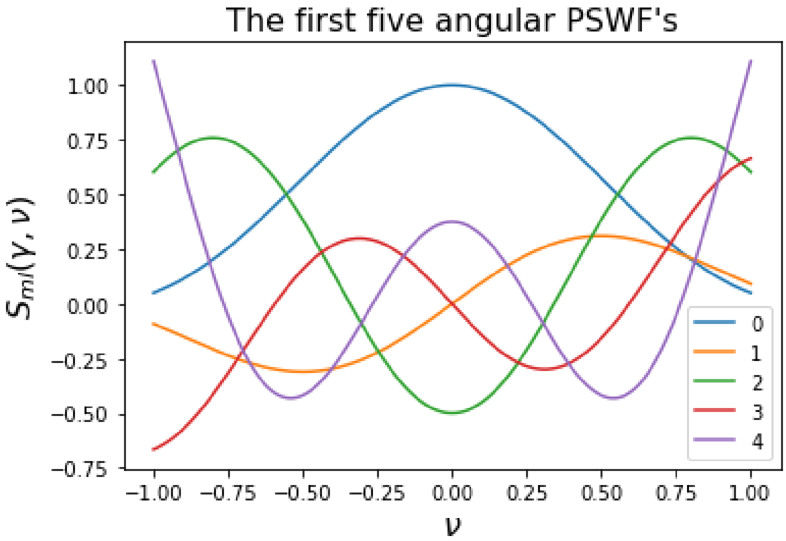

Figure 24.: Example of the angular prolate spheroidal wave-functions with $m = 0$.

Normalisation

The functions in our spatial domain are normalised using the following orthogonality relation:

$$\int_0^{2\pi}\int_{-1}^{1}\int_{1}^{\xi_0} u_{\mathrm{ml}}(\xi,\nu,\phi)u_{\mathrm{nk}}(\xi,\nu,\phi)\sqrt{(\xi^2-1)}\sqrt{(1-\nu^2)}(\xi^2-\nu^2)\mathrm{d}\xi\mathrm{d}\nu\mathrm{d}\phi$$
$$= \begin{cases} 0, & m \neq n, l \neq k, \\ N_{\mathrm{mn}}, & m = n, l = k. \end{cases} \tag{178}$$

We can normalise the angular spheroidal wave functions by the scheme utilised for the associated Legendre polynomials as given in Eq. 300 and hence write $N_{\mathrm{lm}} = \dfrac{2}{2l+1}$.

Our combined solutions give:

$$v(\xi,\nu,\phi,t) = A_{\mathrm{mlp}}R^{(1)}_{\mathrm{ml}}(\xi,\gamma_{\mathrm{mlp}})S_{\mathrm{ml}}(\nu,\gamma_{\mathrm{mlp}})\frac{\sin(m\phi)}{\cos(m\phi)}\mathrm{e}^{-k^2 D_{\mathrm{nuc}}t}, \tag{179}$$

and to find the coefficient A_{mlp} we take our initial condition:

$$v(\xi,\nu,\phi,0) = p_0(\xi)q_0(\nu)s_0(\phi) = A_{\mathrm{mlp}}R^{(1)}_{\mathrm{ml}}(\xi,\gamma_{\mathrm{mlp}})S_{\mathrm{ml}}(\nu,\gamma_{\mathrm{mlp}})\frac{\sin(m\phi)}{\cos(m\phi)}, \tag{180}$$

and multiply by $R^{(1)}_{\mathrm{nk}}(\xi,\gamma_{\mathrm{nkp}})S_{\mathrm{nk}}(\nu,\gamma_{\mathrm{nkp}})\,{}^{\sin(n\phi)}_{\cos(n\phi)}\sqrt{(\xi^2-1)}\sqrt{(1-\nu^2)}(\xi^2-\nu^2)$ and integrate over the whole domain to find:

$$
\begin{aligned}
&A_{\mathrm{mlp}} = \\
&\frac{1}{N_{\mathrm{ml}}}\int_0^{2\pi}\int_{-1}^{1}\int_1^{\xi_0} p_0(\xi)q_0(\nu)s_0(\phi)R^{(1)}_{\mathrm{ml}}(\xi',\gamma_{\mathrm{mlp}})S_{\mathrm{ml}}(\nu',\gamma_{\mathrm{mlp}})\frac{\sin(m\phi')}{\cos(m\phi')} \\
&\times\sqrt{(\xi^2-1)}\sqrt{(1-\nu^2)}(\xi^2-\nu^2)\mathrm{d}\xi\mathrm{d}\nu\mathrm{d}\phi.
\end{aligned}
\tag{181}
$$

Our full solution is therefore given by:

$$
\begin{aligned}
&v(\xi,\nu,\phi,t) = \\
&\sum_{m=1}^{\infty}\sum_{l=m,m+1,}^{\infty}\sum_{p=1}^{\infty}\frac{1}{\pi N_{\mathrm{ml}}}\int_0^{2\pi}\int_{-1}^{1}\int_1^{\xi_0} p_0(\xi)q_0(\nu)s_0(\phi)R^{(1)}_{\mathrm{ml}}(\xi',\gamma_{\mathrm{mlp}}) \\
&\times R^{(1)}_{\mathrm{ml}}(\xi,\gamma_{\mathrm{mlp}})S_{\mathrm{ml}}(\nu,\gamma_{\mathrm{mlp}})S_{\mathrm{ml}}(\nu',\gamma_{\mathrm{mlp}})\frac{\sin(m\phi)\sin(m\phi')}{\cos(m\phi)\cos(m\phi')}\sqrt{(\xi^2-1)} \\
&\times\sqrt{(1-\nu^2)}(\xi^2-\nu^2)\mathrm{d}\xi\mathrm{d}\nu\mathrm{d}\phi\mathrm{e}^{-k^2D_{\mathrm{nuc}}t}+\sum_{l=0}^{\infty}\sum_{p=1}^{\infty}\frac{1}{2\pi N_{0l}}\int_0^{2\pi}\int_{-1}^{1}\int_1^{\xi_0} p_0(\xi) \\
&\times q_0(\nu)s_0(\phi)R^{(1)}_{0l}(\xi',\gamma_{0lp})R^{(1)}_{0l}(\xi,\gamma_{0lp})S_{0l}(\nu,\gamma_{0lp})S_{0l}(\nu',\gamma_{0lp})\sqrt{(\xi^2-1)} \\
&\times\sqrt{(1-\nu^2)}(\xi^2-\nu^2)\mathrm{d}\xi\mathrm{d}\nu\mathrm{d}\phi\mathrm{e}^{-k^2D_{\mathrm{nuc}}t},
\end{aligned}
\tag{182}
$$

This is in the form:

$$
\int_D v(\xi,\nu,\phi,0)G(\xi,\xi',\nu,\nu',\phi,\phi',t)\mathrm{d}\Omega,
\tag{183}
$$

with Green's function:

$$
\begin{aligned}
&G(\xi,\xi',\nu,\nu',\phi,\phi',t) = \sum_{m=1}^{\infty}\sum_{l=m,m+1,}^{\infty}\sum_{p=1}^{\infty}\frac{1}{\pi N_{\mathrm{ml}}}R^{(1)}_{\mathrm{ml}}(\xi',\gamma_{\mathrm{mlp}})R^{(1)}_{\mathrm{ml}}(\xi,\gamma_{\mathrm{mlp}}) \\
&\times S_{\mathrm{ml}}(\nu,\gamma_{\mathrm{mlp}})S_{\mathrm{ml}}(\nu',\gamma_{\mathrm{mlp}})\frac{\sin(m\phi)\sin(m\phi')}{\cos(m\phi)\cos(m\phi')}\mathrm{e}^{-k^2D_{\mathrm{nuc}}t} \\
&+\sum_{l=0}^{\infty}\sum_{p=1}^{\infty}\frac{1}{2\pi N_{0l}}R^{(1)}_{0l}(\xi',\gamma_{0lp})R^{(1)}_{0l}(\xi,\gamma_{0lp})S_{0l}(\nu,\gamma_{0lp})S_{0l}(\nu',\gamma_{0lp})\mathrm{e}^{-k^2D_{\mathrm{nuc}}t} \\
&+\frac{1}{V}.
\end{aligned}
\tag{184}
$$

4.2.2 *Derivation of the Green's function for a prolate spheroidal shell*

For the PNS in the spheroidal case, we consider the diffusion of calcium in a compartment contained within two confocal prolate spheroids, defined by:

$$\xi_0 \leq \xi \leq \xi_1, \qquad -1 \leq \nu \leq 1, \qquad 0 \leq \phi < 2\pi, \tag{185}$$

where ξ_0 defines the spheroidal surface of the nucleoplasm given in the previous section, and $\xi_1 = \frac{b_1}{c_1}$ defines the surface of the outer nuclear membrane. The governing PDE remains the same and hence so does the set of separated ODE's. Eq. 3. of 175 however, is now considered for the domain $\xi_0 \leq \xi \leq \xi_1$ and hence, as the domain does not include $\xi = 1$, our solution is now a linear combination of the radial wave functions of the first and second kind so that $B \neq 0$. In this case we also require our Neumann condition to hold on both radial boundaries:

$$p'(\xi)|_{\xi=\xi_0} = 0, \qquad p'(\xi)|_{\xi=\xi_1} = 0. \tag{186}$$

which can be written as the system:

$$\begin{bmatrix} R^{(1)}_{\mathrm{ml}}{}'(\xi_0,\gamma) & R^{(2)}_{\mathrm{ml}}{}'(\xi_0,\gamma) \\ R^{(1)}_{\mathrm{ml}}{}'(\xi_1,\gamma) & R^{(2)}_{\mathrm{ml}}{}'(\xi_1,\gamma) \end{bmatrix} \begin{bmatrix} 1 \\ B \end{bmatrix} = \begin{bmatrix} 0 \\ 0 \end{bmatrix}, \tag{187}$$

and hence we find our eigenvalue problem:

$$R^{(1)}_{\mathrm{ml}}{}'(\xi_0,\gamma_{\mathrm{mlp}})R^{(2)}_{\mathrm{ml}}{}'(\xi_1,\gamma_{\mathrm{mlp}}) - R^{(1)}_{\mathrm{ml}}{}'(\xi_1,\gamma_{\mathrm{mlp}})R^{(2)}_{\mathrm{ml}}{}'(\xi_0,\gamma_{\mathrm{mlp}}) = 0, \tag{188}$$

to be solved numerically for γ_{mlp}; the p^{th} zero for the m^{th} order, l^{th} degree solution.

From this condition we can write:

$$R^{(1)}_{\mathrm{ml}}{}'(\xi_0,\gamma_{\mathrm{mlp}}) - \frac{R^{(1)}_{\mathrm{ml}}{}'(\xi_1,\gamma_{\mathrm{mlp}})}{R^{(2)}_{\mathrm{ml}}{}'(\xi_1,\gamma_{\mathrm{mlp}})} R^{(2)}_{\mathrm{ml}}{}'(\xi_0,\gamma_{\mathrm{mlp}}) = 0, \tag{189}$$

and therefore, when compared to Eq. 187, we find our coefficient:

$$B = -\frac{R^{(1)}_{\mathrm{ml}}{}'(\xi_1,\gamma_{\mathrm{mlp}})}{R^{(2)}_{\mathrm{ml}}{}'(\xi_1,\gamma_{\mathrm{mlp}})}. \tag{190}$$

We write our solution to the radial equation as:

$$Z_{\mathrm{ml}}(\xi,\gamma_{\mathrm{mlp}}) = R^{(1)}_{\mathrm{ml}}(\xi,\gamma_{\mathrm{mlp}}) + BR^{(2)}_{\mathrm{ml}}(\xi,\gamma_{\mathrm{mlp}}), \tag{191}$$

and therefore recombine our solutions to find:

$$v(\xi,\nu,\phi,t) = A_{\mathrm{mlp}} Z_{\mathrm{ml}}(\xi,\gamma_{\mathrm{mlp}}) S_{\mathrm{ml}}(\nu,\gamma_{\mathrm{mlp}}) \frac{\sin(m\phi)}{\cos(m\phi)} \mathrm{e}^{-k^2 D_{\mathrm{nuc}} t}, \tag{192}$$

and again find our coefficient A_{mlp} by taking our initial condition:

$$v(\xi,\nu,\phi,0) = p_0(\xi) q_0(\nu) s_0(\phi) = A_{\mathrm{mlp}} Z_{\mathrm{ml}}(\xi,\gamma_{\mathrm{mlp}}) S_{\mathrm{ml}}(\nu,\gamma_{\mathrm{mlp}}) \frac{\sin(m\phi)}{\cos(m\phi)}, \tag{193}$$

and multiplying by $Z_{\mathrm{nk}}(\xi,\gamma_{\mathrm{nkp}}) S_{\mathrm{nk}}(\nu,\gamma_{\mathrm{nkp}}) \frac{\sin(n\phi)}{\cos(n\phi)} \sqrt{(\xi^2-1)}\sqrt{(1-\nu^2)}(\xi^2-\nu^2)$ and integrating over the new domain to find:

$$\begin{aligned} &A_{\mathrm{mlp}} = \\ &\frac{1}{N_{\mathrm{ml}}} \int_0^{2\pi} \int_{-1}^{1} \int_{\xi_0}^{\xi_1} p_0(\xi) q_0(\nu) s_0(\phi) Z_{\mathrm{ml}}(\xi',\gamma_{\mathrm{mlp}}) S_{\mathrm{ml}}(\nu',\gamma_{\mathrm{mlp}}) \frac{\sin(m\phi')}{\cos(m\phi')} \\ &\times \sqrt{(\xi^2-1)}\sqrt{(1-\nu^2)}(\xi^2-\nu^2)\mathrm{d}\xi\mathrm{d}\nu\mathrm{d}\phi. \end{aligned} \tag{194}$$

Our full solution is therefore given by:

$$\begin{aligned} &v(\xi,\nu,\phi,t) = \\ &\sum_{m=1}^{\infty} \sum_{l=m,m+1,}^{\infty} \sum_{p=1}^{\infty} \frac{1}{\pi N_{\mathrm{ml}}} \int_0^{2\pi} \int_{-1}^{1} \int_{\xi_0}^{\xi_1} p_0(\xi) q_0(\nu) s_0(\phi) Z_{\mathrm{ml}}(\xi',\gamma_{\mathrm{mlp}}) \\ &\times Z_{\mathrm{ml}}(\xi,\gamma_{\mathrm{mlp}}) S_{\mathrm{ml}}(\nu,\gamma_{\mathrm{mlp}}) S_{\mathrm{ml}}(\nu',\gamma_{\mathrm{mlp}}) \frac{\sin(m\phi)\sin(m\phi')}{\cos(m\phi)\cos(m\phi')} \sqrt{(\xi^2-1)} \\ &\times \sqrt{(1-\nu^2)}(\xi^2-\nu^2)\mathrm{d}\xi\mathrm{d}\nu\mathrm{d}\phi \mathrm{e}^{-k^2 D_{\mathrm{nuc}} t} \\ &+ \sum_{l=0}^{\infty} \sum_{p=1}^{\infty} \frac{1}{2\pi N_{0l}} \int_0^{2\pi} \int_{-1}^{1} \int_{\xi_0}^{\xi_1} p_0(\xi) q_0(\nu) s_0(\phi) Z_{0l}(\xi',\gamma_{0lp}) Z_{0l}(\xi,\gamma_{0lp}) \\ &\times S_{0l}(\nu,\gamma_{0lp}) S_{0l}(\nu',\gamma_{0lp}) \sqrt{(\xi^2-1)}\sqrt{(1-\nu^2)}(\xi^2-\nu^2)\mathrm{d}\xi\mathrm{d}\nu\mathrm{d}\phi \mathrm{e}^{-k^2 D_{\mathrm{nuc}} t}, \end{aligned} \tag{195}$$

which is in the form:

$$\int_D v(\xi,\nu,\phi,0) G(\xi,\xi',\nu,\nu',\phi,\phi',t)\mathrm{d}\Omega, \tag{196}$$

with Green's function:

$$
\begin{aligned}
&G(\xi,\xi',\nu,\nu',\phi,\phi',t) = \\
&\sum_{m=1}^{\infty}\sum_{l=m,m+1,}^{\infty}\sum_{p=1}^{\infty}\frac{1}{\pi N_{\mathrm{ml}}}Z_{\mathrm{ml}}(\xi',\gamma_{\mathrm{mlp}})Z_{\mathrm{ml}}(\xi,\gamma_{\mathrm{mlp}})S_{\mathrm{ml}}(\nu,\gamma_{\mathrm{mlp}})S_{\mathrm{ml}}(\nu',\gamma_{\mathrm{mlp}}) \\
&.\times\begin{matrix}\sin(m\phi)\sin(m\phi') \\ \cos(m\phi)\cos(m\phi')\end{matrix}\mathrm{e}^{-k^2D_{\mathrm{nuc}}t} \\
&+\sum_{l=0}^{\infty}\sum_{p=1}^{\infty}\frac{1}{2\pi N_{0l}}Z_{0l}(\xi',\gamma_{0lp})Z_{0l}(\xi,\gamma_{0lp})S_{0l}(\nu,\gamma_{0lp})S_{0l}(\nu',\gamma_{0lp})\mathrm{e}^{-k^2D_{\mathrm{nuc}}t} \\
&+\frac{1}{V}.
\end{aligned}
\tag{197}
$$

Full details of spheroidal calculations can be found in Appendix. B.

4.3 PUMP AND CHANNEL DYNAMICS

4.3.1 *Deriving the pump and channel equations*

Introducing pumps and channels into our equations involves creating sites at which there may be a flux, J, across the inner nuclear membrane. Taking the spherical geometry, these fluxes are written as the derivative of the concentration normal to the membrane at $r = a$. This is split into flux out of the PNS:

$$J_{\mathrm{pns}}(\theta_{\mathrm{c}},\phi_{\mathrm{c}},\tau) = D_{\mathrm{pns}}\left.\frac{\partial C_{\mathrm{pns}}(r,\theta_{\mathrm{c}},\phi_{\mathrm{c}},\tau)}{\partial r}\right|_{a^+}, \tag{198}$$

through a channel, c, on the luminal side of the membrane, $r = a^+$, where the calcium concentration is measured in the PNS as C_{pns} and flux out of the nucleolus:

$$J_{\mathrm{nuc}}(\theta_{\mathrm{p}},\phi_{\mathrm{p}},\tau) = D_{\mathrm{nuc}}\left.\frac{\partial C_{\mathrm{nuc}}(r,\theta_{\mathrm{p}},\phi_{\mathrm{p}},\tau)}{\partial r}\right|_{a^-}, \tag{199}$$

for pump, p, on the cytosolic side of the membrane, $r = a^-$, where the calcium concentration is measured in the nucleolus as C_{nuc}. Each of these requires an equal and opposite flux from the corresponding compartment due to continuity. That is, for the channel, an equal and opposite flux to that leaving the PNS must enter the cytosol:

$$J_{\mathrm{nuc}}(\theta_{\mathrm{c}}, \phi_{\mathrm{c}}, \tau) = -J_{\mathrm{pns}}(\theta_{\mathrm{c}}, \phi_{\mathrm{c}}, \tau), \tag{200}$$

and for the pumps the outward normal concentration from the cytosol must be balanced with an inward flux into the PNS:

$$J_{\mathrm{pns}}(\theta_{\mathrm{p}}, \phi_{\mathrm{p}}, \tau) = -J_{\mathrm{nuc}}(\theta_{\mathrm{p}}, \phi_{\mathrm{p}}, \tau). \tag{201}$$

For the calcium channels we assume that opening is achieved through calcium-induced calcium release (CICR), that is, channel firing is triggered depending upon the calcium concentration profile immediately adjacent to the channel. This dependence can be represented in the form of a Hill function:

$$\alpha(C) = \frac{C^{\mathrm{n}}}{(KA)^{\mathrm{n}} + C^{\mathrm{n}}}, \tag{202}$$

where the fraction of channel conductance, $\alpha(C) \in [0, 1]$, is determined by the concentration of calcium immediately adjacent to the channel and over a small concentration window, centred around the half maximal effective concentration, KA, the channel can allow partial conduction. KA is dependent upon the equilibrium constant for calcium binding to the channel, Kd, such that:

$$(KA)^{\mathrm{n}} = Kd = \frac{k_{\mathrm{d}}}{k_{\mathrm{a}}}, \tag{203}$$

where k_{d} and k_{a} are the dissociation and association constants for the chemical binding of Ca^{2+} to the channel. The steepness of the curve, and hence the range of concentration values at which partial opening is possible, depends upon the Hill coefficient, $n \in \mathbb{N}$, representing the number of cooperative Ca^{2+} binding sites on the channel. Alternatively a step-function can be used to determine $\alpha(C)$, in which case the channel is exclusively 'off' or 'on' depending on the surpassing of a set threshold concentration C_{th}. The step

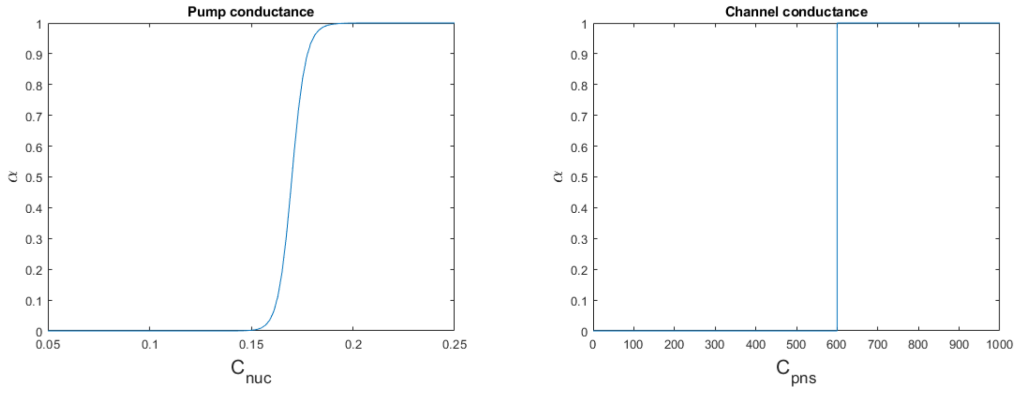

(a) (b)

Figure 25.: (a) Pump Hill-function and (b) channel step-function dynamics. (a) An KA of 0.17 μM results in the pump operating when the concentration in nucleoplasm exceeds its resting level of 0.15 μM. (b) A threshold, c_{th}, of 600 μM results in maximal channel firing when calcium concentration in the PNS is at or exceeds this value.

function is the limiting form of the Hill function for $n \to \infty$ and is written as:

$$\alpha(C) = \begin{cases} 0, & C < C_{\text{th}}, \\ 1, & C \geq C_{\text{th}}. \end{cases} \tag{204}$$

Plots of a Hill function for pump conductance and a step function for channel conductance are shown in Figures. 25 a) and b) respectively.

We model our channels to allow Fickian diffusion across the membrane, which utilises the large concentration difference between the PNS and the nucleoplasm. The transport time taken for calcium to cross the membrane is represented by parameter "g". Using Eq. 202 or 204 for the fraction of channel conductance, $\alpha_c(C)$, the final equation to describe channel opening is given as the flux from the PNS store:

$$\begin{split} J_{\text{pns}}(a, \theta_c, \phi_c, \tau) = \\ -\alpha_c(C_{\text{pns}}(a^+, \theta_c, \phi_c, \tau))g(C_{\text{pns}}(a^+, \theta_c, \phi_c, \tau) - C_{\text{nuc}}(a^-, \theta_c, \phi_c, \tau)). \end{split} \tag{205}$$

for a channel at position (a, θ_c, ϕ_c), at time τ. In mammalian ER, the prevalent view is that channel gating is controlled by the Ca^{2+} concentration in the cytosol, however, luminal binding sites have been discovered [23]. Cytosolic gating would appear logical if the function of the channel was to refill a compartment when concentrations fell too low, for example due to buffering. In this case however, the upstream calcium signal is external and for this reason we have chosen to use the concentration on the luminal side of the INM as the determinant of channel opening. The concentration in the cytosol is still considered a factor however, with the difference between PNS and nucleoplasmic Ca^{2+} concentrations scaling the total flux into the nucleus. Satisfying conservation laws, the corresponding flux into the nucleus is given in Eq. 200, and, using Eq. 198, can also be written in terms of the concentration gradient:

$$\left.\frac{\partial C_{\mathrm{nuc}}(r,\theta_{\mathrm{c}},\phi_{\mathrm{c}},\tau)}{\partial r}\right|_{a^-} = -\frac{D_{\mathrm{pns}}}{D_{\mathrm{nuc}}}\left.\frac{\partial C_{\mathrm{pns}}(r,\theta_{\mathrm{c}},\phi_{\mathrm{c}},\tau)}{\partial r}\right|_{a^+}. \tag{206}$$

Unlike the channels, which work through standard Fickian diffusion, pumps require energy to transport the calcium ions against the concentration gradient. Flux through the pumps is therefore determined by pump currents, I, which are taken from experimental measurements given in the literature. They are converted to flux, using the formula:

$$J = IG, \tag{207}$$

with conversion factor:

$$G = \frac{1}{zFA}, \tag{208}$$

where z is the valency (always equal to 2 for calcium), F is the Faraday constant and A is the pump area. We write the flux out of the nuceloplasm as:

$$J_{\mathrm{nuc}}(\theta_{\mathrm{p}},\phi_{\mathrm{p}},\tau) = -\alpha_{\mathrm{p}}(C_{\mathrm{nuc}}(a^-,\theta_{\mathrm{p}},\phi_{\mathrm{p}},\tau))GI_{\mathrm{p}}^{\mathrm{max}}, \tag{209}$$

with a maximum pump conductance of $I_{\mathrm{p}}^{\mathrm{max}}$ and the fraction of pump conductance, $\alpha_{\mathrm{p}}(C)$, given by the Hill function in Eq. 202. In mammalian cells a SERCA pump is commonly represented by this expression using a Hill coefficient of 2. Again to satisfy continuity across the membrane we have the equal and opposite flux in the PNS given in Eq. 201, which can be written using Eq. 199, as:

$$\left.\frac{\partial C_{\mathrm{pns}}(r,\theta_{\mathrm{p}},\phi_{\mathrm{p}},\tau)}{\partial r}\right|_{a^{+}} = -\frac{D_{\mathrm{nuc}}}{D_{\mathrm{pns}}}\left.\frac{\partial C_{\mathrm{nuc}}(r,\theta_{\mathrm{p}},\phi_{\mathrm{p}},\tau)}{\partial r}\right|_{a^{-}}. \tag{210}$$

These equations are coupled with the semi-analytic solutions for the diffusion of calcium in each compartment, which are in the form given in Eq. 153. We initially set no flux conditions on the radial boundaries of both the nucleoplasm and PNS so that time- and location-dependent fluxes could be added later on. This is achieved by extending our solutions according to the 'magic rule' of Barton [11]:

$$\begin{aligned} C(\mathbf{x},t) = &\int_{\Omega} G(\mathbf{x},\mathbf{x}',t)C(\mathbf{x}',t)\mathrm{d}V' \\ +D &\int_{t}\int_{\omega} G(\mathbf{x},\mathbf{x}',t)\frac{\partial C(\mathbf{x}',t)}{\partial n}\mathrm{d}S'\mathrm{d}t. \end{aligned} \tag{211}$$

where $\mathbf{x} \in \Omega$ are our coordinates in the Volume, V, and ω denotes the domain of our surface, S. Therefore our entire system can be described by the following final set of equations:

$$\begin{aligned} &C_{\mathrm{nuc}}(r,\theta,\phi,t) = \\ &\int_{0}^{\mathrm{a}}\int_{0}^{\pi}\int_{0}^{2\pi} C_{\mathrm{nuc}}(r',\theta',\phi',0)G_{\mathrm{nuc}}(r,\theta,\phi,r',\theta',\phi',t)\mathrm{d}\phi'\sin\theta'\mathrm{d}\theta' r'^{2}\mathrm{d}r' \\ &+ D_{\mathrm{nuc}}\int_{0}^{\mathrm{t}}\int_{0}^{\pi}\int_{0}^{2\pi} \left.\frac{\partial C_{\mathrm{nuc}}(r',\theta',\phi',t)}{\partial r'}\right|_{r'=a} G_{\mathrm{nuc}}(r,\theta,\phi,r',\theta',\phi',t)\mathrm{d}\phi'\sin\theta'\mathrm{d}\theta'\mathrm{d}t', \end{aligned} \tag{212}$$

$$\begin{aligned} &C_{\mathrm{pns}}(r,\theta,\phi,t) = \\ &\int_{\mathrm{a}}^{\mathrm{b}}\int_{0}^{\pi}\int_{0}^{2\pi} C_{\mathrm{pns}}(r',\theta',\phi',0)G_{\mathrm{pns}}(r,\theta,\phi,r',\theta',\phi',t)\mathrm{d}\phi'\sin\theta'\mathrm{d}\theta' r'^{2}\mathrm{d}r' \\ &+ D_{\mathrm{pns}}\int_{0}^{\mathrm{t}}\int_{0}^{\pi}\int_{0}^{2\pi} \left.\frac{\partial C_{\mathrm{pns}}(r',\theta',\phi',t)}{\partial r'}\right|_{r'=a} G_{\mathrm{pns}}(r,\theta,\phi,r',\theta',\phi',t)\mathrm{d}\phi'\sin\theta'\mathrm{d}\theta'\mathrm{d}t', \end{aligned} \tag{213}$$

$$J_{\text{nuc}}(\theta',\phi',t) = \begin{cases} -\alpha_{\text{p}}(C_{\text{nuc}}(a^-,\theta',\phi',t))GI_{\text{p}}^{\max}, & \theta'=\theta_{\text{p}},\phi'=\phi_{\text{p}},t=\tau, \\ -J_{\text{pns}}(\theta',\phi',t), & \theta'=\theta_{\text{c}},\phi'=\phi_{\text{c}},t=\tau, \\ 0, & \text{otherwise}, \end{cases} \tag{214}$$

$$J_{\text{pns}}(\theta',\phi',t) = \begin{cases} -\alpha_{\text{c}}(C_{\text{pns}}(a^+,\theta',\phi',t))g & \\ \quad\times(C_{\text{pns}}(a^+,\theta',\phi',t)-C_{\text{nuc}}(a^-,\theta',\phi',t)), & \theta'=\theta_{\text{c}},\phi'=\phi_{\text{c}},t=\tau, \\ -J_{\text{nuc}}(\theta_{\text{p}},\phi_{\text{p}},\tau), & \theta'=\theta_{\text{p}},\phi'=\phi_{\text{p}},t=\tau, \\ 0, & \text{otherwise}, \end{cases} \tag{215}$$

where α_{p} and α_{c} denote the pump and channel conductance, and G_{nuc} and G_{pns} are as given in Eqs. 152 and 163 respectively.

In prolate spheroidal coordinates these equations become:

$$\begin{aligned} &C_{\text{nuc}}(\xi,\nu,\phi,t) = \\ &\int_1^{\xi_0}\int_{-1}^{1}\int_0^{2\pi} C_{\text{nuc}}(\xi',\nu',\phi',0)G_{\text{nuc}}(\xi,\nu,\phi,\xi',\nu',\phi',t)\mathrm{d}\phi'\sqrt{\xi^2-\nu^2}\mathrm{d}\nu'\mathrm{d}\xi' \\ &+D_{\text{nuc}}\int_0^{\text{t}}\int_{-1}^{1}\int_0^{2\pi}\frac{\partial C_{\text{nuc}}(\xi',\nu',\phi',t)}{\partial\xi'}|_{\xi'=\xi_0}G_{\text{nuc}}(\xi,\nu,\phi,\xi',\nu',\phi',t)\mathrm{d}\phi'\mathrm{d}\nu'\mathrm{d}t', \end{aligned} \tag{216}$$

$$\begin{aligned} &C_{\text{pns}}(\xi,\nu,\phi,t) = \\ &\int_{\xi_0}^{\xi_1}\int_{-1}^{1}\int_0^{2\pi} C_{\text{pns}}(\xi',\nu',\phi',0)G_{\text{pns}}(\xi,\nu,\phi,\xi',\nu',\phi',t)\mathrm{d}\phi'\sqrt{\xi^2-\nu^2}\mathrm{d}\nu'\mathrm{d}\xi' \\ &+D_{\text{pns}}\int_0^{\text{t}}\int_{-1}^{1}\int_0^{2\pi}\frac{\partial C_{\text{pns}}(\xi',\nu',\phi',t)}{\partial\xi'}|_{\xi'=\xi_0}G_{\text{pns}}(\xi,\nu,\phi,\xi',\nu',\phi',t)\mathrm{d}\phi'\mathrm{d}\nu'\mathrm{d}t', \end{aligned} \tag{217}$$

$$J_{\mathrm{nuc}}(\nu',\phi',t)=\begin{cases}-\alpha(C_{\mathrm{nuc}}(\xi_0^-,\nu',\phi',t))GI_{\mathrm{p}}^{\mathrm{max}}, & \nu'=\nu_{\mathrm{p}},\phi'=\phi_{\mathrm{p}},t=\tau,\\ -J_{\mathrm{pns}}(\nu',\phi',t), & \nu'=\nu_{\mathrm{c}},\phi'=\phi_{\mathrm{c}},t=\tau,\\ 0, & \text{otherwise,}\end{cases}\tag{218}$$

$$J_{\mathrm{pns}}(\nu',\phi',t)=$$
$$\begin{cases}-\alpha(C_{\mathrm{pns}}(\xi_0^+,\nu',\phi',t))g & \\ \qquad \mathrm{x}(C_{\mathrm{pns}}(\xi_0^+,\nu',\phi',t)-C_{\mathrm{nuc}}(\xi_0^-,\nu',\phi',t)), & \nu'=\nu_{\mathrm{c}},\phi'=\phi_{\mathrm{c}},t=\tau,\\ -J_{\mathrm{nuc}}(\nu_{\mathrm{p}},\phi_{\mathrm{p}},\tau), & \nu'=\nu_{\mathrm{p}},\phi'=\phi_{\mathrm{p}},t=\tau,\\ 0, & \text{otherwise,}\end{cases}\tag{219}$$

for the Green's functions, G_{nuc} and G_{pns}, given in Eqs. 360 and 376.

4.3.2 *Pumps and channels as a system of ODE's*

Here we look at the above flux equations in the absence of diffusion. In this case we consider simply the movement of calcium between the two compartments through pump and channel dynamics alone. We have no spatial component and hence remove the diffusion coefficients and formulate the above expressions for C_{nuc} and C_{pns} as ordinary differential equations as follows:

$$\frac{\mathrm{d}C_{\mathrm{nuc}}}{\mathrm{d}t}=-V_{\mathrm{R}}\alpha_{\mathrm{p}}GI_{\mathrm{p}}^{\mathrm{max}}+V_{\mathrm{R}}\alpha_{\mathrm{c}}g(C_{\mathrm{pns}}-C_{\mathrm{nuc}}),\tag{220}$$

$$\frac{\mathrm{d}C_{\mathrm{pns}}}{\mathrm{d}t}=-\alpha_{\mathrm{c}}g(C_{\mathrm{pns}}-C_{\mathrm{nuc}})+\alpha_{\mathrm{p}}GI_{\mathrm{p}}^{\mathrm{max}}\tag{221}$$

with,

$$\alpha_{\mathrm{c}}=\frac{C_{\mathrm{pns}}^{\mathrm{nc}}}{C_{\mathrm{pns}}^{\mathrm{nc}}+KA_{\mathrm{c}}^{\mathrm{nc}}},\tag{222}$$

$$\alpha_{\mathrm{p}} = \frac{C_{\mathrm{nuc}}^{\mathrm{np}}}{C_{\mathrm{nuc}}^{\mathrm{np}} + KA_{\mathrm{p}}^{\mathrm{np}}}, \tag{223}$$

and

$$G = \frac{1}{zF}, \tag{224}$$

where we now have no dependence on area. This is accounted for in the additional term:

$$V_{\mathrm{R}} = \frac{V_{\mathrm{pns}}}{V_{\mathrm{nuc}}}, \tag{225}$$

which is the volume ratio between the two compartments, and necessarily appears when reducing our system from three to one dimension in space.

Steady states

Setting

$$\frac{\mathrm{d}C_{\mathrm{nuc}}}{\mathrm{d}t} = 0, \tag{226}$$

and, due to the coupling of compartments,

$$\frac{\mathrm{d}C_{\mathrm{pns}}}{\mathrm{d}t} = 0 \tag{227}$$

also. We let

$$\frac{\alpha_{\mathrm{p}}}{\alpha_{\mathrm{c}}} = \alpha_{\mathrm{R}}, \tag{228}$$

and find:

$$C_{\mathrm{pns}} = C_{\mathrm{nuc}} + G_{\mathrm{R}}\alpha_{\mathrm{R}}. \tag{229}$$

where we have set $G_{\mathrm{R}} = \frac{GI_{\mathrm{p}}^{\mathrm{max}}}{g}$. For α_{p}, α_{c} constant this gives us a straightforward relationship between the concentrations in the two compartments, however as α_{p} and α_{c} depend upon C_{nuc} and C_{pns} respectively furthur analysis is required. Substituting in Eqs. 222 and 223 into Eq. 229 we find:

$$\begin{aligned} C_{\mathrm{nuc}}^{\mathrm{np}+1}C_{\mathrm{pns}}^{\mathrm{nc}} + KA_{\mathrm{c}}^{\mathrm{nc}}C_{\mathrm{nuc}}^{\mathrm{np}}G_{\mathrm{R}} + KA_{\mathrm{p}}^{\mathrm{np}}C_{\mathrm{nuc}}C_{\mathrm{pns}}^{\mathrm{nc}} + G_{\mathrm{R}}C_{\mathrm{pns}}^{\mathrm{nc}}C_{\mathrm{nuc}}^{\mathrm{np}} - C_{\mathrm{pns}}^{\mathrm{nc}+1}C_{\mathrm{nuc}}^{\mathrm{np}} \\ -KA_{\mathrm{p}}^{\mathrm{np}}C_{\mathrm{pns}}^{\mathrm{nc}+1} = 0. \end{aligned} \tag{230}$$

This equation can be solved numerically, with the number of solutions dependent upon the values of np and nc. The system will therefore approach one of these solutions in accordance with the initial conditions.

Numerical evaluation

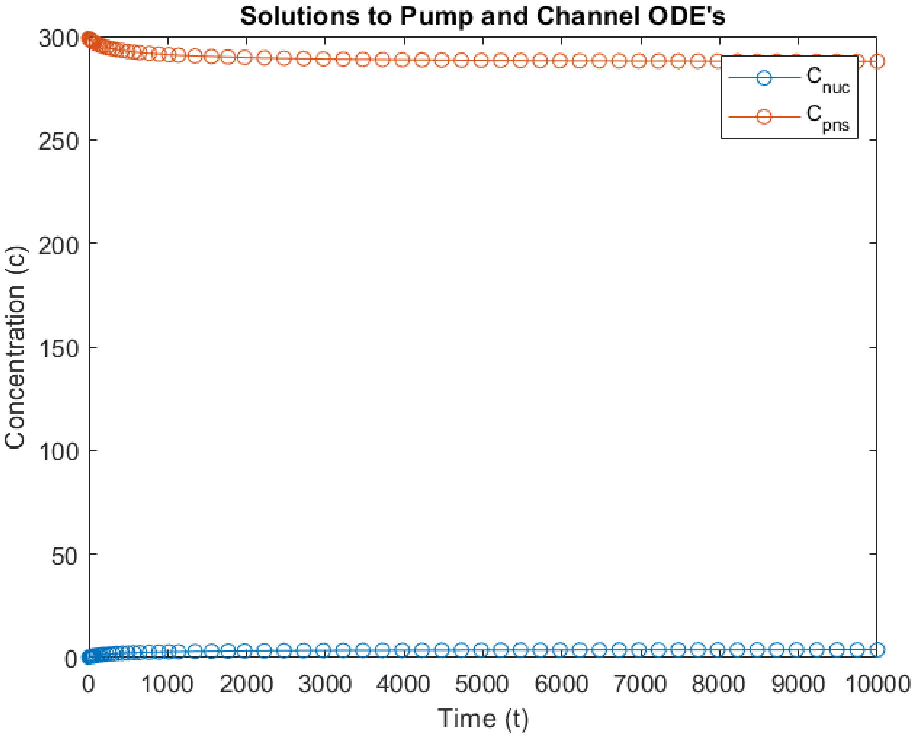

Figure 26.: Numerical solution of the pump and channel ODE's showing a constant concentration is reached in both compartments. Parameter values used are: KA_c = 299.0, I_c^{max} = 4900e-11, nc = 120, np = 20, KA_p = 0.15, I_p^{max} = 1400e-10, $\hat{a}$ = 4.5 and h = 0.45, with initial concentrations $C0_{nuc}$ = 0.15, $C0_{pns}$ =299.

Our pump and channel system of equations was integrated using Matlab's ode45. For the equivalent system without a spatial component we see in Figure. 26 that the system reaches a steady state. The lack of a periodic orbit is confirmed through the use of bifurcation software XPP. Figure. 27 shows the nullcline and phase-space for our system, and we see that the concentration in each compartment will tend towards one of the infinite stable steady state's dependent upon the initial conditions.

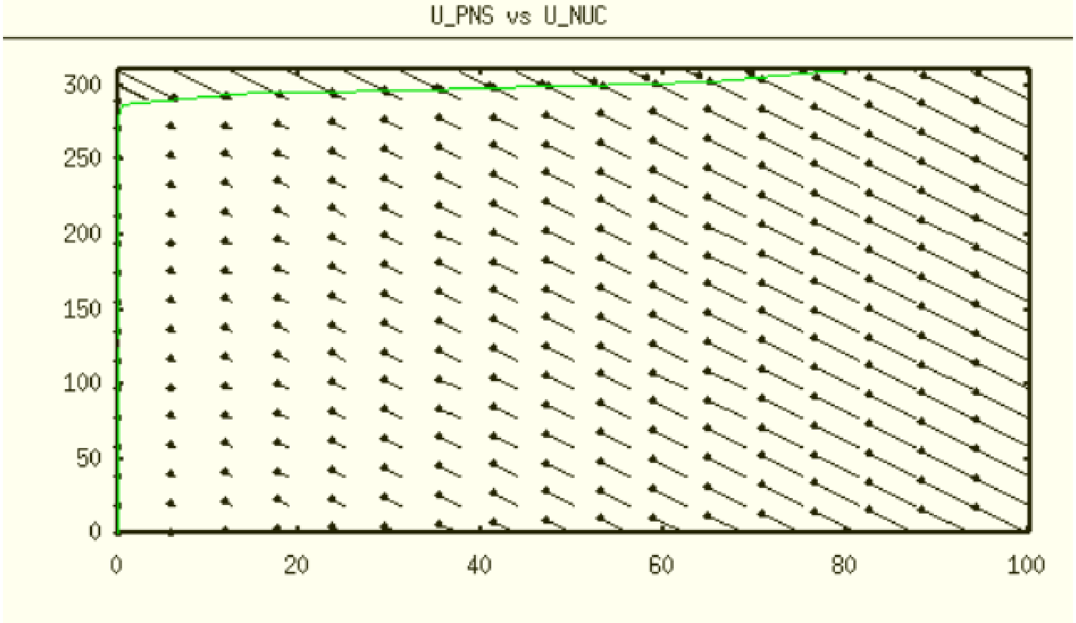

Figure 27.: A phase space diagram for the pump/channel ODE system with the nullcline in green and the bold black line representing the evolution of the system from an initial condition of [300,0.15] μM.

Finally, a parameter space analysis was performed for the channel release rate, g, the number of pumps, N_p, and the half maximal effective concentration of the channels, KA_c, with results given in Figure. 28. We see that for a constant KA_c, the channel release rate has very little effect on the steady state concentrations reached, which are effected predominantly by the number of pumps. As the number of pumps increases from 4 to 26 we see that the steady state concentration in the nucleoplasm increases from approximately 0.5 μM to 3.5 μM whilst the concentration in the PNS decreases from approximately 298 μM to 289 μM.

When the number of pumps is constant however we see that the increasing of both g and KA_c has the effect of increasing nucleoplasmic concentrations and hence decreasing those in the PNS. An interesting artefact is that increasing g has a much greater influence on the steady states below 200 $s^{-1}\mu m^3$, after which furthur increases lead to a diminished return. Increasing g also has a greater effect when the KA_c is larger, demonstrated in the figure by the larger gradient of the contours for a higher KA_c.

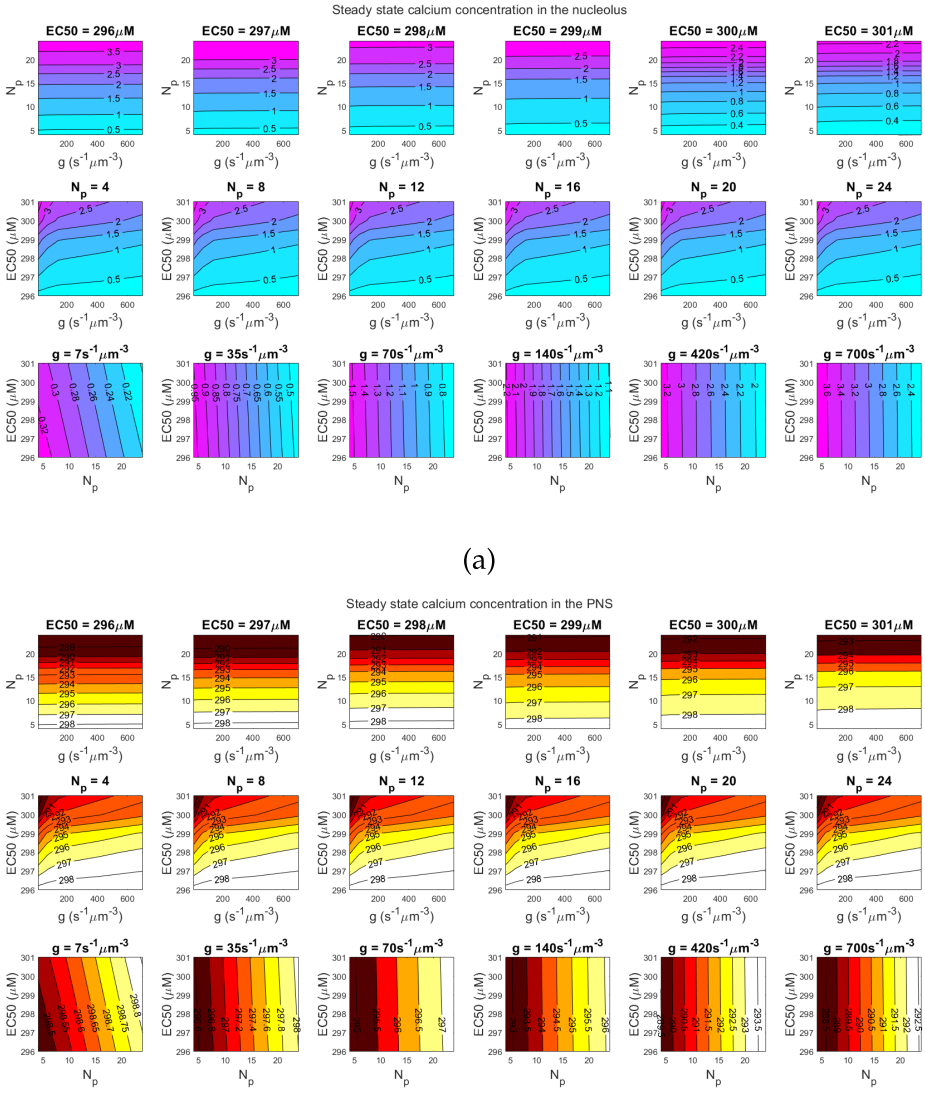

(a)

(b)

Figure 28.: A parameter space evaluation showing the effect of g, N_p, and KA_c on the resultant steady state concentration in a) the nucleoplasm and b) the PNS.

It is also interesting to note how all three parameters interact, as the final row of our figures shows that the value of g determines the proportion of effect that the KA_c will have on steady state concentrations in comparison to N_p. At low channel release rates, an increase in KA_c results in a decrease/increase in the nucleoplasmic/PNS concentrations, whereas as g

increases the KA_c appears to have little to no effect. This is likely due to the coincident effect of increasing the number of pumps when increasing channel release rate, due to the higher requirement for these pumps to balance out the larger influxes through the channels. This is evidenced by the fact that increasing channel release rates from 7 $s^{-1}\mu\text{m}^{-3}$ to 700 $s^{-1}\mu\text{m}^{-3}$ increases the range of concentrations modulated by the pumps from approximately 0.1 μM to 1.2 μM in the nucleoplasm and from 0.3 μM to 4 μM in the PNS.

The lack of calcium oscillations in this system, compared to what we will see in the 3D system in Section. 7, shows that the spatial contribution is critical to patterning and hence emphasises the importance of modelling our domain in full.

4.4 MODEL SUMMARY

- A 3D model was derived for the diffusion of calcium in the nucleoplasm and the PNS for spherical coordinates, using the spherical Bessel functions and Legendre functions.
- A second 3D model was derived for the diffusion of calcium in the nucleoplasm and the PNS for prolate spheroidal coordinates, using the radial and angular prolate spheroidal wave-functions.
- The pump and channel dynamics were formulated as flux equations, written as the normal derivative of the concentration at the membrane, whilst ensuring conservation of concentration.
- The differences between the pumps and channels in terms of their purpose and functionality were considered in order to model their mechanisms as accurately as possible.

- CICR by the channels is modelled by the product of a threshold component for channel opening and Fickian diffusion which utilises the concentration difference across the membrane.
- The pumps are modelled using the fraction of conductance and maximum flux which is converted from values for the cross-membrane current.
- Pump and channel equations are coupled to the diffusion equations through the 'magic rule' of Barton (2005) [11].
- It is shown that, in the absence of diffusion, the system of pumps and channels alone is unable to create oscillatory calcium dynamics, highlighting the importance of a spatio-temporal model.
- A parameter space analysis of the ODE system showed that the number of pumps is a dominating factor in modulating the steady state concentration in each compartment.

5

NUMERICS

The Green's functions calculated in Sections 3 and 4 are increasingly difficult to compute numerically, due to the increase in complexity of the special functions used in higher dimensions. In addition, as our Green's functions are infinite sums, we must computationally approximate our Green's functions by choosing a truncation which allows for the properties of the Green's function to remain satisfied. In this section we will discuss these properties and provide the results of our numerical checks to demonstrate that the Green's functions have been computed correctly. Some test simulation results for the flux and diffusion of calcium will also be given in one- and two-dimensions in order to check the method of simulation. Finally, the limitations of the method will be discussed, in particular the challenges experienced in coding the Green's function in prolate spheroidal coordinates.

5.1 NUMERICAL CHECKS

5.1.1 *Checks for 1D*

For a differential equation of the form:

$$\mathcal{L}c(x) = f(x), \tag{231}$$

where $\mathcal{L}$ is the differential operator $D\nabla^2$, the corresponding Green's function, $G(x, x')$ satisfies:

$$\mathcal{L}G(x, x') = \delta(x - x'), \tag{232}$$

where $\delta(x)$ is the Dirac delta distribution which can be defined, for any well behaved function $f(x)$, such that:

$$\int_{x_1}^{x_2} f(x)\delta(x - x')\mathrm{d}x = \begin{cases} f(x'), & x_1 < x' < x_2 \\ 0, & x' \notin (x_1, x_2). \end{cases} \tag{233}$$

Using this property of the delta function we multiply Equation. (232) by $f(x')$ and integrate over our domain to find:

$$\int_{\Omega} \mathcal{L}G(x, x')f(x')\mathrm{d}x' = \int_{\Omega} \delta(x - x')f(x')\mathrm{d}x', \tag{234}$$

where from Eq. (233) it is clear that the right hand side is equal to $f(x)$, and moving $\mathcal{L}$ outside the integral (as it only operates on x), we find the left hand side equals $\mathcal{L}c(x)$. Therefore we see that this returns the problem in Eq. (231) and that $c(x)$ has the integral form:

$$c(x, x') = \int_{\Omega} G(x, x')f(x')\mathrm{d}x' \tag{235}$$

We use the above to check the numerical computation of our Green's function. Firstly we set $t = 0$ to find the time-independent kernel $G(x, x', 0) = K(x, x')$ where $K(x, x') = \delta(x - x')$. We then choose an appropriate function $f(x')$ and integrate over our spatial domain to find:

$$\int_{\Omega} G(x, x', 0)f(x')\mathrm{d}x' = \int_{\Omega} \delta(x - x')f(x')\mathrm{d}x' = f(x). \tag{236}$$

In the following numerical checks we have chosen a Gaussian distribution with a mean μ and standard deviation σ, such that:

$$f(x') = \mathrm{e}^{\frac{-(x'-\mu)^2}{2\sigma^2}}. \tag{237}$$

This convolution will return the Gaussian if the computed Green's function is indeed a delta function in x at $t = 0$. We are also required to truncate

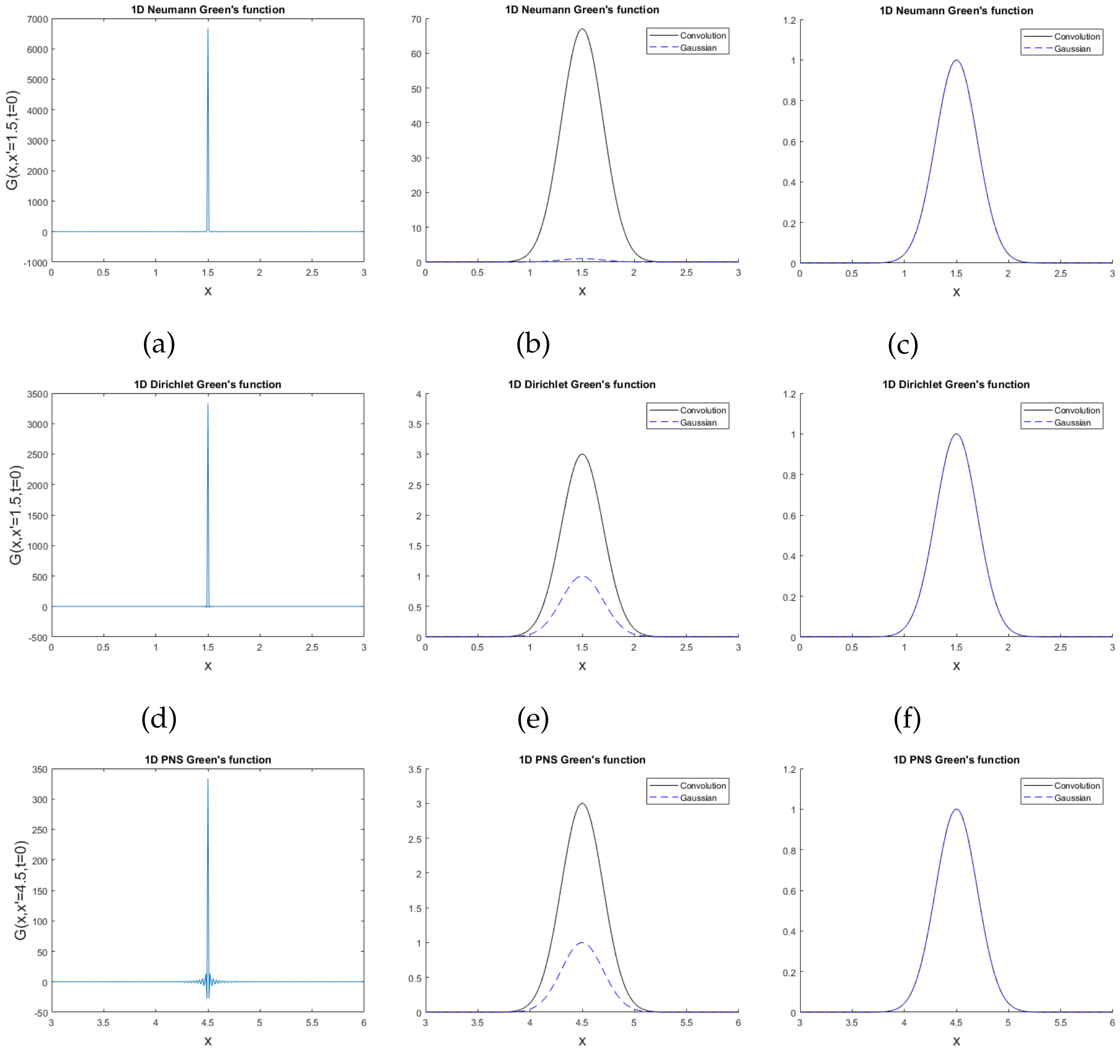

(a) (b) (c)

(d) (e) (f)

(g) (h) (i)

Figure 29.: Checks for the validity of the computed Green's function show that at each point $x_i \in x'$ for $i = 1...N$, where N is the numerical mesh size, we have a delta function at $t = 0$. Here for illustrations sake we show this at the central mesh point for a) the Neumann, d) the Dirichlet and g) the nonzero domain problem. Truncation of the infinite sum at too high a number of eigenvalues will result in incorrect convolution as seen for b) the Neumann, e) Dirichlet and h) nonzero case where the original Gaussian (blue dotted line) and the test function (black solid line) do not coincide. Optimal truncation for the given mesh size results in the return of the Gaussian function $f(x')$, as illustrated by the perfect overlap of the blue dotted and black solid lines, when convolved with the c) Neumann, f) Dirichlet or i) nonzero domain Green's function.

the infinite sum in order to compute our solution. These checks also allow for the calibration of the mesh size aligning with the specific truncation by ensuring the numerical approximation of the solution returns the correct Gaussian function after convolution. If the number of eigenvalues used is too high then the resulting Gaussian will have the correct shape but will be stretched in the y direction. For the final model using the finest possible mesh for our computational capacity, the number of eigenvalues was varied in order to determine the optimal combination. When a correct number of eigenvalues is used, the input and output functions will overlap and the returned Gaussian will have a maximum of 1.0 at $x = \mu$. The results of these checks for the Neumann, Dirichlet and nonzero domain Green's functions, given in Eq. (20), Eq. (27) and Eq. (36) respectively, can be seen in Figure. 29. For a lower number of eigenvalues there are more 'wiggles' around the point source, as demonstrated in Figure. 29 (g), where we have N = 1000 mesh points, however these are small compared to the magnitude of the peak, and will dampen even further with the inclusion of the exponentially decaying time component.

A further general property of the δ-function is:

$$\int_{-\infty}^{\infty} \delta(x)dx = 1, \tag{238}$$

and hence further checks can be performed by integrating our Green's function at $t = 0$ over the entire domain, to obtain a value of 1 at each point $\in x$.

5.1.2 *Checks for 2D polar coordinates*

We extend the theory of section 5.1.1, to two dimensions to perform checks on the numerical accuracy of our Green's functions in 2D. For a differential equation of the form:

$$\mathcal{L}c(\mathbf{x}) = F(\mathbf{x}), \tag{239}$$

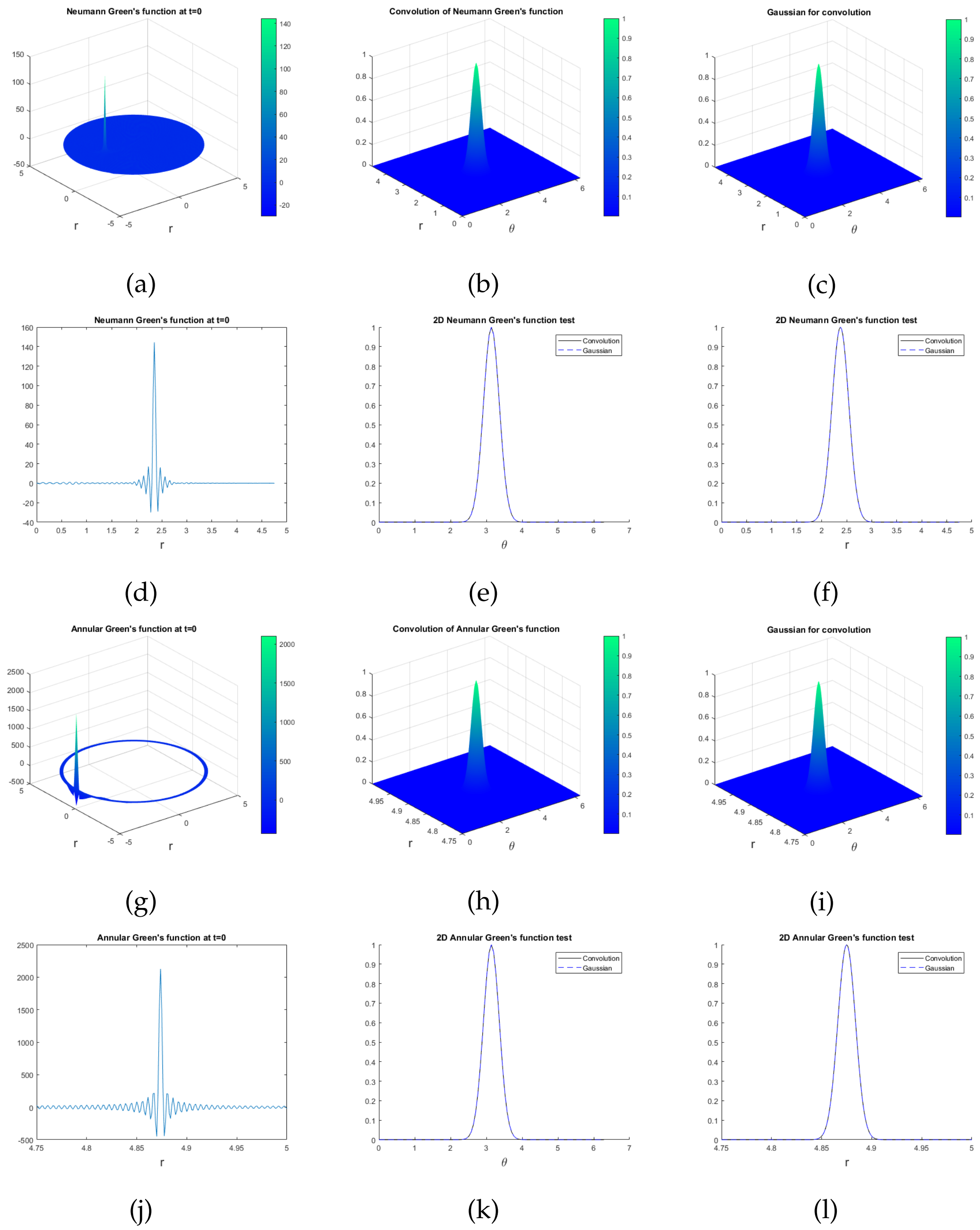

(a) (b) (c)

(d) (e) (f)

(g) (h) (i)

(j) (k) (l)

Figure 30.: Checks for the validity of the computed Green's function in two dimensions. At each point $(r_i, \theta_j) \in \Sigma$ for $i = 1...N$, $j = 1...M$, we expect a delta function at $t = 0$. This is seen in a) for the disc and d) in one dimension for the point $(\frac{a}{2}, \pi)$. This accuracy of the point of truncation is demonstrated in b) and compared to the original Gaussian given in c). By inspection these look identical however we use one dimensional cuts through both Gaussian's so we can check the overlap at different points in 1D, which is shown at a central point for r and θ in e) and f) respectively. Corresponding figures for the annulus are seen in g-l.

where $\mathcal{L}$ is the differential operator $D\nabla^2$ and $\mathbf{x}$ is now the two dimensional space (r, θ), the corresponding Green's function, $G(\mathbf{x}, \mathbf{x}')$ satisfies:

$$\mathcal{L}G(\mathbf{x}, \mathbf{x}') = \delta(\mathbf{x} - \mathbf{x}'). \tag{240}$$

We multiply Equation. (240) by $F(\mathbf{x}')$ and integrate over our domain, Σ, to find:

$$\int_\Sigma \mathcal{L}G(\mathbf{x}, \mathbf{x}')F(\mathbf{x}')\mathrm{d}\mathrm{x}' = \int_\Sigma \delta(\mathbf{x} - \mathbf{x}')F(\mathbf{x}')\mathrm{d}\mathrm{x}', \tag{241}$$

where from the properties of the delta function, given previously in Equation. (233), it is clear that the right hand side is equal to $F(\mathbf{x})$. Moving $\mathcal{L}$ outside the integral (as it only operates on $\mathbf{x}$), we find that this returns the problem in Equation. (239) and the left hand side must equal $\mathcal{L}c(\mathbf{x})$. Therefore we see that $c(\mathbf{x})$ has the integral form:

$$c(\mathbf{x}, \mathbf{x}') = \int_\Sigma G(\mathbf{x}, \mathbf{x}')F(\mathbf{x}')\mathrm{d}\mathbf{x}'. \tag{242}$$

In this case at $t = 0$ we have the time-independent kernel $G(r, r', \theta, \theta', 0) = K(r, r', \theta, \theta')$ where $K(r, r', \theta, \theta') = \delta(r - r')\delta(\theta - \theta')$. We then choose an appropriate function $F(r', \theta')$ and integrate to find:

$$\begin{aligned}\int_\Sigma G(r, r', \theta, \theta', 0)F(r', \theta')r'\mathrm{d}r'\mathrm{d}\theta' &= \int_\Sigma \delta(r - r')\delta(\theta - \theta')F(r', \theta')r'\mathrm{d}r'\mathrm{d}\theta' \\ &= F(r, \theta).\end{aligned} \tag{243}$$

In the following numerical checks we have chosen a Gaussian distribution with a mean $(\mu_\mathrm{r}, \mu_\theta)$ and standard deviation $(\sigma_\mathrm{r}, \sigma_\theta)$, such that:

$$F(r', \theta') = \mathrm{e}^{-\left(\frac{(r'-\mu_\mathrm{r})^2}{2\sigma_\mathrm{r}^2} + \frac{(\theta'-\mu_\theta)^2}{2\sigma_\theta^2}\right)}. \tag{244}$$

This convolution will return the Gaussian if the computed Green's function is indeed a delta function at $t = 0$. The calibration of the mesh size with the truncation of the infinite sum is slightly more difficult in this case as it must be balanced with the number of mesh points in both the radial (N) and angular directions (M). The results of these checks for the Neumann Green's function's functions in both a disc (Eq. (54)) and an annulus (Eq. (70)) can be seen in Figure. 30. Here we show that the convolution and the Gaussian closely coincide, providing evidence that $K(\xi,\xi',\nu,\nu')$ is indeed a delta function in both cases.

5.1.3 *Checks for 2D spheroidal coordinates*

Continuing from, Eq. 242, we take the Green's function in the ellipse from Eq. 113 at $t = 0$ to be $K(\xi,\xi',\nu,\nu') = \delta(\xi-\xi')\delta(\nu-\nu')$. Choosing the Gaussian function:

$$F(\xi',\nu') = \mathrm{e}^{-\left(\frac{(\xi'-\mu_\xi)^2}{2\sigma_\xi^2}+\frac{(\nu'-\mu_\nu)^2}{2\sigma_\nu^2}\right)}, \tag{245}$$

with a mean (μ_ξ,μ_ν) and standard deviation (σ_ξ,σ_ν), we perform the test:

$$\int_\Sigma K(\xi,\xi',\nu,\nu')F(\xi',\nu')(\xi'^2-\nu'^2)\mathrm{d}\xi'\mathrm{d}\nu' = F(\xi,\nu), \tag{246}$$

where we expect the convolution to return the original Gaussian $F(\xi,\nu)$ if the Green's function has been computed correctly. As before the truncation of our sums in Eq. 242 at $m = m_{\max}$ and $p = p_{\max}$ must be correctly balanced with our discrete values of $\mathrm{d}\Sigma$ used for the numerical evaluation of the system. Checks for the Green's functions on the ellipse and elliptic annulus can be seen in Figure. 31. The overlap of the two functions shows a good level of accuracy in our calculations. The apparent instabilities in the radial part of Figure. 31 (c) are due to the limited number of eigenvalues available for calculation and will be discussed later in this section.

5.1.4 *Checks for 3D spherical coordinates*

Extending our checks now to 3-dimensions, we take the Green's function for heat distribution in spherical coordinates, from Eq. 152, at $t = 0$ to be $K(r,r',\theta,\theta',\phi,\phi') = \delta(r-r')\delta(\theta-\theta')\delta(\phi-\phi')$. Choosing the Gaussian function:

$$F(r',\theta',\phi') = \mathrm{e}^{-\left(\frac{(r'-\mu_\mathrm{r})^2}{2\sigma_\mathrm{r}^2}+\frac{(\theta'-\mu_\theta)^2}{2\sigma_\theta^2}+\frac{(\phi'-\mu_\phi)^2}{2\sigma_\phi^2}\right)}, \tag{247}$$

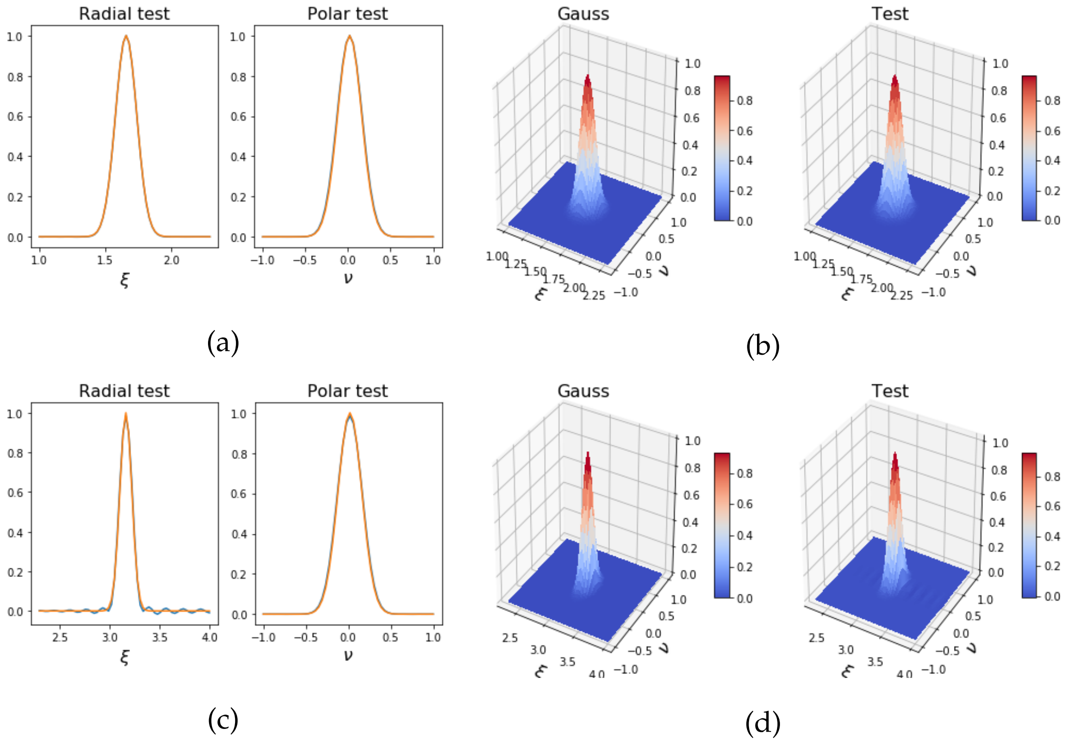

(a)

(b)

(c)

(d)

Figure 31.: Checks for the Green's function in the nucleoplasm in a) 1D and b) 2D, and the corresponding checks Green's function in the PNS.

with a mean $(\mu_{\mathrm{r}}, \mu_\theta, \mu_\phi)$ and standard deviation $(\sigma_{\mathrm{r}}, \sigma_\theta, \sigma_\phi)$, we perform the test:

$$\int_\Sigma K(r, r', \theta, \theta', \phi, \phi') F(r', \theta', \phi') r^2 \sin(\theta) \mathrm{d}r' \mathrm{d}\theta' \mathrm{d}\phi' = F(r, \theta, \phi). \tag{248}$$

In the 3-dimensional case we now have a degree l in addition to m and p over which we have a summation. We therefore require the truncation at $l = l_{\max}$, in addition to $m = m_{\max}$ and $p = p_{\max}$. We are assured by the overlap of the test and the original Gaussian in Figure. 32 that our kernel, $K(r, r', \theta, \theta', \phi,')$, is a δ-function in both compartments.

5.1.5 *Checks for 3D spheroidal coordinates*

As above, we take our Green's function from Eq. 376, at $t = 0$, to be $K(\xi,\xi',\nu,\nu',\phi,\phi') = \delta(\xi-\xi')\delta(\nu-\nu')\delta(\phi-\phi')$. Using the Gaussian function:

$$F(\xi',\nu',\phi') = \mathrm{e}^{-\left(\frac{(\xi'-\mu_\xi)^2}{2\sigma_\xi^2}+\frac{(\nu'-\mu_\nu)^2}{2\sigma_\nu^2}+\frac{(\phi'-\mu_\phi)^2}{2\sigma_\phi^2}\right)}, \tag{249}$$

with a mean $(\mu_\xi,\mu_\nu,\mu_\phi)$ and standard deviation $(\sigma_\xi,\sigma_\nu,\sigma_\phi)$, we perform the test:

$$\int_\Sigma K(\xi,\xi',\nu,\nu',\phi,\phi')F(\xi',\nu',\phi')(\xi'^2-\nu'^2)\mathrm{d}\xi'\mathrm{d}\nu'\mathrm{d}\phi' = F(\xi,\nu,\phi'), \tag{250}$$

We again truncate our sum for the 3 sums at $l = l_{\max}$, $m = m_{\max}$ and

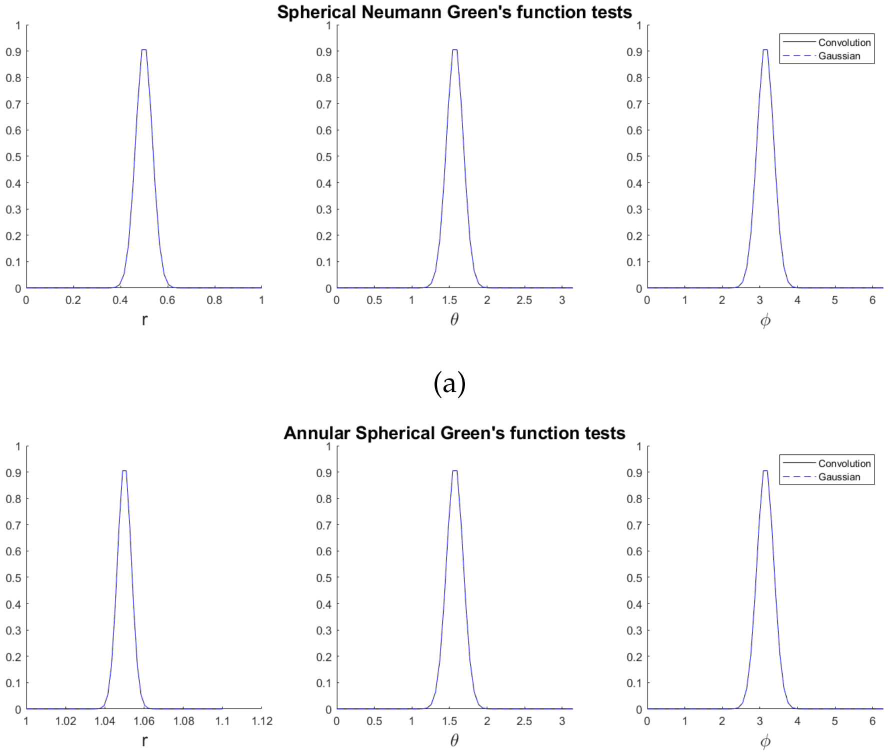

(a)

(b)

Figure 32.: We see a very close recovery of the Gaussian by our test for the spherical Neumann Green's function in a) the nucleus and b) the annulus representing the PNS.

$p = p_{\max}$ in order to generate the function numerically. We see in Figure. 33 that this is achieved in both the nucleus and the PNS. As for the ellipse, we do however observe some 'wiggles' in the radial direction in the annular compartment, due to the low number of eigenvalues we are able to obtain, reasons for which are detailed in Section 5.6.2. These may be acceptable due to the time-dependent component of of the Green's function whose exponential decay has the effect of smoothing out these tails to zero.

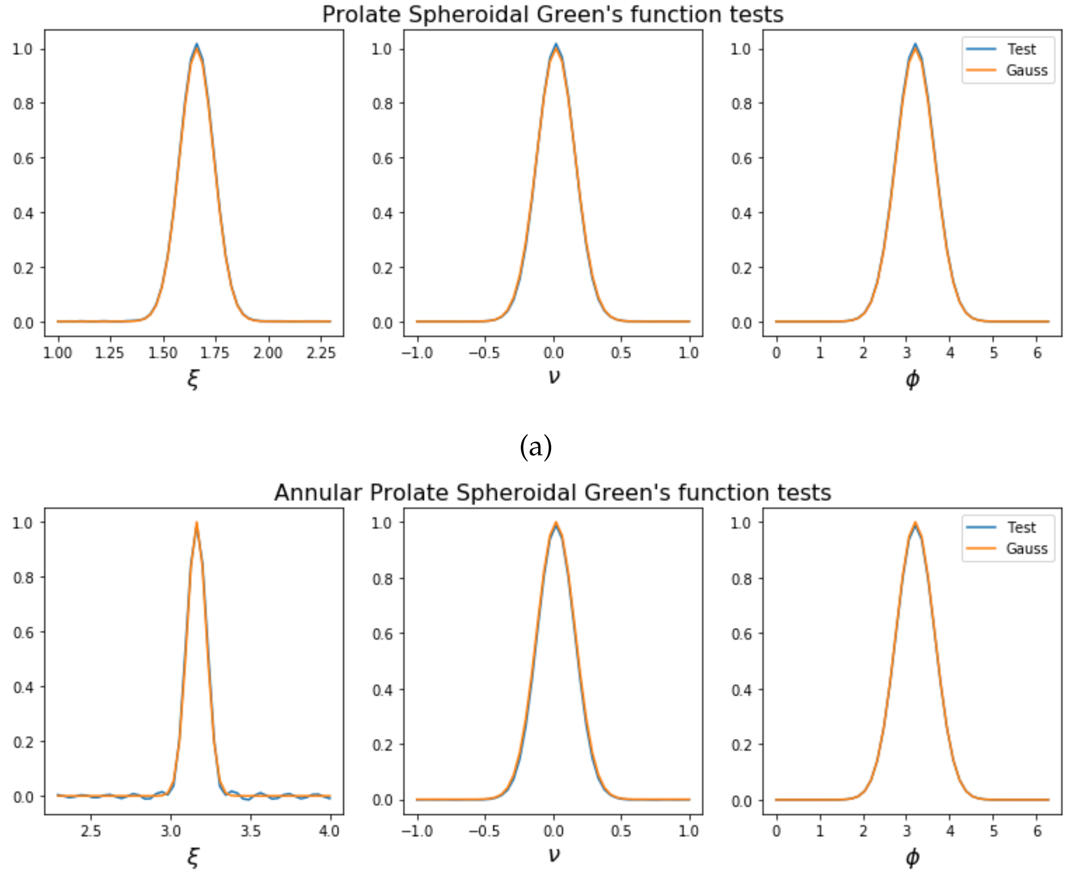

(a)

(b)

Figure 33.: We see a good replication of the Gaussian with our convolution for the Green's function in a) the nucleus and b) the annulus representing the PNS.

5.2 SIMULATIONS

5.2.1 *Simulations in 1D*

The diffusion of a concentration in space and time is evolved through solving the resulting integral for $c(x,t)$ in Eq. (19) numerically. We have computed and checked our Green's function in advance and hence we use this to iterate our solution for τ time-steps by computing the concentration at each time $t_{i+1} = t_i + dt$, for $i = 0, 1 ... \tau$, such that:

$$c(x, t_{i+1}) = \int_0^L G(x, x', dt) c(x, t_i) \mathrm{d}x, \tag{251}$$

from which $c(x, t_{i+1})$ then becomes our new initial condition. We run these simulations over $\tau = 1000$ time-steps for both Neumann and Dirichlet boundary conditions, the results of which are as expected and are shown in figures 34 a) and b) respectively. For the Neumann case, as the simulation is long enough for the system to reach a steady state, we can easily check

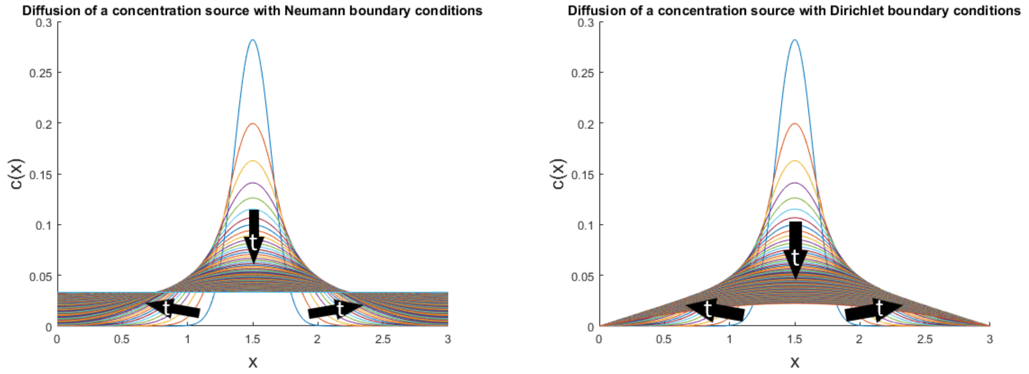

(a) (b)

Figure 34.: Diffusion of an initial point concentration source, $c(x = 1.5, 0) = 10\ \mu M$, for a) Neumann and b) Dirichlet boundary conditions, over τ =1000 time-steps of duration $dt = 0.1\ s$ and with a diffusion coefficient of $D = 0.1\ \mu m^2 s^{-1}$.

that the resulting profile is correct. As we have an initial condition given by:

$$c(x,0) = \begin{cases} 10\ \mu\text{Mnm}^{-1}, & x = 1.5, \\ 0, & \text{otherwise}, \end{cases} \tag{252}$$

we have a total of 0.1 μM given our mesh size $dx = 0.01$ nm. At steady state we have a concentration of $c(x,t) = \frac{1}{30}\ \mu\text{Mnm}^{-1}, \forall x \in (0,3)$ nm, and hence a total of 0.1 μM as expected. Therefore we can be sure that our boundary conditions hold and there is no leak of flux in or out of our domain.

The same simulation result was found for the nonzero domain Neumann Green's function, however over the domain $x = (3,6)$ nm. We then use the Neumann Green's function in each of the domains and allow a single channel between the two compartments to open at certain times. As this is a 1D model this channel occurs at the single point of intersection, $x = 3$. Figure. 35 shows a simulation result where the channel was open at time-steps, $\tau \in (0,200)$ s and $\tau \in (500,700)$ s, to allow a constant flux of $J = 12\ \mu\text{Mnm}^{-1}\text{ms}^{-1}$ from the outer (b) to the inner (a) domain. We set initial conditions of $c_\text{a}(x,t) = 0, \forall x \in a = (0,3)$ and $c_\text{b}(x,t) = 80, \forall x \in b = (3,6)$. Figure. 35 (a) illustrates how each time the channel is opened concentration moves from b into a and then equilibrates to a constant profile in each compartment when the channel is closed. Figures. 35 (b1) and (b2) show the flux profiles into domain a and domain b respectively. The plotted fluxes were calculated by differentiation at the boundaries to ensure that the resultant flux was as expected. We also see that the total flux over the entire domain is equal to zero and so concentration is conserved as required.

5.2.2 *Simulations in 2D polar coordinates*

Simulations are performed using an extension of the Eq. (252) seen in the 1D method. We evaluate our integral solution from Eq. (53) numerically, having computed the Neumann Green's function, Eq. (54), in advance for

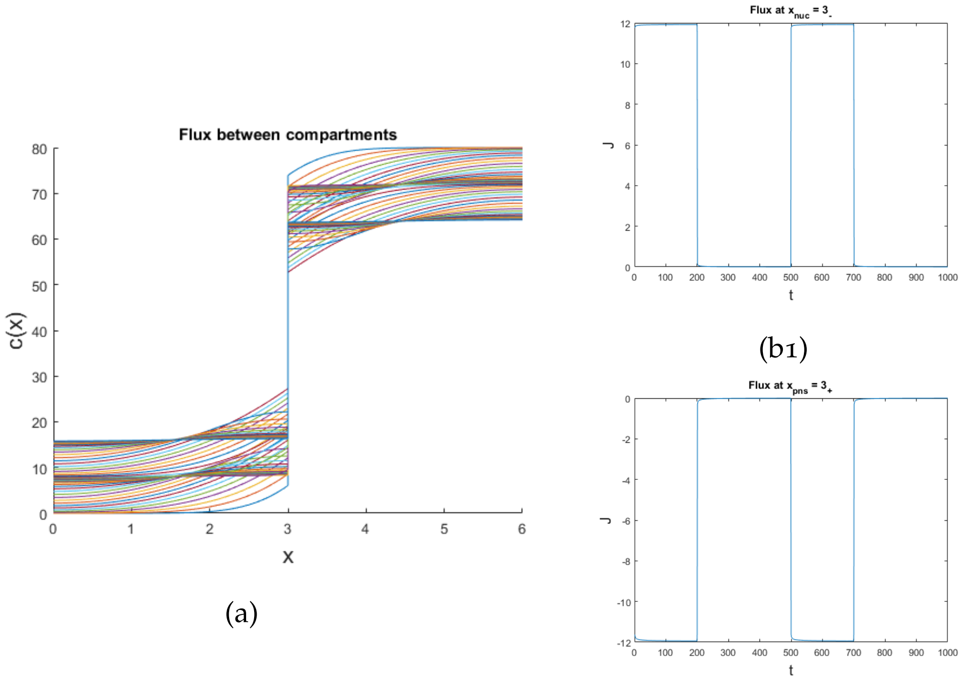

(a)

(b1)

(b2)

Figure 35.: A simulation of a channel between the two domains opening and closing over τ =1000 time-steps of length $dt = 0.1$s with diffusion coefficient of $D = 0.1\ \mu m^2 s^{-1}$. In a) the concentration profile is plotted every 2 time-steps, whilst the corresponding figures in b1) and b2) show checks for the flux and hence the points of channel opening and closure.

fast simulations. The concentration at time $t_{i+1} = t_i + dt$, for $i = 0, 1...\tau$ is given by:

$$c(r, \theta, t_{i+1}) = \int_0^{2\pi} \int_0^{a} G(r, \theta, r', \theta', dt) c(r', \theta', t_i) r' \mathrm{d}r' \mathrm{d}\theta', \qquad (253)$$

where $c(r, \theta, t_{i+1})$ then becomes our new initial condition. The results of these simulations for both Neumann and Dirichlet boundary conditions, as well as the annulus - which is simply integrated over the domain $x \in [a, b]$ - can be seen in Figure. 36. To check that each compartment is in fact closed by the no-flux boundary conditions we can integrate the concentration vector at each time-step over the whole domain to find the total number of molecules of calcium. As expected for a closed system, we find that the total concentration remains constant and hence can be confident that our simulation is numerically correct and our system has no leaks.

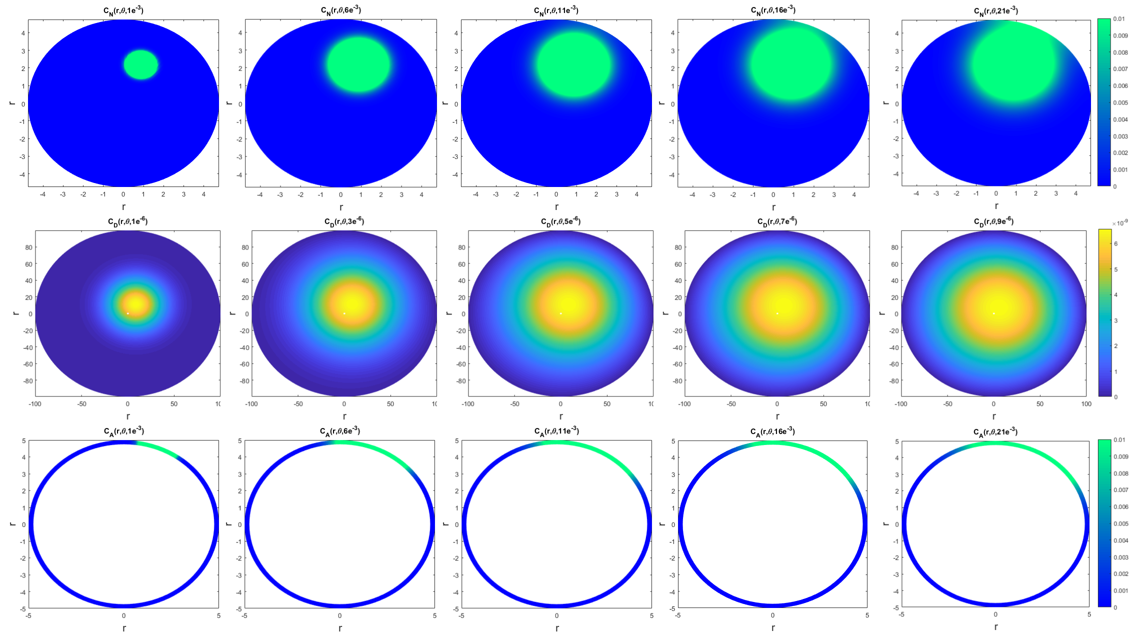

Figure 36.: Simulations in the nuceloplasm for Neumann (first row) and Dirichlet (second row) boundary conditions as well as in the PNS (third row).

Next we wish to add a flux between the two compartments. This is done by using the Neumann Green's function in each of the domains and allowing single channels to open at certain times. This is numerically computed using the 'magic rule' of Barton [11]:

$$\begin{aligned} c(r,\theta,t_{\mathrm{i}+1}) = & \int_0^{2\pi}\int_0^{\mathrm{a}} G(r,\theta,r',\theta',dt)c(r',\theta',t_{\mathrm{i}})r'\mathrm{d}r'\mathrm{d}\theta' \\ & +D\int_0^{\mathrm{dt}}\int_0^{2\pi} G(r,\theta,r',\theta',dt)\frac{\partial\psi}{\partial n}\mathrm{d}\theta'\mathrm{d}dt. \end{aligned} \tag{254}$$

Here the flux is the derivative with respect to the normal of the disc and hence, as this is independent of θ, we can take this outside of the integral and calculate the Green's function integrated over time analytically. This allows us to also store the integrated Green's function and, with no requirement to compute this at each time step, dramatically speeds up simulation time. The integral has the same form for all of the discussed boundary conditions and domains, and is given by:

$$\int_0^{\mathrm{dt}} G(r,r',\theta,\theta',dt)\mathrm{d}dt = \frac{G(r,r',\theta,\theta',0)-G(r,r',\theta,\theta',dt)}{Dk^2}, \tag{255}$$

where k depends on the eigenvalues of the particular problem.

An illustration of a short simulation ($\tau = 10$ time-steps) of flux through a single channel, from the outer to inner compartment, is shown in Figure. 37. We begin with a constant concentration of 0.15 everywhere and a channel is opened at time-step 3 and closes at time-step 6. The flux is set to:

$$\frac{\partial \psi}{\partial n} = \begin{cases} 20, & r' = a, \theta' = \frac{\pi}{2}, t \in [t_3, t_6), \\ 0, & \text{otherwise}, \end{cases} \tag{256}$$

such that the flux out of the outer annular compartment is equal to the flux into the inner disc. The system is otherwise closed and hence we check that the total concentration remains the same throughout by integrating over the entire domain at each time step to find the total number of molecules. We also differentiate the concentration profile at the boundary of each compartment to check that there is no flux anywhere other than that at the specific channel opening times and locations perscribed.

5.3 NUMERICAL SCHEME

We time-step the system according to the 'magic rule' given in Eq. 211, which in discretized form becomes:

$$u_{\mathrm{t+dt}}(\mathbf{r}) = \int_V u_{\mathrm{t}}(\mathbf{r}') G(\mathbf{r}, \mathbf{r}', dt) \mathrm{d}V' + Ddt \int_S \left. \frac{\partial u_{\mathrm{t}}(\mathbf{r}')}{\partial n'} \right|_{r'=s} G(\mathbf{r}, \mathbf{r}', dt) \mathrm{d}S', \tag{257}$$

where we have performed the integration:

$$\int_0^{\mathrm{dt}} G(\mathbf{r}, \mathbf{r'}, s) \mathrm{d}s \approx dt G(\mathbf{r}, \mathbf{r'}, dt). \tag{258}$$

in advance. The integrals were performed using the trapezium rule, over the space $\mathbf{r} = (r, \theta, \phi)$ where the components r, θ and ϕ were discretized into a mesh of N, M and P points respectively. This gives the expression:

$$u_{\mathrm{t+dt}}(\mathbf{r}) = dr' d\theta' d\phi' G(\mathbf{r}, \mathbf{r}', dt) u_{\mathrm{t}}(\mathbf{r}') F_{\mathrm{V}} + Ddt d\theta' d\phi' \left. \frac{\partial u_{\mathrm{t}}(\mathbf{r}')}{\partial n'} \right|_{r'=s} G(\mathbf{r}, \mathbf{r}', dt) F_{\mathrm{s}}, \tag{259}$$

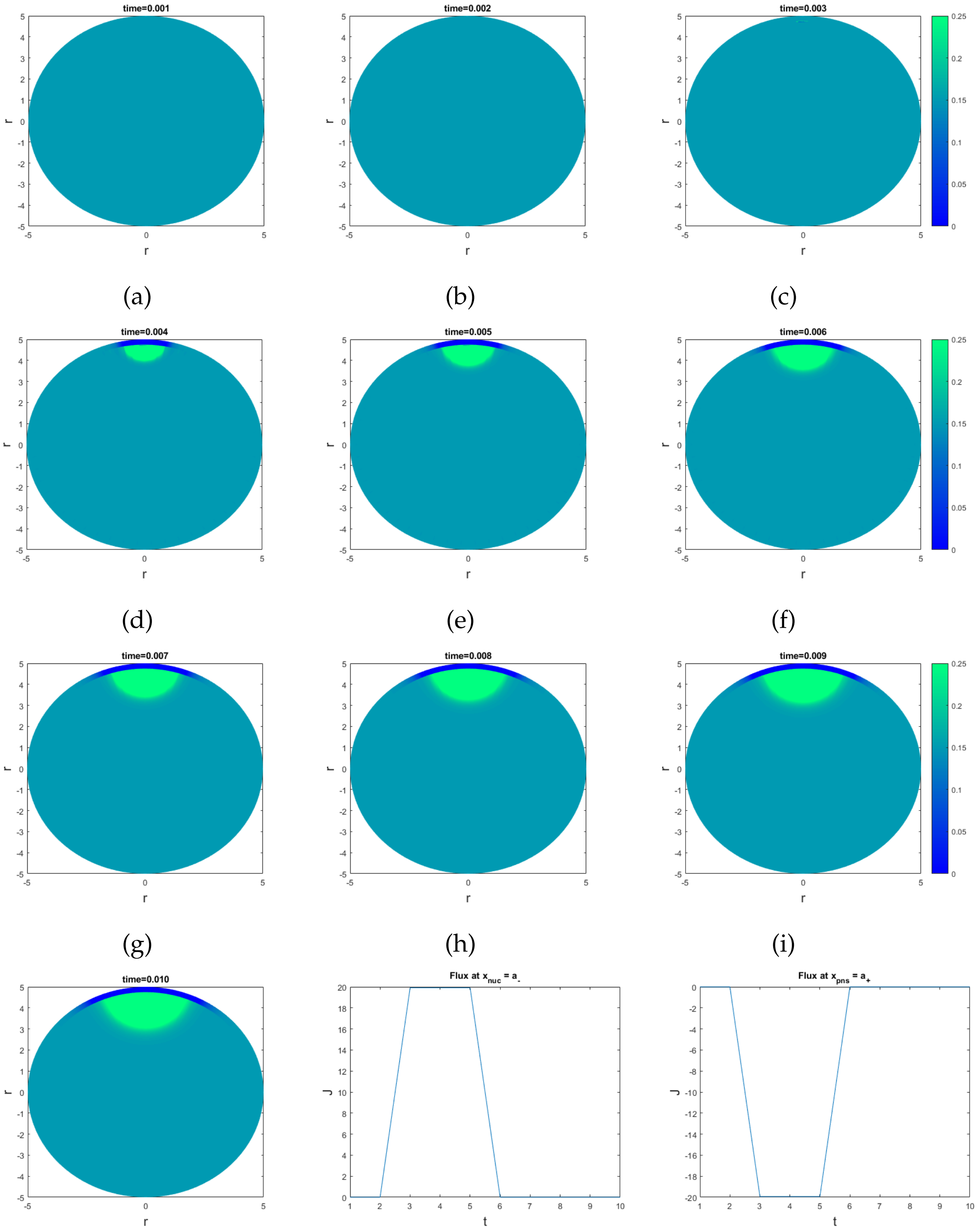

(a) (b) (c)

(d) (e) (f)

(g) (h) (i)

(j) (k) (l)

Figure 37.: a)-j) Simulation results over $\tau = 10$ time-steps for initial condition $C(r, \theta, 0) = 0.15$, $r \in (0, b]$. Differentiating the concentration at $r = a$, $\theta = \frac{\pi}{2}$, either side of the boundary at each time-step returns the applied flux at k) a^- and l) a^+ showing that this has been correctly applied.

for the calcium concentration profile at the current time, $u_{t+dt}(\mathbf{r})$ given the concentration at the previous time-step, $u_t(\mathbf{r})$ where we have used:

$$F_v = \begin{bmatrix} \frac{r_1^2 \sin\theta_1}{4} & \frac{r_1^2 \sin\theta_2}{2} & \cdots & \frac{r_1^2 \sin\theta_{M-1}}{2} & \frac{r_1^2 \sin\theta_M}{4} \\ \frac{r_2^2 \sin\theta_1}{2} & r_2^2 \sin\theta_2 & \cdots & r_2^2 \sin\theta_{M-1} & \frac{r_2^2 \sin\theta_M}{2} \\ \vdots & \vdots & \ddots & \vdots & \vdots \\ \frac{r_{N-1}^2 \sin\theta_1}{2} & r_{N-1}^2 \sin\theta_2 & \cdots & r_{N-1}^2 \sin\theta_{M-1} & \frac{r_{N-1}^2 \sin\theta_M}{2} \\ \frac{r_N^2 \sin\theta_1}{4} & \frac{r_N^2 \sin\theta_2}{2} & \cdots & \frac{r_N^2 \sin\theta_{M-1}}{2} & \frac{r_N^2 \sin\theta_M}{4} \end{bmatrix}, \tag{260}$$

and

$$F_s = \begin{bmatrix} \frac{\sin\theta_1}{2} & \sin\theta_2 & \ldots & \sin\theta_{M-1} & \frac{\sin\theta_M}{2} \end{bmatrix}. \tag{261}$$

These simulations were performed using our own implementation of the trapezium rule which was measured to take 0.0834 s per iteration, as compared to the 3.7408 s to call the inbuilt 'trapz' rule in Matlab. Both alternatives performed at the same accuracy, as would be expected for the same method, and were found to have a 1.02% numerical error in concentration after 1000 time-steps.

5.4 MAPPING

To decrease memory requirements and increase speed of simulation, a mapping was created to reduce the size of the Green's function. Taking the angular variables (θ, ϕ), along with the relation:

$$h(\psi) = \cos(\psi) = \cos(\theta)\cos(\theta') + \sin(\theta)\sin(\theta')\cos(\phi - \phi'), \tag{262}$$

the unique values of $\cos(\psi)$, M, were stored along with the transition matrices, I_d and I_v such that:

$$H(\psi) = h(\psi)[I_d], \tag{263}$$

$$h(\psi) = H(\psi)[I_v]. \tag{264}$$

For a mesh size of M = 50 points in the θ variable and P = 40 points in the ϕ variable the stored Green's function is reduced significantly from 68.7GB to 1.16GB.

5.5 CALIBRATION

Given that Green's functions, are infinite sums, we must truncate these at $l = l_{\max}$ and $p = p_{\max}$ in order to work with these numerically. To ensure the discretized Green's function is sufficiently convergent given the truncation of the infinite sum at $l \times p = l_{\max} \times p_{\max}$ eigenvalues we must carefully balance this with the number of mesh points (N, M, P) as described previously in Section 5.3. We determine these values through checks performed at $t = 0$, where we expect our Green's function to reduce to a delta function:

$$G(r,\theta,\phi,r',\theta',\phi',0) = \delta(r-r')\delta(\theta-\theta')\delta(\phi-\phi'). \tag{265}$$

A scan of a much larger section of the (N, M, P, l, p) parameter space was performed to find the set which gives the absolute minimum error in our Green's function within computationally reasonable limits. In Figure. 38 we show the result of fixing M, P and $p_{\max}$ whilst varying N and $l_{\max}$, and record the magnitude of error between the Green's function at $t = 0$ and the expected delta function. For visualisation purposes we have used the log of the error to improve the sensitivity of the colormap. In Figure. (38) (a) we see that above N = 60 mesh-points and for $l_{\max} \in [30, 170]$ the error is very low, converging in a trough close to the diagonal. These local minima can be see more clearly in the orientation shown in Figure. (38) (b), where we see dips at optimal (N, l) combinations, with the global minimum error of 1.6653×10^{-16} occurring at $(N, M, P, l, p) = [140, 100, 100, 90, 100]$.

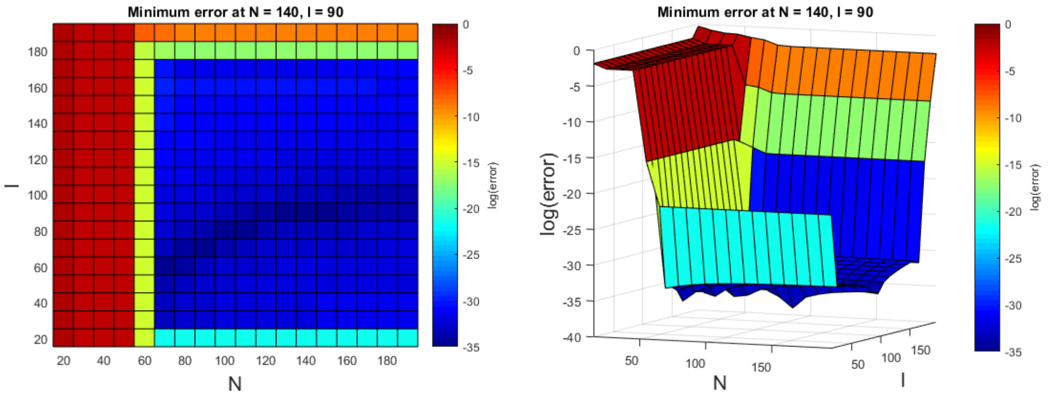

(a) (b)

Figure 38.: Parameter space evaluation of the error in the numerical approximation of the Green's function (155), for a fixed M, P and $p_{\max} = 100$. We have a) the top down-view and b) a surface plot showing dips at local minima.

5.6 LIMITATIONS OF THE METHOD

The functions involved in solving the diffusion equation in elliptical and spheroidal geometries, namely the Mathieu functions and the Prolate Spheroidal wavefunctions introduced in Sections 3.3 and 4.2, are notoriously difficult to compute, lending a possible explanation for the limited usage of the more representative geometry in the literature. Here we highlight some of the difficulties involved with these functions that have been experienced during the simulation phase of this work.

5.6.1 *Mathieu functions*

As described in Cojocaru (2008), the solutions to diffusion problems in spherical polar coordinates involve trigonometric and Bessel functions which are well known and readily available. On the other hand, for an Elliptic cylinder or spheroid, we require the Matheiu functions whose computation remains controversial with algorithms that are largely incomplete [29]. Cojocaru proposes that the reason for this is likely the "*complicated and various* *notation existent in the literature*", a problem which was also highlighted by Gutierrez (2003) who said:

"*We believe that this lack of literature compared to that for other special functions is because the behaviour of Mathieu functions is relatively rich and consequently more difficult to understand. Moreover at least five different nomenclatures are in use, and the computation of the Mathieu functions and their eigenvalues still presents some numerical difficulties*" [47].

These problems have persisted to the present day, with Daniel (2020) more recently highlighting that, although Mathieu functions have a huge importance in representing more accurate and realistic geometries, these methods are as yet unreliable. He states that:

"*The numerical and mathematical difficulties associated with solving Mathieu's equation are tantamount to the intensive mathematical analysis and research applications that both physics and engineering demand. At best, key findings and solutions to Mathieu's equation tend to only exist in numerical tables as drawn from infinite continued fraction methods or approximate expressions for eigenvalue calculations, which at times are represented grossly by stability charts*" [30].

In a similar statement Brimacombe (2021) describes how the use of Mathieu functions is theoretically attractive, being analogous to the harmonic functions, with the potential for efficient computation in comparison with direct numerical solution of the PDE model. Brimacombe acknowledges that in practice however, there are difficulties including; large values of the parameters; approximation properties of the expansion itself and the numerical stability of the expansion. It is also considered how the rapid advancement of computational abilities in comparison to its analytical counterpart may, as a result, "*risk concealing as yet unresolved analytical and computational issues involved in the use of Mathieu functions*". Finally Brimacombe calls for an effort to be made in advancing the algorithms currently available stating that:

"*The task of constructing fully general, bulletproof code for the Mathieu functions is one that calls for dedicated effort and analysis... we know of no such code in existence currently.*" [16].

In the attempt at using the more realistic geometry to represent the nucleus, similar issues have been present. One solution is to use the prolate spheroidal wave functions for the two-dimensional problem, however as an extension to the 2d-elliptic geometry we face similar problems as described in the next section.

5.6.2 *Prolate spheroidal wave-functions*

The sphere is, in fact, a generalisation of the spheroidal geometry, and hence the idealisation of bodies as spheres does not adequately represent the realistic situation [6]. It is recognised that the spheroidal wavefunctions which describe this geometry are difficult to compute and the small number of current programmes available have limitations, most notably the failure of the widely-used numerical schemes as the eigenvalue γ becomes large [41]. This has been addressed by some authors, however the alternative expressions, whilst being accurate for large γ, are limited in other areas, such as a solution by Van Buren which is accurate for ξ close to 1, and $l - m$ small [14]. It is likely that it is for these reasons, that applications requiring the prolate spheroidal coordinates, are often modelling using simplifications such as assuming symmetry around the ϕ axis and reducing the system to 2-dimensions [18] or modelling only the surface and hence requiring only the associated Legendre functions [92].

Figure. 39 shows an example of the problems with the inbuilt prolate spheroidal wave-function in Python. In this example we focus on the derivative of the

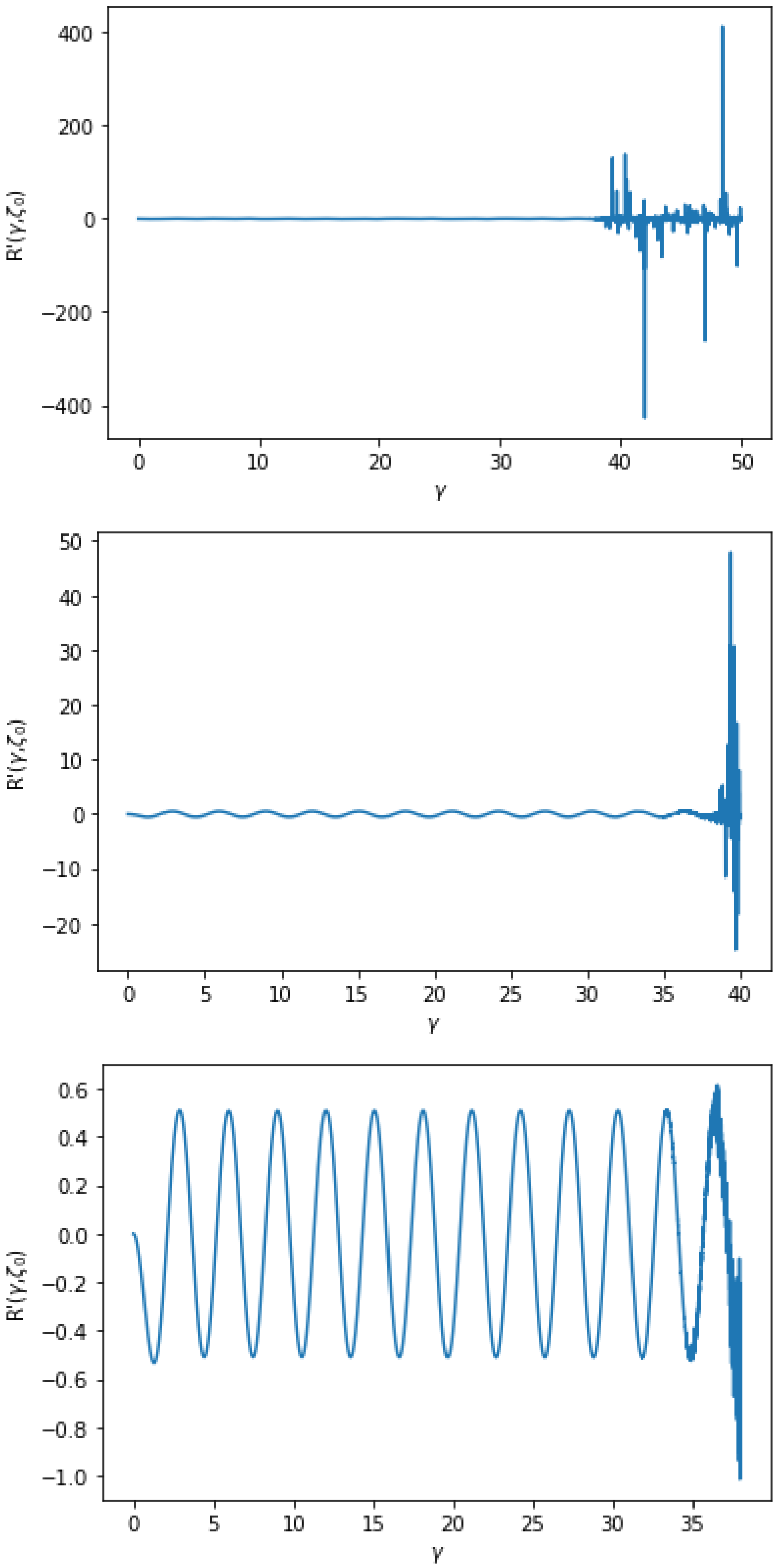

Figure 39.: An increasingly close view of the derivative of the radial prolate spheroidal wave-function for $a = 9$, $b = 10$, $m = 0$ and $l = 0$, demonstrating the numerical instabilities that occur above $\gamma \approx 35$.

radial function, as it is the zeros of this which provide the eigenvalues satisfying the Neumann boundary condition, however the numerical instabilities present in the regular function also. From Figure. 39 we can see that only 22 zeros of the function with $m = 0$ and $l = 0$ can be calculated before the numerical scheme breaks down. This presents some issues with the convergence of the Green's function to a δ-function at $t = 0$, as the truncation, $p_{\max}$, occurs at a much lower value than we would prefer. Despite a large proportion of the instabilities being 'smoothed out' for a nonzero dt, these are large enough to be amplified over the multiple time-steps used in simulation, and hence we are required to manually ensure that the tails are zero before the Green's function can be utilised. An example of pre and post-manual editing of the tails is given in Figure. 40.

The above parameters represent a trade off between modelling a spheroidal nucleus and ensuring that there are sufficient eigenvalues for convergence. As we shall see in Section 6, experimental data proved the mean value of ζ_0 to be 1.185. The difference between this and our 'lowest acceptable value' can be seen in Figure. 42 which shows the comparison between the geometry and the number of possible zeros of the function which can be found numerically for the limiting values of $m = 0$, $l = 0$. This makes it clear that, for truly realistic geometries, it is not possible to compute an accurate Green's function given the limitations of current algorithms.

Furthur problems arise when we wish to compute a thin compartment in modelling the PNS. The closer ζ_0 and ζ_1, the greater the periodicity of the oscillations of the boundary condition, $f(\gamma)$, given in Eq. 188. In this case there are therefore only very few zeros that can be calculated before the numerical instabilities at large γ become a factor. This problem is illustrated in Figure. 41, where we observe that for $\zeta_0 = 2.3$ and $\zeta_1 = 2.5$ we are only able to calculate 5 zeros before the numerical scheme becomes unstable. This

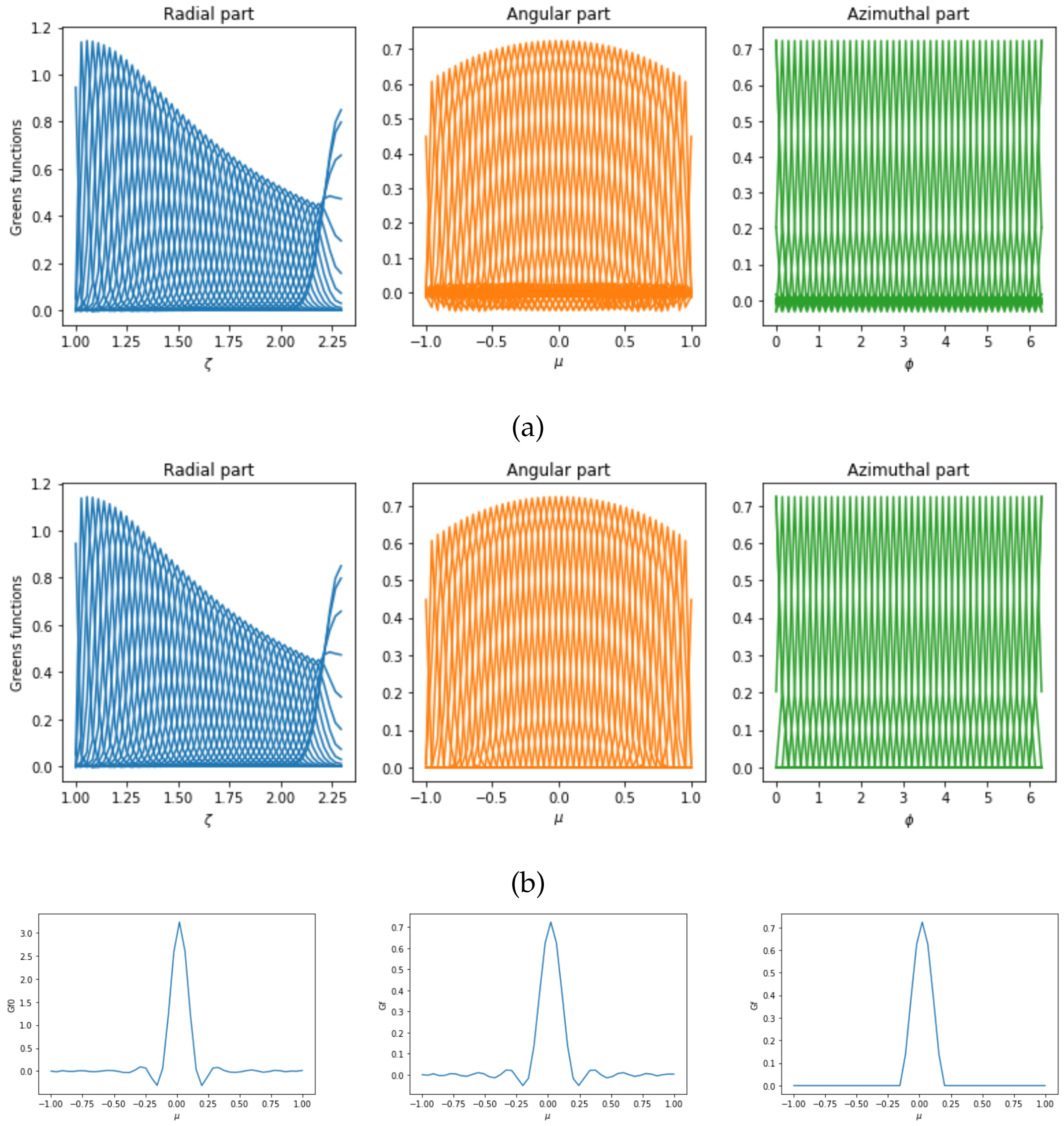

(a)

(b)

(c) (d) (e)

Figure 40.: The Green's functions plotted for $(\zeta', \mu', \phi') = (\frac{\zeta_0 - 1}{2}, 0, \pi)$ a) before any manual intervention and b) after manually setting the tails to zero. This can be seen for a single point, $\mu = 0$, with c) $t = 0$, d) $t = 0.002$ and e) $t = 0.002$ and the tails set to zero.

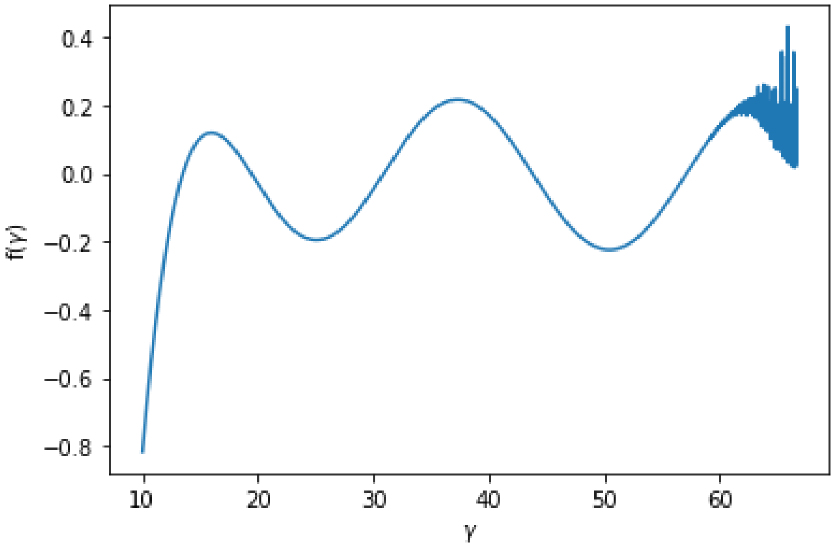

Figure 41.: The Neumann boundary condition for a spheroidal compartment requires the zeros of $f(\gamma)$. We see that very few zeros are available for a thin section with $\zeta_0 = 2.3$, $\zeta_1 = 2.5$ before the inbuilt function fails.

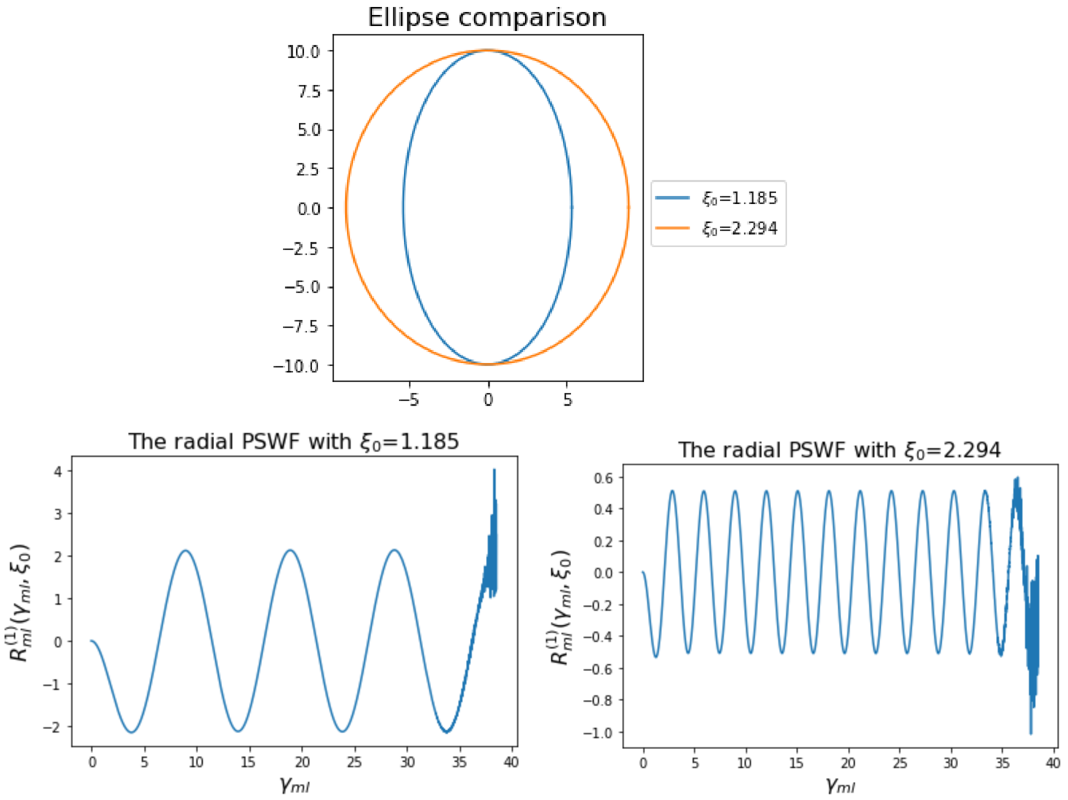

Figure 42.: The lower the sphericity, and hence the closer the value of ξ_0 to 1, the lower the frequency of oscillations. This means that there is a decreasing number of zeros available before the python function becomes numerically unstable.

problem therefore requires us to use a PNS slightly wider than we would prefer.

5.7 NUMERICS SUMMARY

- The general properties of the time-independent Green's function as a $\delta-$function were explained.
- The properties of the $\delta-$function were used to check the numerical accuracy of our codes.
- Successful checks for each Green's function derived in Sections 3 and 4 have been demonstrated.
- Test simulations confirmed that the numerics are accurate and the system remains closed.
- The discretised system was described, along with our time-stepping regime and calibration of the mesh with the number of eigenvalues in order to achieve a minimal computational error.
- The limitations of the method for the spheroidal geometry were explained, with examples of the numerical problems faced using currently available algorithms.

6

EXPERIMENTAL WORK

This chapter presents a wide range of experimental work, used to inform and motivate the geometrical considerations, which have not previously been studied, and measure nuclear calcium signals to compare with the computationally simulated results. Firstly we look at the morphology of the nucleus, taking measurements to parameterise both the sphere and the spheroid. We go on to quantify, for the first time, comparisons in the nuclear geometry between cell types as well as along the elongation zone. Finally we have created a new methodology, utilising a specialised Flow Cell [72], in order to effectively apply stimuli to plant root cells, which we utilised to record the nuclear plant calcium signatures that we are attempting to replicate.

6.1 NUCLEAR MORPHOLOGY

To ensure the highest possible accuracy of modelling results, it is important to ensure the parameter values used are representative of the real-world system. One such necessary biological input is the radius of the plant cell nucleus, given by a in Eq. (135). However, information available in the literature appears extremely limited with the few reported radial measurements varying by up to two orders of magnitude. For non-spherical objects the angular alignment with the light field could also skew measurements if left unaccounted for. Confocal images found in publications are 2-dimensional representations of a 3-dimensional object, and to obtain the radii of a spheroid, we would require the image slice to belong on the (x, y) plane, i.e. at $z = 0$ for that particular object as seen in Figure. 18a. An example of a case where the two dimensional slice could be misleading is illustrated in Figure. 43. Here the top-down view in a) gives the impression that a sphere would be an appropriate approximation, whereas b) shows that the nucleus is clearly closer to ellipsoidal. In this section, the data collection methods will be explained and the resulting morphological parameters will be extracted to be input into the mathematical model.

6.1.1 *Data collection*

Images were taken using a confocal microscope, along the roots of Arabidopsis lines containing Green Fluorescent Protein (GFP) fused to low-temperature induced 6A, LTi6A, protein in the PM as a proxy marker for the cell wall and the nuclei marked with a red fluorescent protein (RFP) linked

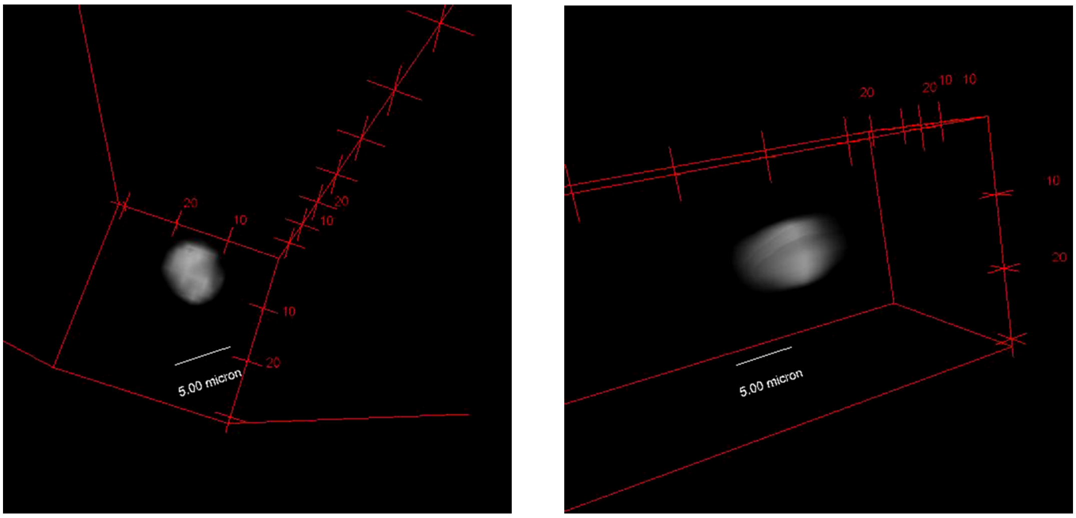

(a) (b)

Figure 43.: A 3D image of a single nucleus, made up from a z-stack of confocal images. The nucleus gives the appearance of a significantly different geometry when viewed from different perspectives.

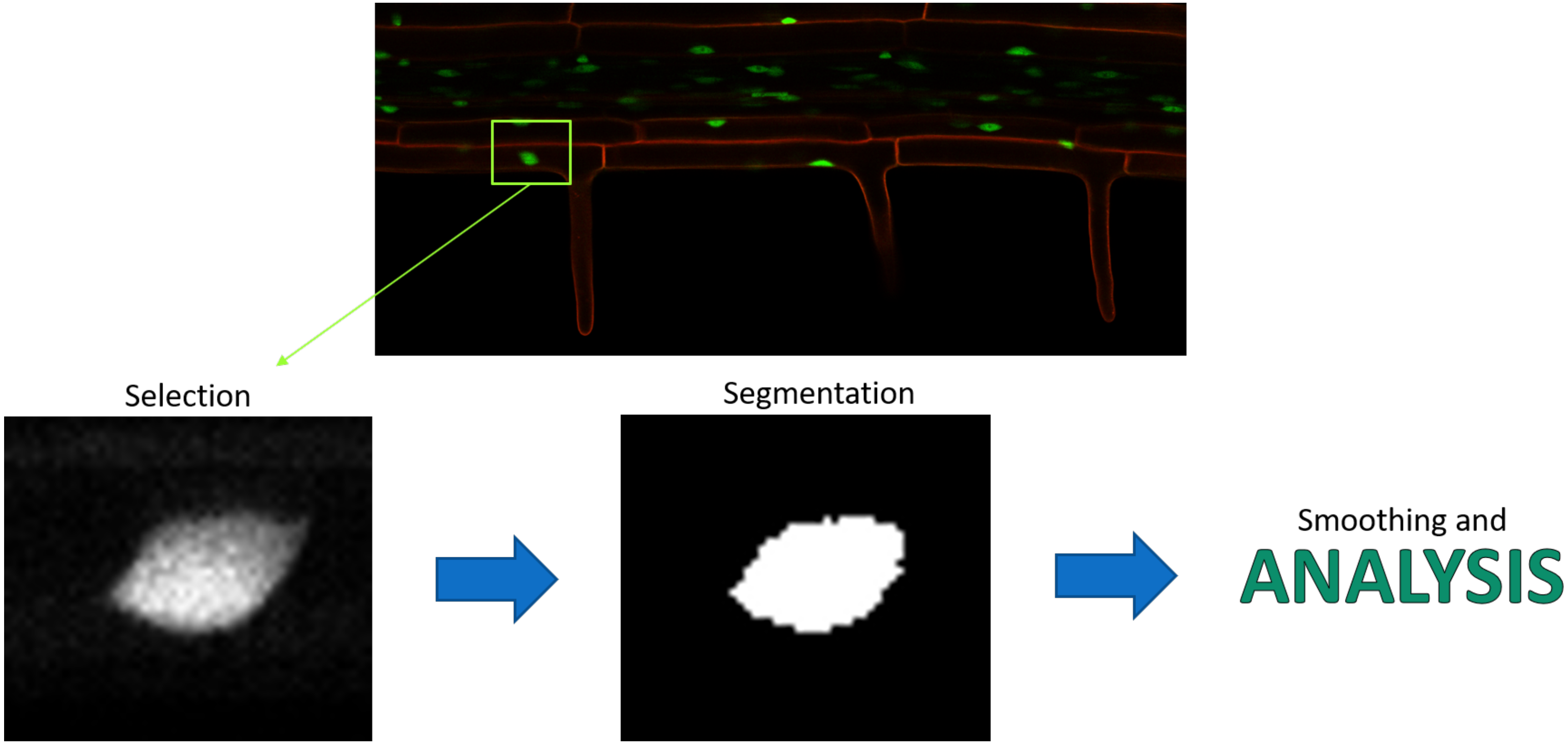

Figure 44.: The process of data collection.

to Histone 2B - a protein which wraps DNA in the nucleus. This allowed us to detect each cell and its nucleus as seen in Figure. 44. For the root hair and root cortex, 58 of each cell type were taken over 9 different plants, and the nuclei were selected for analysis. These images were processed using the NucleusJ software for Fiji [69, 76]. A z-stack was taken of each individual nucleus and a segmentation algorithm was used to create a binary set of images, discerning the nuclear boundary from any noise. The edges were then smoothed and the 3D structure was recreated by extrapolation using the known distance in between each consecutive 2D slice. Measurements could then be taken and a set of two 2D and six 3D parameters describing the nuclear morphology were extracted for each cell type.

6.1.2 *Data analysis*

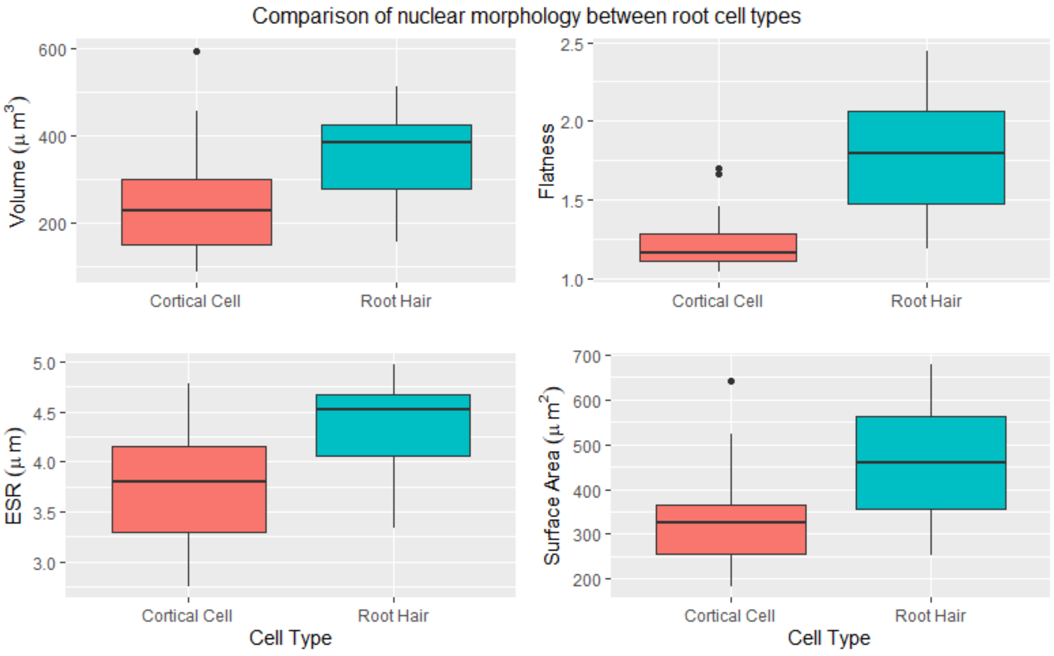

Figure 45.: Results show that root hair cells are generally larger and flatter than cortical cells in Arabidopsis. Statistically significant differences are found between the two cell types for three key morphological parameters: a) Volume*, b) Flatness***, c) Equivalent Spherical Radius** and d) Surface Area** where *** $P < 0.0001$.

A statistical analysis on the parameters showed significant differences in dimensionality of nuclei in root hair cells as compared to those in the root cortex. Selected results of this analysis can be seen in 45. We found that nuclear volume was larger in the root hair cell, with a mean of 366.2 μm^3 as compared to only 245.7 μm^3 in the root cortex. There was also a statistically significant difference in flatness between the cells, that is, the measure of the ratio between the major (longest) and minor (shortest) axes. We see that in the root hair this axis ratio is close to 2, and hence the spheroidal case with radii of $b \approx 2a$ in the notation of Figure. 22, is likely to be the best approximation. In the root hair cortex however, the flatness parameter is close to 1 and therefore modelling a spherical geometry for these cells would be acceptable. Another interesting parameter is the equivalent spherical radius which takes the measured nuclear volume and uses the rearrangement of the equation: $V = \frac{4}{3}\pi r^3$, to find the theoretical radius if this volume represented a perfect sphere. This gives us a key parameter value, the radius of nucleus in the root hair cell, $a = 4.397$ μm to use in our model.

The major and minor axis values were also measured for parameterisation of the spheroid. The measured axis ratio ≈ 2, which would give, for a radius $a = 4.5$ μm, a major axis value of $b = 9$ μm and our coordinate parameter to be $\xi_0 = 1.155$. In order to check these measurements, the nuclei were measured manually using ImageJ at the widest point along the z-stack for each axis. Results gave a mean value for the minor axis as $a = 3.400$ μm, the major axis as $b = 7.212$ μm and hence an axis ratio of 2.274 and a coordinate parameter of $\xi_0 = 1.185$ agreeing closely with that of our previous results using NucleusJ.

6.1.3 *The evolution of nuclear geometry in the root elongation zone*

As it was noted from images that nuclear geometry appears to become less spherical as we move along the root elongation zone (EZ), 96 LTi6A

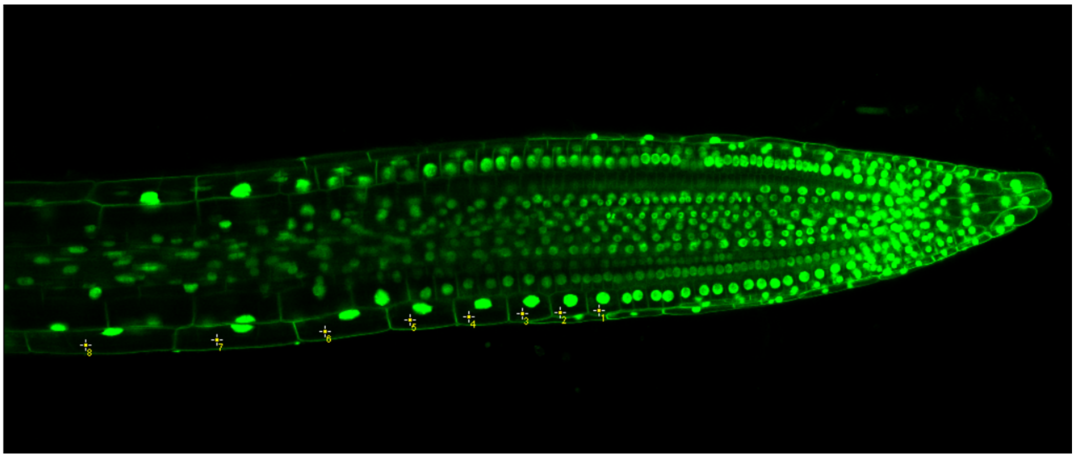

Figure 46.: An illustration of cell number assignment, depicted by the white crosses and yellow numbers, on an Arabidopsis cell file. Cell 1. is deemed to be the first cell in the root elongation zone.

Arabidopsis randomly selected nuclei were measured using ImageJ and the data collection and analysis methodology previously described in Section 6.1.1. In addition to the four parameters described above, here we also include two additional measures; (i) nuclear 'sphericity', calculated as $36\pi\frac{Volume^2}{SurfaceArea^3}$, which results in a value of 1 for a perfect sphere and tends towards zero as the shape becomes less regular; and (ii) elongation, which is the length of the longest axis divided by the length of the intermediate axis [4]. In addition to the measurements extracted from ImageJ we recorded an additional factor that we will call the 'cell number'. The cell number is the number assigned to the cell when counting along the cell file from the transition zone (TSZ), the point where the root EZ begins and cells start expanding rapidly [43]. An example of the cell number assignment can be seen for the bottom row of cells in Figure. 46.

Figure. 46 clearly demonstrates a relationship between cell number and nuclear size and sphericity. However we wish to determine this quantitatively. The data collected is plotted for cell number against the measured nuclear parameters: sphericity, flatness, elongation, volume, surface area, and equivalent spherical radius (esr) in Figure. 47. We see that as the cell elongates,

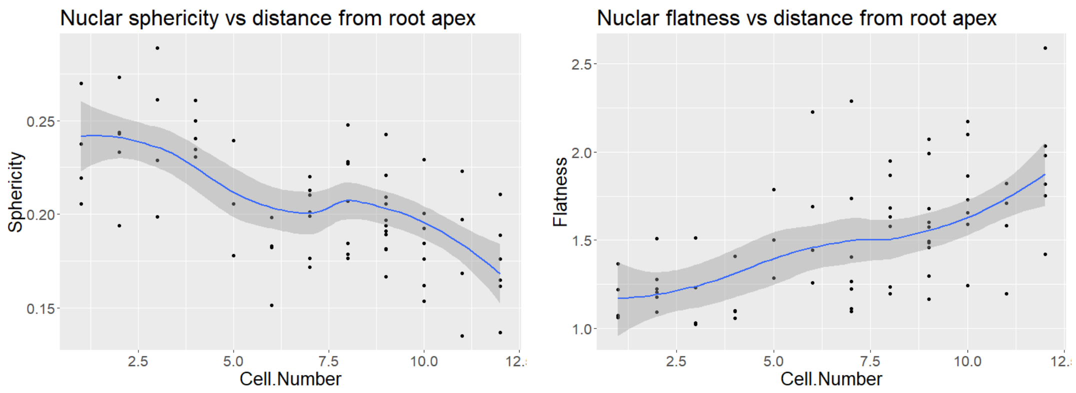

(a) Sphericity (b) Flatness

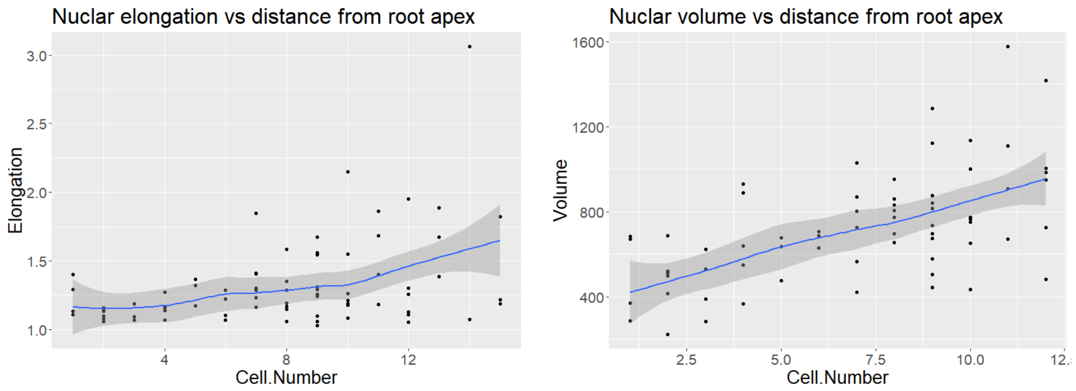

(c) Elongation (d) Volume

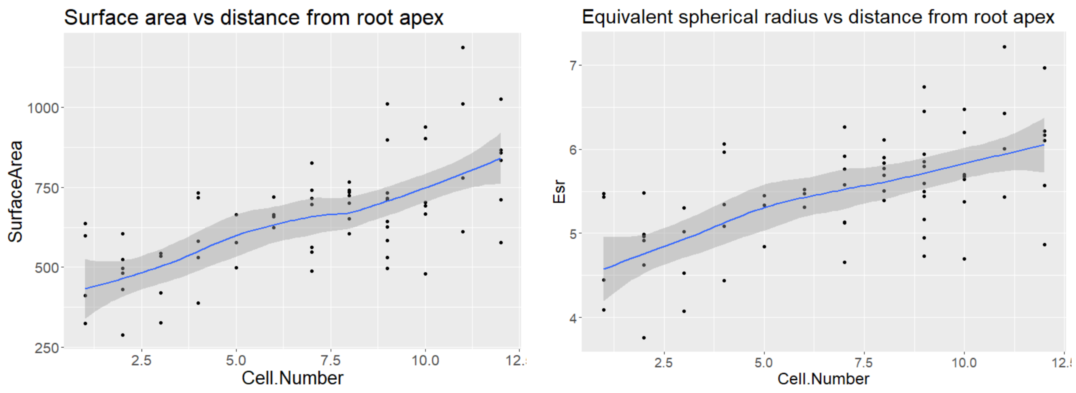

(e) Surface Area (f) Equivalent spherical radius

Figure 47.: Graphs to show the change in nuclear geometry with distance from the root apex, determined by cell number within a file. Nuclear geometry is described by six parameters; a) sphericity; b) flatness; c) elongation; d) volume; e) surface area; and f) equivalent spherical radius (esr).

the nucleus becomes both larger - with a greater esr/volume/surface area - and flatter - with a higher degree of flatness/elongation and lower sphericity. We see a negative correlation between sphericity and esr in Figure. 48, for which a linear regression analysis gave a coefficient of -7.8699 with a statistically significant p-value of 0.000152. The residuals of this analysis show no pattern and are included along with the linear regression summary in Appendix. C, Figure. 87 for completeness.

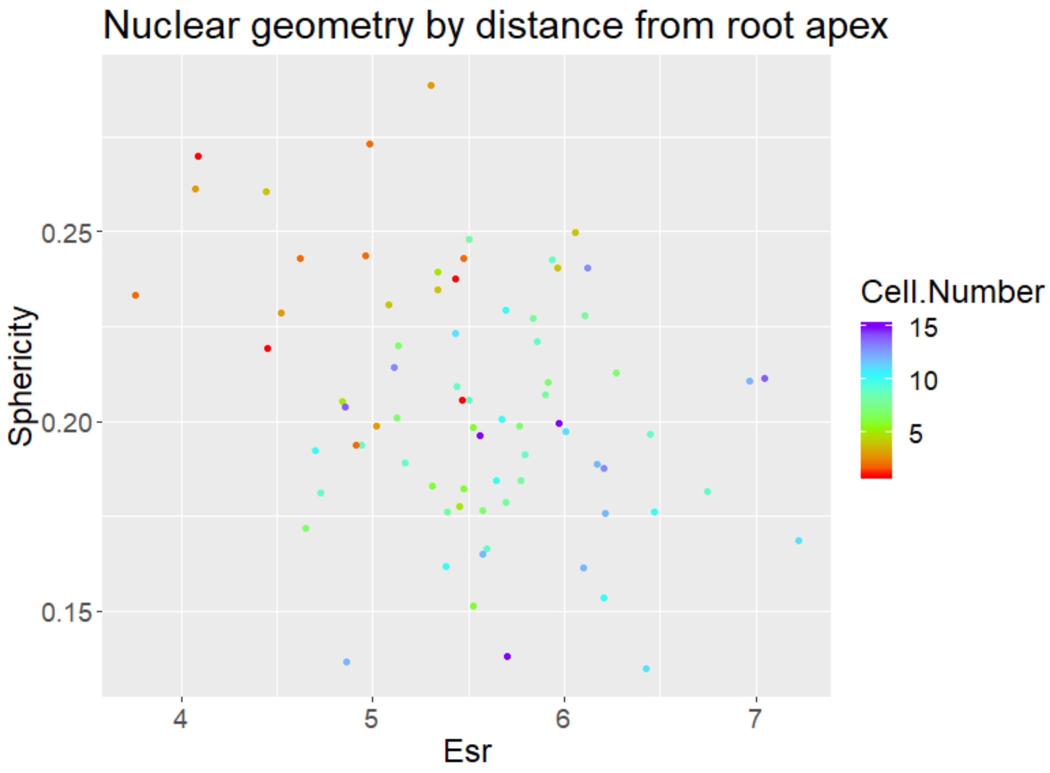

Figure 48.: The relationship between nuclear size and geometry in the root EZ.

6.2 MEASURING THE CALCIUM RESPONSE

6.2.1 *Methodology*

FRET

Transgenic Arabidopsis lines containing the Yellow Chameleon (YC3.6) calcium indicator [67] were kindly provided by Simon Gilroy (University of Wisconsin). The genetic modification allows seedlings to undergo fluorescence resonance energy transfer (FRET) in the presence of Ca^{2+}. This occurs through two connected molecules; CFP and a FRET-dependent YFP which fluoresce under excitation by cyan and yellow wavelengths respectively. Upon binding of Ca^{2+}, the marker undergoes a conformational change, bringing the two molecules closer together and allowing energy transfer from the donor (CFP) to the acceptor (YFP). Hence cells excited with an argon laser show an amplitude shift in the yellow channel in the presence of Ca^{2+}, with the FRET/CFP ratio providing a quantifiable measure of changes in calcium concentration.

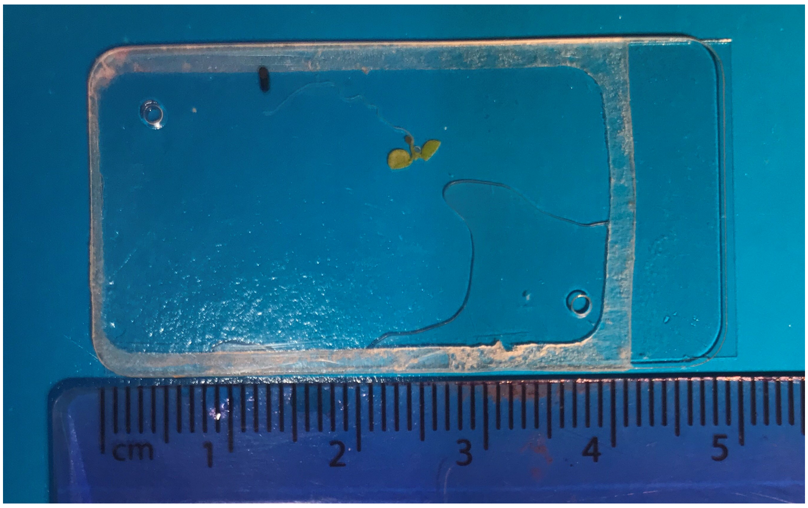

Figure 49.: The experimental setup.

The seeds were germinated on 0.5% Murashige and Skoog media (MS) with 1% (w/v) agar and grown for 7 days in an incubator. The seedlings were then mounted on a glass cover-slip and enclosed by a sealed 22mm x 40mm x 0.25mm chamber containing two filling ports, as seen in Figure. 49. For seedlings with larger cotyledons it was found beneficial to remove the green tissue to prevent contact with the chamber roof, and thus preventing imaging interference. The chamber was then partly filled with 0.16ml of 0.5% MS solution, consistent with the conditions of growth to minimize osmotic shock.

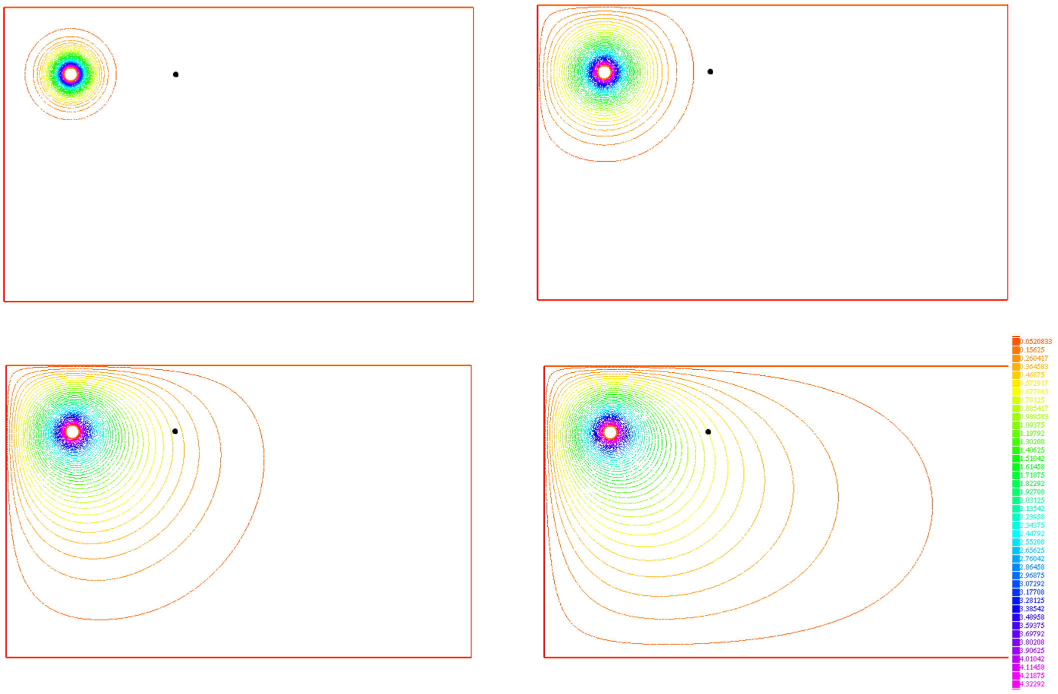

Figure 50.: Simulation results for the diffusion of the stimulus solution into the chamber produced using the FreeFem++ finite element software [48].

In these experiments we use Mastoparan (Mas), a peptide toxin from wasp venom, as a substitute for the Nod-factors released by Rhizobia, due to ease of accessibility. It has been shown in the literature that Mas elicits an effect analogous to Nod-factors [81] however Sun (2007) found that unlike Nod-factor, the Mas-induced calcium response is not restricted to the region associated with the nucleus.

A solution consisting of 0.02ml of mastoparan along with 0.02ml of rhodamine dye was made-up for addition during imaging. The dye is included here as a trace to determine the progress of the solution between the entry port and the root. The main challenge was to ensure that the root remained stationary during addition of the stimulus, a factor addressed with hindsight by the preparation of the slide. This is particularly important for experiments performed at higher resolutions as small perturbations can move the chosen cell out of the imaging frame. Another consideration was the time taken for the stimulus to reach the root and the actual concentration of mastoparan reaching the root when relying on diffusion alone. Both of these parameters can be determined using modelling, which was performed using the FreeFem++ finite element software [48]. Some results can be seen in Figure. 50, which shows a time series representing the diffusion of mastoparan into the chamber after being added to the entry port at $t = 0$. These simulations allow us to measure the concentration of mastoparan at the root apex (denoted by the black dot in the figures) at each time point, allowing us to estimate the time in which the stimuli threshold will be surpassed and hence the time at which we can expect a calcium response. This is particularly important in this type of imaging as prolonged exposure to the laser will cause unwanted photo-bleaching to both the acceptor and donor fluorophores of the FRET reporter. With confocal systems using multiple photo-multiplier tubes for image detection and several excitation lines, degradation of our reporter and the difficulty of efficiency calculations are important factors [17]. Managing this through using modelling to inform a precise experimental setup is therefore an advantage.

It was noted from modelling and initial experiments that the transport of the stimulus to the root was extremely slow when relying on diffusion alone. A variety of methods for were therefore tested for decreasing the transport time. These included forcing an advection using the pipette and using filter paper as a medium for which the stimulus solution could travel along. The delay between the stimulus being added to the system and reaching the root could however be beneficial, as any disturbance of the system caused by the stimuli addition had time to return to a steady state and any necessary repositioning of the frame could occur before any calcium response was to take place.

The root was imaged using the confocal microscope and the CFP reporter was excited with the 458 nm line of the argon laser. The CFP (473−505 nm),

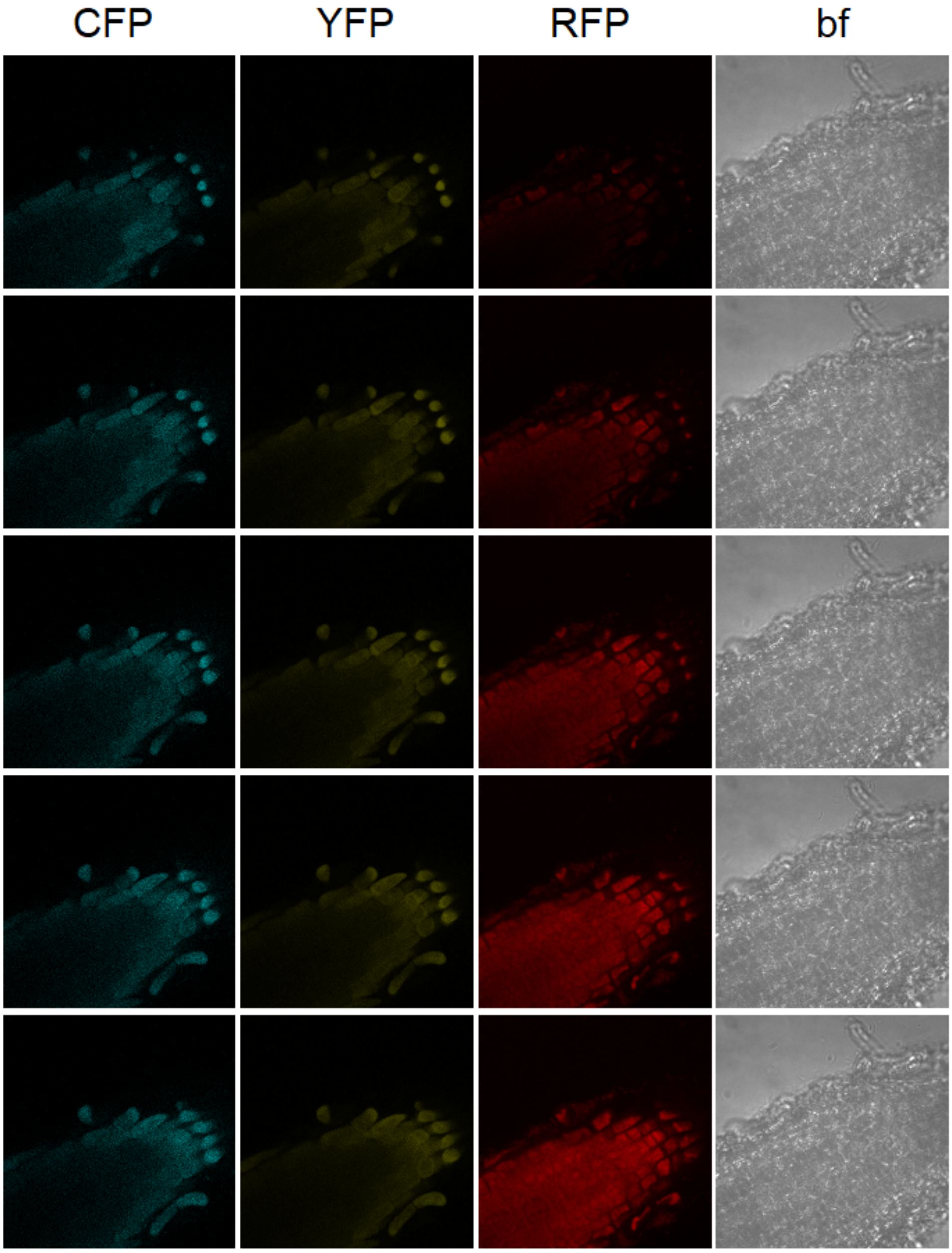

Figure 51.: Imaging of an Arabidopsis root over 4 channels: cyan, yellow, red, and bright-field (columns left to right), with each row corresponding to a subsequent time-step.

FRET-dependent venus (526–536 nm) and RFP (574–592 nm) emissions were acquired simultaneously along with bright-field images, showing the base activity, Ca^{2+} concentrations and the presence of rhodamine respectively. A time-series of images was taken, and can be seen in Figure. 51, during which the mastoparan/rhodamine solution was pipetted into the entry port closest to the root. Using our new experimental setup, it can be seen that minimal movement of the root between frames was achieved. We see changes in the RFP channel, third column from left in Figure. 51, as the rhodamine dye arrives at, and is taken up by, the plant.

GCAMP

Genetically encoded calcium indicator (GECI) Arabidopsis lines, kindly provided by Simon Gilroy (University of Wisconsin) and Marc Knight (University of Durham), were used for these experiments after encountering difficulties with signal strength using the Yellow Cameleon (YC3.7) indicator. In the presence of Ca^{2+} YC3.7 undergoes fluorescence resonance energy transfer (FRET) between two connected molecules; CFP and a FRET-dependent YFP. Upon binding of Ca^{2+}, the marker undergoes a structural change, bringing the two proteins closer together and allowing energy transfer from the donor (CFP) to the acceptor (YFP). As a result cells excited with an argon laser show an amplitude shift in the yellow channel [67]. GCaMP on the other hand are highly sensitive single fluorophore sensors in which the GFP is bound to Calmodulin and an M13 peptide. In the absence of Ca^{2+}, fluorescence is low however, upon the reversible binding of Ca^{2+} to the CaM domain GCAMP undergoes a conformational change which allows for rapid-deprotonation of the chromophore - the region responsible for colour - and hence a change from a low to a high fluorescent state [88]. The binding of GCAMP and Ca^{2+} has a k_d of around 330 nM, matching the concentration ranges we are looking for within the plant cell [33]. GCaMP also requires a less complicated microscope setup than FRET and provides an easier, high quality acquisition with a lower signal to noise ratio.

Post propagation and collection, GCaMP seeds were sterilised in 70% ethanol followed by 5% bleach and washed with deionised water 6 times before sowing onto plates of 0.5% Murashige and Skoog (MS) media adjusted to a pH of 5.7. They were stratified in 4 °C for 2 days before being grown in a controlled environment of 21 °C with a 16/8 hour day/night photoperiod. To allow the application of liquid stimuli to the seedling with limited mechanical disruption whilst maintaining favourable growth conditions, experiments were performed with the plant held in a specialised 3D printed 'FlowCell' device consisting of a main imaging chamber attached to a microfluidics system [72]. These experiments were run alongside collaborator Nicholas Redman (University of Nottingham) who designed the FlowCell. In the system, fluid is supplied from the right by gravity fed-syringes and output through an outlet to the left driven by a dual-flask vacuum pump. This device gives the advantage of allowing imaging over longer time periods than would have been possible on a standard coverslip setup as it allows for maintenance of the plants and prevents drying out. This is very important due to the long time-scales over which a response to mastoparan is sustained, requiring imaging to take place for up to an hour. Furthermore, it allows for more control over the chemical concentrations reaching the plant ensuring they are evenly applied unlike the alternative of using an agar block. The FlowCell design can be seen in Figure. 52a with a photograph of the real-life setup given in Figure. 52b.

A standard coverslip was sealed to the bottom of the FlowCell insert using vacuum grease and clamped into the adjustable holder. A seedling was mounted onto the flow cell with the upper part resting as depicted in Figure. 52a and the root placed on the coverslip in solution which was then covered by the lid containing a coverslip viewing window. With the system flowing at the desired rate, a time series of images was obtained using a Leica SP8 confocal microscope with a 488 nm argon laser for the GFP along with a bright-field image. A 5 minute period was recorded pre-stimulus application from which the base-level fluorescence could be obtained. At 5 minutes the flow cell syringe for the water was closed and the tube containing 50 μM Mastoparan was opened. It is known, from previous tests using a PM stain, that it takes approximately 1 minute for the new solution to reach

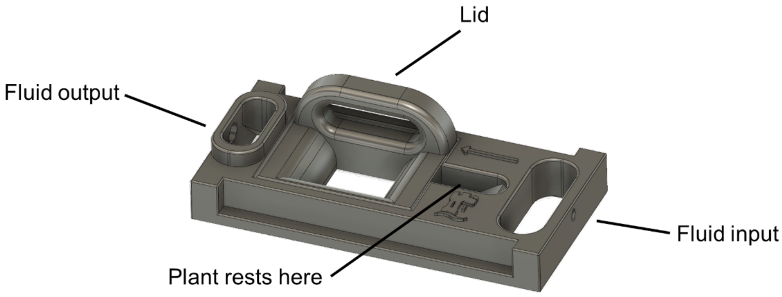

(a) Graphical render of the FlowCell.

(b) FlowCell set up mounted on the Leica SP8 confocal microscope.

Figure 52.: The FlowCell setup used in performing the experiments. Pictures provided by the designer/creator Nicolas Redman [72].

the imaging chamber. Once reached it is acknowledged that the maximum concentration does not reach the seedling immediately due to mixing with the water, however, due to the small chamber volume the concentration of mastoparan within quickly tends to that added. Further mathematical modelling could be performed to determine the exact concentration change in the flow cell chamber over time.

As, at this time, we are interested in the patterning of the response rather than quantitative values, changes in calcium concentration were determined qualitatively using the changes in fluorescence as a proxy. These changes were measured using the Fiji image analysis software [76]. In each nucleus sample the mean fluorescence was measured at each time point over 4 re-

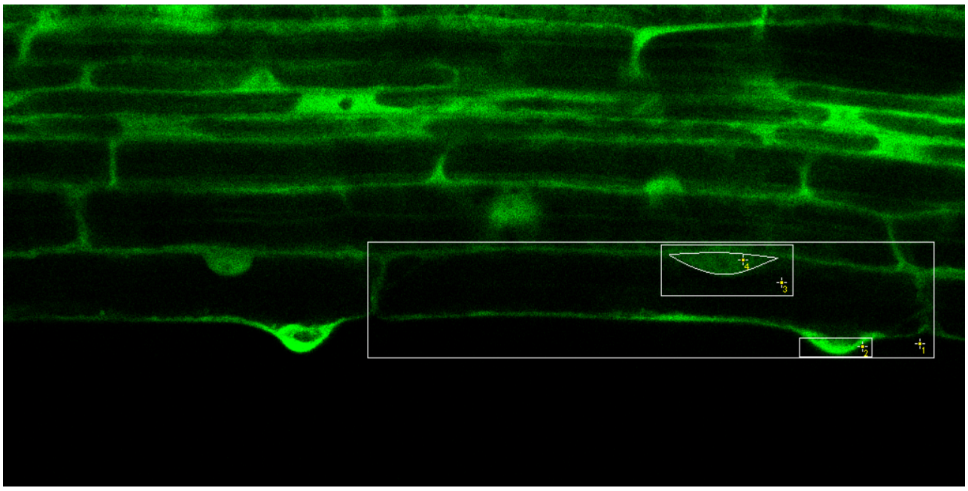

Figure 53.: ROI's used for measurements. (1) Whole Cell, (2) Root hair tip, (3) Nuclear Area, (4) Nucleus.

gions of interest (ROI): the whole cell, the nuclear area (the entire area which the nucleus moves between during the experiment), the root hair tip and the nucleus itself as represented in Figure. 53. For the latter a 'registration' technique was attempted in which the nucleus of interest would be moved to a common position throughout the time-series by movement and rotation of each full image. This would have allowed for bulk processing to calculate the fluorescence however, due to natural shape changes of the nucleus, the nuclear body could not be reliably located in each image by the software. Therefore the ROI was manually adjusted at each step following the movements of the nucleus between time-frames and cross-checking the nuclear outline with the corresponding bright field image.

6.2.2 *The Calcium response of Arabidopsis to Mastoparan in the root hair cell*

We present the recorded time-series data of the fluorescence intensity, $F(t)$, of 5 different root hair cell nuclei along with the results of 2 controls. The level of fluorescence between the different plants varies greatly due to diverse levels of expression of the genetically encoded sensor. The data must therefore be normalised before any intra-plant comparisons can be made. It must be noted that these re-scaling methods come at a cost of reducing variability in the data, however as we require comparison between sequences from different plants and cells it is impossible to do so with without some normalisation. As we are interested in the perturbations from the steady state of the system caused by the addition of mastoparan it is reasonable to measure these values against the fluorescence levels before application. This can be achieved by setting the initial value, $F(0)$, to unity, but to improve this estimate, and take into account the stochastic nature of the cell, we calculate the baseline value, I_0, from the average fluorescence achieved over the pre-stimulus period which here is the first 5 minutes of the time-lapse series. We therefore use the relative fluorescence variation:

$$\Delta F(t) = \frac{F(t) - I_0}{I_0}, \tag{266}$$

as used as standard in the reporting of calcium signals [73]. The normalisation can be further improved by calculating the 'Z-scores':

$$Z(t) = \frac{F(t) - I_0}{\sigma_0}, \tag{267}$$

which include a measure of the variability of the baseline fluorescence, σ_0, which is the standard deviation calculated, as for I_0, over the first 5 minutes recorded before stimuli addition. The advantage of this method of normalisation is a decrease in the sensitivity of the results to natural or stochastic changes in calcium.

Upon addition of the Mas stimulus, we observe large transient elevations of calcium concentration which are not present in controls. When compared between repeats however, it appears this response is not tightly regulated in Arabidopsis, with large variations in both spike intensity and frequency. This is contrary to results found in *M.truncatula* in the literature, where calcium oscillations in response to Mastoparan possess a relatively stable periodicity [39][83]. In Figure. 54a we see that 'Nucleus.1' has the closest to a periodic response however the amplitude of this response is quite small.

In Nuclei 2-5 there appears to be some evidence of two separate larger transients. To ascertain if this is the case, a moving average over 40 time-points was performed on each of the time series, optimising the smoothing of any

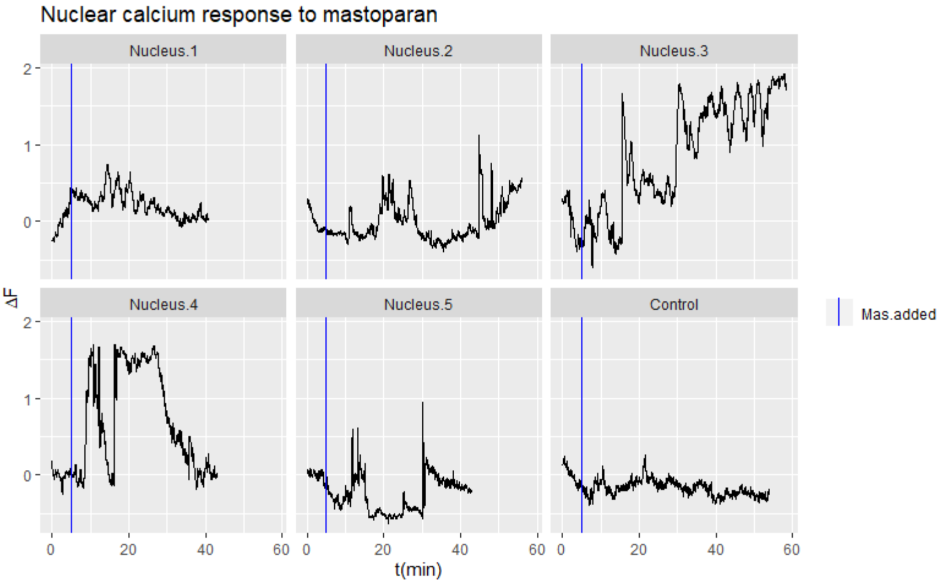

(a) Normalised florescence representing the calcium concentration in the nucleus of the root hair cell over time in response to Mastoparan.

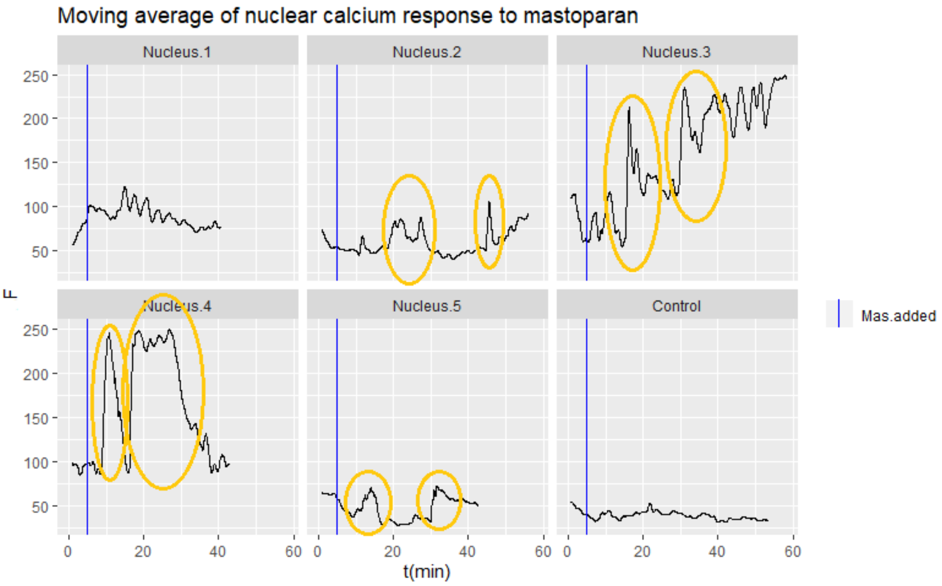

(b) The nuclear calcium response to Mas shown using a moving average over 40 time-points. Regions containing the two possible peaks are enclosed in yellow.

Figure 54.: The calcium response to Mastoparan in 5 nuclei.

noise and hence separating out any overall trends. These are shown in Figure. 54b, where the two distinct periods of calcium elevation in nuclei 2-5 are highlighted in yellow. However the time between these two periods of activity is not uniform between instances and the pattern is also not present in Nucleus 1. Using our data for the 4 different ROI's we can also consider the origin of the calcium signals. This comparison is illustrated in Figure. 55a

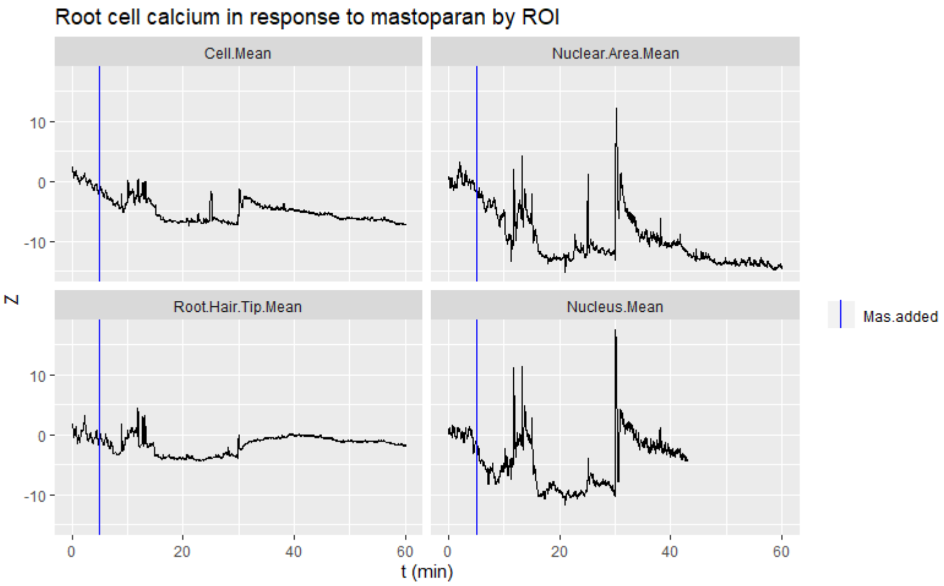

(a) Calcium response for Nucleus 5 measured over 4 ROI's corresponding to those described in Figure. 53.

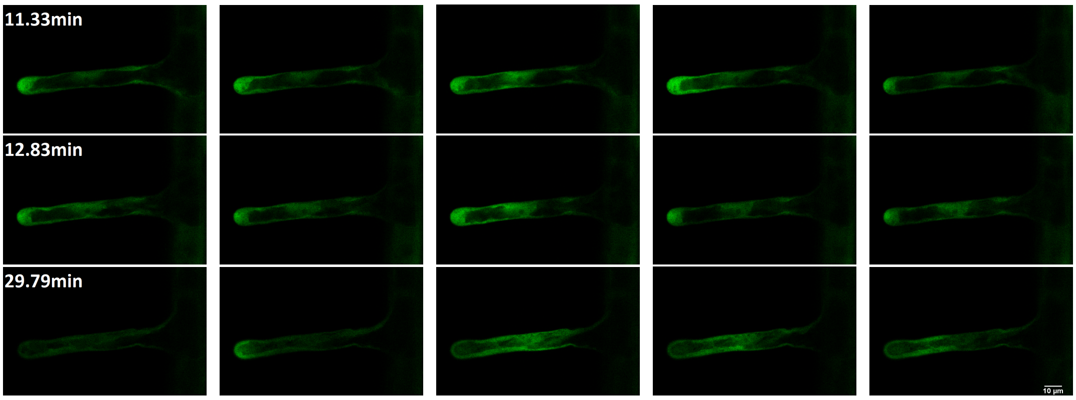

(b) A selection of imaging taken place across the 3 largest calcium spikes. In each row there is 11.61 seconds between each adjacent image.

Figure 55.: Results for nucleus 5 shown as time-series data, and selected images during spiking.

for nucleus 5, with analogous data for the other four instances, along with two controls, left Appendix C. Clearly the magnitude of the response in the nucleus/nuclear area is more significant than that averaged over the whole cell and root-hair tip. In all regions the shape of the signal is very similar although weaker outside of the nucleus suggesting the signal is generated in the nucleus and dissipates out to the rest of the cell as found previously in *M.truncatula* [81] and reproduced here in Figure. 9. Images taken over the period of the three largest calcium spikes, occurring at approximately 12, 13 and 30 minutes, are shown in Figure. 55b. We see a spike in the root hair at a similar time to that in the nucleus - although whether this is pre or post nuclear spike is inconsistent.

As the nuclear area and whole cell contain within them other ROI's, it is of benefit to compare only the nucleus and the root hair tip as two distinct regions of the root hair cell. Figure. 56a shows the calcium signals recorded in these two cellular regions for 6 different nuclei, including a control. In the control data we see that base level activity is very low in the nucleus but higher in the root hair tip with some spiking occurring, possibly signalling for elongation of the root hair. As discussed for nucleus 5, upon addition of mastoparan a similar spike pattern is observed in both regions with the nuclear case exhibiting a much greater change in amplitude and less noise. This can be seen in the boxplot in Figure. 56b which shows the control to have a similar levels of variability in both regions as compared to those with the mastoparan stimulus which in general possess an interquartile range (IQR) in the nucleus which is much greater than in the root hair tip. Although in some cases the signal in the root hair tip is a weaker analogue to that in the nucleus, nucleus 4 in particular, along with nucleus 3 to a lesser extent, exhibits quite distinct signals between regions suggesting that these two signals are, if not entirely independent due to diffusion through the nuclear pores, independent in their generation. The inconsistencies between repeats however perhaps highlights the lack of a tightly regulated calcium

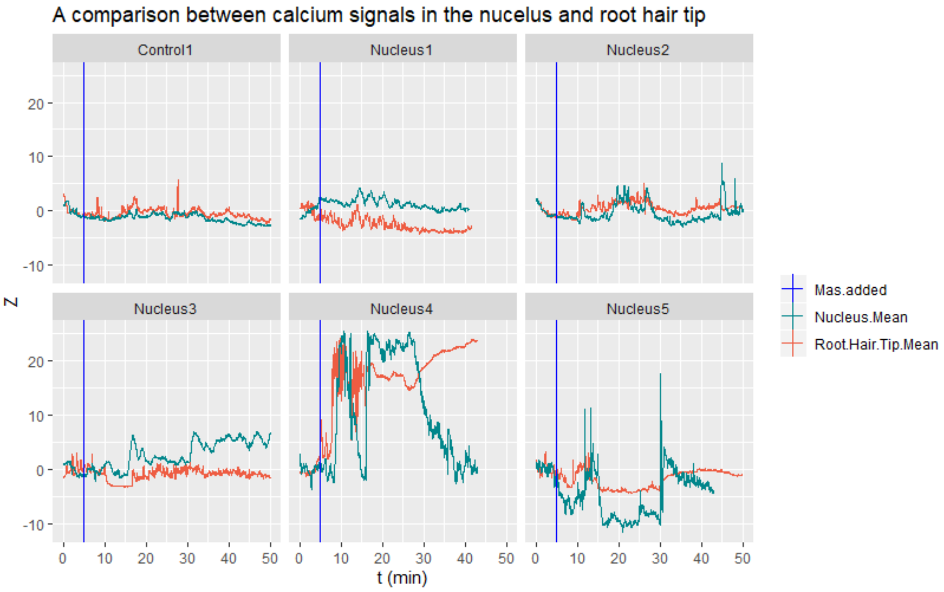

(a) Calcium signals in the root hair tip often follow a similar lower amplitude spiking pattern to that of the nucleus, but in other cases appear autonomous.

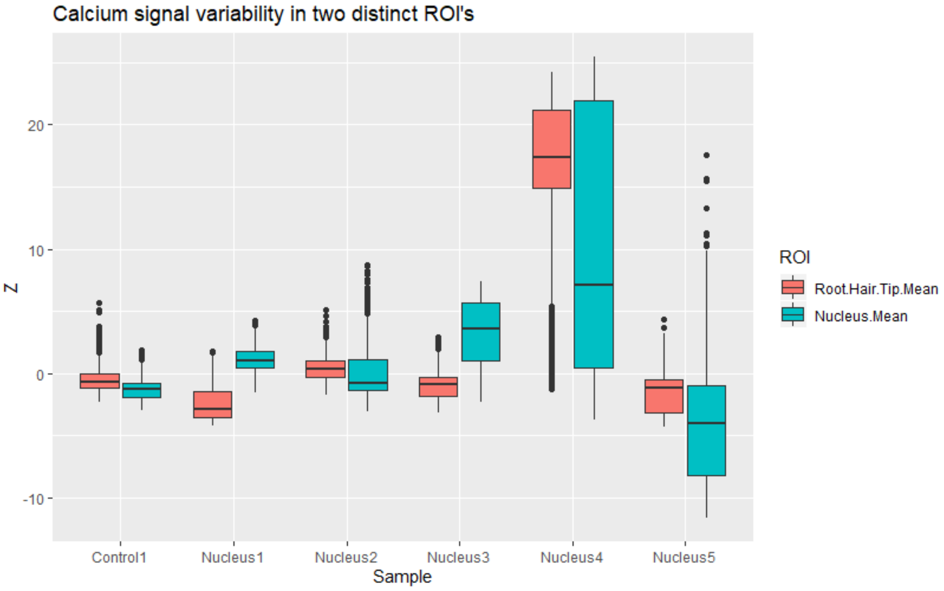

(b) [Ca^{2+}] has a larger distribution in the nucleus than in the root hair tip.

Figure 56.: Comparison between calcium signals in the root hair cells vs those in the nucleus upon addition of a mastoparan stimulus.

response to Mastoparan in Arabidopsis and so points towards a definite gap in any potential signalling pathway.

6.2.3 *The Calcium response of N.benthamiana to Mastoparan in the root hair cell*

In order to explore the difference in the nuclear calcium response between Arabidopsis and known fungal-symbiont *N.benthamiana*, the experiment of the previous section was repeated for this additional genus in order to observe the differences between the nuclear calcium signatures given a mastoparan stimulus. These GCaMP3 *N.benthamiana* seeds were kindly provided by Thomas DeFalco (University of Zurich) [33]. Our results show clear calcium activity as compared to controls, however in multiple attempts, 12 of which are shown in Figure. 57 as compared to 12 controls in Figure. 58, we were unable to consistently recreate the regular spiking described previously.

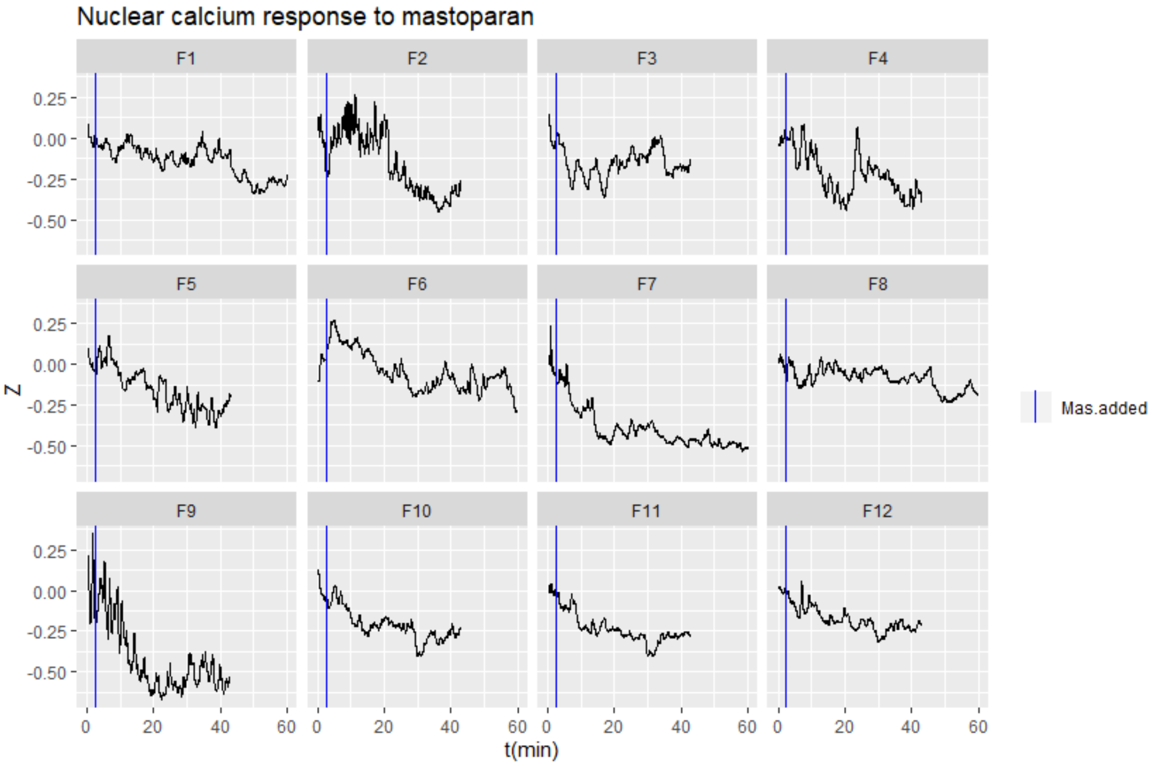

Figure 57.: Normalised fluorescence indicating the calcium concentration in 12 *N.benthamiana* seedlings in response to Mastoparan, added at $t = 2.5$mins as indicated by the vertical blue lines.

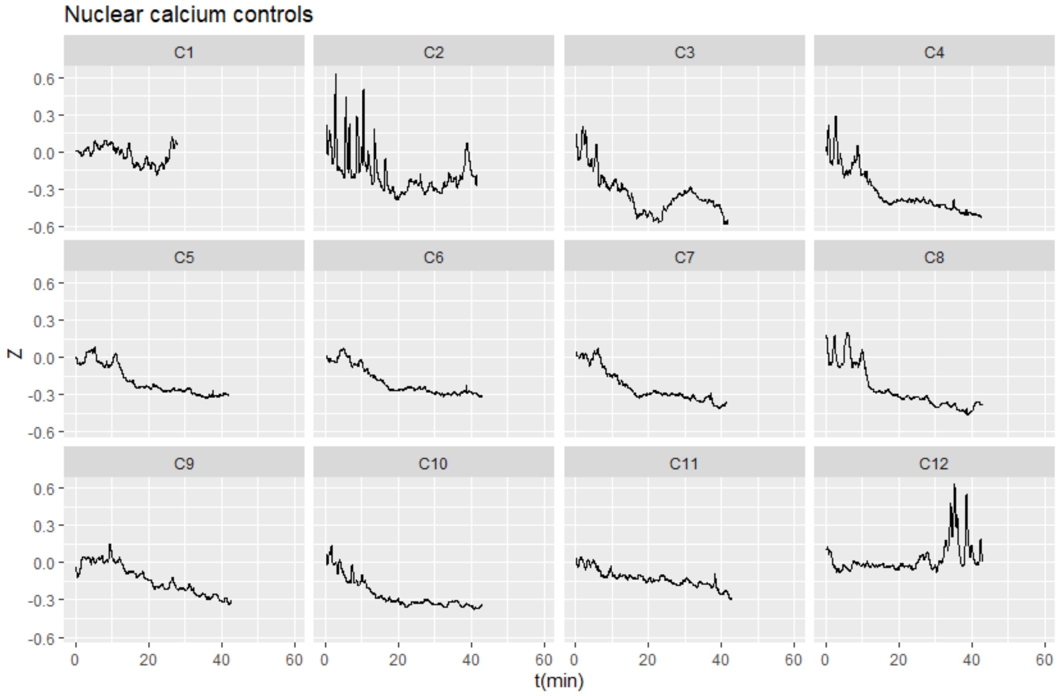

Figure 58.: Normalised control results showing the Ca^{2+} concentration in *N.benthamiana* seedlings placed in the FlowCell flowing with water.

The lack of regularity in the response of *N.benthamiana* to Mastoparan may be due to numerous factors such as it being a replacement for Nod-factors, the Mastoparan having being made into solution too long before use or disruption to the root when being placed in the chamber causing calcium signalling in itself and hence additional noise in the signal. The latter explanation may be furthur strengthened when noting that there appears to be nuclear calcium spiking at the beginning of many of the experiments in our controls. Control 2 in particular shows a high degree of spiking, with spikes perhaps more pronounced than any case with Mas addition, suggesting that nuclear spiking perhaps has a role in signalling mechanical stress. It is known that nuclear calcium spiking occurs in root development [58], however if this were the case here we would expect that to continue through the time-series, in contrast to controls 2,3,4,5,8 and 10 whose experiments begin with spiking and after about 10minutes exhibit very low activity levels. An exception to this is control 12, which shows two large spikes between 30 and 40 minutes.

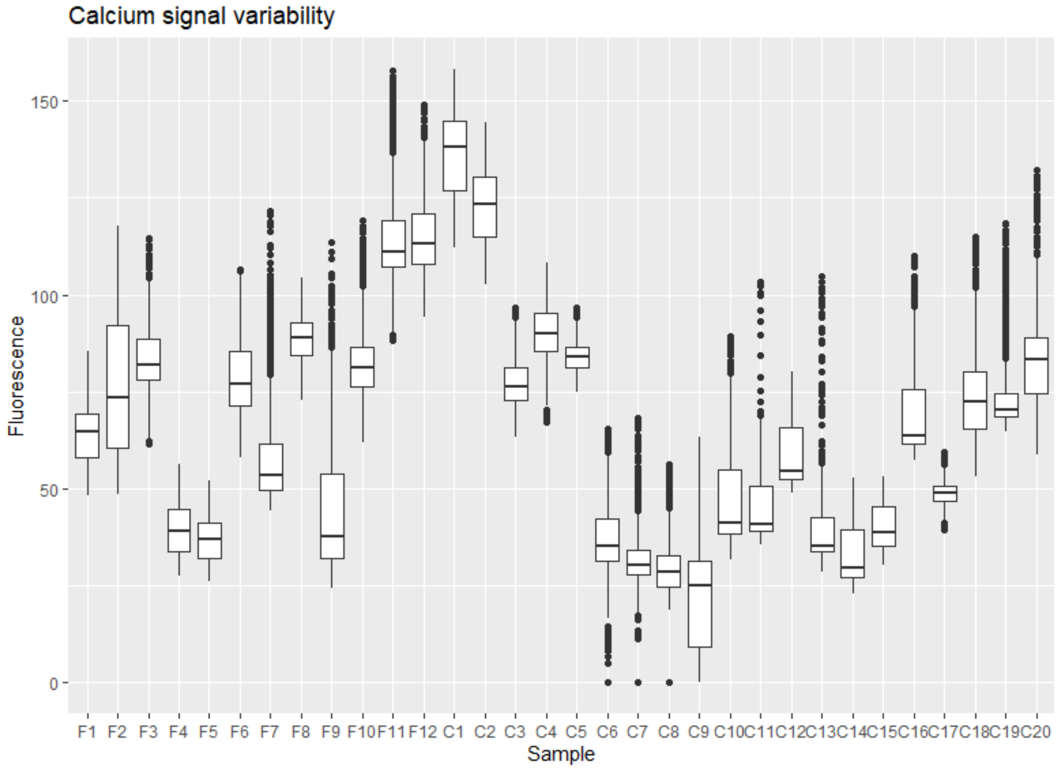

Figure 59.: Boxplots to show the mean and variance of the fluorescence in 12 nuclei in response to Mastoparan and 20 controls.

We compare the variability of the signals in Figure. 59 in an attempt to quantify the differences in the calcium levels that we observe visually between results and controls. We find that our results give a mean fluorescence of 85.76 as compared to 71.19 in controls, while the standard deviation of the fluorescence is 10.75 as compared to 8.40 in controls. Therefore we can infer that the calcium concentration in the nucleus is around 20% higher in the presence of Mastoparan, and around 28% more variable, provided there is a linear relationship between calcium concentration and fluorescence. From Figure. 59 it is also noticeable that the controls possess more anomalous values than our results. This could possible be because stochasticity is the predominant feature in the calcium profile without a stimulus, whereas, when responding to the mastoparan, the more regular spiking dominates over the random fluctuations.

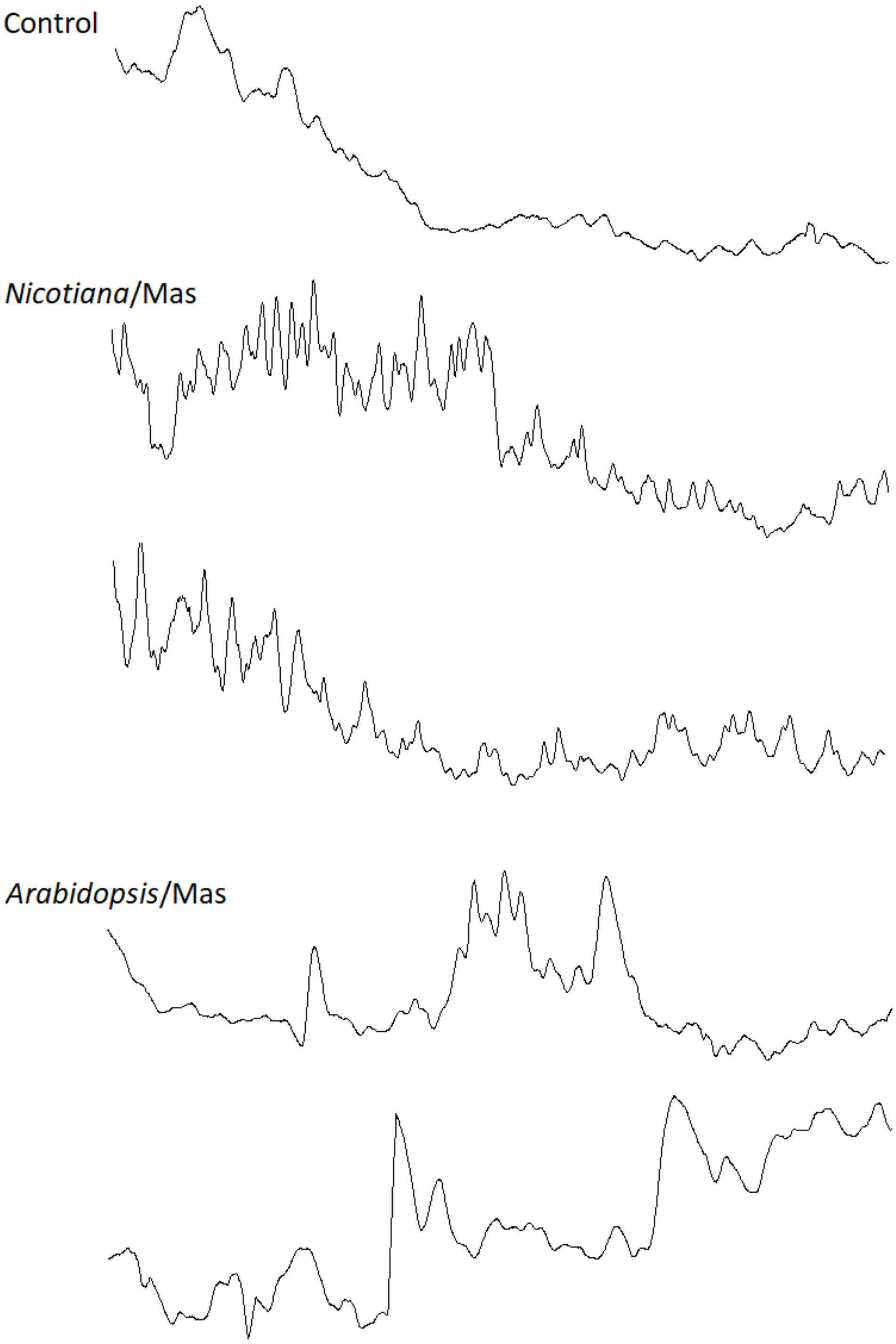

Figure 60.: A comparison between a control nuclear calcium signature with two from both *N.benthamiana* and Arabidopsis in response to Mastoparan.

In Figure. 60 we compare the nuclear calcium response of *N.benthamiana* to that in Arabidopsis. In the previous section we ascertained that Arabidopsis exhibits a nuclear calcium response to Mastoparan in the form of a low number of large-period (of around 5-minutes) spikes, within the hour-long experimental period. We see that in *N.benthamiana* however, the spikes are of higher frequency with a lower periodicity. This spiking concurs with the time frames reported in the literature of between 60 and 100 seconds, as discussed in Section 2.3.2. Arabidopsis has been shown to belong to the minority of plants that are unable to form even bacterial symbiosis due to the evolutionary loss of essential genes in the its lineage [35]. However, with gene transcription occurring downstream of the calcium signal, there must exist a loss of furthur components of the CSP in order for the nucleus not to generate the calcium signature as observed in *N.benthamiana*.

6.3 PARAMETER VALUES

Parameter	**Symbol**	**Value**	**Reference**
Diffusion Coefficient in the nucleoplasm	D_{nuc}	100 $\mu\text{m}^2\text{s}^{-1}$	[68] (T-cells)
		600 $\mu\text{m}^2\text{s}^{-1}$	[85] (Free diffusion)
		530 $\mu\text{m}^2\text{s}^{-1}$	[38] (Free diffusion)
		2-20 $\mu\text{m}^2\text{s}^{-1}$	[61]
		36 $\mu\text{m}^2\text{s}^{-1}$	[71]
Diffusion Coefficient in the PNS	D_{pns}	**100 $\mu\text{m}^2\text{s}^{-1}$**	[68] (ER)
Calcium channel current	I	0.005-0.02pA	[85]
		2pA	[55]
Nuclear Radius	a	6.5 μm	[15]
		8.0 μm	[61]
		4.5 μm	Experimental results
Nuclear semi-axial Radius (Spheroid only)	c	7.5 μm	[15]
Nuclear Volume	V_{nuc}	160 μm^3	[15] [44]
		170-2130 μm^3	[21] (From SA)
		385 μm^3	Experimental Results
Width of PNS	h	**50 nm**	[15] [50]
		30-50 nm	[63]
Width of NPC	l	29 nm	[61]
		9 nm	[62]
		5 nm	[40]
		105 nm	[63]
Density of NPC	S_{NPC}	50 μm^{-2}	[63]
Resting free Ca^{2+} concentration in nucleoplasm	$[Ca^{2+}]_{\text{nuc}}$	100-150 nm	[15]
		170 nm	[91]
		100 nm	[80]
Resting free Ca^{2+} concentration in PNS	$[Ca^{2+}]_{\text{pns}}$	100-1000 μM	[15]
		10 μM	[68]
		50-500 μM	[80] (Animal ER)
MCA8 pump rate	k_s	1 s^{-1}	[61]
		24.9 s^{-1}	[44]
Channel refractory period	τ	2-4 s	[61]
Max conductance of Ca^{2+} channel	$I_c^{\max}$	**2864 pS**	[44]
CAM binding threshold to Ca^{2+}	C_{th}	200 nM	[53]
		500 nM	[74]
CAM Kd	Kd_{CaM}	1200 nM	[53]

Table 1.: A record of all values found in the literature for our model parameters.

6.4 EXPERIMENTAL WORK SUMMARY

- The methodology, including the segmentation process, for measuring the geometry of the nucleus is described.
- Comparison of nuclear morphology between cortical and root hair cells showed statistically significant differences including that root hair nuclei are larger and flatter than those in the root cortex.
- The parameter values for the nuclear radius, a, and our spheroidal parameter, ξ_0, were obtained.
- An investigation into the changes in geometry along a cell file in the elongation zone showed that the larger the distance from the root apex the less spherical the nucleus.
- The development of an experimental set-up to measure the effect of various stimuli on the nuclear calcium concentration is described, including the use of two calcium indicators FRET and GCAMP, and the FlowCell.
- Arabidopsis showed a calcium response to Mastoparan which appears to originate in the nucleus.
- The nuclear calcium signal in response to Mastoparan was recreated in *N.benthamiana*.
- The remaining model parameters were collected from a search of the literature.

7

IN SILICO INVESTIGATIONS

Simulation results of our model are shown in this Chapter. In order to eludicate the mechanism of nuclear calcium signal generation in plants, we wish to use our model to replicate those signals measured experimentally. Successful reproduction of the calcium signature in silico allows us to create hypotheses on how the signal is formed, to then be tested experimentally. Here we focus on the distribution of channels across the membrane, firstly in two-dimensions where we show the effect of channel clustering on the spatial calcium pattern, and secondly in the full three-dimensions where we show that our model can reproduce the specific calcium spiking pattern, provided the channels are clustered. Finally we perform a parameter space analysis to determine the effect of each of the diffusion, geometric, pump and channel parameters.

7.1 2D SIMULATIONS

7.1.1 *The effect of channel distribution*

Simulations were run for two different channel distributions on the INM of a nucleus modelled as a 2-dimensional disc. In each case 11 channels in the half-disc were set to be open at $t = 0$, and a simulation was run over 120 time-steps. Figure. 61a shows the results for the channels at an equal distribution on the membrane. Here the influx profiles merge to create Ca^{2+}

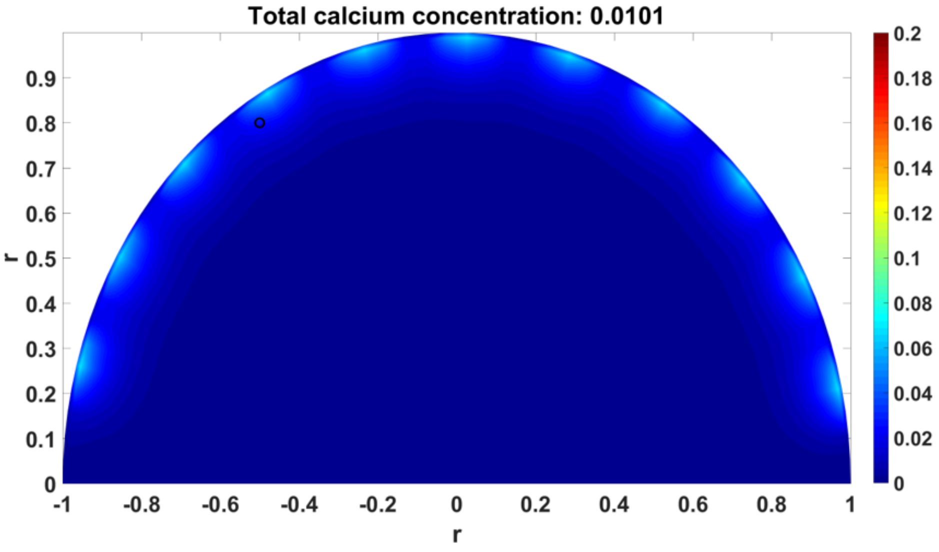

(a) Equally distributed channels.

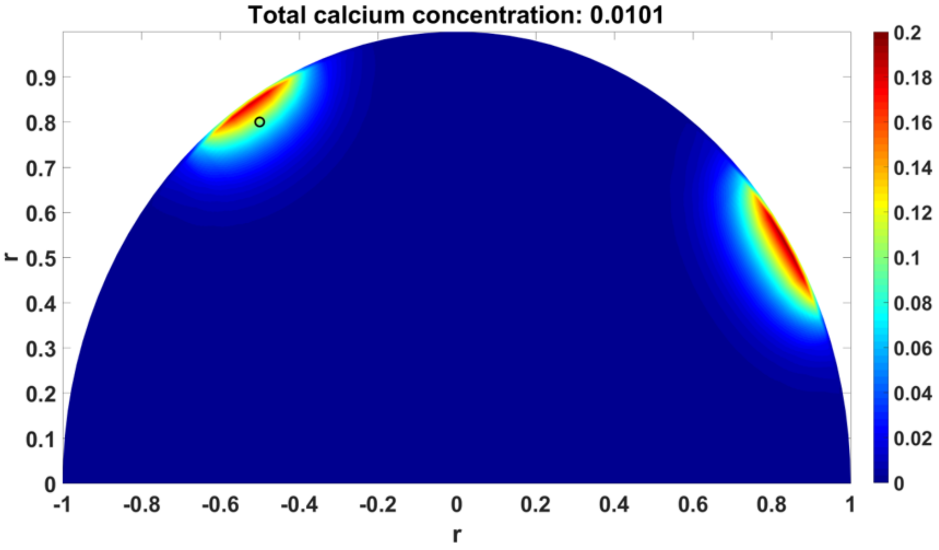

(b) Clustered channels.

Figure 61.: A figure to show the difference in the spatial Ca^{2+} profile for two different channel distributions. We see that, whilst the total calcium concentration is the same, for (a) equally distributed channels, local Ca^{2+} concentration remains low, however for (b) clustered channels, microdomains of high concentration can be formed.

waves moving towards the center of the nucleoplasm. In Figure. 61b, the channels are arranged in two clusters of 5 and 6 channels. Here much higher concentrations of calcium are achieved as a merging of the influx occurs within but not between clusters. We see that, even though the global calcium concentrations are equal, the local profiles are very different between cases, depending on channel proximity. This can have important implications on activation of the downstream signalling pathway which depends on the threshold and localisation of calcium sensory proteins. We let the black circles in Figure. 61 denote the presence of a Ca^{2+} sensory molecule, S, which binds calcium according to:

$$[Ca^{2+}][S] \underset{k_2}{\overset{k_1}{\rightleftharpoons}} [CaS]. \tag{268}$$

The dissociation constant:

$$K_\text{d} = \frac{k_2}{k_1}, \tag{269}$$

is the concentration of free Ca^{2+} at which 50% of the total sensory molecules are associated with calcium. A high K_d represents a low affinity sensory molecule as its dissociation reaction rate is relatively higher than its association rate and therefore requires a high calcium concentration for half-maximal binding. For example, a sensor S with a K_d of 0.1 μM would have its binding threshold surpassed in the case of clustered channels, however, for equally distributed channels the downstream signalling pathway would not be triggered.

7.2 3D SIMULATIONS

7.2.1 *The effect of channel distribution*

We wish to explore the effect that channel configuration has on the generation of the nuclear calcium signature in the symbiosis signalling pathway. To achieve this we create a set of two opposing channel distributions. In both cases we wish for the pumps to be equally distributed across the surface however, except for a few specific numbers - the five special cases/platonic solids - this is not possible to achieve exactly [2]. Therefore, to determine pump positioning, we employ the 'Regular equidistribution' method of Deserno (2004). In this algorithm circles of latitude are drawn at constant intervals on which equidistant points are chosen in a manner such that the distance between the points on the circle, d_ϕ, is approximately equal to the distance between circles, d_θ, giving an average area per point of $d_\phi d_\theta$ [36]. Figure. 62 shows the chosen mesh-points for our pumps and channels to be used in the simulations. In the equally distributed case, channel distribution was also determined by the regular equidistribution method described, whereas the clustered channels were determined manually ensuring that they were not immediately adjacent to a pump.

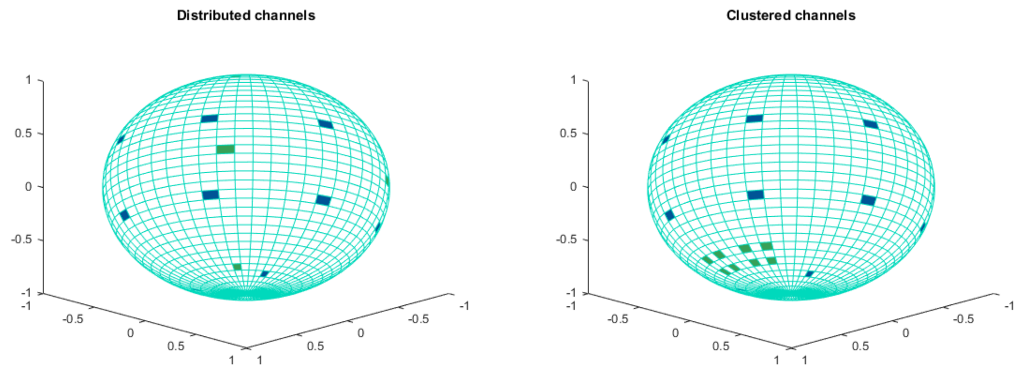

(a) Equally distributed channels.

(b) Clustered channels.

Figure 62.: Pump (blue) and channel (green) distributions used in the simulations, with 20 equally distributed pumps and 8 (a) equally distributed/ (b) clustered channels.

Akin to the findings in two-dimensions, simulations showed small elevations in concentration at channel sites in the equally distributed case and for clustered channels a domain of much greater concentration increase due to the cumulative effect of merging the distinct fluxes. This can be seen in Figure. 63 which shows the concentration profiles on the surface of the nucleoplasm just below the INM, 7 minutes after stimulus application.

In three-dimensions we are also able to observe additional, more sophisticated dynamics, and we find that oscillations in calcium concentration can

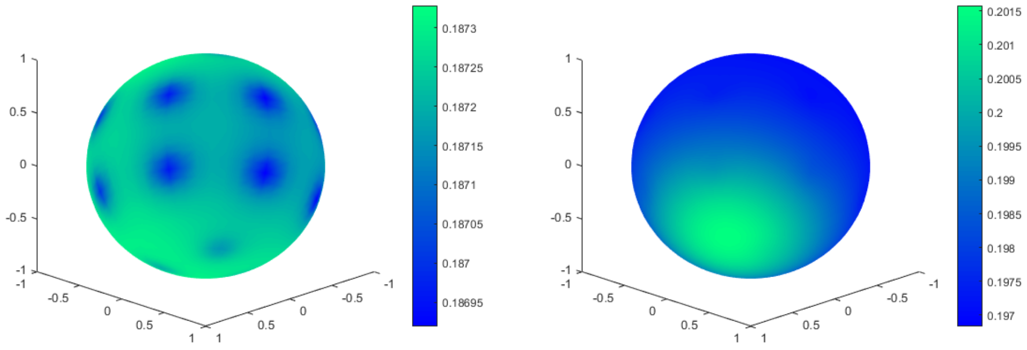

(a) Equally distributed channels.

(b) Clustered channels.

Figure 63.: The calcium concentration profile at the periphery of the nucleoplasm ($r = 4.5$ nm) at $t = 7$min for parameter values highlighted in Table 1

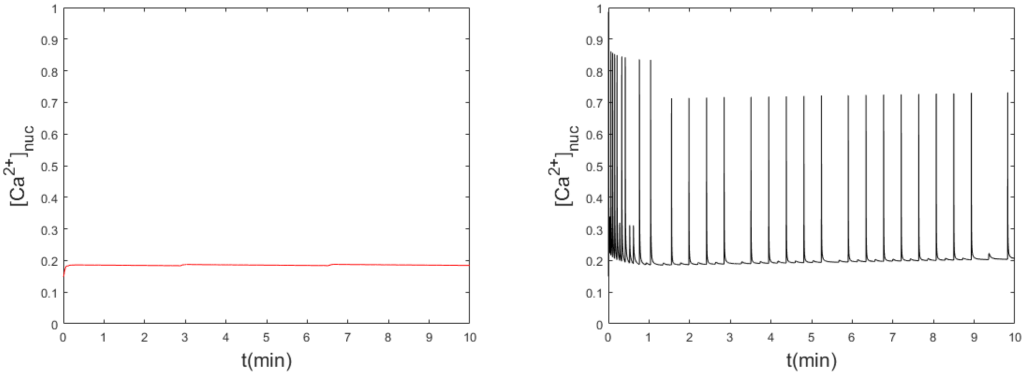

(a) Equally distributed channels.

(b) Clustered channels.

Figure 64.: The time series of the calcium concentration (in μm) at the same point $(r, \theta, \phi) = (0.9153, 2.5777, 2.6928)$ inside the nucleoplasm for each of the channel configurations.

be reproduced only if channel clustering is present. This is a very important finding as it not only reveals how channels must be positioned on the INM but also gives suggestion of a method by which plant cells are able to control signalling. It is possible that, on perception of a signal, channels may be relocated to a particular site on the dynamic nuclear membrane. As discussed in Section 2, experimental results have shown that the nuclear calcium signature typically involves around six initial fast spikes followed by slower oscillations of a magnitude of around 500 nm and a 0.7min^{-1} periodicity [39] [26]. This pattern is autonomously and accurately reproduced by our model, with the only input being an initial signal designed to replicate initiation from an upstream messenger. The resulting time-series of calcium concentrations in both distributed and clustered channels can be seen in Figure. 64.

As well as being necessary for the initiation and maintenance of oscillations, clustering is also required if nuclear calcium concentration is to surpass the dissociation constants (K_d's) of two of the three EF hands of CCaMK. That is, given the parameters measured experimentally, concentrations cannot elevate high enough to trigger the downstream signalling cascade unless the aggregating effect of clustering is present (Figure. 65). At basal concentrations in the nuceloplasm, EF3, which has a K_d of less than 20 nm, is always

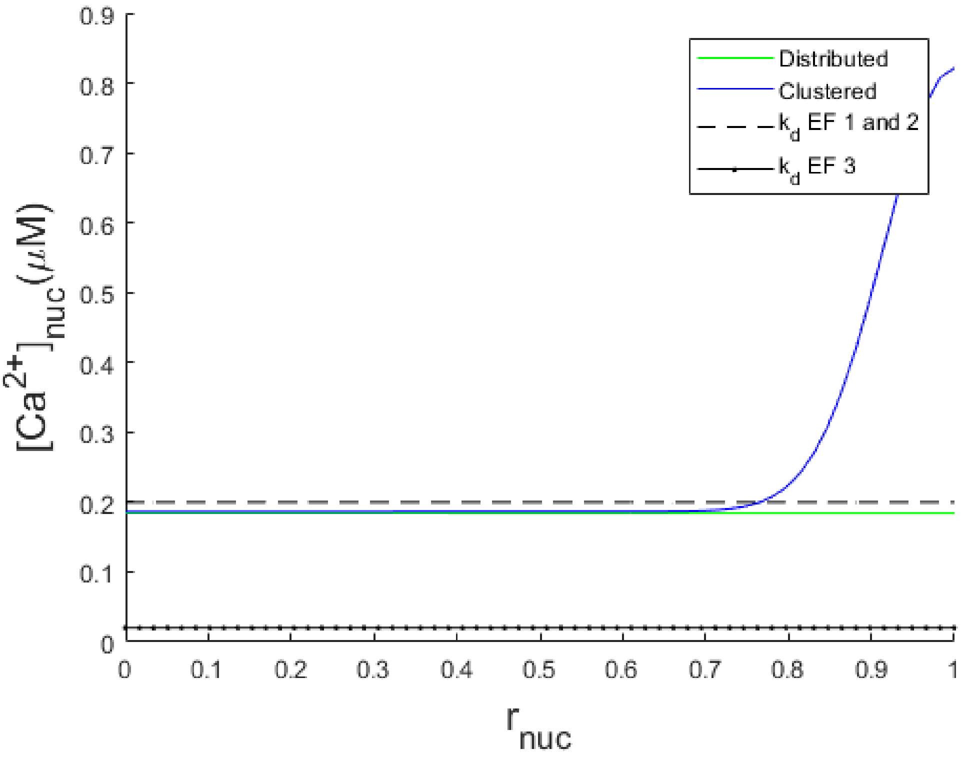

Figure 65.: A comparison between calcium concentrations achieved in the nucleoplasm and the binding affinities of CCaMK shows that channel clustering is necessary to surpass the dissociation constant of the key binding domains.

occupied, however the lower affinity EF1 and EF2 require increased calcium levels. Dissociation constants for these domains have been measured by Swainsbury (2012) to be in the region of 200 nm and hence are reasonably well matched for the interpretation of calcium oscillations [84].

Another important observation is the formation of a micro-domain over which spiking occurs. Figure. 65 shows that there exists a small area around the channel cluster ($r_{\text{nuc}} \in [\sim 0.75, 1]$) in which calcium levels are high, whilst outside this region concentrations remain lower. This increase is seen transiently during calcium oscillations, with Figure. 65 given at a time point coinciding with the oscillation peak, whereas outside this domain concentrations remain relatively constant. It is known that the nuclear interior is also far from homogeneous and consists of sub-compartments which undergo dramatic reorganisation in response to environmental cues. The finding that signals are contained close to the nuclear periphery is therefore in accordance with the dynamic nature of the nucleus and the accepted role of chromatin-NE association in animal cells as an important regulatory tool of gene expression [77]. This is an relatively unexplored area in plants however initial findings, such as the movement of the chlorophyll binding protein from the interior of the nucleus in response to light [42] "shows convincingly that ... gene re-positioning has biological significant in plants" [64]. The phenomenon of micro-domain formation indicated by our results also supports this theory, with our findings also highlighting that this can occur by cluster formation on the INM to coincide with the site of sensory molecule localisation.

Finally, it is important to note that the mathematical formulation of this model give us insights into the channel and pump dynamics as well as their positioning. Previous models have required an added feature, such as a refractory period, in order to observe spiking [21]. We also saw in Section 4.3 that in one dimension the same model led to a steady state only. The mechanism used here relies on CICR, where firing depends on the concentration of calcium at the channel. Channel firing is able to cease automatically here through 'termination by depletion' where the channel does not fire due to the micro-domain of low calcium concentration in the store immediately adjacent to the channel, keeping the channel below its firing threshold. In this scenario, the 'refractory period' occurs naturally, and its length is dependent upon parameters such as the diffusion coefficient and the channel release rate as we shall see from our stability analysis in the next section.

7.2.2 *Parameter space analysis*

In this section we look at the effect of varying all of our model parameters to gain an insight into the sensitivity of our model to parameter fluctuations. For some parameters we have reliable measurements from the data and hence we will look at these with a view to testing the stability of our solutions. For others we have a general idea of their measurements but there may, for example, exist large inconsistencies across published values. In this case it is particularly interesting to observe if the calcium patterns remain stable across the range of values indicated in the literature.

Diffusion parameters

Here we look at the nuclear radius, a, the diffusion coefficient in the nucleus, D_{nuc}, and the diffusion coefficient in the peri-nuclear space, D_{pns}. These appear in our equations within the normalised diffusion parameters due to the way in which the system is normalised to a unit radius (see Section 4.1.1). During this normalisation we set:

$$\begin{aligned}\widehat{D}_{\text{nuc}} &= \frac{D_{\text{nuc}}}{a^2},\\ \widehat{D}_{\text{pns}} &= \frac{D_{\text{pns}}}{a^2},\end{aligned} \tag{270}$$

and hence a simply scales both diffusion coefficients by the true radius of the nucleus, whilst to change the ratio of the diffusion coefficients, D_{nuc} or D_{pns} must be varied individually.

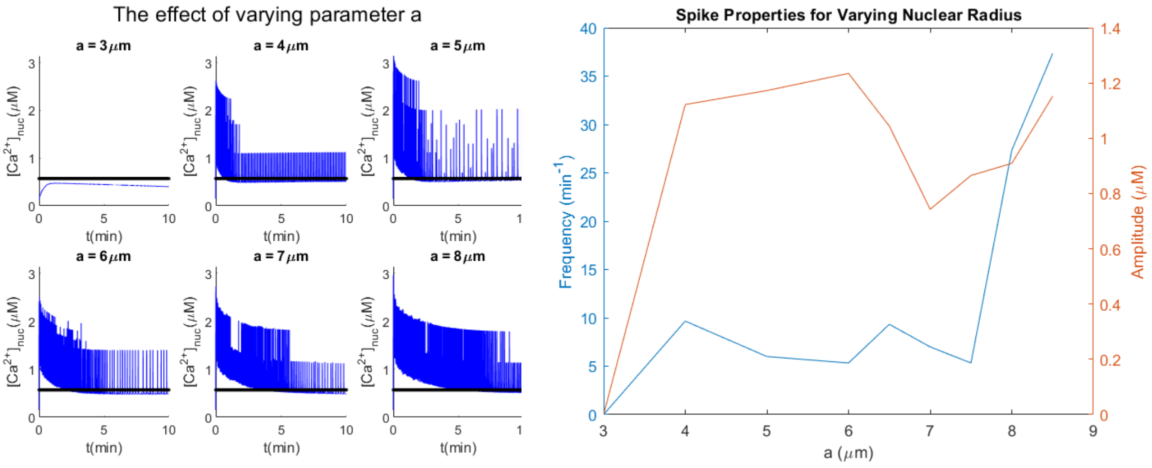

(a)

(b)

Figure 66.: The effect of the nuclear radius a) seen for a single point in the micro-domain and b) quantified by the oscillation amplitude and frequency.

Figure. 66 shows the effect of varying the nuclear radius, with spiking present provided the radius is above 3.5 μm. Interestingly, this value is very close to the lower bound of radius of the root hair cell nuclei measured in Section 6, whilst cortical cell nuclei can be much smaller. We observe that the frequency increases greatly for a radius over 7.5 μm, whilst the amplitude has a minimum at 7.0 μm. In this case, measures of frequency and amplitude may not accurately describe the full picture of the spiking, as the radius also appears to also have an effect on patterning. Rather than generating spikes of a constant amplitude and frequency, which we will observe throughout this section, more complex patterns of small and-large amplitude spikes are produced in various combinations. It would therefore be interesting to compare the spike patterns with experimental data for *N.benthamiana* nuclei at varying stages of development.

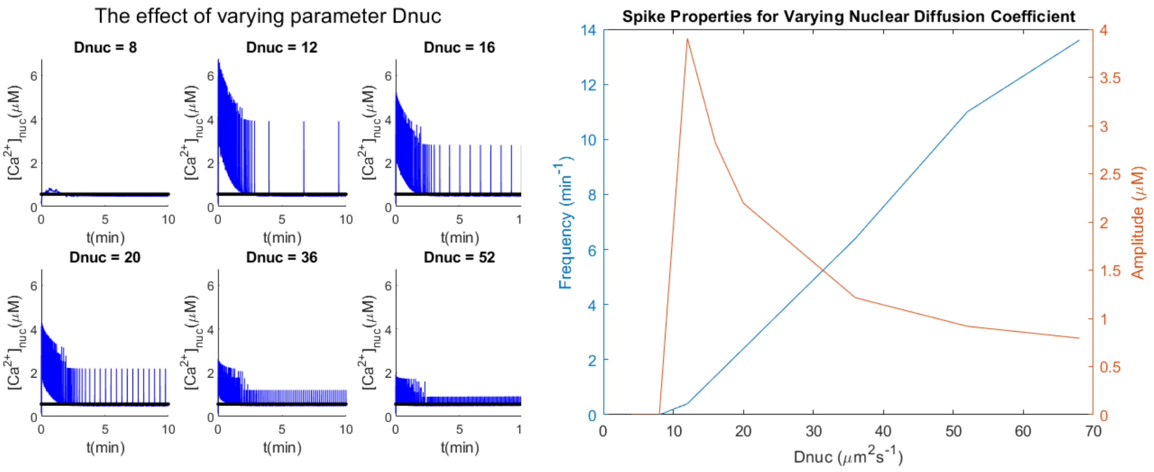

(a)

(b)

Figure 67.: The effect of the nuclear diffusion coefficient a) seen for a single point in the micro-domain and b) quantified by the oscillation amplitude and frequency. There is clearly a positive/negative correlation between D_{nuc} and the frequency/amplitude.

In Figure. 67 we see a clear effect of varying the diffusion coefficient in the nucleoplasm, with our model appearing to be quite sensitive to this parameter. An increase in D_{nuc} results in an increased frequency and decreased amplitude of spiking. Upon spiking, in order for a channel to produce a subsequent spike, enough calcium must be re-sequestered into the store to surpass the firing threshold of the channel. When the diffusion coefficient in the nucleoplasm is lower, it takes longer for the calcium to be dispersed from the channel microdomain and hence to reach a pump and be returned to the store. This explains why there is a longer period between spikes for a lower nuclear diffusion coefficient.

For the diffusion coefficient in the PNS we again see a clear relationship between the parameter value and the frequency/amplitude of spikes. Figure. 68 shows that, in general, as D_{pns} increases, the oscillation frequency decreases whilst the amplitude increases. Initially this appears puzzling as we may expect that a larger diffusion coefficient would mean an increase in spike frequency due to the shorter time taken for the calcium to reach the

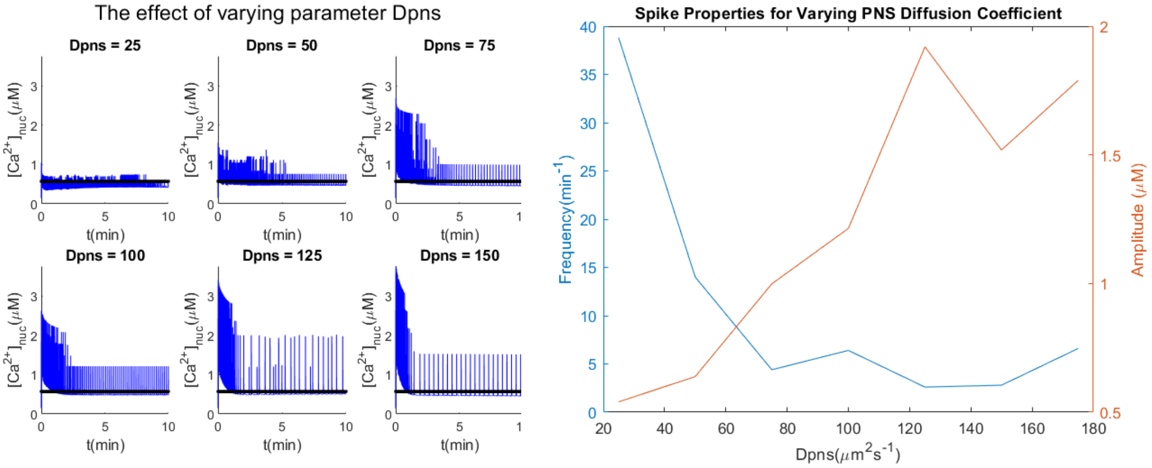

(a) (b)

Figure 68.: The effect of the luminar diffusion coefficient a) seen for a single point in the micro-domain and b) quantified by the oscillation amplitude and frequency. We observe a negative/positive correlation between D_{pns} and the frequency/amplitude.

channel, in the same way that increasing D_{nuc} increases frequency due to the shorter time taken for calcium to reach the pump. However, if we recall that the PNS is extremely thin, it is understood that the calcium diffuses through the entire PNS much more quickly and therefore the calcium actually disperses away from the channel faster. This results in lower frequency spiking as more calcium then needs to be pumped into the PNS to fill the compartment sufficiently to surpass the channel concentration threshold. This simulation was performed using a channel cluster as far away as possible from any pump. To confirm this hypothesis we would therefore expect the effect of varying D_{pns} to be amplified if the channel was closer to a pump.

Channel parameters

The parameters controlling the channel dynamics include the threshold of the step function, KA_c, the channel release rate, g, and the number of channels in the cluster, N_c. Figure. 69 shows the effect of varying the concentration of calcium required for CICR of the channel. A key observation, unique to this parameter, is that a lower KA_c results in a higher base calcium concentration in the nucleoplasm. This is likely due to the fact that less calcium will be required to be returned to the PNS in order for the channel to fire again, and hence the channel fires with a higher calcium concentration remaining in the nucelolar compartment. As a result of this, we see that a higher KA_c correlates to a lower amplitude. The frequency on the other hand peaks for $KA_c = 298\ \mu M$ and the nuclear Ca^{2+} concentration decreases towards a steady state once the channel threshold is sufficiently above the PNS concentration, preventing channel activation. It is also interesting to note that an KA_c of 300 μM does not exhibit the characteristic fast spikes at the beginning as in other cases.

Similarly to the effect we saw in the case of D_{nuc}, g shows a clear trend with spiking amplitude increasing and frequency decreasing as g increases. In Figure. 70b we see that there is a positive, linear relationship between spike amplitude and g, whilst the frequency decays exponentially. As covered

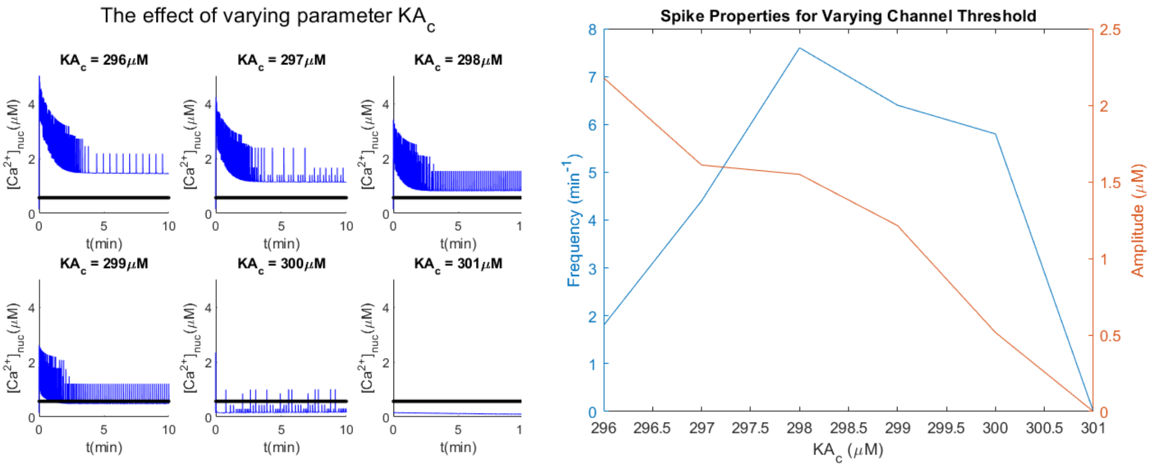

(a) (b)

Figure 69.: The effect of the channel threshold a) seen for a single point in the microdomain and b) quantified by the oscillation amplitude and frequency. We find there is negative correlation between the KA_c and amplitude. The frequency however increases with increasing KA_c until it reaches a peak and then decreases until no oscillations are observed.

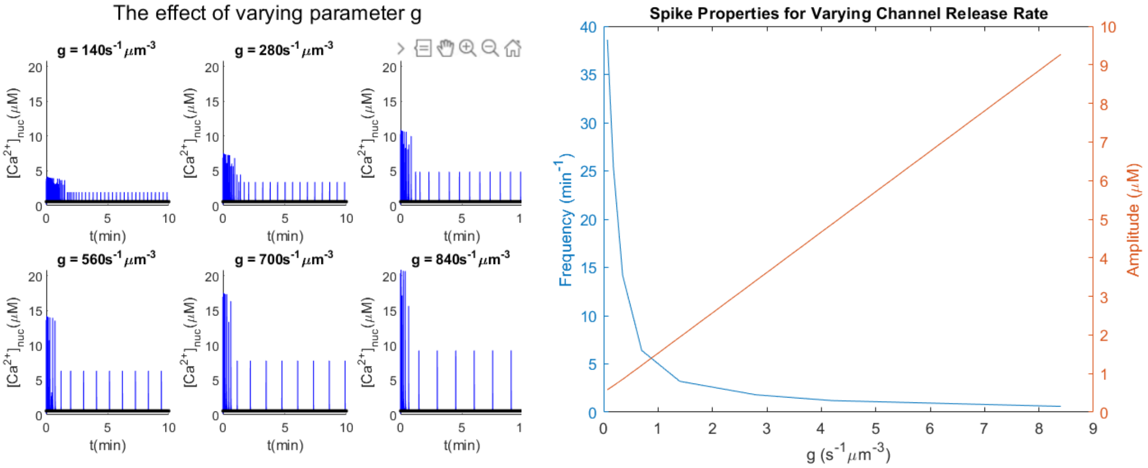

(a) (b)

Figure 70.: The effect of the channel release rate a) seen for a single point in the microdomain and b) quantified by the oscillation amplitude and frequency. We find there is positive linear correlation between the release rate and amplitude and an negative exponential correlation between g and frequency.

previously, the inverse relationship between amplitude and frequency is to be expected as a larger spike will require a longer interval to refill the Ca^{2+} store. It also offers a straightforward explanation as a larger injection of calcium from the channel directly results in a larger spike. The system is highly robust to changes in release rate as, although the effects of variation are clear, the parameter values explored a range over two orders of magnitude.

The number of channels presents unexpected results in that we may have expected that more channels would have a similar effect to increasing the channel release rate. This would however assume that the channels fire simultaneously. Observing the simulation in 3-dimensions shows us that this is not the case for all channel configurations, and in fact it is often a single channel in the cluster which fires at a single point time. In Appendix. C, Figure. 86 illustrates how for 5 channels, the firing channel is different each time, causing the non-uniformity we see in the spikes in Figure. 71a, whereas for 7 channels the same channel is activated each time resulting

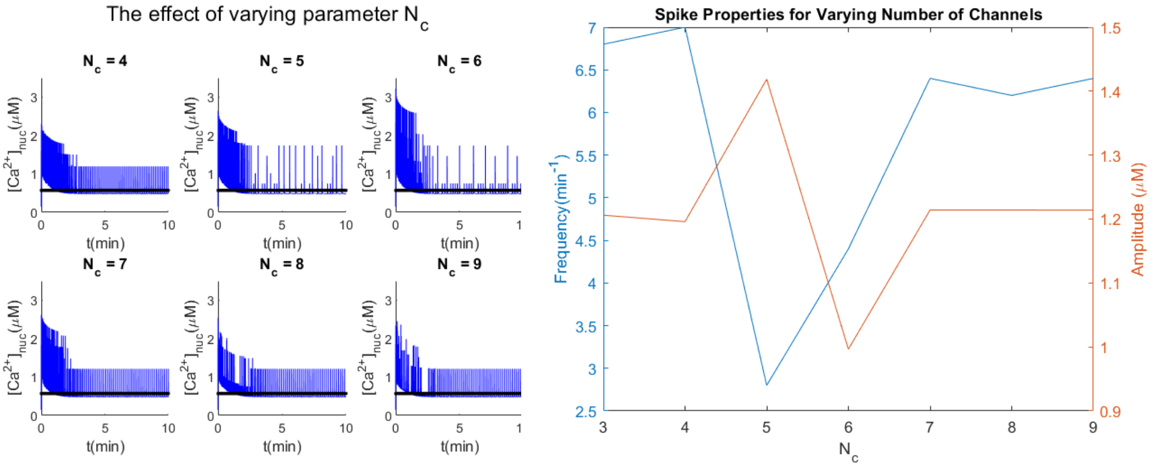

(a) (b)

Figure 71.: The effect of the number of channels a) seen for a single point in the micro-domain and b) quantified by the oscillation amplitude and frequency. We see no clear trend between the oscillation characteristics and N_c except that the resulting calcium pattern is similar in all cases except for $N_c = 5$ and $N_c 6$.

in regular spiking. This leads us to pose questions about the intra-cluster channel dynamics which are left as recommendations for further work. This would ideally include imaging of the INM to observe the precise arrangement of the channels within the cluster.

Pump parameters

Our pump parameters comprise of those responsible for the pump dynamics consisting of; the calcium concentration required for 50% activation of the pump, KA_p; the maximal pump current, I_p^{max}; the Hill coefficient, np; and the number of pumps equally distributed over the nuclear envelope, N_p. We see firstly, in Figure. 72 (paying attention to the very small range of the y-axes in Figure. 72b) that the KA_p has no effect on the frequency or amplitude of oscillations, and only a very small effect on the patterning. This could be due to the pump being close enough to the channel cluster to experience high Ca^{2+} concentrations within the micro-domain and hence is always working to maximum capacity. It may be that the calcium concentrations required for activation are higher than those used in our simulation.

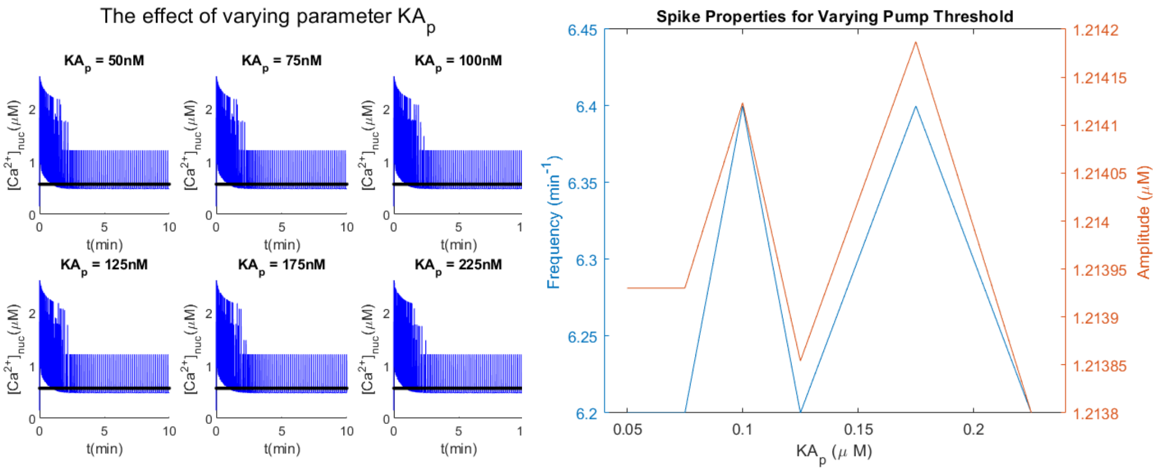

(a)

(b)

Figure 72.: The effect of the pump 50% activation threshold a) seen for a single point in the micro-domain and b) quantified by the oscillation amplitude and frequency. There is little to no effect on spiking when varying the KA_p.

However as it is dangerous to the cell for concentrations to greatly surpass the basal concentration of 0.15 μM for extended periods of time, an KA_p of 0.25 μM would seem a reasonable level for calcium to be pumped out at 50% capacity.

A more pronounced effect in exhibited in Figure. 73 however, where we see that a low pump current leads to a steady state solution that is below the binding threshold of calmodulin. This is likely due to too small of a calcium concentration being pumped into the PNS near the micro-domain, allowing time for the calcium to diffuse away from the micro-domain and prevent the pump/channel cycle of spiking. As the pump current increases we see that the amplitude of oscillations remains stable but the frequency of these oscillations is increased, clearly due to a larger concentration of calcium being returned to the store resulting in a shorter time taken to reach the channel firing threshold. The pump parameter which shows the most pronounced and consistent variation in its spike properties is the number of pumps distributed over the INM. Figure. 74 shows that for a very low

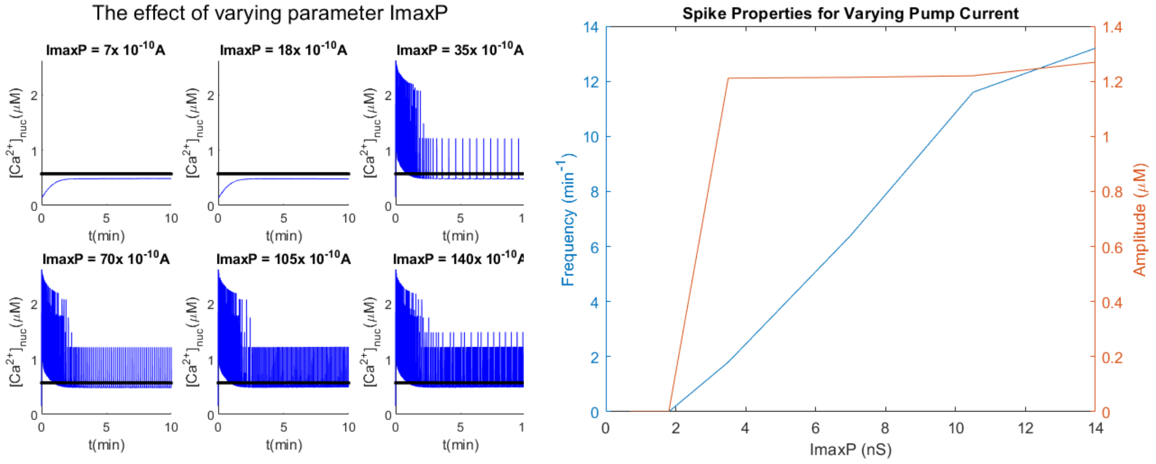

(a) (b)

Figure 73.: The effect of the maximum pump current a) seen for a single point in the micro-domain and b) quantified by the oscillation amplitude and frequency. We observe a positive correlation between $I_{\mathrm{p}}^{\mathrm{max}}$and frequency with negligible effect on amplitude.

number of pumps the system reaches a steady state, possibly similarly to the effect of a low pump current, due to the calcium having time to diffuse through the nucleoplasm before reaching a pump, preventing the formation of pump/channel cycle within a micro-domain. For increasing numbers of pumps, the amplitude of spikes again remains constant for all values, but the frequency increases quite dramatically. A possible explanation is that for more pumps, the probability of both the pumps being closer to the channel and of there being multiple pumps in close proximity to the channel increases, and hence the calcium is returned to the store much more quickly and spike frequency is increased.

Our final parameter, np, with the parameter space analysis results given in Figure. 75, shows again negligible effects on frequency and amplitude of oscillations for a wide variation of values. As this parameter relates closely to the KA_{p} we would expect that this follows the same explanation, i.e. that the pump is at maximum capacity for all parameter values due to the high concentrations in the micro-domain. Overall, we note that the pump param-

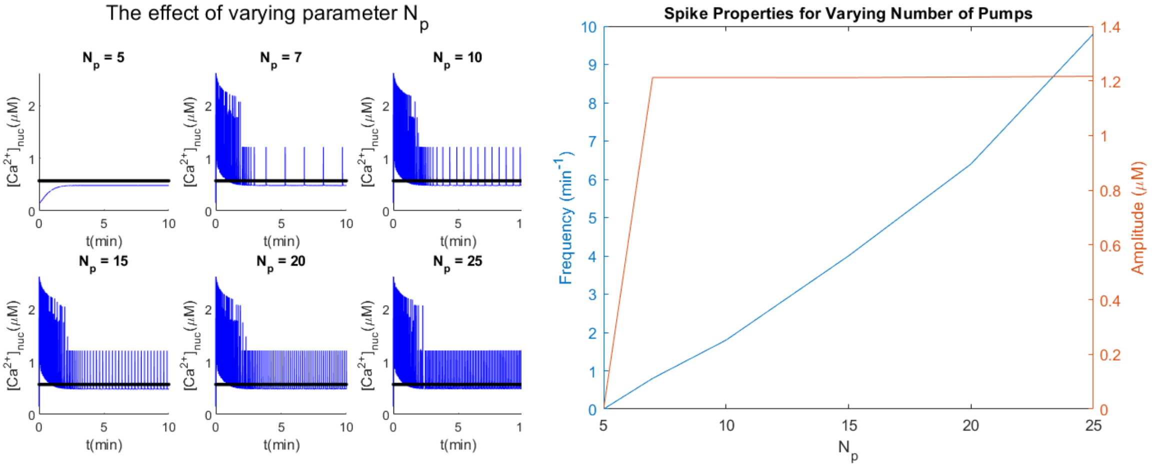

(a) (b)

Figure 74.: The effect of the number of pumps a) seen for a single point in the micro-domain and b) quantified by the oscillation amplitude and frequency. N_p is positively correlated with oscillation frequency whilst, as is the case for all pump parameters, we see no effect of amplitude.

eters have no effect on the amplitude of oscillations. Whilst the parameters from the Hill function, KA_p and np, also have no effect on the frequency of oscillations, I_p^{max} and N_p on the other hand result in an increase in frequency as their value is increased.

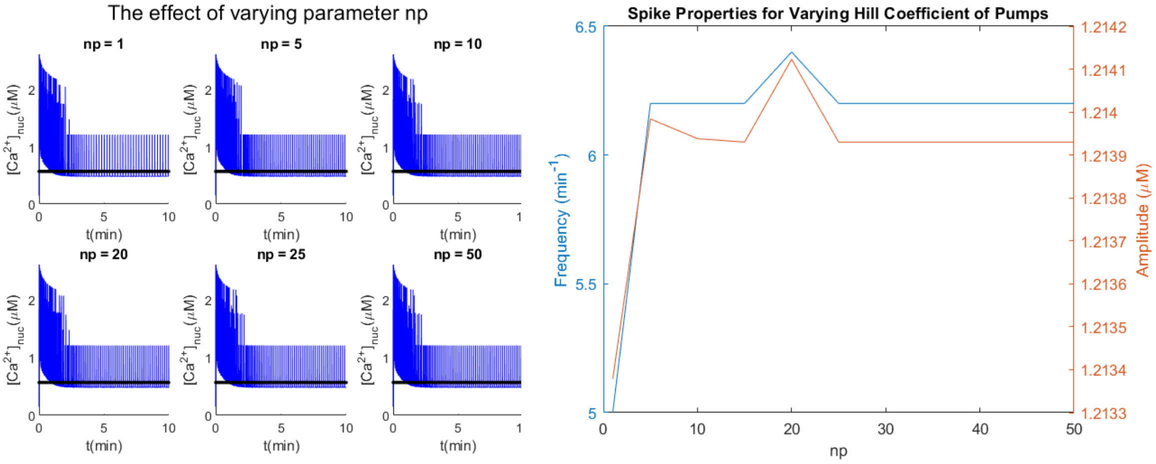

(a) (b)

Figure 75.: The effect of the pump Hill coefficient a) seen for a single point in the micro-domain and b) quantified by the oscillation amplitude and frequency. There is little to no effect on the spike properties observed through varying np.

Parameter combinations

In the previous subsections we have analysed the effects of each parameter, categorised by its function into either pumps, channels or diffusion. The parameter exhibiting the greatest effect was chosen from each category and these were varied simultaneously in order to view the analysis over a 3-dimensional space. Taking the diffusion coefficient in the nucleus, the channel release rate and the number of pumps, we recorded the amplitude and frequency of the calcium spikes generated in our simulations. Results for N_p = 15, are given in Figure. 76a, whilst results for N_p=20, can be seen in Figure. 76b. These two sets of heat-maps show an almost identical picture in that effect upon the frequency is dominated by the nuclear diffusion coefficient with a larger D_nuc resulting in a decrease in spike frequency. Amplitude on the other hand, appears to be equally influenced by both parameters with a lower channel release rate and a higher diffusion coefficient correlating to a higher amplitude.

As mentioned in the previous section, this quantification of spike properties does not sufficiently describe the changes in patterning as the parameters are varied. The calcium signatures generated are therefore shown for the maximal concentration point in the microdomain in Figure. 77 and Figure. 78 from which we can gain further insight than is afforded to us through our quantitative measures. An interesting feature of the calcium signature is the short period of 'fast-spikes' which occurs upon initial receipt of the signal. As discussed in Section 2, we know from experimental evidence that this is a series of 5-7 spikes occurring at higher frequency than the subsequent transients. We see that this pattern is replicated extremely well for $g = 700\ s^{-1}\mu m^{-3}$ whilst for increasingly low channel release rate, the number of initial fast-spikes increases, with the relationship occurring across all values of D_nuc. A furthur insight we gain from observing the individual transients is that in the cases where there are more fast spikes,

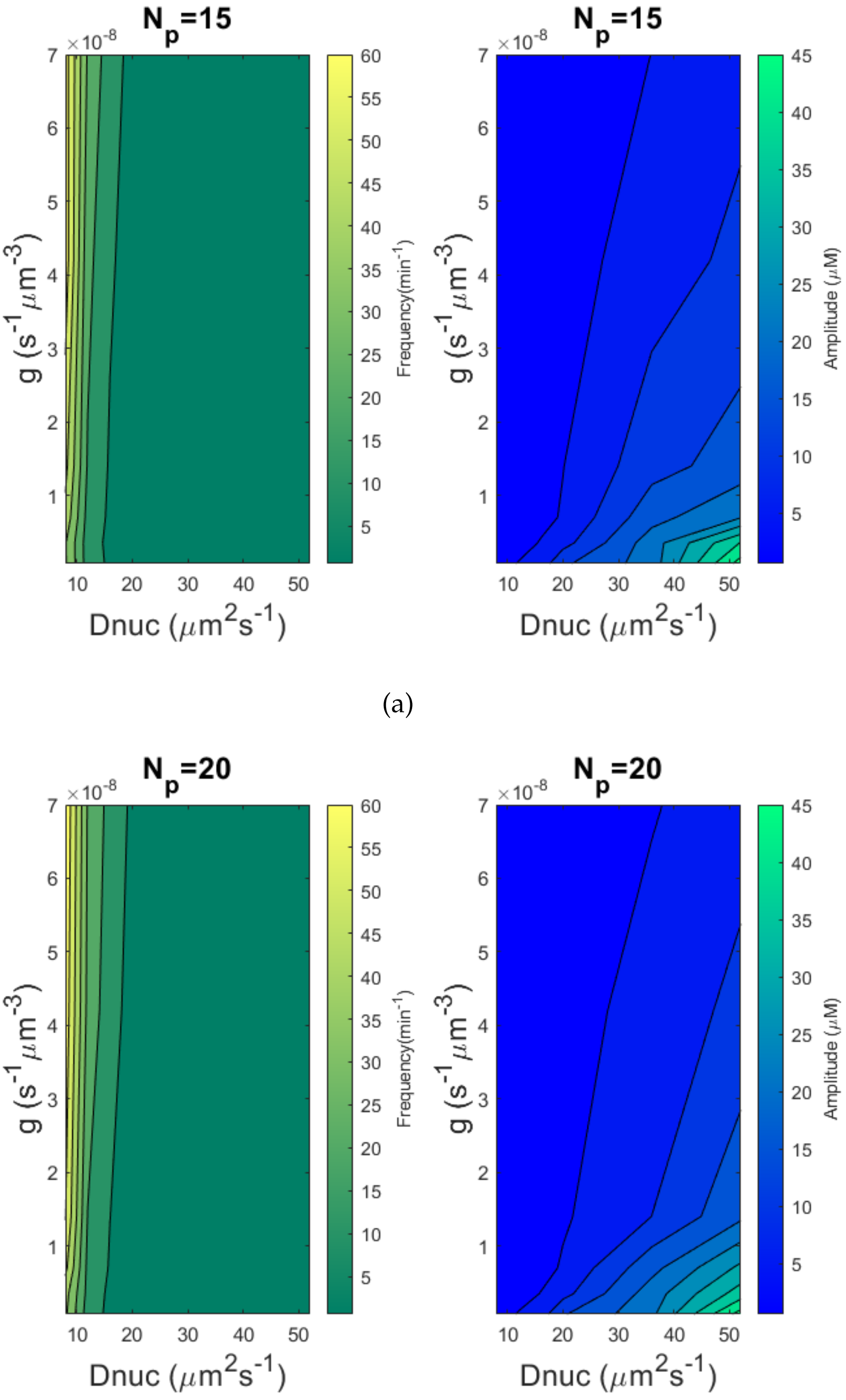

(a)

(b)

Figure 76.: 2-dimensional parameter space analysis results for varying diffusion coefficient and channel release rate with a) 15 pumps and b) 20 pumps.

the concentration does not return to the 'base' concentration in between but rather returns to base level gradually over time. It is also useful to see the results which we have quantified in Figure. 76, as we observe the spike frequency increase from left to right as D_{nuc} increases, and decreases from top to bottom as g increases. Finally we observe for a diffusion coefficient of 12 and below, when N_{p}=15, the system returns to a steady state after the initial

Figure 77.: Parameter space analysis results, viewed as individual calcium signatures within the micro-domain for $N_{\text{p}} = 15$, $D_{\text{nuc}} = [12, 20, 36, 52]$ $\mu m^2 s^{-1}$ and $g = [7, 35, 70, 140, 420, 700]$ $s^{-1}\mu m^{-3}$.

fast-spiking period, which may help to lead us towards an understanding of how the spiking is able to terminate as autonomously as it was initiated. This is the main difference between the results for N_p=15 and N_p=20 which results in high amplitude, low frequency spikes when $D_\mathrm{nuc} = 12$.

Figure 78.: Parameter space analysis results, viewed as individual calcium signatures within the micro-domain for $N_\mathrm{p} = 20$, $D_\mathrm{nuc} = [12, 20, 36, 52]\ \mu m^2 s^{-1}$ and $g = [7, 35, 70, 140, 420, 700]\ s^{-1} \mu m^{-3}$.

7.2.3 *The effect of cluster positioning*

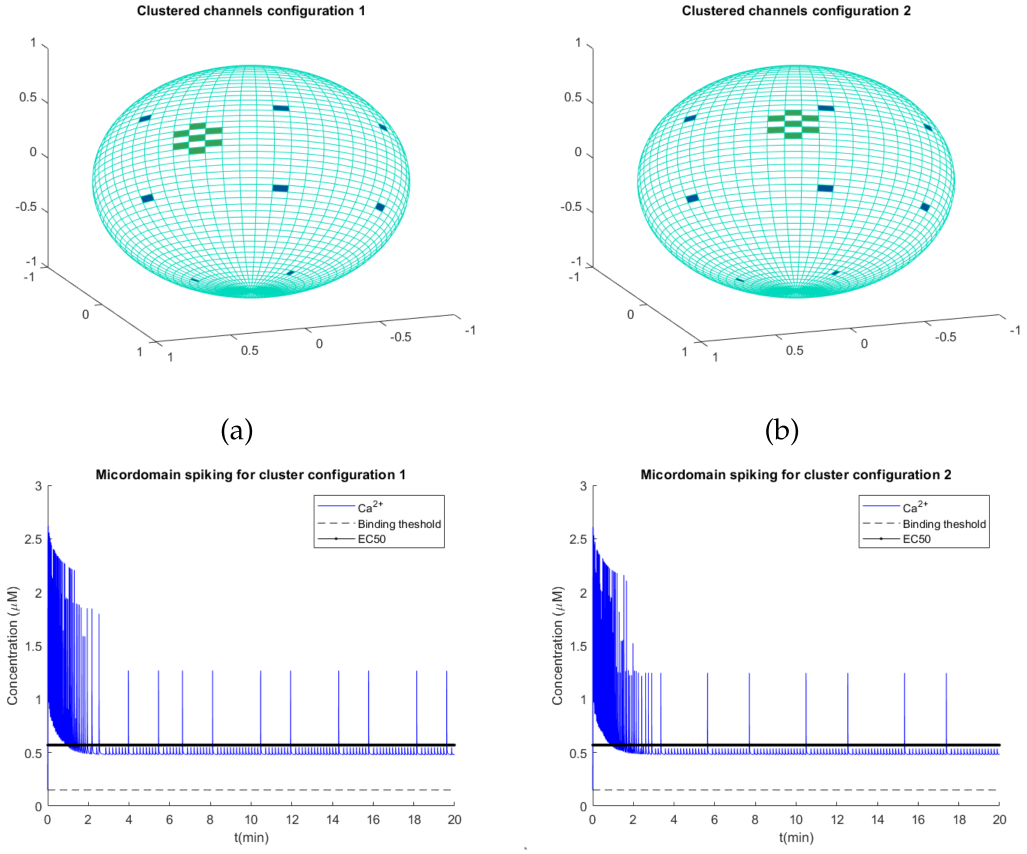

(a) (b)

(c) (d)

Figure 79.: The effect of cluster positioning in relation to the pumps on channel spiking. a) A cluster far from any pumps produces the higher frequency spiking in c). b) A cluster close to a single pump results in low frequency spiking seen in d).

Here we compare the effect of the positioning of a cluster of channels in relation to the pumps which remain equally distributed over the spherical surface. Figure. 79 shows two channel configurations: a) configuration 1 in which the cluster is situated as far from any pump as possible, and b) configuration 2 where the cluster is positioned close to a single pump. We see that cluster positioning has a slight effect on spiking frequency. Whilst configuration 1 results in higher frequency spiking, after the initial characteristic series of fast spikes, configuration 2 results in spikes of a lower frequency.

It may have been expected that the cluster which was close to the pumps would exhibit higher frequency oscillations due to the decrease in distance, and therefore time, for the calcium to be returned to the PNS. These results however highlight the role of multiple pumps in sequestering the calcium ions back into the store, as it is seen that a single pump alone cannot sufficiently refill the PNS for a subsequent channel activation. We do note however, that the pattern observed, with an alternating longer and shorter period, is preserved for both configurations.

7.3 SIMULATIONS SUMMARY

- 2D simulations, comparing the calcium profiles resulting from clustered and equally distributed calcium channels, demonstrated the cooperative effect of a cluster on the formation of microdomains of high concentration.
- It was discovered that oscillations can be generated autonomously in the nucleus provided there is channel clustering.
- Our model is able to reproduce the initial fast spiking followed by slower regular spiking as reported in the literature [26].
- 3D simulations showed that clustering of channels is required in order for the resulting microdomain concentrations to surpass the binding threshold of CCaMK.
- A parameter space analysis showed that the frequency and amplitude of oscillations has a clear relationship with the nuclear diffusion coefficient, the channel release rate and the number of pumps.

- Our model is most sensitive to changes in the nuclear diffusion coefficient, whilst being highly robust to others, particularly those parameterising the pump dynamics.
- Cluster localisation experiments revealed that it is likely that multiple pumps are involved in establishing sustained oscillations.

8

CONCLUSIONS AND FUTURE WORK

In this work we have looked at the calcium signalling pathway which mediates symbiotic associations between legumes and Nitrogen-fixing bacteria. The motivation behind this work lies in the transfer of these symbiotic abilities to cereal crops in order to facilitate a more sustainable biological solution to the problem of feeding an expanding population using increasingly degraded soils whilst decreasing the use of environmentally harmful synthetic fertilisers. Noting that many cereal crops possess many components of the calcium signalling toolbox, and form similar bacterial associations using the common symbiotic pathway, a natural step towards the higher goal is to unravel the details of this pathway in order to pinpoint the points of divergence between them.

A mathematical model representing the flux and diffusion of calcium in and between the two compartments of the plant cell nucleus was derived for up to 3-dimensions in both spherical and prolate spheroidal coordinates. Our final model is the first 3-dimensional representation of nuclear plant calcium signalling. It is also the first to reproduce the exact spiking profile reported in the literature without any additional inputs such as refractory periods or buffers. A novel and exciting finding from this thesis is that nuclear calcium oscillations can be generated autonomously provided that the channels which facilitate them form clusters. The importance of channel clusters is furthur evidenced by the additional finding that microdomain formation is necessary for calcium concentrations to exceed the binding threshold of downstream sensory protein CCaMK. When taken together we see the potential multi-functional role that cluster formation plays in calcium signal generation. This discovery is important because, if confirmed, it provides us with a possible mechanism of signal generation which is currently unknown. This not only adds to our fundamental knowledge of plant cell biology, but also provides a direction in which to look for the missing link in cereal crops prohibiting fungal-symbiont interactions. The mathematical method through which this was achieved provides us with a useful 3-dimensional framework for simulations of various applications requiring spherical polar coordinates which is significantly faster than could be achieved through traditional finite-element methods.

Alongside our in-silico investigations into the mechanism of generation of calcium signals, we have also formulated an experimental set-up which allowed us to observe these signals in-vivo. The evolution of our method using plant lines expressing GCAMP in a FlowCell device will provide a useful framework for experimentation in the future. This method was used for measuring the effect of a Mastoparan stimulus on Arabidopsis root cells as compared to the effect in *N.benthamiana*. We saw that the calcium response in Arabidopsis was present but inconsistent, whereas *N.benthamiana* nuceli exhibited more regular spiking. This is interesting because it highlights the difference in calcium signalling between species and in particular between those with and without nodulation abilities, suggesting that an evolutionary loss of 'tools' as well as changes in the genome has occurred. It would be interesting in future work to tailor our nuclear calcium signalling model to Arabidopsis in an attempt to identify the missing pieces. Experimental investigations also involved collecting data on the geometry of the nucleus. We have shown that there are statistically significant differences in nuclear morphology between cortical and root hair cells, providing an avenue of furthur experimentation into the effects and purpose behind this phenomena. We have also shown that nuclear geometry of cells in the elongation zone is correlated to the distance from the root apex with nuceli becoming less spherical with cell development. Useful data was also collected to determine the average nuclear radius of root hair cells along with the spheroidal equivalent defining the spheroidal nuclear surface which were used to parameterise our model.

Evidence from our experiments indicates that it is important to model the root hair cell nuclei as spheroids or ellipsoids as compared to the more generalised sphere. However, problems were encountered in the computational application of the special functions required to compute the Green's function in the more complex geometries. We have shown that, due to numerical instabilities of available algorithms for computing the prolate spheroidal wavefunctions, it is not possible to model either a nucleoplasm with sufficient flatness or a PNS compartment that is thin enough to be realistic. We have also seen that this breakdown of the inbuilt function in the python programming language only allows for the calculation of a very limited number of eigenvalues, preventing full convergence of the function even with the necessary truncation.

We tested a number of workarounds that may be useful to allow for computation within the existing software limitations. These included manually setting the tails of our function to zero in order to nullify the instabilities. Another involved using a variable diffusion coefficient in the PNS in order to contain the calcium within the inner portion of the membrane, with a slower diffusion coefficient towards the periphery producing the effect of a block and hence an artificially thinner calcium store. The optimal solution of course would be for advancement in the algorithms available to compute the necessary special functions, for which calls have been made in the literature with some having been discussed here. Given an accurate algorithm for computing the PSWF's up to large values of the spheroidal parameter, the same model framework used for the spherical representation could be used with a more accurate geometry.

A key next step in this research, would be to test the main simulation outcomes experimentally. Most importantly this would include confirming if clusters of CNGC15 channels form on the INM in response to the perception of Nod-factors. Using *M.truncatula* lines with tagged nuclear channels through immunogold or GFP labelling of CNGC15, a suggested approach would be to freeze samples before and after stimulus application and imaging using transmission electron microscopy (TEM) at low temperatures. We have suggested that due to microdomain formation, re-positioning of genes and/or transcription factors to the nuclear periphery may be an important feature of the calcium signalling pathway. In a similar manner to the above, future work could look at this re-positioning through the tagging of specific genes or transcription factors and observing their movement in response to a relevant stimulus.

Anomalous calcium spiking observed in our controls, along with the high levels of "noise" in the nuclear calcium signature, remind us that there are multiple functionalities of nuclear calcium signalling in root hair cells. We believe it would therefore be useful to develop a processing method to 'untangle' these overlapping signals in order to ascertain how they interact and determine how a single cell is able to respond to the multiple stimuli it perceives in each single point in time. As well as providing valuable insight into how signalling pathways are intertwined, this would allow for the extraction of clean signals from imaging data which could be more confidently attributed to the stimulus of interest.

Finally, our model provides us with a 3-dimensional framework that can be furthur expanded to include additional aspects of calcium signalling in both space and time. Temporal extensions could include the addition of up/downstream components such as the chemical cascade leading to gene transcription. Spatial expansions could involve adding furthur compartments to the model, for example connecting the nucleus to the cytoplasm through nuclear pores. Challenges in adding the wider cellular compartment's would possibly arise due to the large vacuole present in plant cells and the dynamic nature of the positioning of the nucleus within the cell, as well as the computational space required for storing additional Green's functions. This reliable and realistic modelling framework, however, can continue to be built upon and holds the potential to facilitate furthur elucidation of the details of nuclear calcium signal generation. The model also provides a useful tool for hypothesis testing in-silico in order to direct experimental efforts and move us ever closer towards our ultimate goal of using this knowledge to feed the world sustainably.

A

SEPARATION OF VARIABLES IN SPHERICAL COORDINATES

The diffusion equation is given by:

$$\frac{\partial u}{\partial t} = D\frac{\partial^2 u}{\partial x^2}. \tag{271}$$

We wish to derive and solve the 3D diffusion equation in three different polar coordinate systems corresponding to the relevant nuclear geometries which have been observed in plant root tissues.

A.1 NUCLEOPLASM

Firstly the spherical coordinates (r, θ, ϕ) are introduced as in Figure. 18, such that;

$$\begin{aligned} x &= r\sin\theta\cos\phi, \\ y &= r\sin\theta\sin\phi, \\ z &= r\cos\theta, \end{aligned}$$

$$0 \le r \le a, \qquad 0 \le \theta \le \pi, \qquad 0 \le \phi < 2\pi. \tag{272}$$

The chain rule gives the Laplacian to be:

$$\nabla^2 = \frac{\partial^2}{\partial r^2} + \frac{2}{r}\frac{\partial}{\partial r} + \frac{1}{r^2}\frac{\partial^2}{\partial \theta^2} + \frac{\cot\theta}{r^2}\frac{\partial}{\partial \theta} + \frac{1}{r^2\sin^2\theta}\frac{\partial^2}{\partial \phi^2}, \tag{273}$$

and hence we have the diffusion equation in spherical polar coordinates:

$$\frac{\partial u}{\partial t} = D_{\text{nuc}} \left[\frac{\partial^2 u}{\partial r^2} + \frac{2}{r}\frac{\partial u}{\partial r} + \frac{1}{r^2}\frac{\partial^2 u}{\partial \theta^2} + \frac{\cot\theta}{r^2}\frac{\partial u}{\partial \theta} + \frac{1}{r^2 \sin^2\theta}\frac{\partial^2 u}{\partial \phi^2} \right], \tag{274}$$

where, with foresight, we have denoted the diffusion coefficient D_{nuc} to indicate the diffusion coefficient within the nucleoplasm.

We can first, by arguments of symmetry, neglect the ϕ dependence by remove the ϕ dependent terms, which will be revisited later:

$$\frac{\partial u}{\partial t} = D_{\text{nuc}} \left[\frac{\partial^2 u}{\partial r^2} + \frac{2}{r}\frac{\partial u}{\partial r} + \frac{1}{r^2}\frac{\partial^2 u}{\partial \theta^2} + \frac{\cot\theta}{r^2}\frac{\partial u}{\partial \theta} \right]. \tag{275}$$

Using the separation of variables technique we let:

$$u(r,\theta,t) = p(r)q(\theta)T(t), \tag{276}$$

and substituting Eq. (276) in Eq. (275) we obtain:

$$\frac{1}{D_{\text{nuc}}}\frac{T_{\text{t}}}{T} = \frac{p_{\text{rr}}}{p} + \frac{2}{r}\frac{p_{\text{r}}}{p} + \frac{1}{r^2}\frac{q_{\theta\theta}}{q} + \frac{\cot\theta}{r^2}\frac{q_{\theta}}{q}. \tag{277}$$

Separating $T(t)$ gives us our first ODE in equation 278. As the right hand side of equation 277 does not depend upon t, both sides must be equal to the same constant, which we choose to be $-k^2$:

$$\frac{1}{D_{\text{nuc}}}\frac{T_{\text{t}}}{T} = -k^2, \tag{278}$$

$$\frac{p_{\text{rr}}}{p} + \frac{2}{r}\frac{p_{\text{r}}}{p} + \frac{1}{r^2}\frac{q_{\theta\theta}}{q} + \frac{\cot\theta}{r^2}\frac{q_{\theta}}{q} = -k^2. \tag{279}$$

Next, multiplying through Eq. (279) by r^2 allows us to bring all terms of radial dependence to the left hand side and all terms of angular dependence to the right:

$$-r^2\frac{p_{\text{rr}}}{p} - 2r\frac{p_{\text{r}}}{p} - k^2 r^2 = \frac{q_{\theta\theta}}{q} + \cot\theta\frac{q_{\theta}}{q}. \tag{280}$$

Both sides of Eq. (280) can then be equated to a constant, $-\mu^2$ to give the ODEs:

$$r^2 p_{\text{rr}} + 2r p_{\text{r}} + (k^2 r^2 - \mu^2)p = 0, \tag{281}$$

$$\frac{q_{\theta\theta}}{q} + \cot\theta \frac{q_\theta}{q} = -\mu^2, \tag{282}$$

and Eqs. (278), (281), and (282) are rearranged to give the final set of equations:

$$\begin{aligned} &1. \qquad T' + k^2 D_{\text{nuc}} T = 0, \\ &2. \qquad q'' + \cot\theta q' + \mu^2 q = 0, \\ &3. \qquad r^2 p'' + 2rp' + (k^2 r^2 - \mu^2)p = 0. \end{aligned} \tag{283}$$

Equation 1 of Eq. (283) is easily solved, subject to the initial condition $T(0) = T_0$, to give:

$$T(t) = T_0 \mathrm{e}^{-k^2 D_{\text{nuc}} t}. \tag{284}$$

In equation 2 we set $x = \cos\theta$ for $x \in [-1, 1]$. Using the derivatives:

$$\frac{\mathrm{d}}{\mathrm{d}\theta} = \frac{\mathrm{d}x}{\mathrm{d}\theta}\frac{\mathrm{d}}{\mathrm{d}x} = -\sin\theta \frac{\mathrm{d}}{\mathrm{d}x} = -(1-x^2)^{1/2}\frac{\mathrm{d}}{\mathrm{d}x}, \tag{285}$$

$$\frac{\mathrm{d}^2}{\mathrm{d}\theta^2} = \sin^2\theta \frac{\mathrm{d}^2}{\mathrm{d}x^2} - \cos\theta \frac{\mathrm{d}}{\mathrm{d}x} = (1-x^2)\frac{\mathrm{d}^2}{\mathrm{d}x^2} - x\frac{\mathrm{d}}{\mathrm{d}x}, \tag{286}$$

and the equation for the angular dependence becomes:

$$(1-x^2)q'' - 2xq' + \mu^2 q = 0, \tag{287}$$

which is the Legendre differential equation for separation constant $\mu^2 = l(l+1)$, $l \in \mathbb{Z}_{\geq 0}$. Our solution is therefore given by the Legendre functions of the first $(P_l(x))$ and second $(Q_l(x))$ kinds, of degree l:

$$q(x) = AP_l(x) + BQ_l(x), \qquad x = \cos\theta. \tag{288}$$

It is known that as $x \to \pm 1$, $Q_l(x) \to \infty$ and hence does not not conform to our condition of boundedness, hence $B = 0$ and we take $q(x)$ to be the Legendre polynomial $P_l(x)$:

$$q(x) = AP_l(x). \tag{289}$$

In equation 3 of 283 we set $p(r) = \dfrac{z(r)}{(kr)^{1/2}}$ which has first and second derivatives of:

$$p'(r) = \frac{z'}{(kr)^{1/2}} - \frac{z}{2r(kr)^{1/2}}, \tag{290}$$

and:

$$p''(r) = \frac{z''}{(kr)^{1/2}} - \frac{z'}{r(kr)^{1/2}} + \frac{3}{4}\frac{z}{r^2(kr)^{1/2}}, \tag{291}$$

respectively. Substituting into Eq. 3 of Eq. (283), and recalling that we have set $\mu^2 = l(l+1)$, we find;

$$r^2 z'' + rz' + (k^2 r^2 - (l + \frac{1}{2})^2)z = 0. \tag{292}$$

Setting $s = kr$ and noting that, by the chain rule, $\dfrac{\mathrm{d}}{\mathrm{d}r} = \dfrac{\mathrm{d}s}{\mathrm{d}r}\dfrac{\mathrm{d}}{\mathrm{d}s} = k\dfrac{\mathrm{d}}{\mathrm{d}s}$, the radial equation becomes:

$$s^2 z'' + sz' + (s^2 - (l + \frac{1}{2})^2)z = 0. \tag{293}$$

This is the Bessel equation of order $l + \frac{1}{2}$ with solution:

$$z(s) = Cj_l(s) + Dy_l(s), \tag{294}$$

where $j_l(s)$ and $y_l(s)$ are the spherical Bessel functions of the first and second kind respectively, related to the ordinary Bessel functions, $J_l(s)$ and $Y_l(s)$, by:

$$j_l(s) = \sqrt{\frac{\pi}{2s}} J_{l+\frac{1}{2}}(s), \tag{295}$$

and

$$y_l(s) = \sqrt{\frac{\pi}{2s}} Y_{l+\frac{1}{2}}(s). \tag{296}$$

We require boundedness of $z(r)$, that is $|\lim_{r\to 0} z(r)| < \infty$, and hence as $\lim_{s\to 0} y_l(s) = \infty$, for our solution to hold we must have $D = 0$. Secondly we have no flux at the outer boundary, at which $r = a$. The Neumann boundary condition is applied to our remaining term $z(s) = Cj_l(s)$, recalling we have set $s = kr$:

$$\frac{d}{dr}\left[z(kr)\right]|_{r=a} = C\frac{d}{dr}\left[j_l(kr)\right]|_{r=a} = 0. \tag{297}$$

As we require nontrivial solutions, $C \neq 0$ and we have the eigenvalue problem:

$$j_l'(\alpha_{lp}) = 0, \tag{298}$$

where α_{lp} is the p^{th} zero of the derivative of the l^{th} order spherical Bessel function, j_l'. Our eigenvalues can be found numerically and are written as $ka = \alpha_{lp}$.

The solutions can be combined by $u(r,\theta,t) = z(r)q(\theta)T(t)$ and written as:

$$u(r,\theta,t) = \sum_{l=0}^{\infty}\sum_{p=1}^{\infty} C_{lp} j_l(\frac{\alpha_{lp}}{a}r) A_l P_l(x) T_0 e^{-\left(\frac{\alpha_{lp}}{a}\right)^2 D_{\text{nuc}} t}. \tag{299}$$

We find the weighting coefficient A_l using the orthogonality relation of the Legendre polynomials:

$$\int_{-1}^{1} P_l(x) P_{l'}(x) \mathrm{d}x = \begin{cases} 0, & \text{if } l \neq l' \\ \dfrac{2}{2l+1}, & \text{if } l = l'. \end{cases} \tag{300}$$

and C_{lp} using the orthogonality condition for spherical Bessel functions for each fixed l:

$$\int_0^a j_l(\frac{\alpha_{lp}}{a}r) j_l(\frac{\alpha_{lq}}{a}r) r^2 \mathrm{d}r = \begin{cases} 0, & \text{if } p \neq q \\ \mathcal{N}_{lp}, & \text{if } p = q. \end{cases} \tag{301}$$

where, as given by Ziener (2015) [94]:

$$\mathcal{N}_{lp} = \frac{a}{2}\left[a^2 - l\frac{(l+1)}{\alpha_{lp}^2}\right]\left[j_l(\alpha_{lp})\right]^2 + \frac{a^2}{2\alpha_{lp}} j_l(\alpha_{lp}) j_l'(\alpha_{lp}) + \frac{a^3}{2}\left[j_l'(\alpha_{lp})\right]^2. \tag{302}$$

By our boundary condition, $j_l'(\alpha_{lp}) = 0$, the last two terms of Eq. 302 are zero and our normalization factor becomes:

$$\mathcal{N}_{lp} = \frac{a}{2}\left[a^2 - l\frac{(l+1)}{\alpha_{lp}^2}\right]\left[j_l(\alpha_{lp})\right]^2. \tag{303}$$

Multiplying Eq. 299 at the source (or initial condition), $q(\theta)z(r) = q_0(\theta)z_0(r)$, by $P_{l'}(x) j_l(\frac{\alpha_{lp'}}{a} r) r^2$, and integrating with respect to x between -1 and 1, and between 0 and a with respect to r, we find:

$$\begin{aligned}
\int_{-1}^{1} \int_{0}^{a} & z_0(r) j_l(\frac{\alpha_{lp'}}{a} r) q_0(\theta) P_{l'}(x) r^2 \mathrm{d}r \mathrm{d}x \\
&= \sum_{l=0}^{\infty} \int_{-1}^{1} A_l P_l(x) P_{l'}(x) \mathrm{d}x \sum_{p=1}^{\infty} \int_{0}^{a} C_{lp} j_l(\frac{\alpha_{lp}}{a} r) j_l(\frac{\alpha_{lp'}}{a} r) r^2 \mathrm{d}r \\
&= A_l C_{lp} \int_{-1}^{1} [P_l(x)]^2 \mathrm{d}x \int_{0}^{a} \left[j_l(\frac{\alpha_{lp}}{a} r) \right]^2 r^2 \mathrm{d}r \\
&= A_l C_{lp} \frac{a}{2l+1} \left[a^2 - l \frac{(l+1)}{\alpha_{lp}^2} \right] \left[j_l(\alpha_{lp}) \right]^2 .
\end{aligned} \tag{304}$$

Hence our coefficient is given by our normalization factors, setting $x' = \cos(\theta')$:

$$A_l C_{lp} = \frac{2l+1}{a} \int_{0}^{\pi} q_0(\theta') P_l(\cos\theta') \sin\theta' \mathrm{d}\theta' \frac{\int_0^a z_0(r') j_l(\frac{\alpha_{lp}}{a} r') r'^2 \mathrm{d}r'}{\left[a^2 - l \frac{(l+1)}{\alpha_{lp}^2} \right] \left[j_l(\alpha_{lp}) \right]^2}, \tag{305}$$

and our solution is:

$$\begin{aligned}
u(r, \theta, t) &= z(r) q(\theta) T(t) \\
&= T_0 \sum_{l=0}^{\infty} \frac{2l+1}{a} \int_{0}^{\pi} q_0(\theta') P_l(\cos\theta') P_l(\cos\theta) \sin\theta' \mathrm{d}\theta' \\
& \qquad \sum_{p=1}^{\infty} \frac{\int_0^a z_0(r') j_l(\frac{\alpha_{lp}}{a} r') j_l(\frac{\alpha_{lp}}{a} r) r'^2 \mathrm{d}r'}{\left[a^2 - l \frac{(l+1)}{\alpha_{lp}^2} \right] \left[j_l(\alpha_{lp}) \right]^2} \mathrm{e}^{-\left(\frac{\alpha_{lp}}{a} \right)^2 D_{\mathrm{nuc}} t} .
\end{aligned} \tag{306}$$

Using the methods introduced in Skupin (2010) [79], we include the ϕ dependence explicitly by considering a point on the sphere $P(r, \theta, \phi)$, and the point source $P'(r', \theta', \phi')$. The ϕ dependence depends only on the cosines of the angles of these two points, and hence for each source the coordinate system can be rotated to force one of the angles to be zero [79]. The angle ψ between the points is then given by the spherical law of cosines:

$$h(\psi) = \cos(\psi) = \cos(\theta)\cos(\theta') + \sin(\theta)\sin(\theta')\cos(\phi - \phi'). \tag{307}$$

Initially we have:

$$
\begin{aligned}
h_0(\psi') &= A(\cos^2(\theta') + \sin^2(\theta')\cos(\phi' - \phi')) \\
&= A_0,
\end{aligned}
\tag{308}
$$

hence we integrate this initial condition over the entire period to find the normalization constant:

$$
\begin{aligned}
\int_0^{2\pi} h_0(\psi')\mathrm{d}\psi = \int_0^{2\pi} A_0 \mathrm{d}\psi = 2\pi A_0 \\
\Rightarrow A_0 = \frac{1}{2\pi}\int_0^{2\pi} h_0(\psi')\mathrm{d}\psi'.
\end{aligned}
\tag{309}
$$

Our complete solution is therefore:

$$
\begin{aligned}
u(r,\theta,\phi,t) = \frac{T_0}{2\pi}\int_0^{2\pi} h_0(\psi')\mathrm{d}\psi' \sum_{l=0}^{\infty}\frac{2l+1}{a}\int_0^{\pi} q_0(\theta')P_{\mathrm{l}}(\cos\psi)\sin\theta'\mathrm{d}\theta' \\
\sum_{p=1}^{\infty}\frac{\int_0^{\mathrm{a}} z_0(r')j_{\mathrm{l}}(\frac{\alpha_{\mathrm{lp}}}{a}r')j_{\mathrm{l}}(\frac{\alpha_{\mathrm{lp}}}{a}r)r'^2\mathrm{d}r'}{\left[a^2 - l\frac{(l+1)}{\alpha_{\mathrm{lp}}^2}\right]\left[j_{\mathrm{l}}(\alpha_{\mathrm{lp}})\right]^2}\mathrm{e}^{-\left(\frac{\alpha_{\mathrm{lp}}}{a}\right)^2 D_{\mathrm{nuc}}t},
\end{aligned}
\tag{310}
$$

which is in the form:

$$
u(r,\theta,\phi,t) = \int_V u_0(r,\theta,\phi,t)G(r,r',\theta,\theta',\phi,\phi',t,t')\mathrm{d}V, \tag{311}
$$

where:

$$
u_0(r,\theta,\phi,t) = z_0(r')q_0(\theta')h_0(\phi')T_0, \tag{312}
$$

with Green's function:

$$
\begin{aligned}
&G(r,\theta,\phi,t,r',\theta',\phi') = \\
&\sum_{l=0}^{\infty}\frac{(2l+1)}{2\pi a}P_{\mathrm{l}}(\cos\psi)\sum_{p=1}^{\infty}\frac{j_{\mathrm{l}}(\frac{\alpha_{\mathrm{lp}}}{a}r')j_{\mathrm{l}}(\frac{\alpha_{\mathrm{lp}}}{a}r)}{\left[a^2 - l\frac{(l+1)}{\alpha_{\mathrm{lp}}^2}\right]\left[j_{\mathrm{l}}(\alpha_{\mathrm{lp}})\right]^2}\mathrm{e}^{-\left(\frac{\alpha_{\mathrm{lp}}}{a}\right)^2 D_{\mathrm{nuc}}t}.
\end{aligned}
\tag{313}
$$

A.2 PERINUCLEAR SPACE

The Green's function is derived as in Section A.1, however recalling the equation for the radial dynamics:

$$s^2 z'' + sz' + (s^2 - (l + \frac{1}{2})^2)z = 0, \tag{314}$$

whose solution is a linear combination of the spherical Bessel functions of the first and second kind:

$$z(s) = Cj_l(s) + Dy_l(s), \tag{315}$$

we notice that in this case we are unable to set $D = 0$ as we do not consider the region containing $s = 0$ where $y_l(s)$ becomes unbounded. We must now therefore apply the no flux boundary condition on both radial boundaries:

$$\frac{d}{dr}\left[z(kr)\right]|_{r=a} = 0, \qquad \frac{d}{dr}\left[z(kr)\right]|_{r=\lambda a} = 0, \tag{316}$$

which gives the system:

$$\begin{bmatrix} j_l'(ka) & y_l'(ka) \\ j_l'(\lambda ka) & y_l'(\lambda ka) \end{bmatrix} \begin{bmatrix} C \\ D \end{bmatrix} = \begin{bmatrix} 0 \\ 0 \end{bmatrix}. \tag{317}$$

As we require $C, D \neq 0$ we obtain the condition:

$$j_l'(\alpha_{lp})y_l'(\lambda\alpha_{lp}) - y_l'(\alpha_{lp})j_l'(\lambda\alpha_{lp}) = 0, \tag{318}$$

where we have set $k = \frac{\alpha_{lp}}{a}$. This is an eigenvalue problem where, as before, α_{lp} is the p^{th} solution to the l^{th} order problem. We also see from our boundary conditions that:

$$D = -C\frac{j_l'(\alpha_{lp})}{y_l'(\alpha_{lp})}, \tag{319}$$

and hence we can write:

$$z(s) = C\bar{z}(s), \tag{320}$$

where:

$$\bar{z}(s) = cj_l(s) + dy_l(s), \tag{321}$$

for constants $c = 1$ and $d = -\dfrac{j_l'(\alpha_{lp})}{y_l'(\alpha_{lp})}$.

Fixing l we find the value of our coefficient C using the orthogonality relation [94]:

$$\int_a^{\lambda a} \bar{z}_l(\frac{\alpha_{lp}}{a}r)\bar{z}_l(\frac{\alpha_{lq}}{a}r)r^2\mathrm{d}r = \begin{cases} 0, & \text{if } p \neq q \\ \dfrac{r}{2}\left(r^2 - l\dfrac{(l+1)}{\alpha_{lp}^2}\right)\left[\bar{z}_l(\frac{\alpha_{lp}}{a}r)\right]^2\Big|_a^{\lambda a}, & \text{if } p = q. \end{cases} \tag{322}$$

We multiply the radial part of our initial condition, $z_0(kr)$, by $\bar{z}_l(kr)$ and integrate over our domain to find:

$$\begin{aligned} &\int_a^{\lambda a} z_0(r)\bar{z}_l(\frac{\alpha_{lp'}}{a}r)r^2\mathrm{d}r \\ &\qquad = \sum_{p=1}^{\infty}\int_a^{\lambda a} C_{lp}\bar{z}_l(\frac{\alpha_{lp}}{a}r)\bar{z}_l(\frac{\alpha_{lp'}}{a}r)r^2\mathrm{d}r \\ &\qquad = C_{lp}\int_a^{\lambda a}\left[\bar{z}_l(\frac{\alpha_{lp}}{a}r)\right]^2 r^2\mathrm{d}r \\ &\qquad = C_{lp}\left(\frac{\lambda a}{2}\left((\lambda a)^2 - l\frac{(l+1)}{\alpha_{lp}^2}\right)\left[\bar{z}_l(\lambda\alpha_{lp})\right]^2 \right.\\ &\qquad \left. - \frac{a}{2}\left(a^2 - l\frac{(l+1)}{\alpha_{lp}^2}\right)\left[\bar{z}_l(\alpha_{lp})\right]^2\right), \end{aligned} \tag{323}$$

and hence we have:

$$C_{lp} = \frac{2\int_a^{\lambda a} z_0(r')\bar{z}_l(\frac{\alpha_{lp}}{a}r')r'^2dr'}{\left((\lambda a)^3 - \lambda al\dfrac{(l+1)}{\alpha_{lp}^2}\right)\left[\bar{z}_l(\lambda\alpha_{lp})\right]^2 - \left(a^3 - al\dfrac{(l+1)}{\alpha_{lp}^2}\right)\left[\bar{z}_l(\alpha_{lp})\right]^2}. \tag{324}$$

Combining this result with the angular solutions found in the previous section we have the overall solution:

$$u(r,\theta,t) = \frac{T(0)}{2\pi}\int_0^{2\pi} h_0(\psi')\mathrm{d}\psi' \sum_{l=0}^{\infty}(2l+1)\int_0^{\pi} q_0(\theta')P_l(\cos\psi)\sin\theta'\mathrm{d}\theta'$$
$$\times \sum_{p=1}^{\infty} \frac{\int_a^{\lambda a} z_0(r')\bar{z}_l(\frac{\alpha_{lp}}{a}r')\bar{z}_l(\frac{\alpha_{lp}}{a}r)r'^2 dr'}{\left((\lambda a)^3 - \lambda a l\frac{(l+1)}{\alpha_{lp}^2}\right)\left[\bar{z}_l(\lambda\alpha_{lp})\right]^2 - \left(a^3 - al\frac{(l+1)}{\alpha_{lp}^2}\right)\left[\bar{z}_l(\alpha_{lp})\right]^2}$$
$$\times \mathrm{e}^{-\left(\frac{\alpha_{lp}}{a}\right)^2 D_{\mathrm{pns}}t}, \tag{325}$$

where D_{pns} the the diffusion coefficient in the perinuclear space, which is expected to be different to that in the nucleoplasm, D_{nuc}. The solution is in the form of Eq. (311) for the initial conditions in Eq. (312) with the Green's function:

$$G(r,\theta,\phi,t,r',\theta',\phi') =$$
$$\sum_{l=0}^{\infty}\frac{(2l+1)}{2\pi}P_l(\cos\psi)$$
$$\sum_{p=1}^{\infty} \frac{\bar{z}_l(\frac{\alpha_{lp}}{a}r')\bar{z}_l(\frac{\alpha_{lp}}{a}r)}{\left((\lambda a)^3 - \lambda a l\frac{(l+1)}{\alpha_{lp}^2}\right)\left[\bar{z}_l(\lambda\alpha_{lp})\right]^2 - \left(a^3 - al\frac{(l+1)}{\alpha_{lp}^2}\right)\left[\bar{z}_l(\alpha_{lp})\right]^2}$$
$$\times \mathrm{e}^{-\left(\frac{\alpha_{lp}}{a}\right)^2 D_{\mathrm{pns}}t}. \tag{326}$$

B

SEPARATION OF VARIABLES IN SPHEROIDAL COORDINATES

B.1 NUCLEOPLASM

In a limiting case of the ellipsoidal coordinates, the prolate spheroid, is obtained by rotating the elliptic coordinates about the major axis such that, at $z = 0$, the surface on the two principle axis gives a circle of radius $'a'$. (Figure 22). The system (ξ, ν, ϕ) is related to Cartesian coordinates by:

$$\begin{aligned} x &= c\sqrt{(\xi^2-1)(1-\nu^2)}\cos\phi, \\ y &= c\sqrt{(\xi^2-1)(1-\nu^2)}\sin\phi, \\ z &= c\xi\nu, \end{aligned} \tag{327}$$

$$1 \le \xi \le \xi_0, \qquad -1 \le \nu \le 1, \qquad 0 \le \phi < 2\pi. \tag{328}$$

where $c > 0$ is a constant and ξ_0 is the surface of the prolate spheroid given by:

$$\xi_0 = \frac{b}{c}. \tag{329}$$

for $c = \sqrt{b^2 - a^2}$, where a and b are the radii of the minor and major-axis respectively as seen in Figure. 22. With a similar methodology to the spherical case we use the separation of variables technique to find solutions to the diffusion equation in prolate spheroidal coordinates, where the dependent variable is given by $u(\xi,\nu,\phi,t)$. Again via the chain rule we see that the Laplacian is:

$$\nabla^2 = \frac{1}{c^2(\xi^2-\nu^2)}\left[\frac{\partial}{\partial\xi}\left((\xi^2-1)\frac{\partial}{\partial\xi}\right)+\frac{\partial}{\partial\nu}\left((1-\nu^2)\frac{\partial}{\partial\nu}\right)+\frac{(\xi^2-\nu^2)}{(\xi^2-1)(1-\nu^2)}\frac{\partial^2}{\partial\phi^2}\right]. \tag{330}$$

In order to solve our heat equation in prolate spheroidal coordinates:

$$\frac{\partial u}{\partial t} = \frac{D_{\text{nuc}}}{c^2(\xi^2-\nu^2)}\left[\frac{\partial}{\partial\xi}\left((\xi^2-1)\frac{\partial}{\partial\xi}\right)+\frac{\partial}{\partial\nu}\left((1-\nu^2)\frac{\partial}{\partial\nu}\right)+\frac{(\xi^2-\nu^2)}{(\xi^2-1)(1-\nu^2)}\frac{\partial^2}{\partial\phi^2}\right]u. \tag{331}$$

we let:

$$u(\xi,\nu,\phi,t) = p(\xi)q(\nu)s(\phi)T(t), \tag{332}$$

and by subbing in the variables of Eq. (332) into Eq. (331), the diffusion equation in this case becomes:

$$\begin{aligned}\frac{\partial u}{\partial t}\frac{1}{T(t)} = \frac{D_{\text{nuc}}}{c^2(\xi^2-\nu^2)}&\left[\frac{\partial}{\partial\xi}\left((\xi^2-1)\frac{\partial p(\xi)}{\partial\xi}\right)\frac{1}{p(\xi)}+\frac{\partial}{\partial\nu}\left((1-\nu^2)\frac{\partial q(\nu)}{\partial\nu}\right)\frac{1}{q(\nu)}\right.\\&\left.+\frac{(\xi^2-\nu^2)}{(\xi^2-1)(1-\nu^2)}\frac{\partial^2 s(\phi)}{\partial\phi^2}\frac{1}{s(\phi)}\right].\end{aligned} \tag{333}$$

As the right hand side has no 't' dependence and the left hand side has no ξ, ν or ϕ dependence, we can set both sides equal to a constant $-\kappa^2$, and taking D_{nuc} to the RHS, find the ODE in the time variable:

$$\frac{1}{D_{\text{nuc}}}\frac{T'}{T} = -\kappa^2, \tag{334}$$

with remaining terms:

$$\begin{aligned}\frac{1}{c^2(\xi^2-\nu^2)}&\left[\frac{\partial}{\partial\xi}\left((\xi^2-1)\frac{\partial p(\xi)}{\partial\xi}\right)\frac{1}{p(\xi)}+\frac{\partial}{\partial\nu}\left((1-\nu^2)\frac{\partial q(\nu)}{\partial\nu}\right)\frac{1}{q(\nu)}\right.\\&\left.+\frac{(\xi^2-\nu^2)}{(\xi^2-1)(1-\nu^2)}\frac{\partial^2 s(\phi)}{\partial\phi^2}\frac{1}{s(\phi)}\right] = -\kappa^2.\end{aligned} \tag{335}$$

Writing $\gamma^2 = k^2c^2$ and rearranging we have:

$$\begin{aligned}&\left[\frac{\partial}{\partial\xi}\left((\xi^2-1)\frac{\partial p(\xi)}{\partial\xi}\right)\frac{1}{p(\xi)}+\frac{\partial}{\partial\nu}\left((1-\nu^2)\frac{\partial q(\nu)}{\partial\nu}\right)\frac{1}{q(\nu)}\right.\\&\left.+\frac{(\xi^2-\nu^2)}{(\xi^2-1)(1-\nu^2)}\frac{\partial^2 s(\phi)}{\partial\phi^2}\frac{1}{s(\phi)}\right] = -\gamma^2(\xi^2-\nu^2).\end{aligned} \tag{336}$$

and we can separate the ϕ dependence by multiplying through by $\dfrac{(\xi^2-1)(1-\nu^2)}{(\xi^2-\nu^2)}$:

$$\begin{aligned}\left[\frac{\partial}{\partial\xi}\left((\xi^2-1)\frac{\partial p(\xi)}{\partial\xi}\right)\frac{1}{p(\xi)}+\frac{\partial}{\partial\nu}\left((1-\nu^2)\frac{\partial q(\nu)}{\partial\nu}\right)\frac{1}{q(\nu)}\right]\frac{(\xi^2-1)(1-\nu^2)}{(\xi^2-\nu^2)}&\\ +\gamma^2(\xi^2-1)(1-\nu^2)=-\frac{\partial^2 s(\phi)}{\partial\phi^2}\frac{1}{s(\phi)}=\mu^2,&\end{aligned} \tag{337}$$

and setting equal to a constant μ^2. We can therefore write our second ODE as:

$$s''+\mu^2 s=0, \tag{338}$$

and have remaining terms:

$$\begin{aligned}\frac{\partial}{\partial\xi}\left((\xi^2-1)\frac{\partial p(\xi)}{\partial\xi}\right)\frac{1}{p(\xi)}+\frac{\partial}{\partial\nu}\left((1-\nu^2)\frac{\partial q(\nu)}{\partial\nu}\right)\frac{1}{q(\nu)}+\gamma^2(\xi^2-\nu^2)&\\ =\frac{\mu^2(\xi^2-\nu^2)}{(\xi^2-1)(1-\nu^2)},&\end{aligned} \tag{339}$$

where we have now divided back through by $\dfrac{(\xi^2-1)(1-\nu^2)}{(\xi^2-\nu^2)}$. We separate the term on the RHS by writing:

$$\frac{\mu^2(\xi^2-\nu^2)}{(\xi^2-1)(1-\nu^2)}=\frac{\mu^2}{(1-\nu^2)}+\frac{\mu^2}{(\xi^2-1)}, \tag{340}$$

and, with foresight, write $(\xi^2-\nu^2)=(\xi^2-1)+(1-\nu^2)$, to obtain:

$$\begin{aligned}&\frac{\partial}{\partial\xi}\left((\xi^2-1)\frac{\partial p(\xi)}{\partial\xi}\right)\frac{1}{p(\xi)}-\frac{\mu^2}{(\xi^2-1)}+\gamma^2(\xi^2-1)\\ &=-\frac{\partial}{\partial\nu}\left((1-\nu^2)\frac{\partial q(\nu)}{\partial\nu}\right)\frac{1}{q(\nu)}+\frac{\mu^2}{(1-\nu^2)}-\gamma^2(1-\nu^2).\end{aligned} \tag{341}$$

With no change to our equations we can add γ^2 to both sides, and we set equal to a constant λ:

$$\begin{aligned}&\frac{\partial}{\partial\xi}\left((\xi^2-1)\frac{\partial p(\xi)}{\partial\xi}\right)\frac{1}{p(\xi)}-\frac{\mu^2}{(\xi^2-1)}+\gamma^2(\xi^2-1)+\gamma\\ &=-\frac{\partial}{\partial\nu}\left((1-\nu^2)\frac{\partial q(\nu)}{\partial\nu}\right)\frac{1}{q(\nu)}+\frac{\mu^2}{(1-\nu^2)}-\gamma^2(1-\nu^2)+\gamma\\ &=\lambda\end{aligned} \tag{342}$$

Our final two ODE's are therefore:

$$(\zeta^2-1)p''+2\zeta p'-\left(\lambda-\gamma^2\zeta^2+\frac{\mu^2}{(\xi^2-1)}\right)p=0, \tag{343}$$

and:

$$(1-\nu^2)q''-2\nu q'+\left(\lambda-\gamma^2\mu^2-\frac{\mu^2}{(1-\nu^2)}\right)q=0. \tag{344}$$

Our system of separated ODE's is now:

$$\begin{aligned}
&1. \qquad T'+\kappa^2 D_{\text{nuc}}T=0,\\
&2. \qquad s''+\mu^2 s=0,\\
&3. \qquad (\zeta^2-1)p''+2\zeta p'-\left(\lambda-\gamma^2\zeta^2+\frac{\mu^2}{(\xi^2-1)}\right)p=0,\\
&4. \qquad (1-\nu^2)q''-2\nu q'+\left(\lambda-\gamma^2\mu^2-\frac{\mu^2}{(1-\nu^2)}\right)q=0,
\end{aligned} \tag{345}$$

with separation constants $-\kappa^2$, μ^2 and λ. Clearly Eqs. 3. and 4. of (345) are of identical form however they are defined over different ranges of the independent variable with $-1 \leq \mu \leq 1$ and $1 \leq \zeta \leq \zeta_0$. These equations must be solved subject to the corresponding boundary/initial conditions:

$$\begin{aligned}
&1. \qquad u(\xi,\nu,\phi,0)=T_0\\
&2. \qquad u(\xi,\nu,0,t)=u(\xi,\nu,2\pi,t)\\
&3. \qquad \left.\frac{\mathrm{d}u(\xi,\nu,\phi,t)}{\mathrm{d}t}\right|_{\xi=\xi_0}=0, \qquad \lim_{\xi\to 1}u(\xi,\nu,\phi,t)<\infty,\\
&4. \qquad \lim_{\nu\to\pm 1}u(\xi,\nu,\phi,t)<\infty.
\end{aligned} \tag{346}$$

Eq. 1 of Eq. (345) has form identical to that in the spherical case and hence as previously the solution is given by:

$$T(t)=T_0\mathrm{e}^{-\kappa^2 D_{\text{nuc}}t}. \tag{347}$$

The solution in the ϕ direction is given by:

$$s(\phi)=A_1\cos(\mu\phi)+B_1\sin(\mu\phi), \tag{348}$$

with the boundary condition satisfied provide that μ is a non-negative integer; $m = 0, 1, 2, ...$ Eq. 3 of Eq. (345) is the radial spheroidal wave equation whose general solution is the linear combination of the radial prolate spheroidal radial wave function's of the first and second kind:

$$P(\xi) = A_2 R^{(1)}_{\mathrm{ml}}(\xi, \gamma) + B_2 R^{(2)}_{\mathrm{ml}}(\xi, \gamma). \tag{349}$$

The radial functions are a generalisation of the spherical Bessel functions and hence, as the spherical Bessel function of the second kind is unbounded, $R^{(2)}_{\mathrm{n}}$ is also unbounded and we let $B_2 = 0$:

$$p(\xi) = A_2 R^{(1)}_{\mathrm{ml}}(\xi, \gamma), \tag{350}$$

The no flux boundary condition is applied at $\xi = \xi_0$ to give the eigenvalue problem:

$$R^{(1)\prime}{}_{\mathrm{ml}}(\xi_0, \gamma_{\mathrm{mlp}}) = 0, \tag{351}$$

where the eigenvalue γ_{mlp} denotes the p^{th} zero of derivative of the m^{th} order, l^{th} degree, radial prolate spheroidal wave function.

The general solution of Eq. 4 of Eq. (345) is the angular prolate spheroidal wave function (a generalisation of the Legendre function):

$$q(\nu) = A_3 S_{\mathrm{ml}}(\nu, \gamma), \tag{352}$$

with the degree l giving the number of zeros in the interval $\nu \in (-1, 1)$. We require that u is bounded along the z-axis away from the focal line, this requires $q(\nu)$ to be bounded when $\nu < |1|$ and hence $\lambda = \lambda_{\mathrm{ml}}(\gamma)$ for $m = 0, 1, 2...$ and $l = m, m + 1, m + 2, ...$

We can write our solution as:

$$u(\xi, \nu, \phi, t) = A_{\mathrm{mlp}} R^{(1)}_{\mathrm{ml}}(\xi, \gamma_{\mathrm{mlp}}) S_{\mathrm{ml}}(\nu, \gamma_{\mathrm{mlp}}) \begin{matrix} \sin(m\phi) \\ \cos(m\phi) \end{matrix} \mathrm{e}^{-k^2 D_{\mathrm{nuc}} t}, \tag{353}$$

where we have combined our constants A_1, A_2 and A_3 into A_{mlp}. The normalisation factors are given by the orthogonality condition:

$$\int_0^{2\pi}\int_{-1}^{1}\int_{1}^{\xi_0} u_{\mathrm{ml}}(\xi,\nu,\phi)u_{\mathrm{nk}}(\xi,\nu,\phi)\sqrt{(\xi^2-1)}\sqrt{(1-\nu^2)}(\xi^2-\nu^2)\mathrm{d}\xi\mathrm{d}\nu\mathrm{d}\phi$$
$$=\begin{cases}0, & m\neq n, l\neq k,\\ N_{\mathrm{mn}}, & m=n, l=k.\end{cases} \tag{354}$$

and our initial condition:

$$u(\xi,\nu,\phi)=p_0(\xi)q_0(\nu)s_0(\phi)=A_{\mathrm{mlp}}R^{(1)}_{\mathrm{ml}}(\xi,\gamma_{\mathrm{mlp}})S_{\mathrm{ml}}(\nu,\gamma_{\mathrm{mlp}})\frac{\sin(m\phi)}{\cos(m\phi)}, \tag{355}$$

is therefore multiplied by $R^{(1)}_{\mathrm{nk}}(\xi,\gamma_{\mathrm{nkp}})S_{\mathrm{nk}}(\nu,\gamma_{\mathrm{nkp}})\frac{\sin(n\phi)}{\cos(n\phi)}\sqrt{(\xi^2-1)}\sqrt{(1-\nu^2)}(\xi^2-\nu^2)$ and we integrate over our domain to obtain the coefficient:

$$A_{\mathrm{mlp}}=\frac{1}{N_{\mathrm{ml}}}\int_0^{2\pi}\int_{-1}^{1}\int_{1}^{\xi_0} p_0(\xi)q_0(\nu)s_0(\phi)R^{(1)}_{\mathrm{ml}}(\xi',\gamma_{\mathrm{mlp}})S_{\mathrm{ml}}(\nu',\gamma_{\mathrm{mlp}})$$
$$\times\frac{\sin(m\phi')}{\cos(m\phi')}\sqrt{(\xi^2-1)}\sqrt{(1-\nu^2)}(\xi^2-\nu^2)\mathrm{d}\xi\mathrm{d}\nu\mathrm{d}\phi. \tag{356}$$

Finally this gives:

$$v(\xi,\nu,\phi,t)=$$
$$\sum_{m=1}^{\infty}\sum_{l=m,m+1,}^{\infty}\sum_{p=1}^{\infty}\frac{1}{\pi N_{\mathrm{ml}}}\int_0^{2\pi}\int_{-1}^{1}\int_{1}^{\xi_0} p_0(\xi)q_0(\nu)s_0(\phi)R^{(1)}_{\mathrm{ml}}(\xi',\gamma_{\mathrm{mlp}})R^{(1)}_{\mathrm{ml}}(\xi,\gamma_{\mathrm{mlp}})$$
$$\times S_{\mathrm{ml}}(\nu,\gamma_{\mathrm{mlp}})S_{\mathrm{ml}}(\nu',\gamma_{\mathrm{mlp}})\frac{\sin(m\phi)\sin(m\phi')}{\cos(m\phi)\cos(m\phi')}\sqrt{(\xi^2-1)}\sqrt{(1-\nu^2)}(\xi^2-\nu^2)$$
$$\times\mathrm{d}\xi\mathrm{d}\nu\mathrm{d}\phi\mathrm{e}^{-k^2D_{\mathrm{nuc}}t}$$
$$+\sum_{l=0}^{\infty}\sum_{p=1}^{\infty}\frac{1}{2\pi N_{0l}}\int_0^{2\pi}\int_{-1}^{1}\int_{1}^{\xi_0} p_0(\xi)q_0(\nu)s_0(\phi)R^{(1)}_{0l}(\xi',\gamma_{0lp})R^{(1)}_{0l}(\xi,\gamma_{0lp})$$
$$\times S_{0l}(\nu,\gamma_{0lp})S_{0l}(\nu',\gamma_{0lp})\sqrt{(\xi^2-1)}\sqrt{(1-\nu^2)}(\xi^2-\nu^2)\mathrm{d}\xi\mathrm{d}\nu\mathrm{d}\phi\mathrm{e}^{-k^2D_{\mathrm{nuc}}t}, \tag{357}$$

such that u is in the form:

$$u(\xi,\nu,\phi,t)=\int_D u_0(\xi,\nu,\phi,0)G(\xi,\xi',\nu,\nu',\phi,\phi',t)\mathrm{d}\Omega, \tag{358}$$

with initial condition:

$$u_0(\xi,\nu,\phi,0) = p_0(\xi)q_0(\nu)s_0(\phi)T_0, \tag{359}$$

and Green's function:

$$\begin{aligned}
&G(\xi,\xi',\nu,\nu',\phi,\phi',t) = \\
&\sum_{m=1}^{\infty}\sum_{l=m,m+1,}^{\infty}\sum_{p=1}^{\infty}\frac{1}{\pi N_{\mathrm{ml}}}R^{(1)}_{\mathrm{ml}}(\xi',\gamma_{\mathrm{mlp}})R^{(1)}_{\mathrm{ml}}(\xi,\gamma_{\mathrm{mlp}})S_{\mathrm{ml}}(\nu,\gamma_{\mathrm{mlp}}) \\
&\times S_{\mathrm{ml}}(\nu',\gamma_{\mathrm{mlp}})\frac{\sin(m\phi)\sin(m\phi')}{\cos(m\phi)\cos(m\phi')}\mathrm{e}^{-k^2D_{\mathrm{nuc}}t} \\
&+\sum_{l=0}^{\infty}\sum_{p=1}^{\infty}\frac{1}{2\pi N_{0l}}R^{(1)}_{0l}(\xi',\gamma_{0lp})R^{(1)}_{0l}(\xi,\gamma_{0lp})S_{0l}(\nu,\gamma_{0lp})S_{0l}(\nu',\gamma_{0lp})\mathrm{e}^{-k^2D_{\mathrm{nuc}}t} \\
&+\frac{1}{V}.
\end{aligned} \tag{360}$$

B.2 PERINUCLEAR SPACE

The Green's function is derived as in Section B.1, however we now have the domain:

$$\xi_0 \le \xi \le \xi_0, \qquad -1 \le \nu \le 1, \qquad 0 \le \phi < 2\pi. \tag{361}$$

where ξ_1 is the surface of the outer nuclear membrane given by:

$$\xi_1 = \frac{b_1}{c_1}. \tag{362}$$

for our second focal point $c_1 = \sqrt{b_1^2 - a_1^2}$, such that $c_1 > c$ and $a_1 = a + h$ and $b_1 = b + h$ are the radii of the minor and major-axis respectively as seen in Figure. 22.

Recalling the equation for the radial dynamics given by Eq. 3. (345) whose solution is a linear combination of the spheroidal radial wave functions of the first and second kind:

$$P(\xi) = A_2R^{(1)}_{\mathrm{ml}}(\xi,\gamma) + B_2R^{(2)}_{\mathrm{ml}}(\xi,\gamma), \tag{363}$$

We notice that in this case we are unable to set $B_2 = 0$ as we do not consider the region containing $\xi = 1$, where $R^{(2)}_{\mathrm{ml}}(\xi, \gamma)$ becomes unbounded. We must now therefore apply the no flux boundary condition on both radial boundaries:

$$\frac{d}{d\xi}\left[p(\xi)\right]|_{\xi=\xi_0} = 0, \qquad\qquad \frac{d}{d\xi}\left[p(\xi)\right]|_{\xi=\xi_1} = 0, \tag{364}$$

which results in the system:

$$\begin{bmatrix} R^{'(1)}_{\mathrm{ml}}(\xi_0, \gamma_{\mathrm{mlp}}) & R^{'(2)}_{\mathrm{ml}}(\xi_0, \gamma_{\mathrm{mlp}}) \\ R^{'(1)}_{\mathrm{ml}}(\xi_1, \gamma_{\mathrm{mlp}}) & R^{'(2)}_{\mathrm{ml}}(\xi_1, \gamma_{\mathrm{mlp}}) \end{bmatrix} \begin{bmatrix} A_2 \\ B_2 \end{bmatrix} = \begin{bmatrix} 0 \\ 0 \end{bmatrix}. \tag{365}$$

As we require $A_1, B_1 \neq 0$ we obtain the condition:

$$R^{'(1)}_{\mathrm{ml}}(\xi_0, \gamma_{\mathrm{mlp}}) R^{'(2)}_{\mathrm{ml}}(\xi_1, \gamma_{\mathrm{mlp}}) - R^{'(2)}_{\mathrm{ml}}(\xi_0, \gamma_{\mathrm{mlp}}) R^{'(1)}_{\mathrm{ml}}(\xi_1, \gamma_{\mathrm{mlp}}) = 0, \tag{366}$$

an eigenvalue problem where, as before, γ_{mlp} is the p^{th} solution to the m^{th} order, l^{th} degree problem. We also see from our boundary conditions that we can write:

$$B_2 = -A_2 \frac{R^{'(1)}_{\mathrm{ml}}(\xi_1, \gamma_{\mathrm{mlp}})}{R^{'(2)}_{\mathrm{ml}}(\xi_1, \gamma_{\mathrm{mlp}})}, \tag{367}$$

and hence we can write:

$$p_{\mathrm{ml}}(\xi, \gamma_{\mathrm{mlp}}) = R^{(1)}_{\mathrm{ml}}(\xi, \gamma) + C R^{(2)}_{\mathrm{ml}}(\xi, \gamma)), \tag{368}$$

where:

$$C = \frac{R^{'(1)}_{\mathrm{ml}}(\xi_1, \gamma_{\mathrm{mlp}})}{R^{'(2)}_{\mathrm{ml}}(\xi_1, \gamma_{\mathrm{mlp}})}, \tag{369}$$

Combining this result with the angular and temporal solutions found in Section B.1, we have:

$$v(\xi, \nu, \phi, t) = A_{\mathrm{mlp}} Z_{\mathrm{ml}}(\xi, \gamma_{\mathrm{mlp}}) S_{\mathrm{ml}}(\nu, \gamma_{\mathrm{mlp}}) \frac{\sin(m\phi)}{\cos(m\phi)} \mathrm{e}^{-k^2 D t}, \tag{370}$$

where we have written:

$$Z_{\mathrm{ml}}(\xi, \gamma_{\mathrm{mlp}}) = R^{(1)}_{\mathrm{ml}}(\xi, \gamma_{\mathrm{mlp}}) + C R^{(2)}_{\mathrm{ml}}(\xi, \gamma_{\mathrm{mlp}}). \tag{371}$$

Fixing l we find the value of our coefficient using the orthogonality relation as in Ziener (2015):

$$\int_{-1}^{1}\int_{\xi 0}^{\xi 1} Z_{\mathrm{ml}}(\xi,\gamma_{\mathrm{mlp}})S_{\mathrm{ml}}(\nu,\gamma_{\mathrm{mlp}})Z_{\mathrm{nl}}(\xi,\gamma_{\mathrm{nlq}})S_{\mathrm{nl}}(\nu,\gamma_{\mathrm{nlq}}) \\ (\xi^2-\nu^2)\mathrm{d}\xi\mathrm{d}\nu = \delta_{\mathrm{mn}}, \tag{372}$$

[94]. We multiply the spatial part of our initial condition:

$$v(\xi,\nu,\phi,0) = p_0(\xi)q_0(\nu)s_0(\phi) = A_{\mathrm{mlp}}Z_{\mathrm{ml}}(\xi,\gamma_{\mathrm{mlp}})S_{\mathrm{ml}}(\nu,\gamma_{\mathrm{mlp}})\begin{matrix}\sin(m\phi)\\ \cos(m\phi)\end{matrix}, \tag{373}$$

by $Z_{\mathrm{nk}}(\xi,\gamma_{\mathrm{nkp}})S_{\mathrm{nk}}(\nu,\gamma_{\mathrm{nkp}})\begin{smallmatrix}\sin(n\phi)\\ \cos(n\phi)\end{smallmatrix}\sqrt{(\xi^2-1)}\sqrt{(1-\nu^2)}(\xi^2-\nu^2)$, and integrate over our domain to find:

$$A_{\mathrm{mlp}} = \\ \frac{1}{N_{\mathrm{ml}}}\int_0^{2\pi}\int_{-1}^{1}\int_{\xi_0}^{\xi_1} p_0(\xi)q_0(\nu)s_0(\phi)Z_{\mathrm{ml}}(\xi',\gamma_{\mathrm{mlp}})S_{\mathrm{ml}}(\nu',\gamma_{\mathrm{mlp}}) \\ \times \begin{matrix}\sin(m\phi')\\ \cos(m\phi')\end{matrix}\sqrt{(\xi^2-1)}\sqrt{(1-\nu^2)}(\xi^2-\nu^2)\mathrm{d}\xi\mathrm{d}\nu\mathrm{d}\phi. \tag{374}$$

The final solution is therefore:

$$v(\xi,\nu,\phi,t) = \\ \sum_{m=1}^{\infty}\sum_{l=m,m+1,}^{\infty}\sum_{p=1}^{\infty}\frac{1}{\pi N_{\mathrm{ml}}}\int_0^{2\pi}\int_{-1}^{1}\int_{\xi_0}^{\xi_1} p_0(\xi)q_0(\nu)s_0(\phi)Z_{\mathrm{ml}}(\xi',\gamma_{\mathrm{mlp}}) \\ \times Z_{\mathrm{ml}}(\xi,\gamma_{\mathrm{mlp}})S_{\mathrm{ml}}(\nu,\gamma_{\mathrm{mlp}})S_{\mathrm{ml}}(\nu',\gamma_{\mathrm{mlp}})\begin{matrix}\sin(m\phi)\sin(m\phi')\\ \cos(m\phi)\cos(m\phi')\end{matrix}\sqrt{(\xi^2-1)} \\ \times\sqrt{(1-\nu^2)}(\xi^2-\nu^2)\mathrm{d}\xi\mathrm{d}\nu\mathrm{d}\phi\mathrm{e}^{-k^2 D_{\mathrm{pns}}t} \\ +\sum_{l=0}^{\infty}\sum_{p=1}^{\infty}\frac{1}{2\pi N_{0l}}\int_0^{2\pi}\int_{-1}^{1}\int_{\xi_0}^{\xi_1} p_0(\xi)q_0(\nu)s_0(\phi)Z_{0l}(\xi',\gamma_{0lp})Z_{0l}(\xi,\gamma_{0lp}) \\ \times S_{0l}(\nu,\gamma_{0lp})S_{0l}(\nu',\gamma_{0lp})\sqrt{(\xi^2-1)}\sqrt{(1-\nu^2)}(\xi^2-\nu^2)\mathrm{d}\xi\mathrm{d}\nu\mathrm{d}\phi\mathrm{e}^{-k^2 D_{\mathrm{pns}}t}, \tag{375}$$

such that U is in the form of Eq. (358), with initial conditions as in Eq. (359), and Green's function:

$$\begin{aligned}
&G(\xi,\xi',\nu,\nu',\phi,\phi',t) = \\
&\sum_{m=1}^{\infty}\sum_{l=m,m+1,}^{\infty}\sum_{p=1}^{\infty}\frac{1}{\pi N_{\mathrm{ml}}}Z_{\mathrm{ml}}(\xi',\gamma_{\mathrm{mlp}})Z_{\mathrm{ml}}(\xi,\gamma_{\mathrm{mlp}})S_{\mathrm{ml}}(\nu,\gamma_{\mathrm{mlp}})S_{\mathrm{ml}}(\nu',\gamma_{\mathrm{mlp}}) \\
&\times \begin{array}{c}\sin(m\phi)\sin(m\phi') \\ \cos(m\phi)\cos(m\phi')\end{array}\mathrm{e}^{-k^2 D_{\mathrm{pns}} t} \\
&+\sum_{l=0}^{\infty}\sum_{p=1}^{\infty}\frac{1}{2\pi N_{0l}}Z_{0l}(\xi',\gamma_{0lp})Z_{0l}(\xi,\gamma_{0lp})S_{0l}(\nu,\gamma_{0lp})S_{0l}(\nu',\gamma_{0lp})\mathrm{e}^{-k^2 D_{\mathrm{pns}} t} \\
&+\frac{1}{V}.
\end{aligned} \tag{376}$$

C

SUPPLEMENTARY FIGURES AND DATA

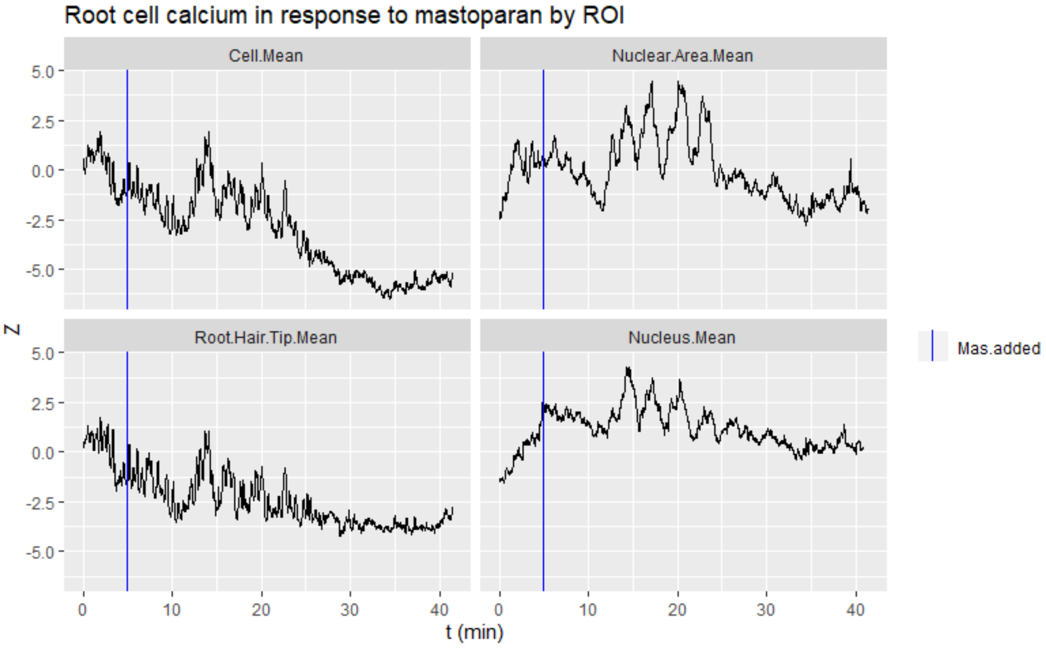

Figure 80.: Calcium response for Nucleus 1 measured over 4 ROI's corresponding to those described in 53.

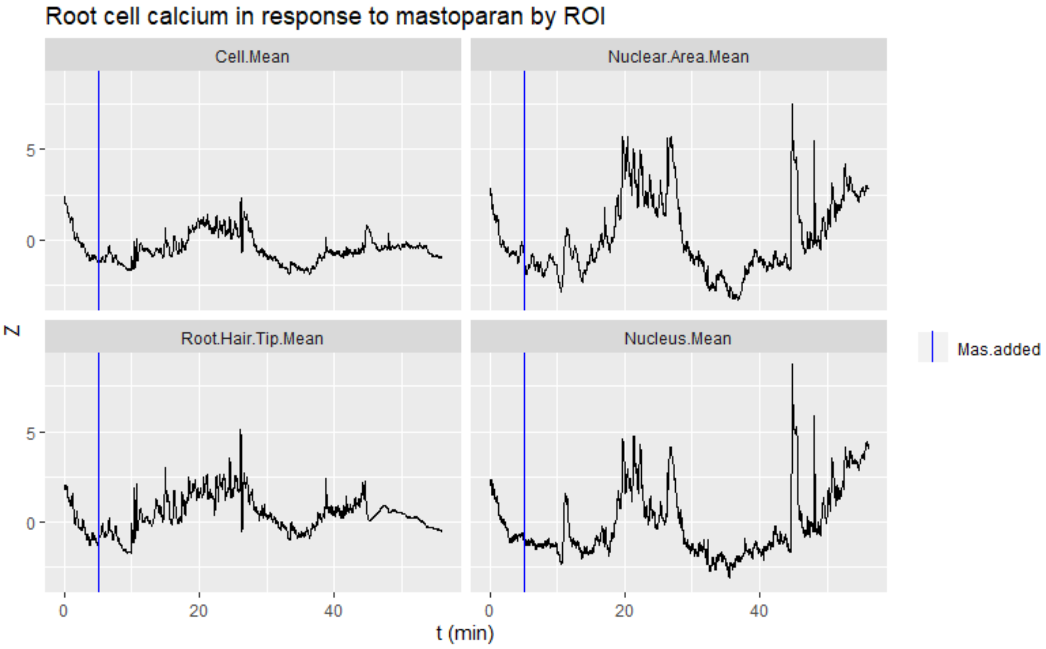

Figure 81.: Calcium response for Nucleus 2 measured over 4 ROI's corresponding to those described in 53.

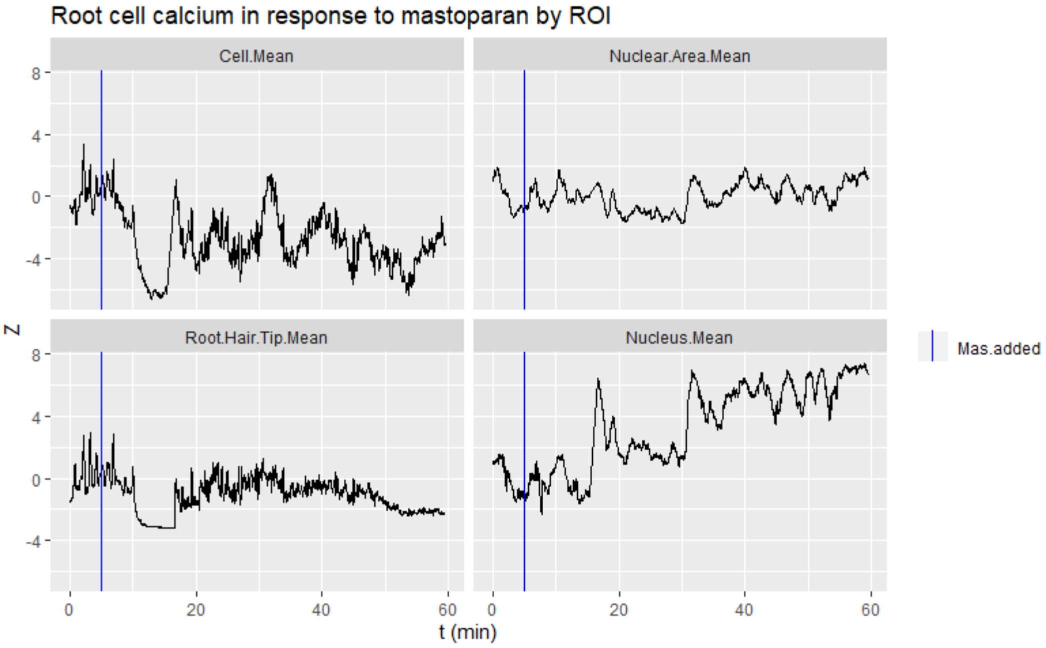

Figure 82.: Calcium response for Nucleus 3 measured over 4 ROI's corresponding to those described in 53.

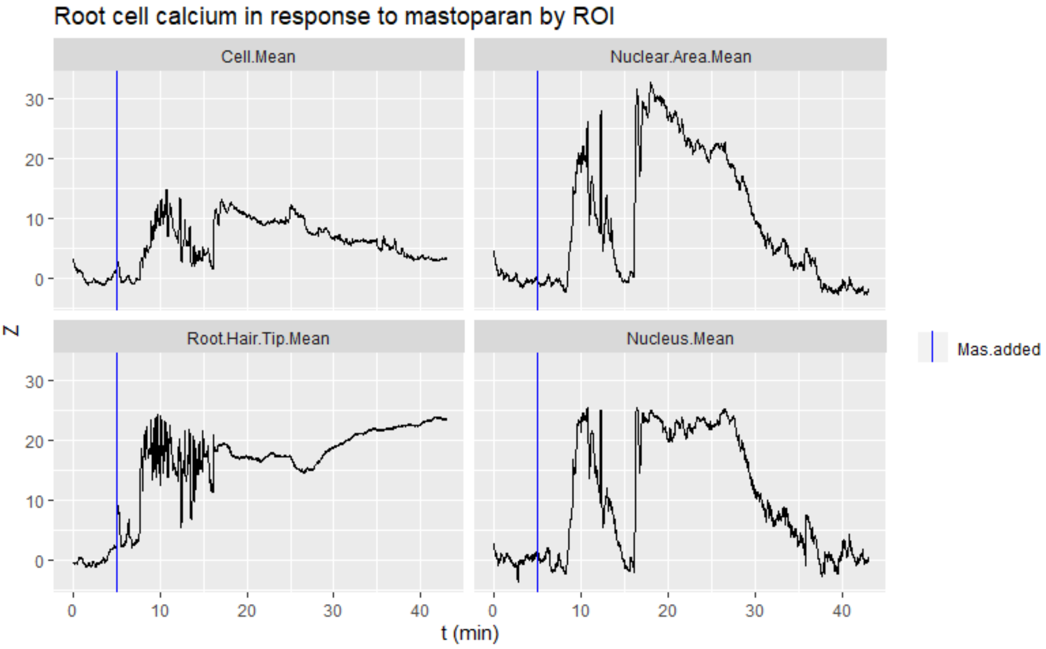

Figure 83.: Calcium response for Nucleus 4 measured over 4 ROI's corresponding to those described in 53.

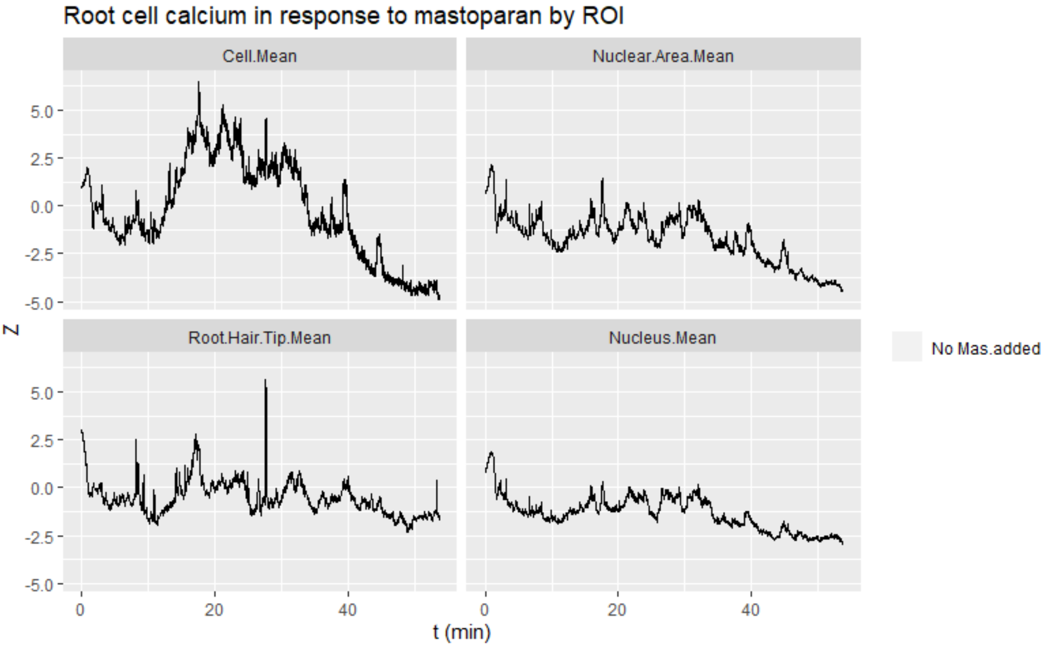

Figure 84.: Calcium response for control 1 measured over 4 ROI's corresponding to those described in 53.

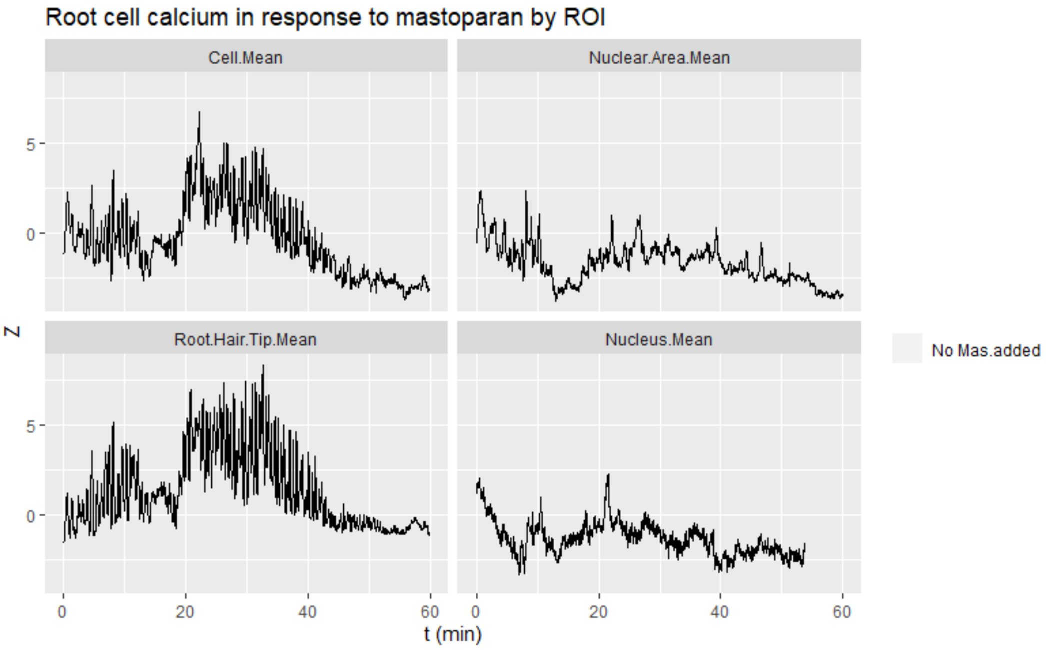

Figure 85.: Calcium response for control 2 measured over 4 ROI's corresponding to those described in 53.

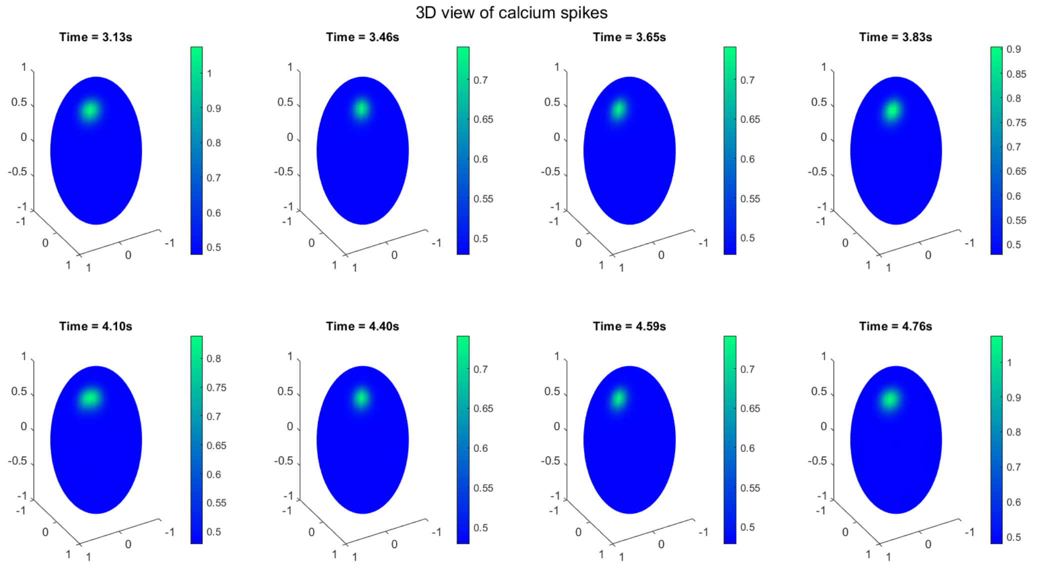

(a)

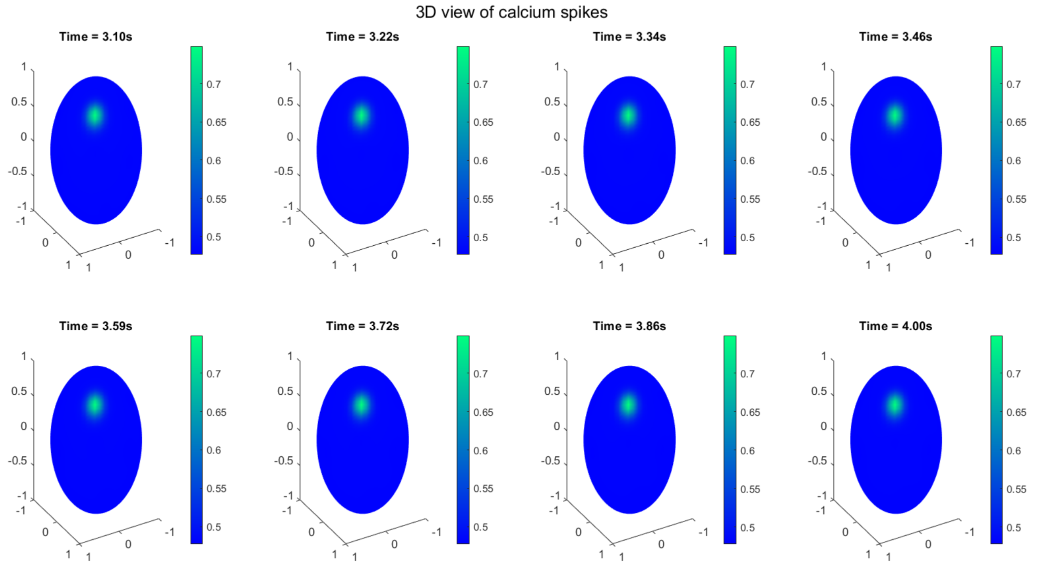

(b)

Figure 86.: Figure showing the different spiking patterns of clusters of varying numbers of channels, with all other simulation conditions remaining equal.

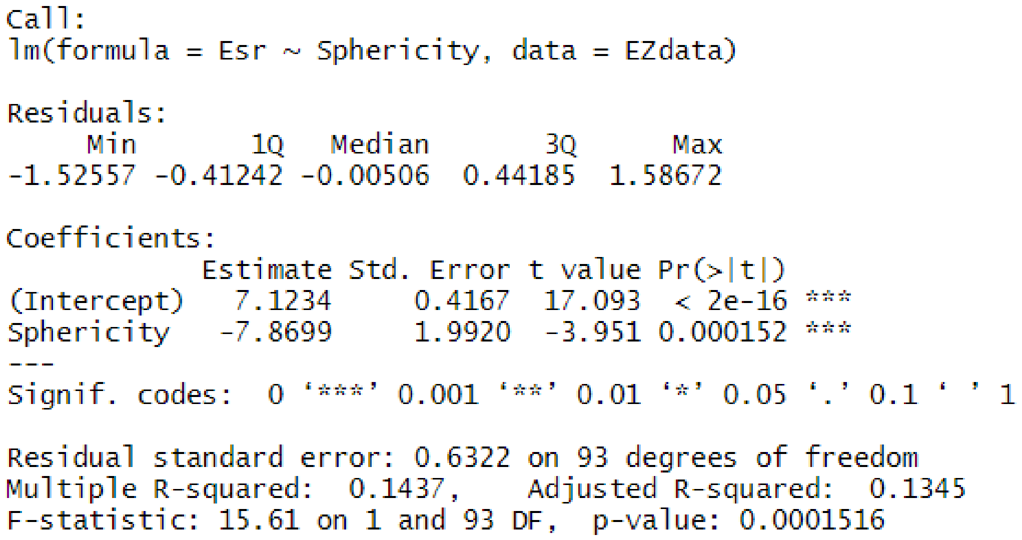

```
Call:
lm(formula = Esr ~ Sphericity, data = EZdata)

Residuals:
     Min       1Q   Median       3Q      Max 
-1.52557 -0.41242 -0.00506  0.44185  1.58672 

Coefficients:
            Estimate Std. Error t value Pr(>|t|)    
(Intercept)   7.1234     0.4167  17.093  < 2e-16 ***
Sphericity   -7.8699     1.9920  -3.951 0.000152 ***
---
Signif. codes:  0 ‘***’ 0.001 ‘**’ 0.01 ‘*’ 0.05 ‘.’ 0.1 ‘ ’ 1

Residual standard error: 0.6322 on 93 degrees of freedom
Multiple R-squared:  0.1437,    Adjusted R-squared:  0.1345 
F-statistic: 15.61 on 1 and 93 DF,  p-value: 0.0001516
```

(a)

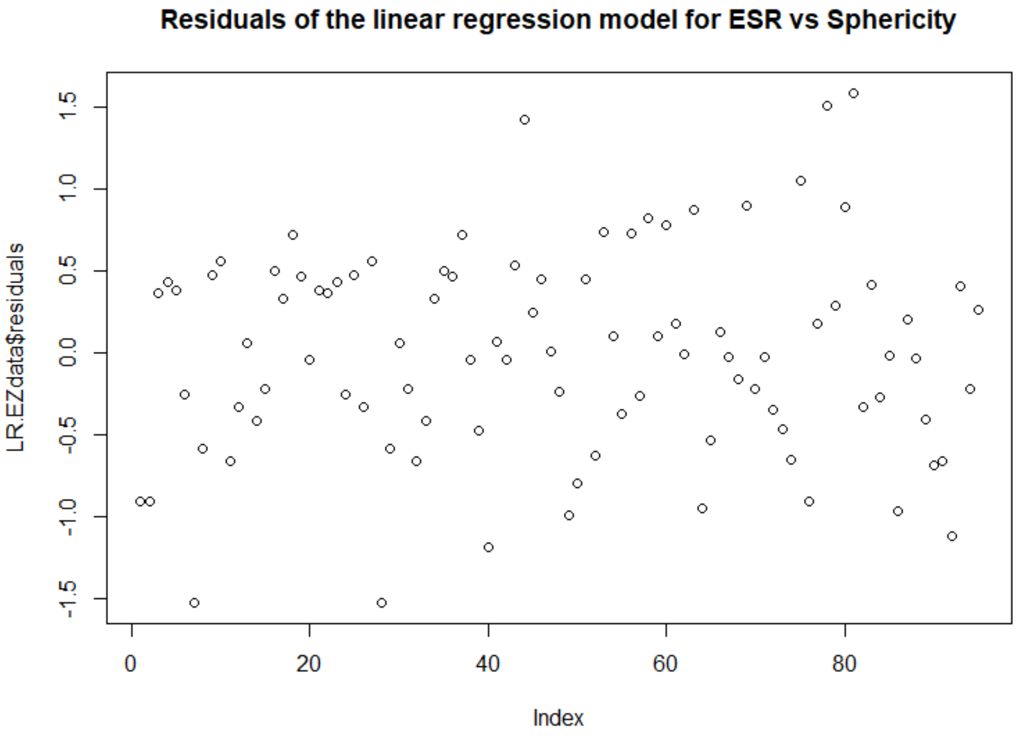

(b)

Figure 87.: The relationship between nuclear size and geometry in the root EZ.

BIBLIOGRAPHY

[1] Beyond the Human Eye: Bacterial Root Nodules. http://beyondthehumaneye.blogspot.com/2011/08/root-noldes.html. Date Accessed: 2018-06-14.

[2] Distributing points on the sphere | School of Mathematics and Statistics. https://www.maths.unsw.edu.au/about/distributing-points-sphere. Date Accessed: 2019-07-19.

[3] Gulf of Mexico 'dead zone' is the largest ever measured | National Oceanic and Atmospheric Administration. https://www.noaa.gov/media-release/gulf-of-mexico-dead-zone-is-largest-ever-measured. Date Accessed: 2019-06-26.

[4] ImageJ Information and Documentation Portal. https://imagejdocu.tudor.lu. Date Accessed: 2021-08-26.

[5] World fertilizer trends and outlook to 2018. Technical report, Food and Agriculture Organisation of the United Nations, 2018.

[6] Rajai Alassar, Mohammed Abushosha, and Mohammed El-gebeily. Transient Heat Conduction from Spheroids. 38(3):373–389, 2014.

[7] George B. Arfken, Hans J. Weber, and Frank E. Harris. Mathematical Methods for Physicists. chapter 32. 7th edition, 2012.

[8] Ling Bai, Xiaonan Ma, Guozeng Zhang, Shufei Song, Yun Zhou, Lijie Gao, Yuchen Miao, and Chun-Peng Song. A Receptor-Like Kinase Mediates Ammonium Homeostasis and Is Important for the Polar Growth of Root Hairs in Arabidopsis. *The Plant cell*, 26(4):1497–1511, 4 2014.

[9] María Laura Barberini, Lorena Sigaut, Weijie Huang, Silvina Mangano, Silvina Paola Denita Juarez, Eliana Marzol, José Estevez, Mariana Obertello, Lía Pietrasanta, Weihua Tang, and Jorge Muschietti. Calcium dynamics in tomato pollen tubes using the Yellow Cameleon 3.6 sensor. *Plant Reproduction*, 31(2):159–169, 6 2018.

[10] David G Barker, Mireille Chabaud, Guilia Russo, and Andrea Genre. Nuclear calcium signalling in arbuscular mycorrhizal and actinorhizal endosymbioses: on the trail of novel underground signals. *The New Phytologist*, 214(2):533–538, 2017.

[11] Gabriel. Barton. *Elements of Green's functions and propagation*. Clarendon Press, 2005.

[12] M J Berridge, P Lipp, and M D Bootman. The versatility and universality of calcium signalling. *Nature Reviews. Molecular cell biology*, 1(1):11–21, 2000.

[13] Tatiana Bibikova and Simon Gilroy. Root Hair Development. *Journal of Plant Growth Regulation*, 21(4):383–415, 12 2002.

[14] Arnie L Van Buren Boisvert and Jeffrey E. Improved calculation of prolate spheoidal radial functions of the second kind and their first derivatives. *Quarterly of Applied Mathematics*, 62(3):493–507, 2004.

[15] Christian Brière, Tou Cheu Xiong, Christian Mazars, and Raoul Ranjeva. Autonomous regulation of free Ca2+ concentrations in isolated plant cell nuclei: A mathematical analysis. *Cell Calcium*, 39(4):293–303, 2006.

[16] Chris Brimacombe, Robert M. Corless, and Mair Zamir. Computation and applications of Mathieu functions: A historical perspective. *arXiv*, pages 1–63, 2020.

[17] Joseph A Brzostowski, Tobias Meckel, Jiang Hong, Alice Chen, and Tian Jin. Imaging protein-protein interactions by förster resonance energy transfer (FRET) microscopy in live cells, 4 2009.

[18] Herdi Budiman and Jamalludin Talib. Prolate spheroidal coordinate: an approximation to modeling of ellipsoidal drops in rotating disc contractor column. *Journal of Science and Technology*, pages 87–96, 2010.

[19] Roy Burrill, Thomas Jonathan; Hansen. Is symbiosis possible between legume bacteria and non-legume plants? *Bulletin (University of Illinois (Urbana-Champaign campus). Agricultural Experiment Station) ; no. 202*, 1917.

[20] Alessia Candeo, Fabrizio G. Doccula, Gianluca Valentini, Andrea Bassi, and Alex Costa. Light Sheet Fluorescence Microscopy Quantifies Calcium Oscillations in Root Hairs of Arabidopsis thaliana. *Plant and Cell Physiology*, 58(7), 2017.

[21] Ward Capoen, Jongho Sun, Derin Wysham, Marisa S Otegui, Muthusubramanian Venkateshwaran, Sibylle Hirsch, Hiroki Miwa, J Allan Downie, Richard J Morris, Jean-Michel Ané, and Giles E D Oldroyd. Nuclear membranes control symbiotic calcium signaling of legumes. *Proceedings of the National Academy of Sciences of the United States of America*, 108(34):14348–53, 8 2011.

[22] Luis Cárdenas, Alenka Lovy-Wheeler, Joseph G Kunkel, and Peter K Hepler. Pollen tube growth oscillations and intracellular calcium levels are reversibly modulated by actin polymerization. *Plant physiology*, 146(4):1611–21, 4 2008.

[23] Amado Carreras-Sureda, Philippe Pihán, and Claudio Hetz. Calcium signaling at the endoplasmic reticulum: fine-tuning stress responses. *Cell Calcium*, 70:24–31, 3 2018.

[24] Jaeger J.C Carslaw, H.S. *Conduction of Heat in Solids*.

[25] Myriam Charpentier. Calcium signals in the plant nucleus: Origin and function, 4 2018.

[26] Myriam Charpentier and Giles E D Oldroyd. Nuclear calcium signaling in plants. *Plant Physiology*, 163(2):496–503, 2013.

[27] Myriam Charpentier, Jongho Sun, Teresa Vaz Martins, Guru V Radhakrishnan, Kim Findlay, Eleni Soumpourou, Julien Thouin, Anne-Aliénor Véry, Dale Sanders, Richard J Morris, and Giles E D Oldroyd. Nuclear-localized cyclic nucleotide-gated channels mediate symbiotic calcium oscillations. *Science (New York, N.Y.)*, 352(6289):1102–5, 5 2016.

[28] Myriam Charpentier, Teresa Vaz Martins, Emma Granqvist, Giles E D Oldroyd, and Richard J Morris. The role of DMI1 in establishing calcium oscillations in legume symbioses. *Plant Signalling & Behaviour*, 8(2), 2013.

[29] E. Cojocaru. Mathieu functions computational toolbox implemented in Matlab. 2008.

[30] Derek J. Daniel. Exact solutions of Mathieu's equation. *Progress of Theoretical and Experimental Physics*, 2020(4):1–14, 2020.

[31] Irene S Day, Vaka S Reddy, Gul Shad Ali, and A S N Reddy. Analysis of EF-hand-containing proteins in Arabidopsis. *Genome biology*, 3(10), 9 2002.

[32] Thomas A. DeFalco, Wolfgang Moeder, and Keiko Yoshioka. Opening the Gates: Insights into Cyclic Nucleotide-Gated Channel-Mediated Signaling. *Trends in Plant Science*, 21(11):903–906, 11 2016.

[33] Thomas A. Defalco, Masatsugu Toyota, Van Phan, Purva Karia, Wolfgang Moeder, Simon Gilroy, and Keiko Yoshioka. Using GCaMP3 to Study Ca 2+ Signaling in Nicotiana Species. *Plant and Cell Physiology*, 58(7):1173–1184, 2017.

[34] Pierre-Marc Delaux, Nathalie Séjalon-Delmas, Guillaume Bécard, and Jean-Michel Ané. Evolution of the plant–microbe symbiotic 'toolkit'. *Trends in Plant Science*, 18(6):298–304, 6 2013.

[35] Pierre Marc Delaux, Kranthi Varala, Patrick P. Edger, Gloria M. Coruzzi, J. Chris Pires, and Jean Michel Ané. Comparative Phylogenomics Uncovers the Impact of Symbiotic Associations on Host Genome Evolution. *PLoS Genetics*, 10(7), 2014.

[36] Markus Deserno. How to generate equidistributed points on the surface of a sphere. pages 55–128, 2004.

[37] Min Diao, Xiaolu Qu, and Shanjin Huang. Calcium imaging in Arabidopsis pollen cells using G-CaMP5 FA.

[38] Brian S. Donahue and R.F. Abercrombie. Free diffusion coefficient of ionic calcium in cytoplasm. *Cell Calcium*, 8(6):437–448, 12 1987.

[39] David W Ehrhardt, Rebecca Wais, and Sharon R Long. Calcium Spiking in Plant Root Hairs Responding to Rhizobium Nodulation Signals. *Cell*, 85(5):673–681, 5 1996.

[40] Kateryna Fal, Atef Asnacios, Marie Edith Chabouté, and Olivier Hamant. Nuclear envelope: a new frontier in plant mechanosensing?, 2017.

[41] P E Falloon, P C Abbott, and J B Wang. Theory and computation of spheroidal wavefunctions. *Journal of Physics A: Mathematical and General*, 36(20):5477, 2003.

[42] Chun-Miao Feng, Yongjian Qiu, Elise K. Van Buskirk, Emily J. Yang, and Meng Chen. Light-regulated gene repositioning in Arabidopsis. *Nature Communications*, 5(1):3027, 5 2014.

[43] Andrew P. French, Michael H. Wilson, Kim Kenobi, Daniela Dietrich, Ute Voß, Susana Ubeda-Tomás, Tony P. Pridmore, and Darren M. Wells.

Identifying biological landmarks using a novel cell measuring image analysis tool: Cell-o-Tape. *Plant Methods*, 8(1), 2012.

[44] E. Granqvist, D. Wysham, S. Hazledine, W. Kozlowski, J. Sun, M. Charpentier, T. V. Martins, P. Haleux, K. Tsaneva-Atanasova, J. A. Downie, G. E. D. Oldroyd, and R. J. Morris. Buffering Capacity Explains Signal Variation in Symbiotic Calcium Oscillations. *Plant Physiology*, 160(4):2300–2310, 2012.

[45] Claire Grierson, Erik Nielsen, Tijs Ketelaarc, and John Schiefelbein. Root Hairs. *The Arabidopsis Book*, 12, 1 2014.

[46] Qingmei Guan, Jianmin Wu, Xiule Yue, Yanyan Zhang, and Jianhua Zhu. A Nuclear Calcium-Sensing Pathway Is Critical for Gene Regulation and Salt Stress Tolerance in Arabidopsis. *PLoS Genetics*, 9(8), 2013.

[47] J. C. Gutiérrez-Vega, R. M. Rodrı´guez-Dagnino, M. A. Meneses-Nava, and S. Chávez-Cerda. Mathieu functions, a visual approach. *American Journal of Physics*, 71(3):233–242, 2003.

[48] F Hecht. New development in freefem++. *J. Numer. Math*, 20(4):251–265, 2012.

[49] Peter K. Hepler. Tip growth in pollen tubes: calcium leads the way. *Trends in Plant Science*, 2(3):79–80, 3 1997.

[50] Martin W Hetzer. The nuclear envelope., 3 2010.

[51] Feifei Huang, Jin Luo, Tingting Ning, Wenhan Cao, Xi Jin, Heping Zhao, Yingdian Wang, and Shengcheng Han. Cytosolic and nucleosolic calcium signaling in response to osmotic and salt stresses are independent of each other in roots of Arabidopsis seedlings. *Frontiers in Plant Science*, 8:1–13, 2017.

[52] International Fertilizer Association. Statistics Home Page. https://www.fertilizer.org/En/Statistics/Statistics_Databases/En/Statistics/Statistic
d355-48c7-a646-31acd. Date Accessed: 2018-06-14.

[53] M Kern, M Wisniewski, L Cabell, and G Audesirk. Inorganic lead and calcium interact positively in activation of calmodulin. *Neurotoxicology*, 21(3):353–63, 6 2000.

[54] Min Chul Kim, Woo Sik Chung, Dae-Jin Yun, and Moo Je Cho. Calcium and calmodulin-mediated regulation of gene expression in plants. *Molecular Plant*, 2(1):13–21, 2009.

[55] B Klüsener, G Boheim, H Liss, J Engelberth, and E W Weiler. Gadolinium-sensitive, voltage-dependent calcium release channels in the endoplasmic reticulum of a higher plant mechanoreceptor organ. *The EMBO journal*, 14(12):2708–14, 6 1995.

[56] Sonja Kosuta, Saul Hazledine, Jongho Sun, Hiroki Miwa, Richard J Morris, J Allan Downie, and Giles E D Oldroyd. Differential and chaotic calcium signatures in the symbiosis signaling pathway of legumes. *Proceedings of the National Academy of Sciences of the United States of America*, 105(28):9823–8, 2008.

[57] Jörg Kudla, Oliver Batistic, and Kenji Hashimoto. Calcium Signals: The Lead Currency of Plant Information Processing. *The Plant Cell*, 22(3):541–563, 2010.

[58] Nuno Leitão, Pierre Dangeville, Ross Carter, and Myriam Charpentier. Nuclear calcium signatures are associated with root development. *Nature Communications*, 10(1), 2019.

[59] Chaoqun Lu and Hanqin Tian. Global nitrogen and phosphorus fertilizer use for agriculture production in the past half century: shifted hot spots and nutrient imbalance. *Earth Syst. Sci. Data*, 9:181–192, 2017.

[60] Teresa Martins, Matthew Evans, Hugh Woolfenden, and Richard Morris. Towards the Physics of Calcium Signalling in Plants. *Plants*, 2(4):541–588, 2013.

[61] Teresa Vaz Martins, Matthew J. Evans, Derin B. Wysham, and Richard J. Morris. Nuclear pores enable sustained perinuclear calcium oscillations. *BMC Systems Biology*, 10(1):55, 2016.

[62] Iris Meier. Composition of the plant nuclear envelope: Theme and variations. In *Journal of Experimental Botany*, volume 58, pages 27–34. Narnia, 6 2007.

[63] Iris Meier and Jelena Brkljacic. The Arabidopsis Nuclear Pore and Nuclear Envelope. *The Arabidopsis Book*, 8, 2010.

[64] Iris Meier, Eric J. Richards, and David E. Evans. Cell Biology of the Plant Nucleus. *Annual Review of Plant Biology*, 68(1):139–172, 4 2017.

[65] Gabriele B Monshausen, Mark A Messerli, and Simon Gilroy. Imaging of the Yellow Cameleon 3.6 indicator reveals that elevations in cytosolic Ca2+ follow oscillating increases in growth in root hairs of Arabidopsis. *Plant physiology*, 147(4):1690–8, 8 2008.

[66] D Muraro, H M Byrne, J R King, and M J Bennett. Mathematical Modelling Plant Signalling Networks. *Mathematical Modelling of Natural Phenomena*, 8(4):5–24, 2013.

[67] Takeharu Nagai, Shuichi Yamada, Takashi Tominaga, Michinori Ichikawa, and Atsushi Miyawaki. Expanded dynamic range of fluorescent indicators for Ca2+ by circularly permuted yellow fluorescent proteins. *Proceedings of the National Academy of Sciences of the United States of America*, 101(29):10554–10559, 2004.

[68] Martin Peglow, Barbara A Niemeyer, Markus Hoth, and Heiko Rieger. Interplay of channels, pumps and organelle location in calcium microdomain formation. *New Journal of Physics*, 15(5), 5 2013.

[69] Axel Poulet, Ignacio Arganda-Carreras, David Legland, Aline V. Probst, Philippe Andrey, and Christophe Tatout. NucleusJ: An ImageJ plugin for quantifying 3D images of interphase nuclei. *Bioinformatics*, 31(7):1144–1146, 2015.

[70] Gillian Queisser, Simon Wiegert, and Hilmar Bading. Structural dynamics of the cell nucleus. *Nucleus*, 2(2):98–104, 3 2011.

[71] Gillian Queisser and Gabriel Wittum. A method to investigate the diffusion properties of nuclear calcium. *Biological Cybernetics*, 105(3-4):211–216, 2011.

[72] Nicholas Redman. *Flow cell design and set-up*. PhD thesis, University of Nottingham, 2020.

[73] Sebastián A. Romano, Verónica Pérez-Schuster, Adrien Jouary, Jonathan Boulanger-Weill, Alessia Candeo, Thomas Pietri, and Germán Sumbre. An integrated calcium imaging processing toolbox for the analysis of neuronal population dynamics. *PLoS Computational Biology*, 13(6), 2017.

[74] Yoshiro Saimi and Ching Kung. Calmodulin as an Ion Channel Subunit. *Annual Review of Physiology*, 64(1):289–311, 3 2002.

[75] John W Schiefelbein, Al Shipley, and Paul Rowse. Calcium influx at the tip of growing root-hair cells of Arabidopsis thaliana. *Planta*, 187(4):455–459, 1992.

[76] Johannes Schindelin, Ignacio Arganda-Carreras, Erwin Frise, Verena Kaynig, Mark Longair, Tobias Pietzsch, Stephan Preibisch, Curtis Rueden, Stephan Saalfeld, Benjamin Schmid, Jean-Yves Tinevez, Daniel James White, Volker Hartenstein, Kevin Eliceiri, Pavel Tomancak, and Albert Cardona. Fiji: an open-source platform for biological-image analysis. *Nature Methods*, 9(7):676–82, 2012.

[77] Eric C. Schirmer, Nikolaj Zuleger, and Michael I. Robson. The nuclear envelope as a chromatin organizer. *Nucleus*, 2(5):339–349, 2011.

[78] B. J. Sieberer, M. Chabaud, A. C. Timmers, A. Monin, J. Fournier, and D. G. Barker. A Nuclear-Targeted Cameleon Demonstrates Intranuclear Ca2+ Spiking in Medicago truncatula Root Hairs in Response to Rhizobial Nodulation Factors. *Plant Physiology*, 151(3):1197–1206, 11 2009.

[79] Alexander Skupin, Helmut Kettenmann, and Martin Falcke. Calcium Signals Driven by Single Channel Noise. *PLoS Comput Biol*, 6(8):17–19, 2010.

[80] Simon Stael, Bernhard Wurzinger, Andrea Mair, Norbert Mehlmer, Ute C. Vothknecht, and Markus Teige. Plant organellar calcium signalling: An emerging field. *Journal of Experimental Botany*, 63(4):1525–1542, 2012.

[81] J. Sun, H. Miwa, J. A. Downie, and G. E.D. Oldroyd. Mastoparan Activates Calcium Spiking Analogous to Nod Factor-Induced Responses in Medicago truncatula Root Hair Cells. *Plant Physiology*, 144(2):695–702, 2007.

[82] Jongho Sun, J. Benjamin Miller, Emma Granqvist, Audrey Wiley-Kalil, Enrico Gobbato, Fabienne Maillet, Sylvain Cottaz, Eric Samain, Muthusubramanian Venkateshwaran, Sébastien Fort, Richard J. Morris, Jean-Michel Ané, Jean Dénarié, and Giles E.D. Oldroyd. Activation of Symbiosis Signaling by Arbuscular Mycorrhizal Fungi in Legumes and Rice. *The Plant Cell*, 27(3):823–838, 2015.

[83] Jongho Sun, Hiroki Miwa, J Allan Downie, and Giles E D Oldroyd. Mastoparan activates calcium spiking analogous to Nod factor-induced responses in Medicago truncatula root hair cells. *Plant physiology*, 144(2):695–702, 2007.

[84] David J.K. Swainsbury, Liang Zhou, Giles E.D. Oldroyd, and Stephen Bornemann. Calcium ion binding properties of medicago truncatula calcium/calmodulin- dependent protein kinase. *Biochemistry*, 51(35):6897–6907, 9 2012.

[85] Michael R Tadross, Richard W Tsien, and David T Yue. Ca2+ channel nanodomains boost local Ca2+ amplitude. *Proceedings of the National Academy of Sciences of the United States of America*, 110(39):15794–15799, 2013.

[86] Stephen D Thorpe and Myriam Charpentier. Highlight on the dynamic organization of the nucleus. *Nucleus*, 8(1):2–10, 1 2017.

[87] Muthusubramanian Venkateshwaran. Exploring the Feasibility of Transferring Nitrogen Fixation to Cereal Crops. In *Principles of Plant-Microbe Interactions: Microbes for Sustainable Agriculture*, pages 403–410. Springer International Publishing, Cham, 2015.

[88] Thomas R Vincent, James Canham, Masatsugu Toyota, Marieta Avramova, Sam T Mugford, Simon Gilroy, Anthony J Miller, Saskia Hogenhout, and Dale Sanders. Real-time in vivo recording of Arabidopsis calcium signals during insect feeding using a fluorescent biosensor. *Journal of Visualized Experiments*, 2017(126):56142, 2017.

[89] Alex A R Webb, Mark G. Larman, Lucy T. Montgomery, Jane E. Taylor, and Alistair M. Hetherington. The role of calcium in ABA-induced gene expression and stomatal movements. *Plant Journal*, 26(3):351–362, 2001.

[90] Lawrence J. Winship, Caleb Rounds, and Peter K. Hepler. Perturbation analysis of calcium, alkalinity and secretion during growth of lily pollen tubes. *Plants*, 6(1):859–865, 12 2017.

[91] Tou Cheu Xiong, Alain Jauneau, Raoul Ranjeva, and Christian Mazars. Isolated plant nuclei as mechanical and thermal sensors involved in calcium signalling. *The Plant Journal*, 40(1):12–21, 8 2004.

[92] Changfeng Xue and Shaozhong Deng. Green's function and image system for the Laplace operator in the prolate spheroidal geometry. *AIP Advances*, 7(1), 2017.

[93] Xiaohong Zhu, Aaron Taylor, Shenyu Zhang, Dayong Zhang, Ying Feng, Gaimei Liang, and Jian-Kang Zhu. Measuring spatial and temporal calcium signals in Arabidopsis plants. *Journal of Visualized Experiments*, (91):1–9, 9 2014.

[94] Christian H Ziener, Felix T Kurz, Lukas R Buschle, and Thomas Kampf. Orthogonality, Lommel integrals and cross product zeros of linear combinations of Bessel functions. *SpringerPlus*, 2015.

[95] Cyril Zipfel and Giles E. D. Oldroyd. Plant signalling in symbiosis and immunity. *Nature*, 543(7645):328–336, 2017.